

## **ABSTRACT**

BEDDINGFIELD, RICHARD BYRON. High Power Medium Frequency Magnetics for Power Electronics Applications (Under the direction of Dr. Subhashish Bhattacharya).

The development of wide bandgap semiconductors has enabled rapid growth and advancement in power electronics based power converters. However, in order to take full advantage of these devices, the complete converter system must be redesigned. This approach has been relatively straight forward for the low power, high frequency space but the high power medium frequency converters have been slower to develop. A significant limitation has been the passive magnetic components for these designs. This is, in part, a materials problem. New, metal amorphous nanocomposite materials have been proposed as a material solution to meet these needs. However, their adoption has been slow and this is a magnetics design problem. As such, there is significant need for a combined study of both magnetic materials and power electronics to utilize the available material advancements while meeting the needed design requirements to provide solutions that enable high power medium frequency converters.

This thesis will provide a pathway and guidance towards the utilization of ribbon based magnetic cores. The work will enable improved designs of nanocomposite and amorphous materials for magnetic devices. It will show that, with a more nuanced understanding of the magnetic materials, better utilization and selection cores enables higher efficiency and higher power density systems. This thesis introduces multiparameter screening and characterization methods for informed material choices. It will demonstrate a new magnetic test bed that leverages novel test circuitry magnetic core harnesses to provide an in-depth analysis into magnetic material behavior. It explains and quantifies loss mechanics that are unique to the high power medium frequency design space. It also showcases new design techniques that take

advantage of advanced manufacturing processes to utilize strain induced magnetic anisotropy, strain annealing, for advanced magnetic core performance and anisotropic thermal design.

Whether it is a DC active filter or multiport dual active bridge, high power medium frequency magnetics are as critical a component as the wide bandgap semiconductors are to the operation of the power converter. This thesis provides the tools needed to characterize, design and improve the magnetics to enable further advancements in high power wide bandgap power converters.

© Copyright 2018 by Richard Byron Beddingfield

All Rights Reserved

High Power Medium Frequency Magnetics for Power Electronics Applications

by  
Richard Byron Beddingfield

A dissertation submitted to the Graduate Faculty of  
North Carolina State University  
in partial fulfillment of the  
requirements for the degree of  
Doctor of Philosophy

Electrical Engineering

Raleigh, North Carolina

2018

APPROVED BY:

---

Dr. Subhashish Bhattacharya  
Committee Chair

---

Dr. Mesut Baran

---

Dr. Gregory Buckner

---

Dr. Leonard White

---

Dr. Paul Ohodnicki Jr.  
External Member

**DEDICATION**

I dedicate this work to my family and their tireless support and especially my wife, McKenna, who gave me the liberty and freedom to focus myself to this work.

## **BIOGRAPHY**

Richard Byron Beddingfield was born in Atlanta, GA in 1990. He started undergraduate research in 2012 focusing on active filters after completing a three semester CO-OP rotation with Nucor Steel Hertford, NC. He completed a Bachelor of Science in Electrical Engineering, Magna Cum Laude, and the University Honors Program from North Carolina State University in 2013. He then completed his Professional Science Masters in Electric Power Systems Engineering with a Renewable Electric Energy Systems Certificate in 2014.

## ACKNOWLEDGEMENTS

Thank you to my committee members for their guidance and support. Your mentorship and collaboration has greatly enhanced my experience in this process and provided me with many great ideas and insights.

I would also like to thank the FREEDM laboratory for the facilities and equipment support that made much of this research and personal and professional development possible. The Oak Ridge Institute for Science Education and the National Energy Technology Lab that have been a tremendous source of financial support, allowing me to focus on research and affording me many opportunities for collaboration and knowledge sharing. I would also like to thank my undergraduate research mentors, Babak Parkhideh and Hesam Mirzaee who encouraged and supported my research and graduate school entrance.

I also am grateful for all of the support, teaching and collaboration in materials science for Dr. Mike McHenry's group, Alex Leary, Natan Aronhime, Vladimir Keylin and many others whose patience gave me the material science background I needed for so much of my work. Over the years, I have had the privilege to mentor many undergraduate research students. I would like to thank them for all of their efforts and for their contributions to my work. Finally, I would like to thank the Nucor Steel, Hertford, family who introduced me to practical electrical engineering and power electronics. Chris, thank you for hiring me for my first COOP. Kyle, Tom, and all of the electricians, mechanics and operators in the Castor and the Furnace, thank you for all of the mentoring and guidance.

## TABLE OF CONTENTS

LIST OF TABLES .....	xi
LIST OF FIGURES .....	xiii
LIST OF ACRONYMS .....	xxiv
CHAPTER 1: INTRODUCTION .....	1
1.1 Motivation.....	1
1.2 Contributions.....	5
1.2.1 Journal Publications .....	5
1.2.2 Conference Publications, Primary Author .....	5
1.2.3 Conference Publications, Assisting Author .....	6
1.2.4 Invention Disclosures.....	6
1.2.5 Presentations .....	6
CHAPTER 2: MAGNETIC CORE MATERIALS.....	8
2.1 Motivation.....	8
2.2 Introduction.....	8
2.3 Magnetic Relaxation .....	10
2.4 Magnetic Viscosity .....	13
2.5 Domain Wall and Magnetization Vector Motion .....	17
2.6 Numerical Models of Bulk Core Loss .....	22
2.6.1 Separating Losses.....	25
2.6.2 Hysteresis Curve Predictions .....	27
2.6.3 Loss Map Curve Fitting .....	31
2.7 Material Classifications and Comparison .....	38
2.8 Conclusion and Future Work .....	41
CHAPTER 3: CORE CHARACTERIZATION TECHNIQUES .....	43
3.1 Motivation.....	43

3.2 Measurement Circuitry .....	43
3.2.1 Triangular Flux Injection .....	46
3.2.2 DC Premagnetization .....	47
3.2.3 Duty Cycle Testing .....	49
3.2.4 Drawbacks to Traditional Testing Circuit.....	51
3.3 Extracting Steinmetz Parameters and Material Properties.....	55
3.3.1 Nine Point Linear Method .....	55
3.3.2 Software Surface Fitting .....	57
3.4 Other Parameters of Interest .....	58
3.5 Minimizing Error .....	58
3.5.1 Sensor Approaches to Minimizing Error .....	59
3.5.2 Circuit Based Techniques to Minimize Error .....	60
3.6 Preliminary Laboratory Setup.....	61
3.7 New Core Testing Harness .....	63
3.7.1 Core Harness .....	64
3.7.2 Stray Eddy Losses in Harness .....	66
3.7.3 Material Characterization Example .....	67
3.8 New Core Excitation Circuit.....	75
3.8.1 Introduction.....	75
3.8.2 Dual Voltage Source Converter .....	77
3.8.3 Switch Gating of Proposed Converter .....	79
3.8.4 Simulation Verification of Gating .....	80
3.8.5 Switching Progression for Trapezoidal Excitation .....	81
3.8.6 Switching Noise Reduction.....	83
3.8.7 Confirmation of Magnetic Core Behavior .....	86

3.8.8 High Power, Low THD Sinusoidal Excitation .....	88
3.8.9 High Power Dielectric Testing.....	90
3.8.10 Alternative Uses of New Converter .....	91
3.9 Trapezoidal Induction Study.....	92
3.9.1 Analysis of Excitation Levels in Active Bridge Transformer .....	92
3.9.2 Preliminary Trapezoidal Excitation Results .....	93
3.9.3 Test Conditions .....	95
3.9.4 Test Results .....	96
3.9.5 Baseline Triangular Excitation .....	96
3.9.6 Dual Slope, Quarter Duty Cycle .....	98
3.9.7 Dual Slope, Duty Cycle Sweep.....	100
3.9.8 Comparison of Excitations.....	101
3.10 Conclusions and Future Work .....	104
<b>CHAPTER 4: LEAKAGE FLUX AND OTHER PARASITIC ELEMENTS IN</b>	
<b>LAMINATED MAGNETIC CORES .....</b>	
4.1 Motivation.....	106
4.2 Introduction.....	106
4.3 Leakage Flux.....	108
4.3.1 Flux Path at the Interface of Materials.....	108
4.3.2 Permeance for Gap Fringing.....	112
4.3.3 Permeance for Leakage Flux .....	113
4.4 Modelling Leakage Flux and Losses .....	120
4.5 Induced Eddy Currents in Ribbon.....	124
4.6 Modified Transformer Electrical Model.....	126
4.7 Leakage Flux Control and Loss Mitigation .....	127
4.8 Leakage Flux Shield Penalties .....	136

4.9	Experimental Results .....	137
4.9.1	Fiber Optic Thermal Mapping .....	138
4.9.2	Three Dimensional Flux Mapping.....	139
4.9.3	Adjacent Winding Case Study .....	140
4.10	Stray Capacitance models.....	151
4.11	Winding Losses.....	154
4.12	Conclusions and Future Work .....	157
CHAPTER 5: STRAIN ANNEALED CORE ANISOTROPIC THERMAL MODELLING....		159
5.1	List of Symbols .....	159
5.2	Motivation.....	160
5.3	Introduction.....	162
5.4	Heating from Magnetizing flux .....	165
5.5	Heating from Normal Stray Flux .....	166
5.6	Anisotropic Thermal Model.....	167
5.6.1	Heating Impact.....	171
5.7	Strain annealing profiles .....	172
5.7.1	Assumptions used in Analysis .....	173
5.7.2	Constant Permeability.....	175
5.7.3	Linear Graded Permeability.....	178
5.7.4	Linear Graded Permeability with Offset.....	181
5.7.5	Exponential Permeability.....	184
5.8	Example Comparison of Permeability Profiles.....	186
5.9	Hardware Example.....	189
5.10	Implications and Recommendations for Thermal Management.....	192
5.11	Future Work and Conclusions .....	194

CHAPTER 6: APPLICATION EXAMPLES .....	196
6.1 Motivation.....	196
6.2 Series DC Active Filter Coupling Transformer .....	196
6.2.1 Introduction.....	196
6.2.2 DC Bus Low Pass Filter.....	201
6.2.3 SDAF Switching Ripple Filter Design .....	201
6.2.4 General SDCT Design Considerations .....	204
6.2.5 Overview of DC Bias Mitigation Techniques .....	209
6.2.6 Air Gap Flux Mitigation Design Methodology .....	216
6.2.7 Active DC Flux Mitigation.....	221
6.2.8 Hardware Realization of SDCT .....	230
6.2.9 MVDC Amplifier Performance with Air Gap Mitigation .....	241
6.2.10 MVDC Amplifier Performance with Active Mitigation.....	243
6.2.11 Conclusions and Discussion .....	248
6.3 Magnetics for Active Bridges .....	249
6.3.1 Emulating Active Bridge Power Flow .....	251
6.3.2 Concentric Design.....	253
6.3.3 Axial Design .....	262
6.4 Conclusion and Future Work.....	273
CHAPTER 7: CONCLUSION AND FUTURE WORK .....	275
REFERENCES .....	279
APPENDICES .....	292
Appendix A: Derivation for Linear Graded with Offset Permeability Profile.....	293
Appendix B: Soft Start Switch for Medium Voltage .....	294
Appendix B.1: Motivation.....	294
Appendix B.2: Proposed Switch.....	295

Appendix B.3: Converters with Proposed Switch .....	296
Appendix B.4: Charge Up .....	297
Appendix B.5: Steady State .....	299
Appendix B.6: Fault Conditions .....	300
Appendix B.7: Conclusion and Future Work .....	302

## LIST OF TABLES

Table 2.1:	Example Magnetic Materials: Basic Properties Part A.....	40
Table 2.2:	Example Magnetic Materials: Basic Properties Part B. ....	40
Table 3.1:	Steinmetz Parameters for JNHF Using Nine Point Method.....	57
Table 3.2:	Steinmetz Coefficients from Surface Map.....	58
Table 3.3:	Test Equipment and Important Figures of Merit.....	62
Table 3.4:	Physical Properties of Test Core. ....	68
Table 3.5:	Dual Voltage Source Converter Switch Timing and Stresses.....	81
Table 3.6:	Waveform Dependent Fit Parameters Using Classic Steinmetz Equation.....	102
Table 4.1:	Permeance Equations for Constitutive Geometries.....	118
Table 4.2:	Common Ribbon Core Assemblies.....	119
Table 4.3:	Number of Broad Surfaces Normal Flux Encounters for Various Core Connections and Flux Path Region. ....	120
Table 5.1:	List of Variables Used in CHAPTER 5 .....	160
Table 5.2:	Description of Thermal Impedances for Anisotropic Core Model. ....	168
Table 5.3:	Losses and Peak Flux Density for Various Strain Annealing Profiles.....	188
Table 6.1:	MVDC Performance Requirements.....	199
Table 6.2:	DC Active Filter Topology Variations.....	200
Table 6.3:	Switching Ripple Filter Component Values.....	204
Table 6.4:	Summary of Flux Mitigation Techniques. ....	209
Table 6.5:	Frequency Dependent Steinmetz Parameters for 10JNHF JFE Steel. ....	229
Table 6.6:	Experimental Parameters.....	232
Table 6.7:	Measured Transformer Noise.....	235

Table 6.8:	Comparison of Transform Designs. ....	236
Table 6.9:	DCAF Circuit Breaker Timing.....	247
Table 6.10:	10 kW Concentric Design Parameters. ....	256
Table 6.11:	Predicted and Measured Values of 10 kW Concentric Transformer. ....	258
Table 6.12:	10 kW Triaxial Design Parameters .....	266
Table 6.13:	Predicted and Measured Values of 10 kW Triaxial Transformer. ....	269

## LIST OF FIGURES

Figure 2.1:	Time Scales of Spin Related Magnetic Phenomena.....	9
Figure 2.2:	Ball in Mud Analogy of Magnetic Viscosity. ....	14
Figure 2.3:	Graphical Representation of Magnetic Domain Wall Movement.....	18
Figure 2.4:	Magnetic Vector Direction and Domain Wall Size based on Hysteresis Loop Location.....	19
Figure 2.5:	Example of Flyback Converter Topology (Left) and Associated Transformer Current and Flux Waveforms(Right). ....	24
Figure 2.6:	Single Leg of Three Leg SRM Driver and Associated Stator Current and Flux During Chopping Mode. ....	24
Figure 2.7:	Hysteresis Loop For Trapezoidal Excitation.....	28
Figure 2.8:	Pi Model of Transformer for Dual Active Bridges. ....	34
Figure 2.9:	Spider Chart Normalized Multiparameter Comparison of Soft Magnetic Materials.....	41
Figure 3.1:	Circuit Topology of Basic Magnetic Core Test Bed.....	45
Figure 3.2:	Excitation Waveform Template Continuous (Left) and Discontinuous (Right) .....	46
Figure 3.3:	CUT Excitation Demonstrating Nonidealities. ....	47
Figure 3.4:	Circuit for DC Premagnetization Test.....	48
Figure 3.5:	Sinusoidal Core Excitation with DC Premagnetization. ....	48
Figure 3.6:	Comparison of Loss Calculations to Measured Losses Of CUT with DC Premagnetization (Left) and Loss Prediction Error for DC Premagnetization (Right). ....	49

Figure 3.7:	Varying Duty Cycle Triangular Flux. ....	50
Figure 3.8:	Predicted Losses for Variable Duty Cycle Test. ....	50
Figure 3.9:	Ideal DAB Waveforms.....	52
Figure 3.10:	H Bridge Conduction Path: Positive Applied Voltage.....	52
Figure 3.11:	H Bridge Uncontrolled Voltage Conduction Paths: Free Wheeling Diode (Left) and Blanking Time (Right). ....	53
Figure 3.12:	Parasitic Effects On Single H Bridge Core Excitation Waveforms .....	55
Figure 3.13:	Manufacturer and Steinmetz Calculated Core Loss Curves for 10JNHF600. ....	56
Figure 3.14:	Error Between Calculated and Manufacturer Provided Data for 10JNHF600. ..	57
Figure 3.15:	Surface for Steinmetz Loss Fitting.....	58
Figure 3.16:	Maximum Error for Different Current Probes' Delay and Tolerance.....	60
Figure 3.17:	First Generation Experimental Test Bed (Left) and Example Material Characterization Setup (Right).....	62
Figure 3.18:	Magnetic Core Testbed Harness. ....	65
Figure 3.19:	Medium frequency, Low Excitation Core Harness FEA. ....	67
Figure 3.20:	Core Loss and Excitation Energy at Room Temperature.....	69
Figure 3.21:	Relative Permeability vs. Flux Density and Magnetizing Force at Room Temperature. ....	69
Figure 3.22:	Core Loss, Magnetizing Power for Various Air Gaps at 10 kHz.....	70
Figure 3.23:	Magnetic Core Temperature Over Time Profile. ....	72
Figure 3.24:	Core Loss and Exciting Power with Respect to Face Temperature. ....	72
Figure 3.25:	BH Loops at Various Temperature. ....	73
Figure 3.26:	Temperature Induced Permeability Decay.....	73

Figure 3.27:	High Temperature Core Harness Prototype. ....	75
Figure 3.28:	Typical Circuit of Dual Active Bridge. ....	76
Figure 3.29:	New Dual Voltage Source Converter Topology. ....	77
Figure 3.30:	Dual Voltage Source Core Tester Laboratory Prototype .....	78
Figure 3.31:	Ideal Trapezoidal Excitation. ....	79
Figure 3.32:	Waveforms of Dual Voltage Source Core Tester. ....	81
Figure 3.33:	Positive High Voltage Applied to the CUT Through Mosfets S1 and S4. ....	82
Figure 3.34:	Mosfets S1' and S4' are Pre-Gated On for Overlap Time. ....	82
Figure 3.35:	Low Voltage Excitation Through Mosfets and Reverse Diodes Conduction. ....	82
Figure 3.36:	Freewheeling Diodes Conduction: Positive to Negative Voltage Transition. ....	83
Figure 3.37:	Negative High Voltage Applied to the Core Under Test Through Mosfets. ....	83
Figure 3.38:	Time Zoomed Positive Transition From 50V to 12.5V. ....	84
Figure 3.39:	Time Zoomed Positive Transition From 50V to 18V. ....	85
Figure 3.40:	Time Zoomed Positive Transition From 50V to 18V with Reduced Ringing. ....	86
Figure 3.41:	Air Core Inductor at Reference Excitation. ....	86
Figure 3.42:	A Lossy Core Material at Reference Excitation. ....	87
Figure 3.43:	Air Core Inductor at Reference Excitation and Lossy Core Scale. ....	87
Figure 3.44:	BH Loops for Dual Voltage Source Core Tester Verification .....	88
Figure 3.45:	Three Level Sinusoidal Configuration. ....	89
Figure 3.46:	Output Waveforms of Multilevel Voltage Source Core Tester. ....	90
Figure 3.47:	Prototype Dielectric Testing Harness. ....	91
Figure 3.48:	High Power Dielectric Test Waveform. ....	91
Figure 3.49:	Pi Model of MF Transformer .....	92

Figure 3.50:	Flat Top Trapezoidal Excitation of AMCC Amorphous.....	94
Figure 3.51:	Dual Slope Excitation of HTX Nanocrystalline Core.....	94
Figure 3.52:	Verification of $-di/dt$ Despite All Positive Voltage.....	95
Figure 3.53:	Triangular Excitation Waveforms.....	97
Figure 3.54:	Triangular Excitation Power Map.....	97
Figure 3.55:	Triangular Excitation Permeability Variation.....	98
Figure 3.56:	Trapezoidal Excitation Waveforms.....	99
Figure 3.57:	Trapezoidal Excitation Power Map.....	99
Figure 3.58:	Trapezoidal Excitation Permeability Map.....	99
Figure 3.59:	20% Duty Cycle Excitation Waveform.....	100
Figure 3.60:	20% Duty Cycle Power Map.....	101
Figure 3.61:	20% Duty Cycle Permeability Map.....	101
Figure 3.62:	Excitation Dependent Core Loss Comparison Map.....	102
Figure 3.63:	10 kHz, 0.6 T Hysteresis Loop Comparison.....	103
Figure 3.64:	20 kHz, 0.6 T Hysteresis Loop Comparison.....	104
Figure 4.1:	Tangential Component of Magnetic Flux at Material Interface (Left) and Normal Component of Magnetic Flux at Material Interface (Right).....	109
Figure 4.2:	Angle of Flux Between Two Materials.....	110
Figure 4.3:	Flux Components At Material Interface, $\mu_B \gg \mu_A$ .....	110
Figure 4.4:	Induced Eddy Current Impact on Tangential and Normal Flux At Interface....	111
Figure 4.5:	Fringing Permeance Paths for Half of a UI Core Geometry.....	112
Figure 4.6:	Adjacent Winding Configuration Leakage FEA.....	115
Figure 4.7:	Abutting Winding Configuration Leakage FEA.....	116

Figure 4.8:	Concentric Winding Configuration Leakage FEA.....	116
Figure 4.9:	Rotated Edge Core Assembly. ....	119
Figure 4.10:	Wound Ribbon Core Assembly.....	119
Figure 4.11:	Edge on Edge Core Assembly.....	119
Figure 4.12:	Face on Edge Core Assembly. ....	119
Figure 4.13:	Simplified Geometry for Adjacent Winding Transformer.....	121
Figure 4.14:	Flux Path Segmentation of Adjacent Winding Transformer.....	121
Figure 4.15:	Magnetic Equivalent Circuit Considering Componentized Leakage Paths. ....	122
Figure 4.16:	Magnitude (Left) and Path Proportion (Right) of Winding Configuration Dependent Total Surface Leakage Flux.....	124
Figure 4.17:	Eddy Current in Magnetic Ribbon Paths. ....	126
Figure 4.18:	Modified Transformer Electrical Equivalent Circuit.....	127
Figure 4.19:	Graded Permeability Based Normal Leakage Flux Reduction. ....	129
Figure 4.20:	High Conductivity Based Normal Leakage Flux Reduction.....	130
Figure 4.21:	Permeance Paths with Leakage Flux Bar Shield.....	131
Figure 4.22:	3D FEA Model of Bar Shield.....	133
Figure 4.23:	Permeance Paths with Leakage Flux Wing Shield.....	134
Figure 4.24:	3D FEA Model of Wing Shield. ....	135
Figure 4.25:	Magnetic Equivalent Circuit of Componentized Wing Shield. ....	136
Figure 4.26:	Comparison of Magnetizing and Leakage Test Thermal Profiles.....	138
Figure 4.27:	Optical Line Scan Measurement of Transformer Thermal Profile. ....	139
Figure 4.28:	Measured Leakage Flux Field Around Transformer Upper Right Octant . ....	140
Figure 4.29:	Unshielded 10 kW DAB Transformer. ....	141

Figure 4.30:	10 kW Unshielded DAB Transformer Thermal Profiles. ....	142
Figure 4.31:	Zoomed 10 kW Unshielded DAB Transformer Thermal Profile.....	142
Figure 4.32:	10 kW DAB Transformer Case Study, Unshielded Top View. ....	143
Figure 4.33:	Loss Map for Magnetizing and Leakage Losses of F1AH1171 Core.....	144
Figure 4.34:	10 kW DAB Transformer Case Study, Bar Shielded.....	145
Figure 4.35:	10 kW Bar Shielded DAB Transformer Thermal Profiles.....	145
Figure 4.36:	Bar Shield Leakage Top View Thermal Profile.....	146
Figure 4.37:	10 kW DAB Transformer Case Study, Wing Shielded.....	146
Figure 4.38:	10 kW Wing Shielded DAB Transformer Thermal Profiles.....	147
Figure 4.39:	10 kW, 10 kHz Unshielded / Shielded Loss Map. ....	148
Figure 4.40:	Shielded vs Unshielded Loss Reduction. ....	149
Figure 4.41:	Variation in Leakage Loss k Term.....	149
Figure 4.42:	Change in Effective Permeability Due to Addition of Leakage Shielding Component.....	150
Figure 4.43:	Winding Layout for Magnetic Devices.....	152
Figure 4.44:	Turn to Turn Winding Alignment.....	153
Figure 5.1:	Toroid Geometry with Dimensions.....	166
Figure 5.2:	2D Thermal Model for Anisotropic Magnetic Ribbon Cores.....	168
Figure 5.3:	Ratio of Loss Calculation Methods Surface.....	177
Figure 5.4:	Contours of Baseline Values for Losses of Various Toroid Designs.....	178
Figure 5.5:	Graded Permeability Toroid Magnetization Loss Percent Change.....	180
Figure 5.6:	Graded with Offset Permeability Toroid Magnetization Loss Percent Change.....	183

Figure 5.7:	Exponential Permeability Toroid Magnetization Loss Percent Change. ....	185
Figure 5.8:	FEA Analysis of Constant Strain Annealed Toroids. ....	187
Figure 5.9:	Comparison of Thermal Line Plots of Steady State Temperature. ....	191
Figure 6.1:	Navy NGPIS Technology Projection .....	199
Figure 6.2:	Photograph of US Navy More Electric Ship: Zumwalt Destroyer. ....	199
Figure 6.3:	Illustration of MVDC Amplifier Performance.....	199
Figure 6.4:	Connection of Rectifier with Filter Options.....	200
Figure 6.5:	Topology of Thyristor Based MVDC with SDCT.....	201
Figure 6.6:	C-Type Topology Switching Ripple Filter with Resonant Trap.....	202
Figure 6.7:	Parallel Shunt Switching Ripple Filter with Resonant Trap. ....	203
Figure 6.8:	Compensation Requirement for the SDAF During.....	205
Figure 6.9:	Gapped SDCT FEA.....	210
Figure 6.10:	Gapped SDCT BH.....	211
Figure 6.11:	Permanent Magnet SDCT FEA.....	212
Figure 6.12:	Permanent Magnet SDCT BH.....	212
Figure 6.13:	SDCT Auxiliary Converter for DC Injection.....	213
Figure 6.14:	Auxiliary Winding SDCT FEA.....	213
Figure 6.15:	Auxiliary Winding SDCT BH.....	214
Figure 6.16:	Proposed Circuit Topology for Active DC Injection. ....	215
Figure 6.17:	Active DC Injection SDCT FEA.....	215
Figure 6.18:	Active DC Injection SDCT BH.....	216
Figure 6.19:	SDCT Winding and Core Geometry: M Rows and N Columns. ....	218
Figure 6.20:	Slice View of Circular Winding Around a Core Leg.....	219

Figure 6.21:	SDCT Normalized Volume and Copper Loss vs. Turns and Gap Length. ....	221
Figure 6.22:	Volume and Loss Comparison of JFE and AMCC Cores gap = 4mm. ....	221
Figure 6.23:	Variations in Magnetic Permeability for 10JNHF JFE Steel Core. ....	223
Figure 6.24:	Resonant Voltage Control and PI Current Control for SDAF. ....	224
Figure 6.25:	Simulated MVDC Amplifier Voltages for Air Gap (Light) and Active Injection (Dark) SDCT. ....	225
Figure 6.26:	Plecs Magnetics B-H Loop for Both Control Modes. ....	226
Figure 6.27:	FEA Analysis for Air Gapped SDCT. ....	227
Figure 6.28:	FEA Analysis of Active DC Injection SDCT. ....	227
Figure 6.29:	Loss Factors For JFE Steel Magnetic Core. ....	229
Figure 6.30:	Medium Voltage DC Test bed Experimental Set-Up. ....	231
Figure 6.31:	AMCC Core: Steady State Filtering, 1kW Load. ....	232
Figure 6.32:	AMCC Core: 300w Load Step. ....	233
Figure 6.33:	JNHF Core: Steady State Filtering, 1kW Load. ....	233
Figure 6.34:	JNHF Core: 300w Load Step. ....	233
Figure 6.35:	Hysteresis Loop for one 720Hz Cycle. ....	234
Figure 6.36:	Hysteresis Loop for Oscilloscope Window During Step Load Change. ....	235
Figure 6.37:	Comparison of Series DC Coupled Transformers. ....	236
Figure 6.38:	2 kW DCAF Without (Left) and With (Right) Active DC Injection Operation with Voltage Type Filter. ....	237
Figure 6.39:	Measured BH Curve of SDCT Without (Left) and With (Right) DC Flux Cancellation. ....	238

Figure 6.40:	2 kW DCAF Without (Left) and With (Right) Active DC Injection Operation with Current Type Filter.....	240
Figure 6.41:	Measured BH Curve of SDCT Without (Left) and With (Right) DC Flux Cancelation with Current Type Filter.....	240
Figure 6.42:	Air Gapped SDCT Impedance and Load DC Field, No Output Saturation. ....	242
Figure 6.43:	Output Voltage of DCAF vs Load Power Showing VDC Output Limit. ....	242
Figure 6.44:	SDAF Current Output with Resulting Voltage Ripple vs Load.....	243
Figure 6.45:	6th Harmonic Component of DC Ripple Compared to Loading. ....	244
Figure 6.46:	12th Harmonic Component of DC Ripple Compared to Loading. ....	244
Figure 6.47:	18th Harmonic Component of DC Ripple Compared to Loading. ....	245
Figure 6.48:	24th Harmonic Component of DC Ripple Compared to Loading. ....	245
Figure 6.49:	Overall DC Output Ripple.....	246
Figure 6.50:	DC Circuit Breaker Operation of DCAF with Active DC Injection. ....	247
Figure 6.51:	Active Bridge Emulation Waveforms Using Dual Voltage Source Converter. ....	251
Figure 6.52:	Calculated Active Bridge Waveforms From Dual Voltage Source Converter. ....	252
Figure 6.53:	DAB Instantaneous Power Waveforms Emulated by Dual Voltage Source Core Tester .....	252
Figure 6.54:	Three Port Concentric Winding Transformer with Auxiliary Inductor Dimensions.....	254
Figure 6.55:	Prototype 10 kW Three Port Concentric Transformer. ....	256
Figure 6.56:	Concentric Winding Open Circuit Admittance Bode Plot. ....	257
Figure 6.57:	Auxiliary Inductor for 10 kW Concentric Transformer. ....	259

Figure 6.58:	Effective Electric Circuit of Concentric Transformer with Auxiliary Inductors.....	259
Figure 6.59:	Effective Permeability of Concentric Transformer with Auxiliary Leakage Inductors.....	260
Figure 6.60:	Effective Permeability of Open Circuit Winding in Triaxial Transformer with Strain Annealed Cores. ....	261
Figure 6.61:	Efficiency Map of Concentric Transformer With Auxiliary Inductors Design.....	262
Figure 6.62:	Three Port Axial (Triaxial) Transformer.....	263
Figure 6.63:	Equivalent Circuit of Triaxial Transformer. ....	264
Figure 6.64:	Inductance Sensitivity of Axial Designs. ....	266
Figure 6.65:	Prototype 10 kW Three Port Triaxial Transformer.....	267
Figure 6.66:	Concentric Winding Open Circuit Admittance Bode Plot.....	267
Figure 6.67:	Triaxial Resistive Load Test: Primary to Secondary and Tertiary.....	269
Figure 6.68:	Triaxial Short Circuit Test: Secondary to Primary and Tertiary. ....	270
Figure 6.69:	Effective Relative Permeability of Power Flow Paths in Triaxial Transformer with Strain Annealed Cores.....	271
Figure 6.70:	Effective Permeability of Open Circuit Winding in Triaxial Transformer with Strain Annealed Cores. ....	271
Figure 6.71:	Efficiency Map of Triaxial Transformer with Strain Annealed Leakage Cores.....	272
Figure 6.72:	Normalized Specific Losses of Triaxial Transformer.....	273
Figure B.0.1:	IGBT Thyristor Topology. ....	295

Figure B.0.2: SST With Soft Start Switch.....	296
Figure B.0.3: MMC With Soft Start Switch.....	297
Figure B.0.4: Three Phase Active Front End with Soft Start Switch.....	297
Figure B.0.5: Surge Start Through Low Resistance.....	298
Figure B.0.6: Soft Start Through IGBT Thyristor Switch.....	299
Figure B.0.7: Steady State Operation.....	300
Figure B.0.8: Fault Condition in Traditional Active Front End.....	301
Figure B.0.9: Fault Suppression with Proposed Switch.....	302

## LIST OF ACRONYMS

AEC: anomalous eddy current .....	27
AFE: active front end .....	201
AMR: amorphous metal ribbons .....	27
CSE: classical Steinmetz equation .....	35
CUT: core under test .....	63
DYNAC: dynamic current .....	3
FEA: finite element analysis .....	68
GSE: generalized Steinmetz equation .....	37
I <sup>2</sup> GSE: twice improved generalized Steinmetz equation .....	35
IGSE: improved generalized Steinmetz equation .....	37
MANC: metal amorphous nanocomposites .....	41
MF: medium frequency .....	38
MSE: modified Steinmetz equation .....	34
MV: medium voltage .....	4
MVDC: medium voltage DC .....	200
NGIPS: next generation intelligent power system .....	200
PM: permanent magnet .....	216
PV: photovoltaic, colloqually; solar panel .....	94
PWM: pulse width modulation .....	29
SDAF: series DC active Filter .....	202
SDCT: series DC coupling transformer .....	202
SPG: Steinmetz premagnetization graph .....	38

SST: solid state transformer ..... 4

SuNLaMP: SunShot National Laboratory Multiyear Partnership ..... 254

WBG: wide bandgap..... 1

## CHAPTER 1: INTRODUCTION

### 1.1 Motivation

There have been significant improvements in power electronic topologies and switching devices with the advent of wide-bandgap semiconductors. There are two significant trends that are enabling high power medium frequency converters. First the rapid commercialization of wide bandgap (WBG) semiconductors has increased the voltage and current rating of devices traditionally used in lower power circuits in high power applications [1]. Second, advancements in magnetic materials have provided the energy storage and coupling capabilities necessary for the realization of these converters. This has resulted in increases in efficiency and power density. However, this rapid change in topology has created unique issues with regards to the design of the magnetic materials. New power converter topologies are pushing the limits of existing passive components. With the complex excitation waveforms of these converters it no longer trivial to predict the core loss. This makes design and optimization difficult with lots of possibility for error. It is critical then to investigate the behavior and classification of soft magnetic materials. This can then influence the development of new magnetic core characterization techniques and modelling. From this, algorithms that incorporate a more complete picture of the magnetics can greatly influence and improve designs.

Metal amorphous nanocrystalline (MANC) magnetic materials show great promise for the highest power densities in the medium frequency range. [2] uses nanocrystalline cores for three and five limb three phase transformer designs. The author chooses five limb designs because the flux density is shared more equally among all of the cores. Unmentioned by the author, this design methodology also improves excess eddy current losses caused by leakage flux. The authors predict designs with >98% efficiency and high power density, >35MW/m<sup>3</sup>.

These results compare very favorably against designs using amorphous material and ferrites. This efficiency and power density is critical for offshore windfarms where the transformer is housed on a remote platform.

For the medium voltage solid state transformer, a three phase transformer provides the additional smoothing to transformer current and enables reduced  $dv/dt$  across the transformer input, [3]. The transformers are made with nanocrystalline material due to its low loss and high magnetizing inductance. The exact structure and design was outsourced to a professional company so the construction details are not clear. A provided equivalent model showing a three limb design is mentioned. Given the material, it is safe to assume it is some form of magnetic ribbon. However, it is known that the transformer has very low leakage inductance and requires an external inductor to meet the desired leakage for the dual active bridge. It also highlights the need for common mode chokes for blocking noise. Again, this is an ideal application space for ribbon wound cores. Finally, the authors demonstrate an auxiliary transformer in series with the original DAB. This auxiliary transformer is used to inject reactive power and enable an extension of the ZVS range. Again, in [4], magnetic ribbon cores are shown to have many design benefits. This author uses amorphous ribbon. In this work, the author uses a five limb core design to accommodate the third harmonic in a three phase transformer. In [5], the author presents a three phase axial transformer where the outer core is a magnetic ribbon nanocrystalline. This design combines the advantage of five limb and axial transformers to allow zero sequence, triplen harmonics, without nonidealities such as asymmetrical inductances.

The author of [4] Demonstrates coaxial transformer design with an integrated leakage inductor. Using an inner core between the primary and secondary windings, the authors are able to fine tune the leakage inductance. Nanocrystalline is used as the outer core due to its high

permeability and flux density capability. Since the flux is in the same alignment as the magnetic ribbon, there are no excess induced eddy currents. Furthermore, with the integrated inductance, the transformer can be made very compact.

Magnetic ribbon cores are also advantageous when the magnitude of magnetizing inductance is paramount such as in isolated gate drivers. [6] demonstrated a medium voltage gate driver power supply isolation transformer with reasonable coupling capacitance and exceptional magnetizing inductance. The low capacitance was very important for the 50kHz switching frequency of the supply and the high inductance ensured that the supply would have low reactive losses. However, for the additional inductors used to in the high power SST, the authors used ferrite cores. This required designs with 60 turns and 3 paralleled cores to achieve desired  $B_{max}$  for a 5kHz switching and 1kHz resonate frequency. Had the authors used magnetic ribbon type cores such as amorphous, nanocrystalline or even high silicon steel, they could have greatly reduced the design size. At high power, the ribbon based designs require more thought and require a more nuanced understanding of the magnetics and therefore were likely avoided for the simplicity of the ferrite designs.

The magnetic ribbon cores high saturation flux density is advantageous in high power current source converters as well. [7] demonstrates several traditional current source converters and proposes a novel reduced switch, partially resonant current source converter. The magnetic device, either inductor or transformer, is subjected to multiple linear slopes excitations and resonant behavior during the switching period. The proposed Dynamic Current (DYNAC) converter is back to back current source converter with large shunt inductance made with a nanocrystalline core. The continuous conduction mode has large DC offset current while discontinuous conduction mode enables ZCS. With a flyback transformer, both system isolation

and auxiliary supplies, such as battery banks, can be integrated with the converter. In the proposed topology a partial resonant branch includes a capacitor to resonantly recharge the link voltage.

Ferrite cores are often used instead of magnetic ribbon despite the clear advantages of latter. It is generally easier to match the paper design of a ferrite transformer with the end result due to the materials isotropy. In [8] and [9], the author presents a dual active bridge and a multiterminal dual active bridge, with an application emphasis for the solid state transformer. The multiterminal transformer is used for cascaded front ends to a single output as in the MV SST. At a higher power, system scale, the multiterminal transformer can magnetically connect multiple converters for a green energy hub. However, the author's use of ferrite for the core material limited the predicted power density and design scalability.

With the clear benefits of magnetic ribbon based cores and in particular nanocrystalline materials, it is essential to have accurate characterization and modelling techniques. This work will outline the appropriate materials and develop clear guidelines for material application spaces. It will then introduce methods for characterizing the materials. Next, this thesis will provide modelling techniques for both parasitic elements and thermal domains with an emphasis on the nuances and caveats associated with magnetic ribbon cores. Finally, this thesis will provide application examples that demonstrate the efficacy of the presented characterization and modelling techniques. It will include converter controller designs that leverage the benefits of the improved magnetics designs. This work will enable wider adoption and application of metal amorphous nanocrystalline magnetic ribbon materials for high power medium frequency applications.

## 1.2 Contributions

### 1.2.1 Journal Publications

1. R. Beddingfield, K. Byerly, S. Simizu, A. Leary, S. Bhattacharya, P. Ohodnicki, M. McHenry, "Thermal Profile Shaping and Loss Impacts of Strain Annealing on Magnetic Ribbon Cores," *Journal of Materials Research*, To Be Published
2. K. Byerly, R. Ohodnicki, S. R. Moon, A. M. Leary, V. Keylin, M. E. McHenry, S. Simizu, R. Beddingfield, Y. Yu, G. Feichter, R. Noebe, R. Bowman, S. Bhattacharya "Metal Amorphous Nanocomposite (MANC) Alloy Cores with Spatially Tuned Permeability for Advanced Power Magnetics Applications," *Journal of Materials*, 2018

### 1.2.2 Conference Publications, Primary Author

3. R. Beddingfield, H. Mirage, S. Bhattacharya, "Performance Investigation of AC Active Filter with New Voltage Synchronization," 2017 IEEE Energy Conversion Congress and Exposition (ECCE), Cincinnati, OH, 2017, pp. 5222-5228.
4. R. Beddingfield, D. Storelli, S. Bhattacharya, "Trapezoidal Characterization of Magnetic Materials with a Novel Dual Voltage Test Circuit," *Energy Conversion Congress and Exposition (ECCE)*, 2017
5. R. Beddingfield, D. Storelli, S. Bhattacharya, "A Novel Dual Voltage Source Converter for Magnetic Material Characterization with Trapezoidal Excitation", *Applied Power Electronics Conference and Exposition (APEC)*, 2017 IEEE, To Be Published
6. R. Beddingfield, D. Storelli, S. Bhattacharya, "Active Elimination of DC Bias Flux in Series DC Active Filter Coupling Transformer", 2017 IEEE Energy Conversion Congress and Exposition (ECCE), Cincinnati, OH, 2017, pp. 439-446.
7. R. Beddingfield, S. Bhattacharya, "Multi-parameter Magnetic Material Characterization for High Power Medium Frequency Converters", *Sup. Proc. To The Materials, Metals, & Materials Society (TMS) Annual Meeting and Exhibition*, San Diego, CA, 2017, pg. 693-708
8. R. Beddingfield, A. Davis, H. Mirzaee and S. Bhattacharya, "Investigation of series DC active filter and hybrid AC active filter performance in medium voltage DC amplifier," 2015 IEEE Electric Ship Technologies Symposium (ESTS), Alexandria, VA, 2015, pp. 161-166.
9. Beddingfield, R.; De, A.; Mirzae, H.; Bhattacharya, S., "Design methodology of series DC coupling transformer in a medium-voltage DC amplifier system," *Applied Power Electronics Conference and Exposition (APEC)*, 2015 IEEE, vol., no., pp.183,190, 15-19 March 2015

### 1.2.3 Conference Publications, Assisting Author

10. V. Nair, S. Guler, R. Chattopadhyay, R. Beddingfield, S. Mathur, S. Bhattacharya, G. Gohil, P. R. Ohodnicki, "Large Scale Grid Integration of Photovoltaic and Energy Storage Systems Using Triple Port Dual Active Bridge Converter Modules," Power and Energy Society (PES) General Meeting, Portland, OR, August 2018
11. P. Lu, K. Byerly, M. Buric, P. Zandhuis, C. Sun, A. Leary, R. Beddingfield, M. E. McHenry, P. Ohodnicki, "Distributed fiber-optic sensor for real-time monitoring of temperature rise of energized transformer cores," SPIE Defense and Commercial Sensing 17
12. Y. Cho, Y. Han, R. B. Beddingfield, J. I. Ha and S. Bhattacharya, "Seamless black start and reconnection of LCL-filtered solid state transformer based on droop control," 2016 IEEE Energy Conversion Congress and Exposition (ECCE), Milwaukee, WI, 2016, pp. 1-7.
13. Mirzaee, H.; Beddingfield, R.; Bhattacharya, S.; Parkhideh, B., "Performance investigation of hybrid converter systems for mobile mining applications," Energy Conversion Congress and Exposition (ECCE), 2013 IEEE, pp.825,831, 15-19 Sept. 2013
14. Parkhideh, B.; Mirzaee, H.; Beddingfield, R.; Bhattacharya, S., "Enabling Energy Storage Integration in High Power Multi-Motor Applications with Active Filter Solutions," Industry Applications Society Annual Meeting IAS, 2011 IEEE, pp.1-5, 9-13 Oct. 2011

### 1.2.4 Invention Disclosures

1. R. Beddingfield, S. Bhattacharya, D. Storelli, Circuit for Providing Variable Waveform Excitation, Provisional Patent: 98192/1063283, 62/583,843, November 10, 2017, United States
2. R. Beddingfield, S. Bhattacharya, P. Ohodnicki, K. Byerly, Mixed Material Magnetic Core for Shielding of Eddy Current Induced Excess Losses Provisional Patent: 221404-8470, 62/582,107, November 6, 2017, United States
3. R. Beddingfield, S. Bhattacharya, A Semiconductor Topology and Device for Soft Starting and Active Fault Protection of AC-DC Converters, Provisional Patent: 62/611,806, December 29, 2017, United States
4. P. Ohodnicki, M. Buric, A. Leary, R. Beddingfield, M. McHenry, Distributed Sensing in Transformer, Inductor, and Motor Components Using Optical Based Methods, Provisional Patent: 62/606,160, September 6, 2017, United States

### 1.2.5 Presentations

1. R. Beddingfield, K. Byerly, S. Bhattacharya, P. Ohodnicki, "Application Impact of Magnetic Ribbon Core Strain Annealing", The Minerals, Metals & Materials Society (TMS), Phoenix, AZ, March 2018

2. R. Beddingfield, K. Byerly, M. Juds, S. Bhattacharya, P. Ohodnicki, "Leakage Flux Induced Losses and Shielding in Magnetic Ribbon Cores", The Minerals, Metals & Materials Society (TMS), Phoenix, AZ, March 2018
3. R. Beddingfield, E. Herbert, " Multi-parameter Magnetic Material Characterization for High Power Medium Frequency Converters ", Power Supply Manufacturer Association (PSMA) at Applied Power Electronics Conference (APEC), Invited
4. C. Sullivan, S. Ehrlich, M. Rylko, E. Herbert, R. Beddingfield, R. Ridley, "Panel Discussion", Power Supply Manufacturer Association (PSMA) at Applied Power Electronics Conference (APEC), Invited
5. R. Beddingfield, S. Bhattacharya, P. Ohodnicki, "Physics of Leakage Flux and Induced Eddy Currents in Power Magnetics Components", Conference on Magnetism and Magnetic Materials (MMM), Pittsburgh, PA, Nov. 2017

## CHAPTER 2: MAGNETIC CORE MATERIALS

### 2.1 Motivation

This chapter will investigate magnetization physics and magnetic materials to provide insight into the core modelling and selection processes. This is primarily a review of existing work but will tie together aspects of material science and electrical engineering. It will work to define the design spaces where different magnetic effects and have a significant impact on system design and operation. Specifically, this chapter will try to define the effects and materials that are most applicable to the medium frequency range. It will further clarify the application spaces for various materials and define outlines for informed material selection in the magnetics design.

### 2.2 Introduction

The magnetic core losses are an important consideration in the design of transformers and inductors. It is well known that the excitation wave shape plays a role in determining the extent of the losses. As such, it is valuable to characterize potential core materials with a profile of the specific excitation waveforms that would be seen in the final power electronics converter. In historical, low frequency sinusoidal applications this was a fairly trivial exercise. Furthermore, results of these studies were easily scalable to wave shapes and amplitudes near the original study. This led to heuristic curve fitting approaches and practical simplifications of physical processes to accurately model and predict the core losses in the local neighborhood of excitation waveforms.

As power electronics have enabled the use of higher frequencies and more arbitrary excitation waveforms, new and different magnetic behaviors have begun to play a more significant role. For high power converters, the scope of the magnetic behavior occurs in the

medium frequency range and higher. As can be seen in Figure 2.1, there are several processes of different time scales that fit this metric [10]. While traditional magnetic designs need only to focus a low frequency fundamental, the advent of power electronics has introduced more excitation waveforms. While the power converter fundamental may be of a low or medium frequency, the excitation discontinuities, e.g. triangular and trapezoidal excite magnetic materials at higher frequency harmonics. These harmonics can cause different magnetization processes there were previously neglected in single frequency or low frequency studies.

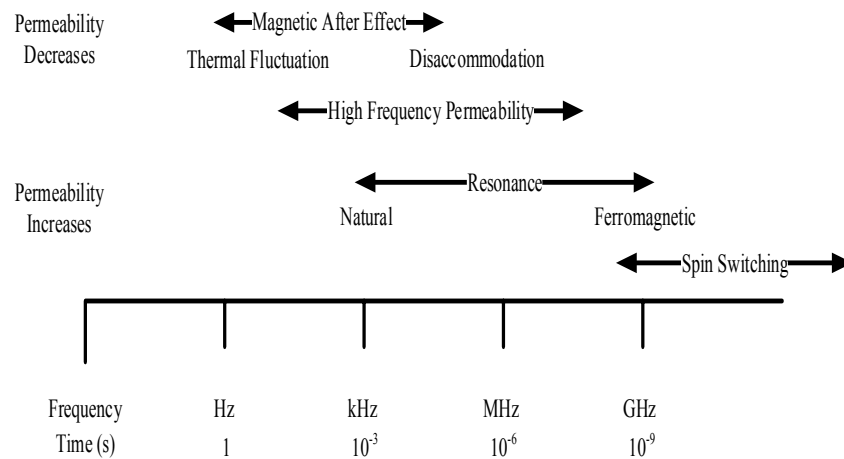


Figure 2.1: Time Scales of Spin Related Magnetic Phenomena.

The following literature review explores the prior work that can be used to explain these different phenomena. First, this chapter describes two behavior models of magnetism in soft magnetic materials known as magnetic relaxation and magnetic viscosity. The next section describes the dominant lossy behavior of domain wall and magnetization vector motion. The next part provides a review of works that develop mathematical models to describe and predict magnetic behavior, including losses, for complex waveforms. The final section provides an overview of material classifications and provides a comparison of figures of merit. This will chapter provides a physical background and historical study of the important properties of magnetic materials. From this, the gaps in understanding and material characterization methods

that are needed for modern medium and high frequency power converters can be identified and solved.

### 2.3 Magnetic Relaxation

Loss separation is a typical approach with many other methods of defining the relationship between the different loss components and the excitation waveform. Some researchers have attempted to incorporate the concept of magnetic relaxation or magnetic slippage in the loss models. This nomenclature is a little ambiguous as relaxation is also used to define the decrease of remnant flux density in permanent magnetics. This section will explore works that use the magnetic relaxation as part of the core loss prediction and definition.

In [11], the authors focus on the amount of energy absorbed by the different loss components. The claim is that the hysteresis losses are independent of frequency and wave shape excitation. Using conductivity  $\sigma$  and thickness  $d$ , magnetic polarization  $j$  the authors define the losses in (2.1) and (2.2). They hysteresis losses need to be measured for the material at a low frequency and will be constant for that specific material regardless of application. The authors lump the loss variations due to wave shape in the excess loss component in (2.3) and (2.4) for sinusoidal and triangular excitation respectively.

$$(2.1) \quad \frac{P_{clas}}{Volume} = \frac{1}{12} \sigma d^2 B(\dot{t})^2 \cong \frac{1}{12} \sigma d^2 j(\dot{t})^2$$

$$(2.2) \quad P(t)_{exc} = \frac{n_o V_o |J(t)|}{2} \sqrt{1 + \frac{4\sigma G S V_o}{n_o^2 V_o^2} |J(t)|} - \frac{n_o V_o |J(t)|}{2}$$

As mentioned before the excess loss component is used to distinguish the losses between sinusoidal and triangular excitation. It is interesting to note that the variation in losses are close to other scalar relationships of triangular and sinusoidal losses using the  $\pi/4$  factor.

$$(2.3) \quad W_{exc-sin} = 8.76\sqrt{\sigma GSV_o}J_p^{\frac{3}{2}}f^{\frac{1}{2}} \quad (2.4) \quad W_{exc-tri} = 8\sqrt{\sigma GSV_o}J_p^{\frac{3}{2}}f^{\frac{1}{2}}$$

In the preceding equations,  $V_o$  is a parameter defining the statistics of the magnetic objects,  $G$  is a dimensionless coefficient of 0.1356, and  $S$  is the cross-sectional area. The number of simultaneously active magnetic objects,  $n_0$ , represents the magnetically correlated regions in the sample cross section is defined in [12].  $W_h$  and  $V_o$  are calculated at very low frequencies. They are Y intercept and slope towards higher frequency losses on a graph comparing losses and  $\sqrt{f}$ . One difficulty in this approach is the need of a constraint approximation that requires more advanced estimation equations.

The authors in [13] the authors showed graphics of the hysteresis plots for a three phase DAB. This circuit produces dual slope excitation and the hysteresis plot shown is similar to that seen in Figure 2.7. The authors compare their measured losses to the classical Steinmetz and the IGSE equations. The IGSE over estimates the losses which they claim is because eddy currents were neglected. An important figure shows how losses decrease faster at higher phase angles above  $60^0$  in the phase angle of the DAB.

The authors in [14], seek to directly define these losses seen in the DAB and three port DAB. Using IGSE, the authors propose that the core losses depend on the speed of the domain wall movement leading to the dB/dt terms in the original loss equation. However, during zero excitation periods or low excitation periods, seen the aforementioned converters, the IGSE predicts no losses despite measured losses. The authors claim that this is an artifact of magnetic relaxation where the domain wall continues to move even though no dynamic field is applied. They add (2.5) to IGSE to account for this motion. In this equation,  $\Delta E$  is the maximum energy-loss increase which occurs when the magnetic material has enough time to reach the new thermal equilibrium (2.6).

$$(2.5) \quad E = \Delta E \left(1 - e^{-\frac{t_1}{\tau}}\right)$$

$$(2.6) \quad \Delta E = k_r \left| \frac{d}{dt} B(t_-) \right|^{\alpha_r} (\Delta B)^{\beta_r}$$

The new terms  $k_r$ ,  $\alpha_r$ ,  $\beta_r$  are new Steinmetz like terms that need to be found through curve fitting.  $\tau$  is relaxation time to be determined and  $T_l$  is the time zero excitation is applied. One interesting point about this work is that the hysteresis curves shown do not quite match excitation waveforms shown. There is a negative  $B$  section in the loop when the excitation is flat. Without actual measurements of current and induced voltage, it is unclear if the presented hysteresis curve is correctly labeled. However, given the demonstrated test circuit topology and parasitic losses within, it is more likely that the applied ‘zero’ voltage period is in fact slightly negative giving rise to the reported results. Therefore, the test circuit is introducing some degree of loss error with an applied field.

In [15], the authors predict a cascaded effect of losses. Hysteresis and steady-state losses of the Weiss domains occur when a variable magnetic field is applied to the magnetic material. However, referring to [12], the authors predict continued excess losses that occur after magnetic domain movement. Dynamic losses of the Weiss domains occur when a variable magnetic field is applied to the magnetic material. From a simple point of view, these losses are due to Block walls’ discontinuous movements with the production of the Barkhausen jumps. Since the Barkhausen jumps are very fast, they produce eddy currents and related joule losses. At the initial jump, eddy currents are produced which induce more domain wall motion and more jumps and so on. They extend this concept to modify the classical loss term to be dominated by eddy current based losses as shown in (2.7). The authors propose two methods and corresponding measurement techniques to modify loss equations for PWM sinusoids where the cascaded losses occur despite zero excitation times. These eddy current losses are strongly dependent on the skin effect. Where  $b$  is a constant,  $f$  is the frequency,  $d$  is the depth and  $B_p$  is the peak induction.

$$(2.7) \quad P_{\text{eddy}} = \frac{bf^{1.5}B_p^2(\sinh(d\sqrt{f})-\sin(d\sqrt{f}))}{\cosh(d\sqrt{f})-\cos(d\sqrt{f})}$$

As mentioned before, relaxation refers to many processes in magnetic materials. In [16] and [17], the authors discuss permeability relaxation in crystalline materials. This is due to thermally activated diffusion of single impurity atoms or solute atom pair rotation and can be estimated in a single time constant  $\tau$  (2.8). Where  $Q$  is the activation energy,  $\tau_0$  is near  $1/f_d$ , the Debye frequency,  $= 10^{-13}$ s.

$$(2.8) \quad \tau = \tau_0 e^{\frac{Q}{kT}}$$

A wide range of  $Q$ s is considered instead of  $\tau_0$ . This is because a range of  $\tau_0$  would imply different atomic clusters relaxing and not the more likely cause of structural instabilities in amorphous materials. The permeability relaxation is an activated phenomenon which occurs over a wide range of energy barriers. These phenomena likely do not involve interstitial impurity diffusion or solute atom pair rotation. Rather atomic instabilities intrinsic in amorphous structures might be present.

With magnetic relaxation being an ambiguous term, it is useful to look at other work that describes similar behavior by a different name. There have been many works that have explored the concept of magnetism a viscous system. This work is reviewed in the next section.

## 2.4 Magnetic Viscosity

In order to understand the apparent viscosity of magnetism it is helpful to consider an analogy from Snoek [18]. In this analogy one is to consider a ball resting in a mud pit where position represents the induction level. As a magnetic field,  $H$ , is applied, the ball is moved back and forth through the pit. At intermediate temperatures,  $T_I$ , this mud is like a sludge causing a lag between the applied  $H$  and the resulting ball motion, viscous behavior. Snoek extended the

analogy to temperature extremes too. At very low,  $T_C$ , and very high,  $T_H$ , temperatures, the mud is solid and liquid respectively and allow for fast responses implying that there is less viscous behavior. This is illustrated below in Figure 2.2.

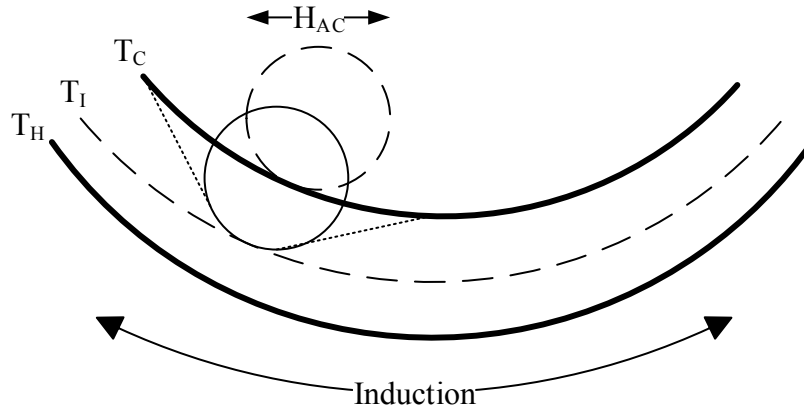


Figure 2.2: Ball in Mud Analogy of Magnetic Viscosity.

The temperature dependence is further explored in [19] and [20]. These authors expanded the viscosity concept by identifying that the effect is impurities sensitive and is most noticeable on steepest part of BH curve. This could be problematic as an explanation for the phenomena of interest where the effects are more pronounced as horizontal changes of  $H$ . However, it will be part of continued testing to gauge the sensitivity of the effect of interest to previous position on the hysteresis loop. Notably, the authors describe the viscosity in (2.9).

$$(2.9) \quad \Delta I = \hat{i} p k T F(t) + c$$

Where  $\Delta I$  is the change in magnetization intensity due to thermal energy from domain motion with measured time,  $t$ , after the corresponding change in applied field.  $T$  is absolute temperature of the magnetic material. The average magnetization intensity is  $\hat{i}$  with a scaling constant,  $p$ . The function,  $F(t)$ , is either  $Ct$  or  $\log(t)$  depending on if  $Ct \ll I$  or  $Ct \gg I$  where  $C$  is a constant that is material specific. While there are several scaling terms in (2.9), the behavior can be seen to have a lag effect when the function  $F(t)$  is logarithmic. The authors of [20]

identify three major parts the slope of induction, an initial spike, a decay, and then a logarithmic increase resulting in a bell shape.

Another expansion of the viscosity concept from [18], is in the description of high coercivity alloys. there are pseudo domain boundaries where the particles are too small to form full domain boundary creation and instead constitute a less ferromagnetic matrix. Therefore, only rotation of the magnetization vector is possible and can result in discontinuous changes in certain hysteresis loop locations. There are minimum values of domain free energy before and after the discontinuous changes and thus a minimum energy threshold. Obviously a change in applied magnetic field could overcome the threshold but another effect from thermal agitation could contribute to a baseline energy resulting in the necessary activation energy.

It is important to note that a similar mathematical description of the behavior is seen from [21], despite the authors only seeking to model the behavior in finite element analysis. The authors then provide an equation for relating the lag due to material impurities described in (2.10). First the authors provide an overview of hysteresis models with a discussion different statistical models of hysteresis. They identify models that are history independent models, e.g. Jiles-Atherton, and that are only appropriate for large, symmetric loops without minor loops. The authors then review the Priesach model which is history dependent leading to a better model for complex hysteresis loops with the presence of minor loops.

$$(2.10) \quad \frac{dB(t)}{dt} = \frac{\delta}{g(B)} |H(t) - H_{LF}(B)|^\alpha$$

The loop function  $H_{LF}$  is calculated using very low frequency hysteresis curves measured in the range of 1-5Hz. To determine which half of the curve the model is on,  $\delta$  is a directional parameter: +1 for rising induction, -1 for falling induction. For a particular material the parameter  $\alpha$  relates to the loop dynamics and is close to 2 for the range of materials studied by

the authors. The function  $g(B)$  is material dependent and is shown in (2.11). Better accuracy in the FEA study can be gained modifying the material constants  $G_m$  and  $\alpha$  as a feedback to match a known loop.

$$(2.11) \quad g(B) = \frac{G_m}{1 - \left(\frac{B}{B_{max}}\right)^2}$$

An improvement over earlier models in this contribution is that previous models related  $dB/dt$  to changes in the induction level. However, this did not yield as accurate results as (2.10). One drawback to this model is the amount of data needed for the accurate recreation of arbitrary hysteresis loops. First, a look up table of the static or semi-static major hysteresis loop and the first-order reversal curves. The sheet thickness and the material resistivity is also needed. Two additional loops are also needed to identify the dynamic components of the model. In [22], the structure of (2.10) and (2.11) is reproduced by applying tests of constant  $dB/dt$ . These authors found that higher slopes of applied conduction from the remnant flux density,  $B_r$ , to saturation, caused further rightward shifts, higher loss hysteresis loops. They provide telling figures by correlating the components of the bulk material losses with the segments of hysteresis loop. Specifically, and of practical use to the current work, they define the segments in terms of excitation, separated in a similar manner to loss separation. These components are shown in (2.12), (2.13), and (2.14). However,  $g(B)$  is modified in these equations from its definition in (2.11) to be more of an empirical hysteresis loop fitting component.

$$(2.12) \quad H_{hys} = H_{LF}(B)$$

$$(2.13) \quad H_{clas}(t) = \frac{d^2}{12\rho} \frac{dB}{dt}$$

$$(2.14) \quad H_{exc}(t) = g(B) \left(\frac{dB}{dt}\right)^{\frac{1}{\alpha}}$$

While much of this work fits imperfectly with the observed behavior it is useful to understand where prior work has sought answers. Many of the models represent behavioral fits

that sought engineering solutions to physical problems. Despite not being grounded in the physical interactions of materials and magnetization, the models can provide insight into what processes are most dominant in the bulk system. In order to assess these relationships, a review of applicable physical phenomena is provided in the next section.

## **2.5 Domain Wall and Magnetization Vector Motion**

Again, it is important to clear up mixed nomenclature and similar concepts by other names. For instance, engineers and electricians have tended to describe the losses in terms of hysteresis and eddy current losses. Material scientists and physicists describe the same concepts using physical models with the concept of magnetization domain movement. This mixed use of nomenclature can lead to confusion and implication of different and distinct processes despite them being the same phenomena. In this section, the focus will be on physical models and the resulting processes and subprocesses that lead to the implications of loss separation.

The principal physical model for core losses relies on the concept of magnetic domains of a material. One of the origins of losses then, is movement of the domain walls as they grow or shrink due to an applied field. Figure 2.3 shows a graphical representation of the arbitrary nature of individual magnetic domains, where the vertical arrows represent the direction and relative size of a saturated domain and the horizontal arrows represent the movement of domain walls as the global magnetization increases. In [23] and [24], Bertotti describes two important concepts in the domain wall loss models. First, that the net change of magnetization is due to the contribution of multiple regions distributed through the material. Second, the number of these regions is functionally dependent on the magnetic field. [25] describes in detail the movements that the domain walls can make. It further describes how these movements result in the generation of eddy currents causing core loss. The movement of the domain walls is spatially

discrete instead of uniform throughout the material. The speed of this movement has also been shown to be discrete in time. [26] shows that impurities in the material can cause domain wall velocity spikes despite slow global magnetization changes.

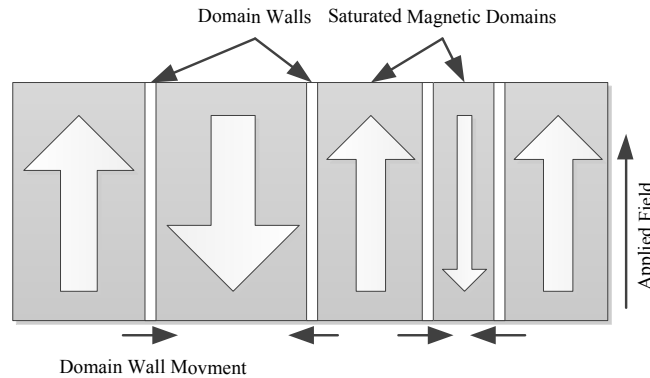


Figure 2.3: *Graphical Representation of Magnetic Domain Wall Movement.*

It is from this work that we have the understanding of domain walls that we do today. That is, the magnetic material can be subdivided into two sets of fully saturated magnetic domains. These domains are separated by domain walls. The global magnetization of a material is a result of the individual contributions of the different domains. Changes in the global magnetization occur as the domain walls move and the rotation of domain vectors resulting in increasing or decreasing the effect of local magnetization domains. An important figure of merit for a given material is the magnetic coercivity,  $H_c$ . The coercive field is defined in [27] by (2.15). Where  $\sigma_{dw}(x)$  is the domain wall potential, and  $M_s$  is the saturation magnetization density.

$$(2.15) \quad H_c = \frac{\left(\frac{d\sigma_{dw}}{dx}\right)_{max}}{2M_s}$$

This point on a hysteresis loop is defined as the largest gradient of wall energy. A semi-empirical model is discussed in [28]. There the focus is on the effect of flux switching which occurs by domain-wall motion at low fields, close to the coercive force, and by rotation of magnetization at high fields. At intermediate fields, flux switching occurs by incoherent rotation

in such a way that the demagnetizing fields effectively cancel out by having closely spaced surface poles of alternate polarity. This topic is discussed at some length in [29] and [30].

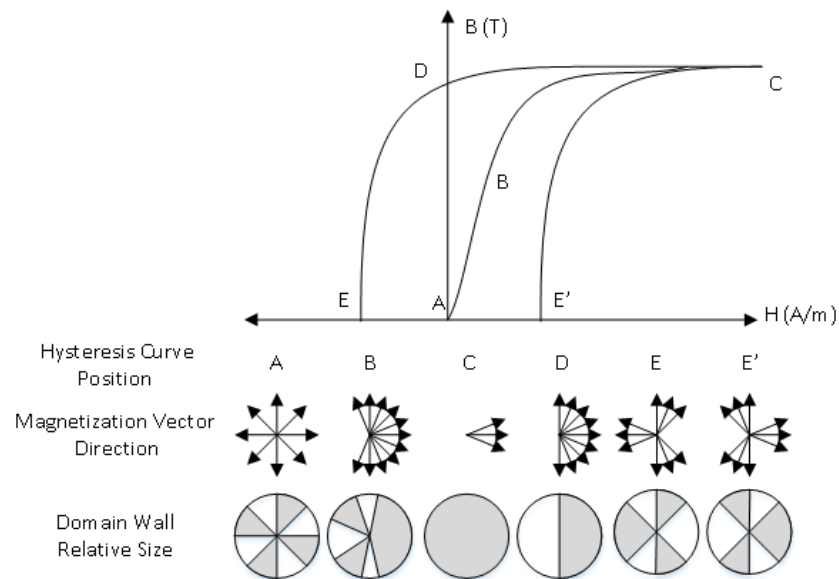


Figure 2.4: Magnetic Vector Direction and Domain Wall Size based on Hysteresis Loop Location.

The above graphic, Figure 2.4, shows magnetic vector rotation and domain wall size and rotation as it relates to a hysteresis curve. It is important to note that saturation means all of the domains point in the same direction, effectively creating a monolithic domain. As field is applied, the reverse pointing domains first shrink, then turn to alignment, then aligned domains grow. As field is reduced from saturation, domains rotate to the nearest easy direction, not the original orientation, resulting in the remnant flux density,  $B_r$ . A Magnetic after-effect occurs when the magnetization change does not respond immediately to changes in magnetic field. This appears as a magnetic viscosity as discussed above. While eddy currents can influence this after-effect, there are distinct magnetization processes. This is part of the reason for the confusion in nomenclature between electrical engineers and material scientists. Furthermore, aging effects, where changes occur slowly or at room temperature and are structural in nature, e.g. phase transition, precipitation or diffusion, are also a separate phenomenon that can lead to variations in  $B_r$ . There is an instantaneous change of magnetization  $I_I$  and then a time dependent change in a

similar structure to (2.6), shown in (2.16). Where  $\tau$  is a relaxation time constant and  $I_{n0}$  is the difference  $I_{n-inf} - I_I$ . It is important to note that  $B = u_0H + I$  in this notation.

$$(2.16) \quad I_n(t) = I_{n0} \left( 1 - e^{-\frac{t}{\tau}} \right)$$

Similarly, induced eddy currents can result discontinuities. The eddy current losses for small crystals are described in [30] as (2.17) and (2.18). Two types of induced eddy currents are described depending on the crystal model, homogeneous and heterogeneous, due to the change in domain wall differences for the crystal model. The homogenous model describes the change of domain walls in a cylindrical crystal while the heterogeneous model is domain wall grow in a more realistic crystal shape like a picture frame. In the equations,  $B$  is magnetization,  $d$  is material depth and  $\rho$  is resistivity.

$$(2.17) \quad P_{homog} = \frac{d_0^2}{2\rho} \left( \frac{dB}{dt} \right)^2$$

$$(2.18) \quad P_{het} = \frac{d_0^2}{8\rho} \left( \frac{dB}{dt} \right)^2$$

The induced eddy currents can also create a countervailing magnetic field at a skin depth shown in (2.19) where  $\omega$  is angular frequency  $\mu_r$  is permeability. This countervailing field reduces the amplitude of the changing magnetization at the skin depth by  $1/e$ . With the aforementioned effects in place, it is appropriate to now define the equations for motion of both the magnetization vector, (2.20) and the domain wall motion, (5.27). (2.20) holds with the assumption that  $\alpha^2 \ll 1$  and  $\alpha = \frac{4\pi\mu_0\lambda}{vI}$  where  $v$  is a unit less constant and  $\lambda$  is a damping constant, the relaxation frequency, in 1/s units.

$$(2.19) \quad d_{skin} = \sqrt{\frac{2\rho}{\omega\mu_r\mu_0}}$$

$$(2.20) \quad \frac{dI}{dt} = -v \left\{ I \times \left( H - \frac{4\pi\mu_0\lambda}{(vI)^2} \frac{dI}{dt} \right) \right\}$$

Careful inspection of (2.20) leads to the observation of precession movement. Without the damping term, the external field does not rotate the magnetization into alignment. With damping, the magnetization rotates towards alignment with the applied field. This is a spiraling

motion described by the non-zero derivatives of the applied field normal axis. The precession dominates in the plane for which the applied field is normal to but also provides some damping precession in the applied field vector.

$$(2.21) \quad 2I_s H = m \ddot{s} + \beta \dot{s} + \alpha s$$

The domain wall motion is described in (2.21) where the left term is the  $180^\circ$  wall pressure,  $90^\circ$  wall pressure is reduced by a factor of  $\sqrt{2}$ . Beta,  $\beta$ , is a damping coefficient and alpha is a restoring coefficient, finally  $m$  is a mass of the wall per unit area.  $I_s$  is the saturation magnetization vector and  $s$  is the wall displacement length. This ‘mass’ term originates from the momentum developed by the spin that comprise the wall. The wall motion forces rotation of spins. This causes an apparent demagnetization field of  $H = -I/u_0$ . Furthermore, this wall motion is normal to the applied field and can persist after removal of the applied field. Hence, the domain wall has an inertia. In [31], the author determines the power loss per unit volume for a given wall’s motion shown in (2.22) where  $W_{AB}$  is the distance traveled by the domain wall during the time interval of the half cycle. If the material is driven into saturation,  $W_{AB}$  is the average distance between domain walls. It is important to note that the domain walls have a threshold excitation field, below which no motion will occur. It is interesting to note that the solution for (2.22), for sinusoidal excitation, results in the form very similar to Steinmetz original work showing the influence of physical process appearing in accurate curve fitting, (2.23).

$$(2.22) \quad P_v = \frac{1}{W_{AB}\Delta t} \int_{t_A}^{t_B} \beta \dot{x} dt$$

$$(2.23) \quad P_v = \beta W_{AB} \omega^2 B_m^2$$

It is important to note two caveats to (2.22). First, the actual paths of the induced eddy currents are much shorter than the classical assumptions. Rather than traveling along the perimeter of the sample, the eddy currents travel in micro-elliptical arcs through cross section. This results in an increase in eddy current loss as seen in (2.24) where  $h$  is the wall height. This

is a major contributor to the anomalous loss component in loss separation. Second, the effect of many walls in a sample is to crowd the area where eddy currents can exist. This has the effect of reducing the losses predicted in (2.24). If there are a very large number of crowded domains, this reduction leads to losses that approach the classical eddy current loss prediction.

$$(2.24) \quad \frac{P_{micro}}{vol} = \frac{P_{clas}}{vol} \frac{W_{AB}}{2\pi^3 h}$$

In this section, the trapezoidal magnetic excitation waveform is shown. Understanding the magnetic effects from this waveform is critical to better understanding the magnetics design for active bridges. Furthermore, the magnetic behavior seen during this excitation can lead to better modelling and understanding of more general excitations seen in WBG power converters. Other researches have shown similar behavior with magnetic components but none have isolated the phenomena quite as distinctly. Therefore, it is important to review behavioral as well as physical models that could describe the phenomena. The interlinked descriptions of microscale magnetic behavior lead to some insights in the macroscale magnetic behavior that is observed in Figure 2.7. One insight relies on the concept that domain walls have inertia. This could cause excess losses during the transition from a high applied field to a lower applied field. Similarly, the spin precession could cause increased losses as the field force vector decreases in amplitude but does not change direction. At the very least, these concepts allow for explanations of behavior more closely related to the physical processes involved and less reliant on approximations of sets of observed behavior.

## 2.6 Numerical Models of Bulk Core Loss

Understanding why the magnetic core constitutes a loss element in a circuit does not yet provide a good method for calculating or predicting the losses in bulk material. Because the losses depend on the original domain state, domain motion, impurities and magnetizing spin,

there are still too many variables and states for accurate prediction. As such there has been a tremendous amount of research for developing monolithic models that allow engineers and designers accurate loss calculations. The three main approaches have been to predict the hysteresis path, separate losses into perceived physical phenomena and finally curve fit multiple loss profiles.

The core loss prediction technique, presented by [32] and improved in [33], known as Steinmetz Equation has been widely used to calculate core losses in magnetic materials. Many manufacturers provide the parameters for core materials in datasheets as a standard practice. If not provided, simple curve fitting of core loss graphs can be used to determine the values of Steinmetz parameters. Steinmetz Equation, (2.25) calculates the core loss per unit volume where  $k$ ,  $\alpha$ , and  $\beta$  are the Steinmetz parameters and  $f$  and  $B$  are the sinusoidal excitation frequency and peak flux.

$$(2.25) \quad P_v = kf^\alpha B^\beta$$

While (2.25) has proven to be well suited for applications where sinusoidal flux is present in the core, it performs poorly for nonsinusoidal excitation and cannot account for DC flux. This is critically important as increasingly power converters and electrical machines subject the core material to nonsinusoidal remagnetization. The transformer in a flyback converter and the stator in a switched reluctance machine, Figure 2.5 and Figure 2.6, are examples of nonsinusoidal and possibly DC bias magnetic excitation.

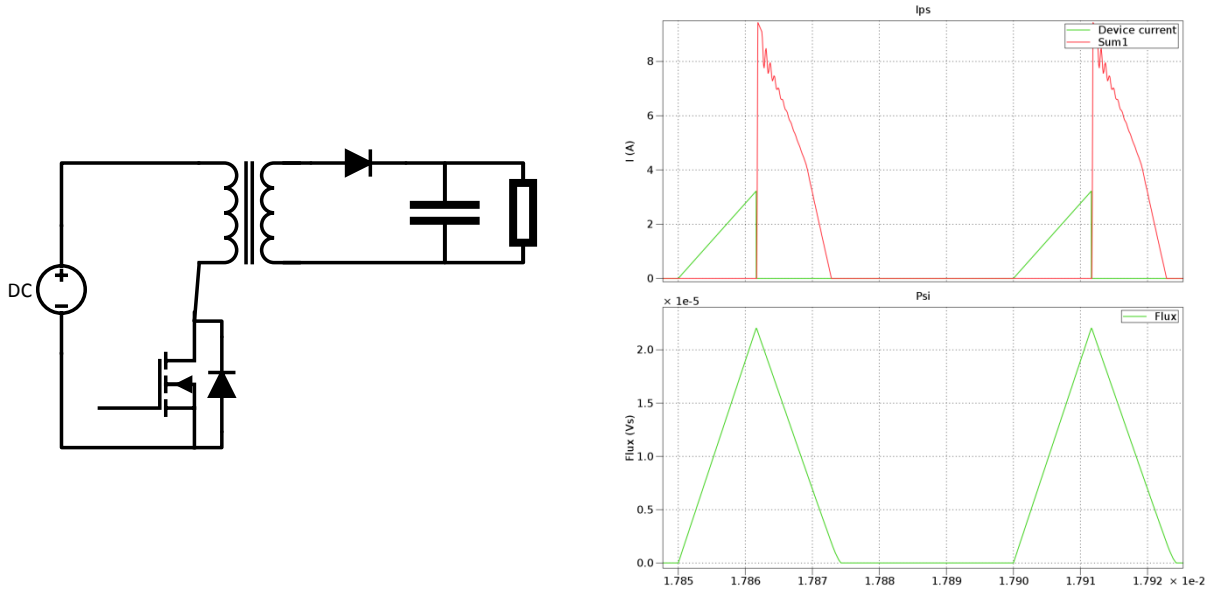


Figure 2.5: Example of Flyback Converter Topology (Left) and Associated Transformer Current and Flux Waveforms(Right).

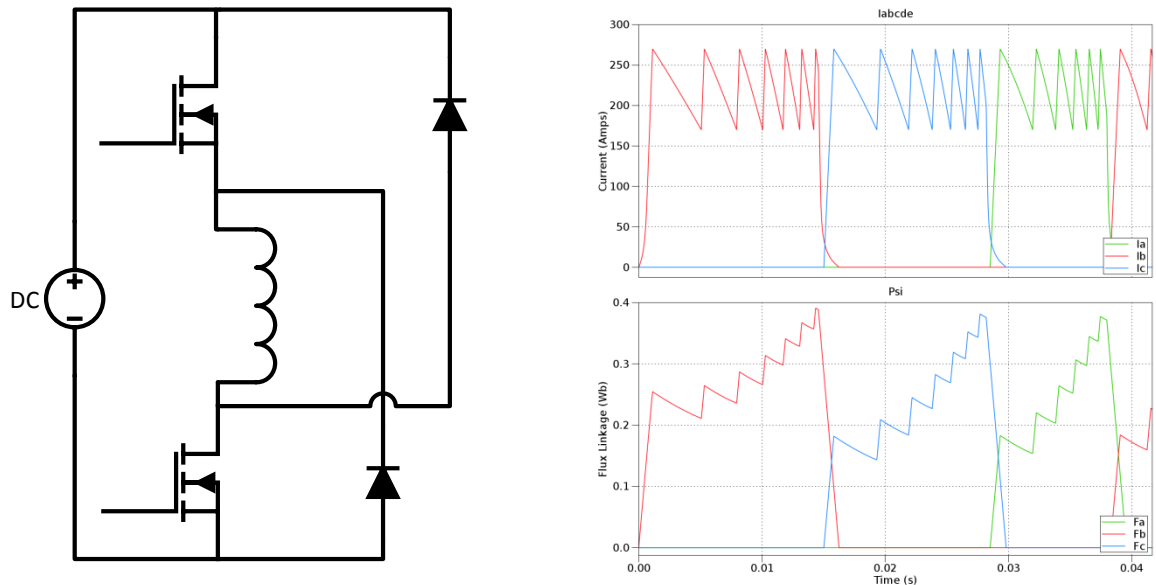


Figure 2.6: Single Leg of Three Leg SRM Driver and Associated Stator Current and Flux During Chopping Mode.

Clearly a core loss model that accurately accounts for flux that is not sinusoidal is needed. In order to ensure adoption of the model, one that utilizes the existing Steinmetz parameters is preferable to an entirely new equation. This section will review existing core loss alternatives to Steinmetz equation.

### 2.6.1 Separating Losses

This method has arisen and developed away from the original well defined simple geometries. While at small sample sizes the numerical models accurately follow physical processes, over time the models have been modified to better predict bulk materials at the expense of true physical basis. Loss separation has been used historically and has developed over time [34]. The principal approach is to separate the total losses into the eddy current,  $P_e$ , and hysteresis,  $P_h$ , components and an extra anomalous loss,  $P_a$ , component (2.26). These losses can be described in terms of magnetizing force functions as previously mentioned in (2.12), (2.13), and (2.14). A more direct breakdown is shown in (2.28), (2.31), and (2.32).

$$(2.26) \quad P_t = P_h + P_e + P_a$$

The Steinmetz fittings are often further expanded to consider loss partitioning in terms of different operative mechanisms as shown in [32]. An alternate loss model, emphasizing loss separation, is the 3-term Steinmetz equation that is expressed using scalars  $k_{hys}$ ,  $k_{eddy}$ , and  $k_{exc}$  which are used to partition power loss density per unit volume for (i) hysteresis, (ii) classical eddy current, and (iii) excess loss components, respectively. In product literature it is common to lump the last two terms as total eddy current losses with a power law exponent,  $\beta$ , to denote the dependence on induction. Static hysteresis loss dominates at low frequencies and eddy currents dominate at high frequencies.

$$(2.27) \quad P_t = k_{hyst}fB + k_{eddy}(fB)^2 + k_{exc}(fB)^{\frac{3}{2}}$$

The partitioning constant,  $k_{eddy}$ , is proportional to the square thickness of the material and inversely proportional the material's resistivity. Therefore, high resistivity is desired for magnetic components operating at high AC frequencies. Resistivity's in amorphous metal ribbons, (AMR) , MANCs and crystalline materials are both tunable with chemistry but typically

are 2-3 times larger in AMR which significantly reduces eddy current losses. Hysteretic losses are diminished in AMR, MANCs and bulk amorphous materials through random magnetic anisotropy [35]. Typically, magnetic induction is sacrificed for glass forming ability (and resistivity) in AMR and bulk amorphous alloys as compared with crystalline materials e.g. Si steels. MANCs offer a middle ground between the highest inductions of crystalline materials and high resistivity of amorphous materials. The ability to cast AMR's and MANCs in thin cross sections significantly impacts eddy current losses to reduce high-f losses [35].

The anomalous eddy current (AEC) losses, third term in the three-term Steinmetz equation is associated with dynamic domain wall motion. AEC contributions originate at a mesoscale due to local heterogeneities in magnetic domain structure [36], [37]. Just as laser scribing is used for pinning magnetic domain walls in Si-steels to limit their dissipation of energy at high frequencies, inducing anisotropy in AMR and MANCs have been employed to lower losses at high frequencies. In AMRs, anisotropy is typically induced by transverse (to the AMR length) field annealing, rolling and more recently strain annealing [37].

The loss separation technique suffers the same need for empirical studies as many of the earlier mentioned methods. Both  $P_h$ ,  $P_a$  must be calculated beforehand while Maxwell's equations can be used to determine  $P_e$ . As such, a measurement for each waveform of applied field to the core material would need to be determined, suffering from the same inaccuracies that the sinusoidal predictions have for core loss. However as new core testing circuits enable direct excitation of various waveforms, there may be trends or other fit functions that provide more generalized parameters for predicting core losses. In a way similar to the Steinmetz premagnetization graphs for DC bias, [38], it could be possible that the coefficients in of the loss separation fit nicely on excitation dependent sets of curves.

### 2.6.2 Hysteresis Curve Predictions

There are two main approaches developing hysteresis models. The first attempts to take a holistic and global approach to calculating the energy used in magnetic core material. The other approach is to use statistical techniques to predict domain wall movement.

A macroscopic energy model was developed in [39] and is generally referred to as the Jiles-Atherton model. This model is based on an approximation of the mean field in the material. It assumes that all of the domain walls interact with the field and magnetization through a weighting function. The JA method does show a strong ability to predict temperature and mechanical stress impacts on the hysteresis curve and consequential losses and could be used as the starting point of a design. Research has continued on this path to model more complex features. Li, [40], develops another set of equations that help to model anhysteretic losses and others have shown that the JA method can be extended to dynamic calculations [41]. Despite the continued research, this model and its extensions require many empirically calculated material parameters. [41] showed that seven parameters were needed for the dynamic model.

Complex and non-linear waveforms are still difficult to replicate with the aforementioned models. This presents a significant problem for power electronics converters. Trapezoidal excitation is an example of a common waveform. The hysteresis curve that results from the trapezoidal excitation pattern presented below in Figure 2.7. The vertical jerk in current in the excitation waveform translates to a horizontal shift in the BH loop. This represents a change in  $H$  without corresponding change in  $B$ . Because this phenomenon provides such distinct BH curves, various approaches for predicting BH loops were investigated to see the state of the art and to potentially predict these wave shapes. Since pulse width modulation (PWM) converters have

similar transitions to the newly applied excitation, works focusing on PWM modelling were of particular interest.

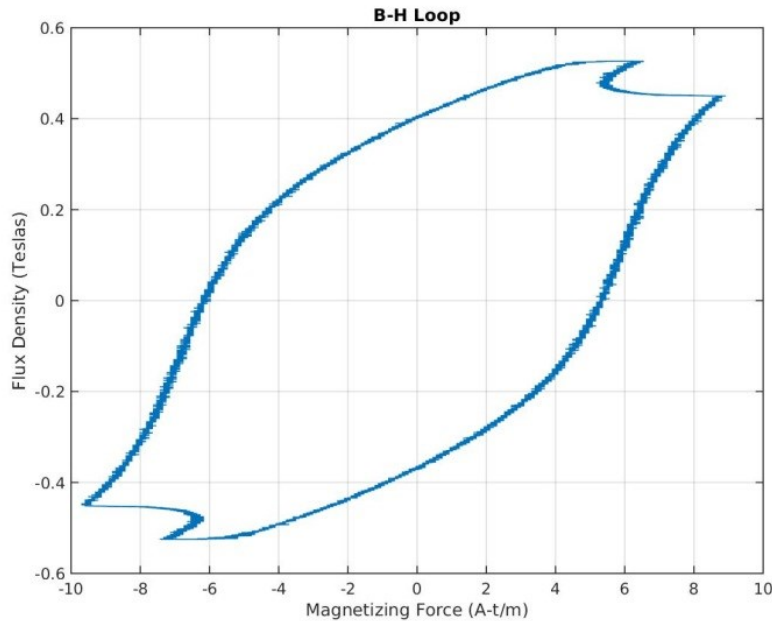


Figure 2.7: *Hysteresis Loop For Trapezoidal Excitation.*

A history dependent model was proposed by [42]. This model approaches the development of the hysteresis curve and PWM associated minor loops by adapting the curve shape and progression based on the turning point. That is, the authors' algorithm adapted depending on where magnetic excitation turned from increasing to decreasing, and vice versa. This enabled the accurate reproduction of complex BH loops with PWM artifacts. In order to achieve these results, the major BH loop and a sufficient set of first order return curves need to be determined for the desired material.

The second curve prediction method is to use a statistical models developed by Preisach [43] and applied to the magnetic hysteresis curve [44]. The method utilizes a weight function that models material characteristics. This model has limitations in modeling minor loops and is more

of a static representation. The weighting function can also be viewed as a limitation as it requires several empirically developed material parameters.

In [45], the simple wave shape hysteresis loops are created by expanding the typical loss separation equations. The basic concept for the loss separation for which the loop generation equations are derived by is shown below in (2.28), (2.29), and (2.30). In the improved equations,  $P_h = P_h(f)$  that expands with frequency,  $f$ . The classical and excess loss components are expanded as shown in (2.31) and (2.32). With these three loss components, and the instantaneous state of the excitation waveform, the authors show an accurate BH loop representation of basic wave shapes. In (2.31),  $n$  is the number odd harmonics plus one and  $d$  is the material thickness with conductivity of  $\sigma$ . In (2.32),  $G$  is a material coefficient with a cross sectional area  $S$ .  $V_o$  is the statistical distribution of local coercive fields.

$$(2.28) \quad P_{hysteresis} \propto \left| \frac{dB}{dt} \right|$$

$$(2.29) \quad P_{classical} \propto \frac{dB^2}{dt}$$

$$(2.30) \quad P_{excess} \propto \frac{dB^3}{dt}$$

$$(2.31)$$

$$P_{classical} = \frac{\sigma d^2}{12} \frac{1}{T} \int_0^T \dot{B}^2 dt = \frac{\sigma \pi^2 f^2 d^2}{6} \sum n^2 B_n^2$$

$$(2.32) \quad P_{excess} = \frac{\sqrt{\sigma G V_o S}}{T} \int_0^T |\dot{B}|^{\frac{3}{2}} dt$$

There does exist work that attempts to describe physical impacts on the loss separation models. Fish provides an extensive overview of the engineers' approach to core loss [34]. In this publication the core loss is shown as the separation of hysteresis, eddy current and excess eddy current losses. It also describes many different manufacturing processes, pointing to possible physical explanations for this loss model. Fish also describes how the magnetic domains are influenced by the material development and how these domains contribute to the overall loss.

The authors of [46] approach the BH loop modelling in a different manner. Instead of developing the hysteresis loop based on separation of losses, the authors directly determine the position on the horizontal axis with (2.33) based on an applied voltage,  $dB(t)/dt$ . Here  $H_h(B)$  represents the static hysteresis component which is measured at very low frequencies.  $\delta$  is a directional term used to ensure proper ascending and descending behavior of induction.  $g(B)$  controls shape of the loop.

$$(2.33) \quad H(t) = H_h(B) + \delta \left[ \delta g(B\delta) \frac{dB(t)}{dt} \right]^{\frac{1}{\alpha}}$$

The function,  $g(B)$ , is a viscosity function that is likely unique for each material. This concurs with other works which use similar equation modifying functions to describe the statistical distribution of activation energies and will be described further in the Magnetic viscosity section. Similarly, both peak and instantaneous induction levels influence the value and behavior of  $g(B)$ .

Finally, a sinusoid with third harmonic is studied in depth in [47]. This study is of import because of the similarity excitation wave shape progression. That is, the applied voltage dips to a lower amplitude value after a peak. This is very similar to the effective trapezoidal current excitation voltage waveform in. The authors demonstrate that when the third harmonic component is displaced by  $180^\circ$  the losses are a maximum.

The reliance on many parameters limits the practical use of these models. Practitioners would be required to experimentally determine all these parameters as manufactures seldom if at all provide the parameters. The methods presented for developing hysteresis loops as well as those for predicting the magnetic core losses provide insight into the nature of the excitation phenomenon. While these methods vary in degree in physical origin, they have been shown to be reasonably accurate for specific measured behavior.

### 2.6.3 Loss Map Curve Fitting

As mentioned in the introduction, [32] presented an empirical equation that is derived from fitting the loss curves of a material. Generally, Steinmetz equation (2.25) is used to curve fit sinusoidal core loss profiles for a material. The coefficients  $k$ ,  $\alpha$ , and  $\beta$  are loss parameters while the sinusoidal wave is characterized by frequency,  $f$ , and peak induction level,  $B$ . The elegance of this approach is that there are only three principal parameters. Often times, manufacturers provide these constants in material datasheets further simplifying the use and broadening the adoption. Critically, (2.25) is only effective for sinusoidal remagnetization. Researches have expanded the equation and utilized more sophisticated relationships to expand this curve fit to other wave shapes and generalize the equation [48], [49]. Despite these works, DC excitation and trapezoidal excitation is problematic and requires more parameters. Furthermore, establishing this excitation is non-trivial and often requires additional circuits coupled to the core through auxiliary windings [50]. This section will discuss the extensions to (2.34), shown again below for convenience, for broadening the applicable waveforms.

$$(2.34) P_v = kf^\alpha B^\beta$$

Some core materials show a distinct change in the loss profile over the entire frequency range of the material. To account for this, [51] modifies  $k$  and  $\beta$  to be adaptive. Similarly, they show how a multi-order polynomial term to account for temperature  $g(T)$ . These new terms are shown below in updated Steinmetz equation (2.35).

$$(2.35) P_v = (aln(f) + b)f^\alpha B^{(cf+d)}g(T)$$

In order to account for nonsinusoidal waveforms, [52] uses a Fourier expansion of the waveform and applies (2.25) to each term of the expansion. However, this approach is not mathematically appropriate for many materials. That is, as  $\beta > 2$ , for many materials, there is a

highly nonlinear relationship between induction and core loss. Superposition is only valid for linear systems and so this approach breaks down for many materials [53].

Another variation of (2.25) accounts for losses due to specific core geometries. This model is shown below in (2.36) where the new value  $C_2$  accounts for the impact of the geometry.  $C_2$  is dependent on the core cross section and material conductivity i.e., how the eddy currents are changed by the specific core structure.

$$(2.36) \quad P_t = kf^\alpha B^\beta + C_2 f^2 B^2$$

The authors in [38] and [54], have shown some modifications of (2.25) that enables a designer to accurately account for arbitrary waveforms. This method will be explored in depth in the next section.

### 2.6.3.1 The Modified Steinmetz Equation Approach

In order to utilize the advantages of the Steinmetz equation of only three parameters, and widely published values [38] extended this fundamental equation to apply to arbitrary waveforms. [41] showed that the core losses are directly related to the global remagnetization rate,  $dM/dt$  which is proportional to the induction change rate,  $dB/dt$ . Therefore, the first step is to find the average induction change rate over an entire cycle (2.37). Were  $\Delta B = B_{max} - B_{min}$ . This integral can be transformed to a time integral by multiplying the integrand by  $dt/dt$  (2.38).

$$(2.37) \quad \dot{B} = \frac{1}{\Delta B} \oint \frac{dB}{dt} dB$$

$$(2.38) \quad \dot{B} = \frac{1}{\Delta B} \int_0^T \left( \frac{dB}{dt} \right)^2 dt$$

There must now be a normalization that relates  $\dot{B}$  to the frequency of remagnetization,  $f$ . Durbaum showed that normalization factor is simply  $2/\Delta B\pi^2$ . This allows us to calculate an equivalent frequency of applied field as can be seen below in (2.39). This allows the calculation specific energy loss for each cycle (2.40), and total power loss per unit volume, (2.41), as the

waveform repeats at a frequency of  $f_r = \frac{1}{T_r}$  and  $\hat{B} = \frac{\Delta B}{2}$ . The symbol  $f_{eq}$  does not take into consideration dc flux, it only considers the periodic excitation and modifies the arbitrary wave shape to that of a sinusoidal one through frequency modification.

$$(2.39) \quad f_{eq} = \frac{2}{\Delta B^2 \pi^2} \int_0^T \left( \frac{dB}{dt} \right)^2 dt$$

$$(2.40) \quad w_v = k f_{eq}^{\alpha-1} \hat{B}^\beta$$

$$(2.41) \quad p_v = f_r k f_{eq}^{\alpha-1} \hat{B}^\beta$$

The advantage of this Modified Steinmetz Equation (2.41) (MSE) calculation is that it fully describes the losses in the time domain for arbitrary induction wave shapes. Furthermore, it adds no additional parameters to the Classical Steinmetz Equation (2.25) (CSE) allowing for simple adoption.

### 2.6.3.2 Excitation Shape Fitting

While it is not clear that other authors have shown negative  $\frac{di}{dt}$  during transitions between the application of two positive voltages, others have shown surprisingly high  $\frac{di}{dt}$  during positive to negative transitions. In [55], the author attributed solely to core loss. The author relates the nearly vertical change in current to core loss by describing triangular current and square voltage peak to peak values with the on time,  $D$ , in (2.42). It is important to note that in (2.42),  $I_{pp}$  is the peak to peak current when the vertical slippage is removed. That is,  $I_{pp} = I_{max} - I_{min} - I_{vert}$  where  $I_{vert}$  is the amplitude of one vertical slip of current

$$(2.42) \quad P_{core} = D(1-D)^2 V_{pp} I_{pp} + D^2(1-D) V_{pp} I_{pp} = D(1-D) V_{pp} I_{pp}$$

The authors of [48] extend this idea with a variable parallel resistance similar to that of Figure 2.8 that is proportional to the sinusoidal losses. This core loss is described by (2.43) where the ratio of triangular excitation to sinusoidal excitation is related to the duty cycle,  $D$  and a fitting factor  $\gamma$ . The authors show that (2.43) fits closer to the measured core losses than the

IGSE though they do not compare it to the twice improved generalized Steinmetz equation ( $I^2$ GSE) equations that considers relaxation effects as presented in [14].

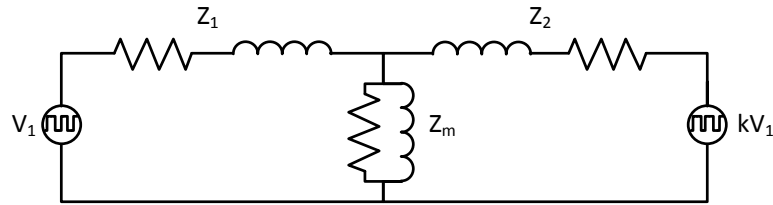


Figure 2.8: Pi Model of Transformer for Dual Active Bridges.

$$(2.43) \quad \frac{P_{tri}}{P_{sin}} = \frac{8}{\pi^2} 4D(1 - D)^{\gamma+1}$$

The authors of [14] report similar current behavior but it is difficult to fully verify as the results presented do not clearly show this effect in the waveforms. This is because current is omitted while the hysteresis loop presented is qualitatively a similar shape. The authors suggest that magnetic relaxation is the likely cause for this phenomenon and will be discussed in more detail in the following sections. In [56], the authors identified that unexpected losses occur during voltage transitions. In particular, there are losses occurring when an applied voltage transitions to a zero applied voltage state. However, they do not provide an explanation nor justification for these measured losses.

With others demonstrating similar  $\frac{dI}{dt}$  effects in their studies, it strengthens the argument the phenomenon experienced is indeed an artifact of the magnetic material. It is particularly striking now however due to the uniqueness of the excitation waveform the unexpected sign change in  $\frac{dI}{dt}$  without a corresponding sign change in the applied voltage. Where previous works have noticed the effect in positive to negative voltage transitions or positive to ‘zero’, in reality negative to conduction losses, transitions they could ostensibly argue that the wave shapes were not unexpected or at least fit within expected behavior and sensor inaccuracies.

The gross effects of the core under non-sinusoidal excitations did not go unnoticed however and work has been performed to model, predict and characterize the core loss. It should be logical then that advanced hysteresis prediction models would incorporate similar effects.

A similar approach was presented by [56]. Here the excitation waveform is separated into various components. This is coined as the composite-waveform hypothesis. This is a more complex signal parsing method than a Fourier transformer which has been shown to produce inaccurate loss predictions. This hypothesis posits that the total losses of any pulse pattern can be broken into the sum of energy losses of component pulses. In order to achieve this mapping, square wave losses over wide frequency range were recorded. The total loss is taken as the composition of the energy losses as a function of applied voltage and on time. It is important to note that the authors present specific voltage waveforms of interest that would result in the excitation waveforms that are the subject of investigation. However, these drawings are not reflected in the recorded results and it appears to be merely a suggestion of the value of the approach without realizing the excitation.

### 2.6.3.3 Generalizations of Steinmetz Equations

It should be mentioned that there has been continued development on modifying parameters of Steinmetz Equations as was done to develop the MSE. Another equation has been developed by [49], the Generalized Steinmetz Equation (GSE) (2.44) and (2.45). The authors showed that for a sinusoidal flux with  $h^{th}$  harmonic, the MSE underestimates the core loss by a factor  $h^{\alpha-2}$ .

$$(2.44) \quad \bar{p}_v = \frac{1}{T} \int_0^T k_1 \left| \frac{dB}{dt} \right|^\alpha |B(t)|^{\beta-\alpha} dt$$

$$(2.45) \quad k_1 = k / (2\pi^{\alpha-1} \int_0^{2\pi} |\cos(\theta)|^\alpha |\sin(\theta)|^{(\beta-\alpha)} d\theta)$$

This model shows some error due to the fact that it relies on the instantaneous loss parameters as noted by  $B(t)$ . Thus, the improved GSE (IGSE) was presented by [57] [58] that uses the peak to peak flux density, remaining consistent with CSE. The modifications proposed are shown below in (2.46) and (2.47).

$$(2.46) \quad \bar{p}_v = \frac{1}{T} \int_0^T k_1 \left| \frac{dB}{dt} \right|^\alpha \Delta B^{\beta-\alpha} dt$$

$$(2.47) \quad k_1 = k / (2\pi^{\alpha-1} \int_0^{2\pi} |\cos(\theta)|^\alpha 2^{(\beta-\alpha)} d\theta)$$

The changes are subtle but  $B(t)$  is replaced with  $\Delta B$  in (2.46) and  $|\sin(\theta)|$  is replaced with 2 in (2.47). The work of [58] does require separation of major and minor loops of flux but it predicts core losses very well. A simplification of the use of Steinmetz for triangular induction is the waveform-coefficient Steinmetz equation method [59]. There, the losses for different waveforms are shown to be a scalar of sinusoidal losses. However, this only works for a very limited set of excitation patterns.

The iGSE predicts losses independent of any DC bias. As such work by [50] has shown an approach to account for DC Premagnetization. These authors introduce the concept of a Steinmetz Premagnetization Graph (SPG). The SPG provides a curve fit for the variation of Steinmetz parameters based on the DC field strength  $H_{DC}$  and temperature.

Research continues to develop and improve upon the CSE in different ways. In [60], the latest in Steinmetz models is coupled with hysteresis curve predictions of the previous section as an example. However, there has yet to be a monolithic solution to predicting core losses for arbitrary conditions. However, many approaches are available to satisfy a subset of conditions that would be useful for design.

A common and important topology that subjects the magnetic materials to trapezoidal excitation is the dual active bridge (DAB) [61]. This topology combines the energy storage with

isolation in a medium frequency (MF) transformer. This circuit provides significant capabilities and meets the needs of many application spaces. As such, it has been the subject of many researches work to optimize and improve circuit performance [62], [63]. One readily used technique is to adjust the converter switching pattern which increases the MF transformer applied voltage from the traditional two to three levels [64], [65]. This exaggerates the trapezoidal nature of the exciting waveform.

The authors of [66], [67] proposed and demonstrated the benefits of a deliberately designed inductor that is in addition to and in series with the MF transformer. This enables researches to design a finely tuned inductive storage element without being beholden to the MF transformer leakage inductance. This improves the control stability and enables an increased operating range. In a similar approach, the researchers of [68] use an auxiliary transformer as a controllable inductance in series with the MF transformer. In both of these cases, the exciting flux of the magnetic elements is trapezoidal.

Another contributing factor to the prevalence of trapezoidal excitation in the magnetic material is when the MF transformer has a leakage inductance mismatch. This occurs when there is a large turns ratio and the normalized inductance is unevenly distributed [69]. One example of this situation is in electric vehicles where battery voltages are stepped up to drive voltages. The three port DAB utilizes multiply sloped trapezoidal excitation over most operating conditions [13]. Other topologies subject magnetic components to trapezoidal excitation as well including the flyback converter and brushless DC motors [70], [71].

Due to the fact that the aforementioned loss prediction models scale loss maps of excitations other than the trapezoidal case, these core loss models are inadequate for fully understanding or representing the magnetic core losses in the active bridge topology. In order to

determine and predict the specific losses in a DAB the authors of [72] designed a dual active bridge with a shared DC bus. This allowed the determination of the total system losses. While this method provides an accurate transformer excitation, it is difficult to isolate the losses of the transformer from the other circuit components. Furthermore, a full control suite is also needed to ensure that the transformer excitation is balanced during transients. Parasitic elements such as common mode capacitance can also play a role in obscuring meaningful data. Most importantly, this method is only applicable to the desired transformer and is difficult to scale.

With all of the applications that experience trapezoidal excitation of the magnetic components, it is critical that materials be well defined and understood for this specific waveform. The full section will demonstrate a new electrical testing topology. It will expand upon the preliminary results to provide a meaningful characterization and comparison of materials. The full section will put the results in the context of existing material performance metrics and enable insight and further work on new design approaches and optimization techniques.

## **2.7 Material Classifications and Comparison**

While it is fairly elementary and a basic component of many textbooks on the topic, it is useful to provide a basic overview of the classifications of magnetic materials. Following the definitions provided in [73]. Ferromagnetic materials are materials where the magnetic moment of adjacent atoms is aligned for additive fields. This alignment allows the magnetic flux to be linked to externally applied fields. In antiferromagnetic, the magnetic moments oppose each other and cannot link to the externally applied fields. However, if the spacing between atoms is increased, through alloying, antiferromagnetic can align in a ferromagnetic configuration. Similarly, combining materials with magnetic moments with varying degrees of alignment or

misalignment can be used to create weakly ferromagnetic or ferromagnetic materials. Three of the most fundamental ferromagnetic materials, often alloyed for various changes to properties, are iron, cobalt and nickel whose saturation inductions are 2.2, 1.8 and 0.64 respectively. If a ferromagnetic material is capable of changing its magnetization vector easily, it is said to be a soft magnetic material and is useful for power converter applications. A hard or permanent magnetic material is also useful but seen more in motor and generator designs.

Among soft magnetic materials, isotropic materials exhibit similar properties in all material directions. Examples of these materials are ferrites and powder cores. Anisotropic materials have different properties along different axis. For instance, the magnetization vector can change with little resistance along the easy axis while the hard axis requires significantly more excitation to cause vector changes. Anisotropic materials are often metallic crystals that are cast into thin ribbons or laminations. These are then rolled or stacked to build up a bulk core. There are a wide range of properties and lamination chemistries from relatively simple iron to more complex metal amorphous nanocomposites (MANC). [74] provides significant information many materials as well as general information tables. Other details or material specific parameters are often only found in production literature.

With so many different materials it is often difficult to determine the best options for a given application. Table 2.1 and Table 2.2 show several properties as well as selected loss measurements for several properties. An Ashby chart, [75], is often useful to two parameters of several or groups of materials as was done in [76]. However, it is difficult to compare multiple parameters simultaneous. This requires several traditional charts or complicated tables where it is difficult to quickly identify potential material candidates.

Table 2.1: Example Magnetic Materials: Basic Properties Part A.

Material ID	Material Type	$\mu_r$	$B_{sat}$ (T)	Lamination Thickness (in)	Density (kg/ m <sup>3</sup> )	Resistivity ( $\Omega m$ )	Permittivity ( $\epsilon_r$ )
Finemet Uncut FT-3TL	Nano-Crystalline	20000	1.23	0.0007	7300	0.0000012	1
JFE 6.5% Si 10JNHF600	Electrical Steel	4,000	1.88	0.0040	7,530	8.20E-07	1.0
CA Not-Impregnated	ARPA-E HTX012B	80,000	1.20	0.0008	7,600	1.10E-06	1.0
Metglas - 2605SA3	Amorphous	35000	1.41	0.001	7290	0.00000138	1
Ferrox-Cube - 3C95	Ceramic Ferrite	5,000	0.53	0	4,800	5.00	20.0
Fair-Rite - 73	Ceramic Ferrite	2,500	0.39	0	4,800	1.00	20.0

Table 2.2: Example Magnetic Materials: Basic Properties Part B.

Material ID	T <sub>Curie</sub> (°C)	Thermal Conductivity (w/mK)	P <sub>Loss</sub> 1 kHz (w/kg)	P <sub>Loss</sub> 10 kHz (w/kg)	P <sub>Loss</sub> 20 kHz (w/kg)	P <sub>Loss</sub> 50 kHz (w/kg)	P <sub>Loss</sub> 100 kHz (w/kg)
FT-3TL	570	8.15	0.04	2.25	7.55	37.27	124.76
10JNHF600	746	18.0	7.4	198.2	533.4	1973.9	5311.4
CA	600	8.2	0.10	4.9	15.7	73.2	234.3
2605SA3	358	9	0.60290117	21.39174074	62.63868327	259.2087354	759.0076035
3C95	215	3.6	0.05	6.2	26.0	175.0	739.4
73	160	3.6	0.03	1.85	6.44	33.5	116.8

A different method is needed for more sophisticated screening of materials. An option is the spider chart. Figure 2.9 shows a spider chart comparing all of the values of Table 2.1 and Table 2.2 normalized for better performance e.g. highest  $B_{sat}$  and lowest loss etc. As can be seen, clear trends between groups of materials emerge. Similarly, unique design options become apparent. For instance, the losses of the Finemet nanocrystalline material are similar to the Fair-Rite ferrite material. However, the nanocrystalline has a higher flux density and relative permeability. This opens new design flexibilities for full converter system optimization as the two materials perform best at significantly different fundamental frequencies.

What is not shown in this example graphic is the option to do weighted parameter comparison. Aerospace applications may prioritize designs using light materials while commercial manufactures would design for lower costs. Once an application's weights are applied designers can compare many materials simultaneously. A material's enclosed area provides a useful metric that can be used to evaluate a material holistically.

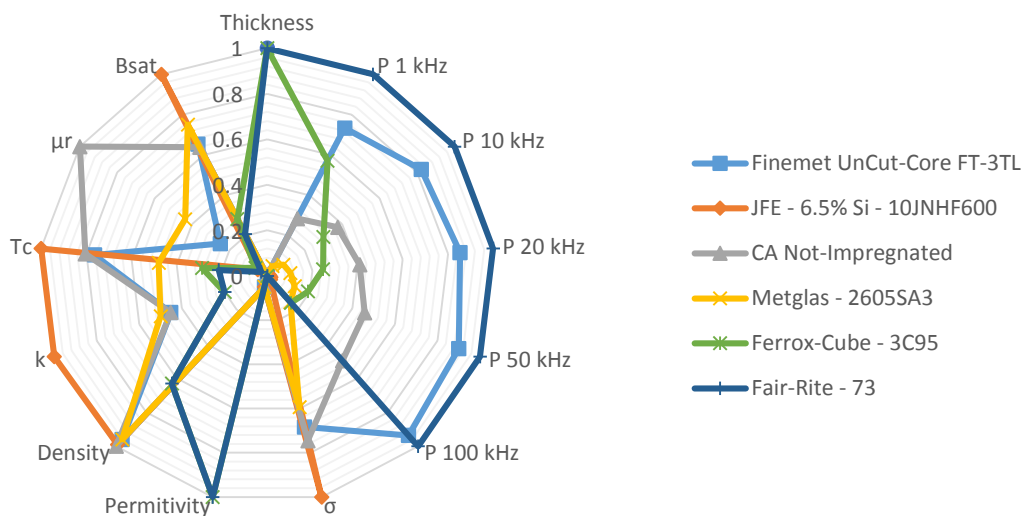


Figure 2.9: Spider Chart Normalized Multiparameter Comparison of Soft Magnetic Materials.

## 2.8 Conclusion and Future Work

Magnetization process and physics were reviewed in this chapter. While physics can accurately describe the magnetization behavior small, a few crystals in size, scale specimens, these models break down at practical engineering scales, a few kg. A brief overview explored how these phenomena have been used to inspire analytical models and prediction tools for bulk materials. These models have many limitations and are limited to a few specific applications. As such, engineers have tried to provide abstracted models that describe fitting functions to observed behavior. Finally, a method for screening materials using a spider chart was shown. This charting method allows the direct comparison of several materials and material parameters simultaneously.

More work is needed to better integrate physical behavior with modelling and behavior fitting techniques. This requires more advanced characterization testing and systems as presented in CHAPTER 3:. New screening techniques and improved material data will enable more informed design decisions. This proposed screening method will enable more advanced application solutions as shown in CHAPTER 6:.



## CHAPTER 3: CORE CHARACTERIZATION TECHNIQUES

### 3.1 Motivation

This chapter will present existing techniques and limitations of characterizing magnetic materials at high power. It will introduce new solutions to overcome these limitations. It will also demonstrate the multiple variables that need to be considered when characterizing materials. This is essential for the magnetic design as this chapter will show many parameter deviations from general datasheet values. This will enable more informed designs that meet expectations during operation. This is particularly critical for designs in the medium frequency range as preferred materials, like nanocrystalline or amorphous, demonstrate anisotropy and nonlinear behavior.

### 3.2 Measurement Circuitry

In order to characterize magnetic material at practical levels, a test circuit is needed to excite the core. The excitation drive converts the DC power into the desired excitation waveform. In order to focus on the high power medium frequency application domain, Silicon Carbide WBG mosfets are used in an H-bridge topology as seen in Figure 3.1. The core under test is connected to the two legs of the converter to enable bipolar excitation. As can be seen in Figure 3.1, the primary current and the secondary voltage are measured for analysis. The primary voltage can also be measured but is not used for characterizing the core material due to the loss artifacts that appear in the waveform.

In many power electronics applications, the exciting current is triangular in shape. This is due to the square wave voltages applied to the magnetic components. Figure 3.2, below, shows two examples of applied waveforms that the magnetic testbed is capable of producing. In the two figures, the switching frequency defines the period,  $T$ . In cold temperature, baseline tests, a

single excitation wave will be used. To study full operation of the magnetic material the exciting waveforms should be applied for a longer duration. An additional aspect of this longer test is blanking time between excitation waves. Figure 3.2, left, shows more traditional excitation waveforms where the flux wave is continuous and bipolar while the right waveform can be used to explore modern advanced excitation waveforms specifically used in dual active bridge topologies [62], [64], [77], and [78].

The primary core parameters of core loss, excitation power and relative permeability are easily extracted by measuring the primary current and the open circuit secondary voltage. The magnetizing force and the flux density are calculated from (3.1) and (3.2) respectively. The primary current is scaled by the primary turns,  $N_p$  and magnetic path length  $l_m$  to determine magnetizing force,  $H$ . The induction is calculated by integrating the recorded secondary voltage in post processing and scaling by the secondary turns  $N_s$  and core cross sectional area  $A_c$ .

Using (3.1) and (3.2), the relative permeability is calculated as the ratio between the two when the magnetizing force is at its maximum, (3.3). For this test, the BH curve was constructed directly from measurements. That is, the primary current was used to determine  $H$  and the secondary voltage was measured for  $B$  as seen in (3.1) and (3.2) respectively. These measurements were recorded through an oscilloscope and post-processed in a Matlab script to perform the calculations and remove DC bias in the measurements. By plotting (3.1) and (3.2) on an XY graph and taking the area enclosed the power loss is measured as shown in (3.4).

Because the load is predominately inductive, the converter operates in zero voltage switching mode [62]. This allows for effective driving of the circuit in the hundreds of kilohertz where 500 kHz operation has been confirmed for this particular system. With such a high switching frequency, it is easy to generate a variety of waveforms. A simple LC low pass filter

can be used to create sinusoidal excitation while triangular excitation is trivial. This means that the converter can generate the specific waveform that the magnetic core would see in the actual WBG converter.

The magnetic material test bed is a flexible platform that enables the testing of magnetic materials for multiple environmental and application specific parameters. The harness is designed to isolate the core and allow the study of physical stresses that would be present in a practical system. The power converter and supply provide the necessary excitation energy and excitation waveform creation to study the specifics that different high power, medium frequency wide bandgap power converters would use. In order to show the efficacy of the test bed, several basic tests will be demonstrated with analysis of the core losses using the above functions and losses using the modified Steinmetz equation.

$$(3.1) \quad H(t) = \frac{N_p i(t)}{l_e}$$

$$(3.2) \quad B(t) = \frac{1}{N_s A_e} \int_0^T v(t) dt$$

$$(3.3) \quad \mu_r = \frac{B(t)}{\mu_0 H(t)} \Big|_{H_{max}}$$

$$(3.4) \quad \frac{P}{V_c} = f \oint H dB$$

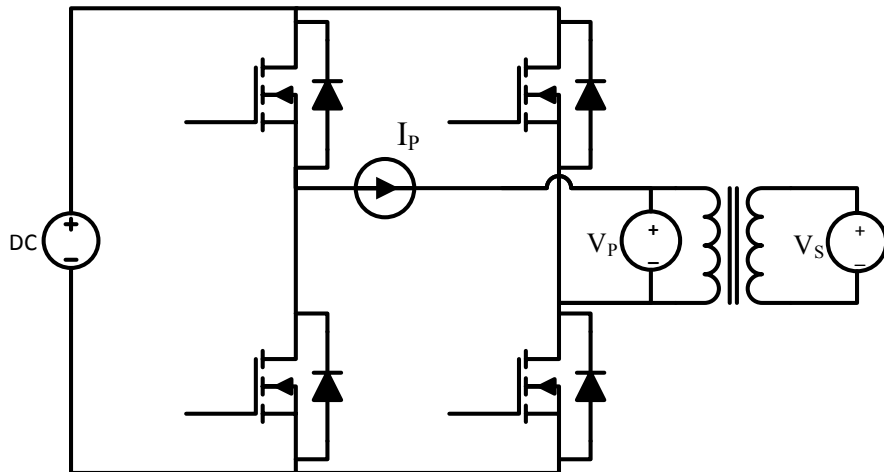


Figure 3.1: Circuit Topology of Basic Magnetic Core Test Bed.

### 3.2.1 Triangular Flux Injection

In this test, the CSE and MSE are compared to the measured core loss for triangular flux. A square voltage is applied to the primary coil, resulting in triangular current. The circuit for this test is shown in Figure 3.1.  $V_{DC}$  is controlled with a DC power supply and a DSP is used to control the PWM pulses to the CUT.

In Figure 3.2, below, a traditional excitation waveform is shown on the left and a semi discontinuous waveform is shown on the right where the applied voltage is dashed, and the current is solid. For these experiments,  $T$  is a test period and is  $50\mu\text{s}$ . The value  $n$  is an integer incremented from 1 to 9. This provides switching pattern with a frequency that ranges from 2kHz to 20kHz with an initial 20kHz pulse.

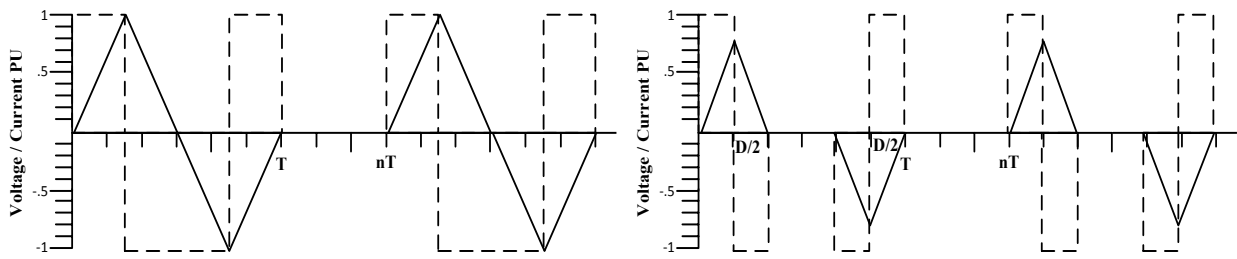


Figure 3.2: Excitation Waveform Template Continuous (Left) and Discontinuous (Right)  
Solid = Exciting Current, Dash = Applied Voltage.

For calculating the losses using the MSE, this pulse pattern can be separated into piecewise linear components making the integration simpler. Following this procedure, the equivalent frequency used in (2.41) leads to the new power loss calculation of (3.5).

$$(3.5) \quad p = \frac{k}{nT} \left( \frac{2}{\pi^2} \frac{4}{T} \right)^{\alpha-1} \hat{B}^\beta$$

While Figure 3.2 was the intended pulse pattern, the actual applied voltage had some resonant ringing and additional spikes. This can be seen in the scope capture below in Figure 3.3. These differences can be attributed to of the resonance of the transformer, the impact of deadband and the conduction of freewheeling diodes leading to unbalanced volt-seconds.

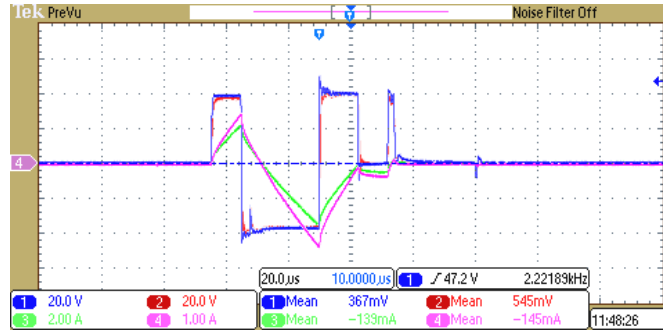


Figure 3.3: CUT Excitation Demonstrating Nonidealities.  
 Ch1:  $V_{Drive}$ , Ch2:  $V_{Sense}$ , Ch 3:  $I_{Drive Alt}$ , Ch 4:  $I_{Drive}$ .

### 3.2.2 DC Premagnetization

Another important characteristic that can influence the core loss is a DC bias. As seen in Figure 2.5 and Figure 2.6 and numerous other applications, DC bias is ubiquitous in the magnetics of power converters and electric machines. While many applications require this bias, very few manufacturers provide details of the materials behavior in these conditions. Reinert showed that modification of  $k$  in the MSE can account for DC flux as in (3.6) [38].

$$(3.6) \quad k_{new} = k \left( 1 + k_{DC} B_{DC} e^{\frac{-B_{AC}}{k_{AC}}} \right)$$

The test circuit shown in Figure 3.4 was used to subject the CUT to a controlled ac flux on the primary winding. The tertiary winding was connected to a DC power supply operating in current control mode. The same procedure used in V.C was used to calculate the core loss in the transformer.

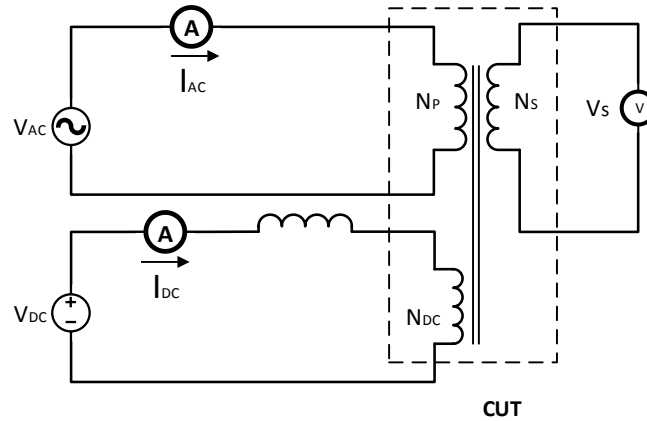


Figure 3.4: Circuit for DC Premagnetization Test.

An example of the injected waveforms is shown in Figure 3.5. Here  $I_{AC}$  was recorded using the Pearson 6600.  $I_{DC}$  was measured with the Tektronix 202A. And the primary and secondary voltages were measured with the same TPP0200 probes.

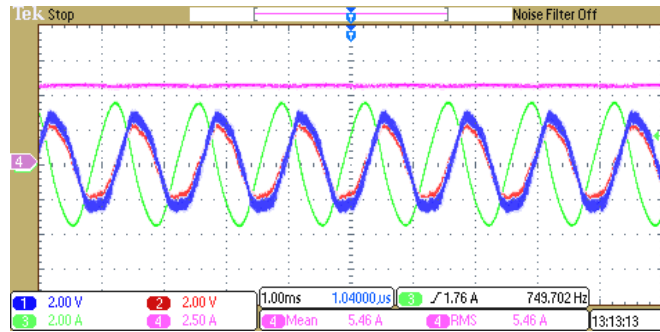


Figure 3.5: Sinusoidal Core Excitation with DC Premagnetization.  
Ch1:  $V_{Drive}$ , Ch2:  $V_{sense}$ , Ch3:  $I_{Drive}$ , Ch4:  $I_{DC}$ .

In order to calculate the DC flux, the following (3.7) was used. This is acceptable because the inductance factor,  $A_{LDC}$ , does not vary greatly with the levels of DC current used for this test [79].  $B_{AC}$  was maintained at 0.17 Tesla.

$$(3.7) \quad B_{DC} = \frac{N_{DC} A_{LDC} I_{DC}}{A_c}$$

The measured core loss and predicted core loss using CSE and MSE are shown below in the left of Figure 3.6 and the error between the measured and calculated values is presented on the right.

Through curve fitting, the good values for  $k_{DC}$  and  $k_{AC}$  were found to be 32 and 5 respectively. Again, the advantage of the MSE over the CSE method is clear. The MSE is able to accommodate DC flux injection for predicting core losses with much higher accuracy than the CSE.

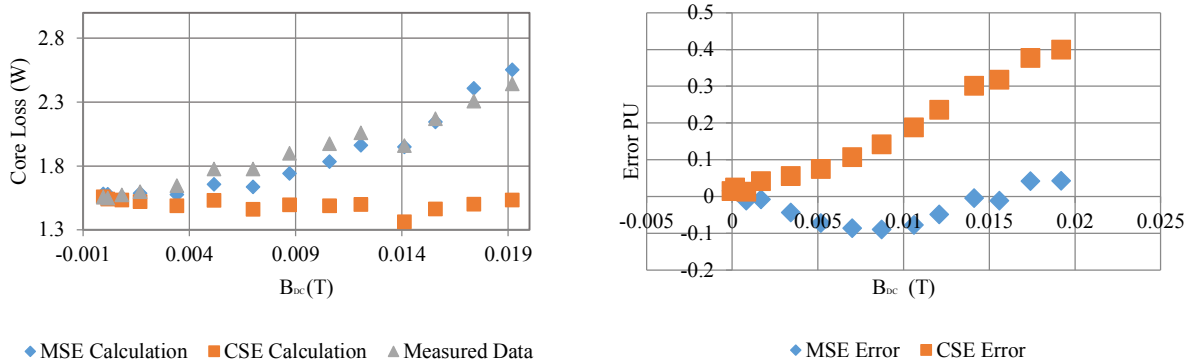


Figure 3.6: Comparison of Loss Calculations to Measured Losses Of CUT with DC Premagnetization (Left) and Loss Prediction Error for DC Premagnetization (Right).

### 3.2.3 Duty Cycle Testing

Through the investigation presented in this section, the basic advantages of the Modified Steinmetz Equation were shown. However, there is room to improve the test apparatus. Namely a closed loop testing platform that regulated the injection current and measured the output voltage could reduce measurement errors as well as make the post processing work easier. Similarly, a converter that could, in a controlled way, apply variable duty cycle excitation is needed.

Temperature effects were neglected in this work. This is acceptable as the core temperature was measured periodically with a thermal camera. It was seen that the core temperature never rose above a few degrees but this is an important aspect of the loss measurements. Other work has used heating chambers to pre-heat the core material and maintain it at that specific temperature.

Another application of the MSE shown in [38] is calculating core losses for triangular flux with varying duty cycles. This would change the  $dB/dt$  for each of the three piece-wise linear components of  $B$ . An example of the changing duty cycle is shown by the dashed lines below in Figure 3.7.

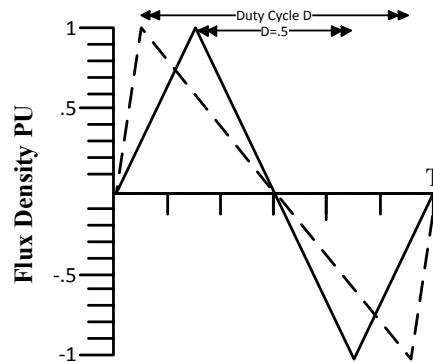


Figure 3.7: *Varying Duty Cycle Triangular Flux.*

This test would be particularly interesting and useful for validating the MSE as it predicts significantly different core losses from CSE as seen in Figure 3.7. However, it would require a special configuration of the circuit in Figure 3.1 where each leg of the H bridge has its own DC link and DC voltage controlled based on the duty cycle under test or similar. Importantly, two different voltages with different on durations would need to be applied to the core under test.

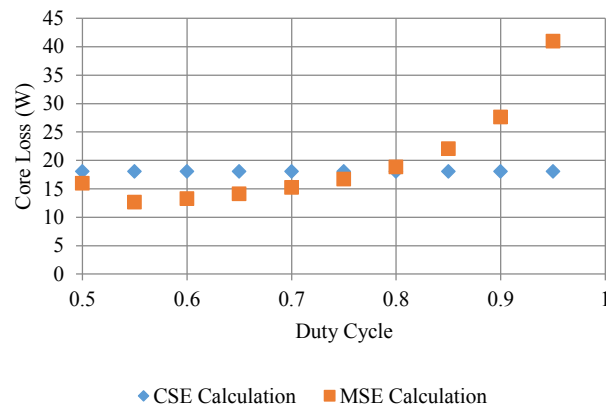


Figure 3.8: *Predicted Losses for Variable Duty Cycle Test.*

### 3.2.4 Drawbacks to Traditional Testing Circuit

Difficulty arises in generating the trapezoidal excitation for experimental validation of the aforementioned curve fitting based predictions. In the approach of [50], an auxiliary winding is coupled to the magnetic core under test enabling the injection from another converter. A system analysis of the DAB losses is made possible by connecting the two converters to the same DC bus thus transferring loss power through the MF transformer [72]. However, this approach does not provide a clear characterization of the magnetic materials. Furthermore, a full design is needed for meaningful study and thus results are limited in scalability and generalization.

In the dual active bridge circuit, a standard H bridge circuit is used to apply square wave voltages to both sides of the medium frequency transformer. In the standard operation, both primary and secondary transformer voltages are 50% duty cycle. As mentioned previously alternative switching techniques utilize some amount of extended dead time as well to provide zero current and zero voltage switching operation. Power is controlled and transferred by varying the relative phase shift between the two square voltages. Figure 3.9 top shows the applied voltages to the MF transformer. This results in an induced flux that is proportional to the current into and out of the transformer, Figure 3.9 middle. The principal energy transfer is through the leakage inductance of the transformer. The voltage across this inductance is seen in Figure 3.9 bottom.

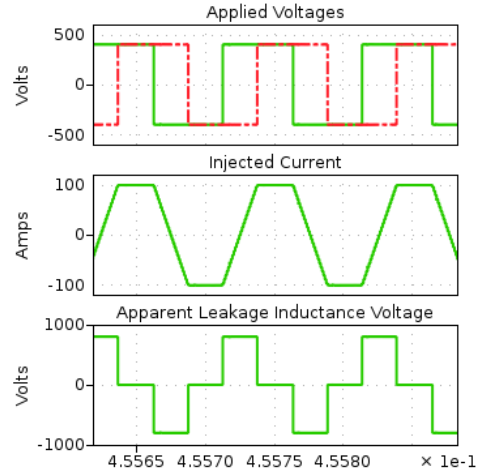


Figure 3.9: Ideal DAB Waveforms.  
 Top = Applied Voltages, Middle =  $I_{Drive}$ , Bottom = Effective  $V_{Drive}$ .

In order to test a particular transformer core material under for the stresses and waveforms seen in the dual active bridge, a single H bridge should intuitively satisfy the necessary voltage profile. However, the single H bridge fails to recreate the desired excitation profile because of the conduction path through the free-wheeling diodes and parasitic elements during zero voltage times. The traditional switching patten of a single H bridge is shown in Figure 3.10 and Figure 3.12. In Figure 3.10, we can see that the conduction path is, as desired, through two mosfets that are gated on. This would last for a duration necessary to realize phase shift time of the DAB.

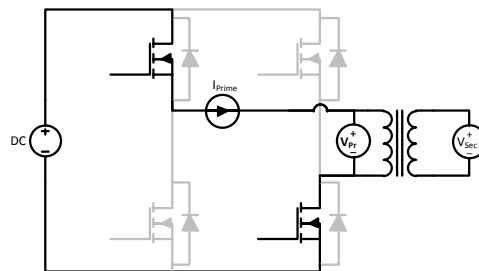


Figure 3.10: H Bridge Conduction Path: Positive Applied Voltage.

In the next two stages, the applied voltage is desired to be zero such that current remains constant and in the same direction, positive with respect to the ammeter in Figure 3.10 -Figure

3.11. In order to achieve this, first the bottom right switch is cut off for an amount of dead time. This causes the upper right freewheeling diode to conduct because there is not a path for current to flow otherwise. Then the upper right mosfets is gated on such that only the conducting resistance parasitic is in the circuit, Figure 3.11.

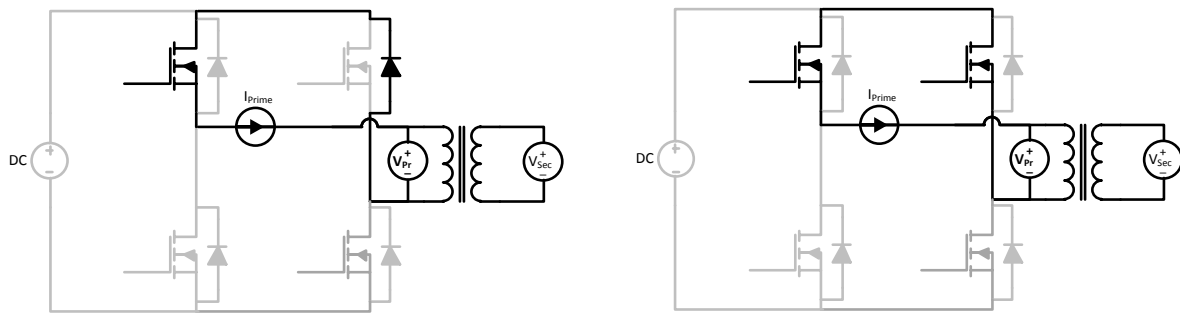


Figure 3.11: H Bridge Uncontrolled Voltage Conduction Paths: Free Wheeling Diode (Left) and Blanking Time (Right).

If both mosfets are cut off, the conduction path is through the negative freewheeling diodes that would cause a reversal of polarity in voltage across the transformer under test, with a higher negative voltage than the normally applied positive voltage. This is especially true if the body diodes of the mosfets are used without a lower forward voltage drop anti-parallel diode. This is because during normal conduction, the on resistance voltage drop of the mosfets subtracts from the applied voltage by 2 times that of a single mosfet (3.8). During the zero voltage period, the forward voltage of the diode and the on resistance contribute to the voltage across the magnetic core under test in (3.9) and (3.10). Where  $V_{TX}$  is the transformer voltage,  $V_{DC}$  is the applied DC voltage,  $i(t)$  is the time varying current and  $R_{cu}$  is the conduction path resistance including the coil around the core under test. One method of minimizing  $R_{cu}$  is to use litz wire to establish this coil.  $R_{on}$  is the mosfet on resistance and  $V_{on}$  is the forward voltage drop of the freewheeling diodes. The applied voltage during deadband is seen in (3.9). When phase shift gating is used, the ‘zero’ voltage period is in fact the voltage seen in (3.10).

$$(3.8) \quad V_{TX} = V_{DC} - i(t)(2R_{on} + R_{cu})$$

$$(3.9) \quad V_{TX} = V_{on} - i(t)R_{cu}$$

$$(3.10) \quad V_{TX} = -i(t)(2R_{on} + R_{cu})$$

This effect is demonstrated in both simulation and hardware. This is clearly evident at any excitation voltages as well. In Figure 3.12, left top, the desired excitation voltage is shown. Upon close inspection of the ‘zero’ voltage period, there is a non-zero voltage that does diminish corresponding to (3.9) and (3.10). This causes a collapse of the field, Figure 3.12, left bottom, in the transformer. It can lead to over inflated core loss measurements due to continued  $db/dt$ . The spurious voltage spiking can easily be seen as freewheeling operation when the applied voltage is compared to the mosfet gating signals, Figure 3.12, left middle.

Hardware results confirm this undesired action as seen in the right of Figure 3.12. Here, the applied voltage was 100V and there is still a spurious spike leading to a high  $di/dt$  and high  $db/dt$  during the deadband. It is important to point out that the deadband period in these results is nearly enough to fully de-energize the transformer. For these results, the deadband time was increased for emphasis of effect. A shorter deadband would result in less dramatic of an effect. It is clear from both the simulation and experimental results that a new circuit topology is needed to provide the trapezoidal excitation present in practical dual active bridge converters.

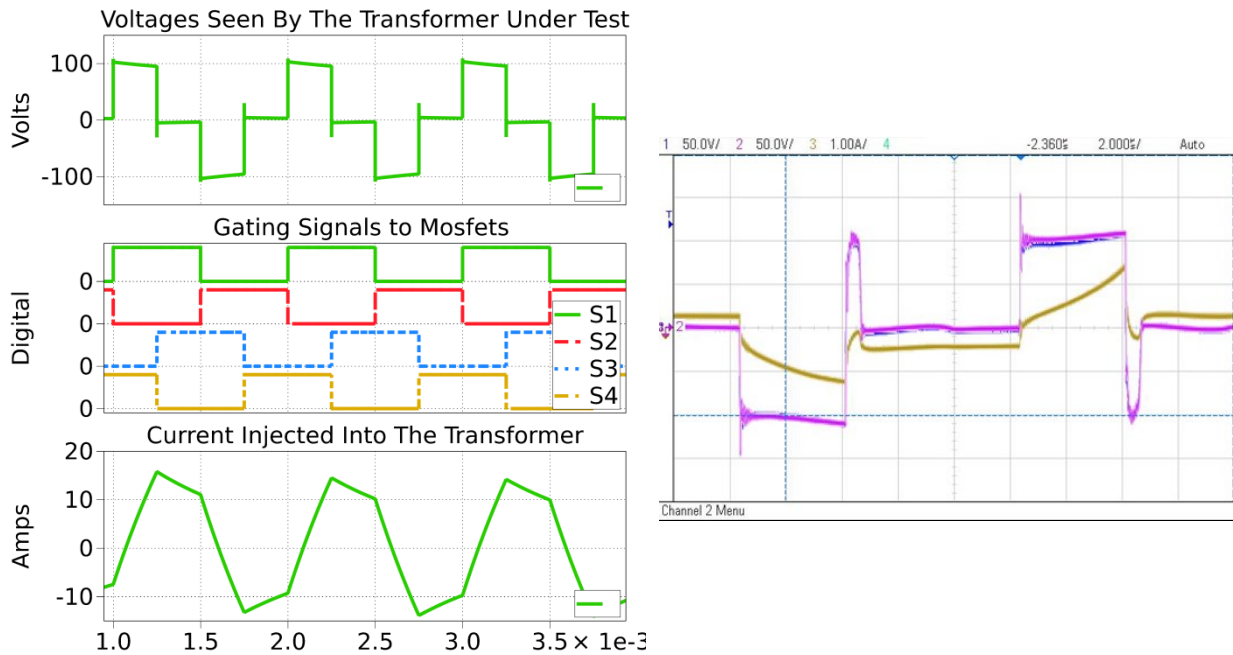


Figure 3.12: Parasitic Effects On Single H Bridge Core Excitation Waveforms Simulated Blanking Time (Left) and Measured Free Wheeling Diode (Right: Ch1 (Blue):  $V_{Drive}$ , Ch2 (Purple)  $V_{sense}$ , Ch3 (Gold):  $I_{Drive}$ .)

### 3.3 Extracting Steinmetz Parameters and Material Properties

#### 3.3.1 Nine Point Linear Method

In order to test and optimally design for a particular core material, the original Steinmetz parameters need to be determined. When these values are not provided by the manufacturer but a table of loss data is provided obtained, (3.11) can fit the parameters.  $P_n$ ,  $f_n$  and  $B_n$  are data points for a single curve  $n$ . It is important to note that for the constants extracted, are valid for the specific excitation only, e.g. square, sinusoidal or trapezoidal. If the curve map is for sinusoidal induction, the extracted constants will only accurately predict the losses of other sinusoidal waveforms. The exception of course is the use of scaling techniques or modifications of the basic Steinmetz equation as mentioned in the previous chapter. If the loss map is for a different wave shape, it is not clear if the coefficients are scalable back to sinusoidal ones.

$$(3.11) \begin{bmatrix} \ln(P_1) \\ \ln(P_2) \\ \ln(P_3) \end{bmatrix} = \begin{bmatrix} 1 & \ln(f_1) & \ln(B_1) \\ 1 & \ln(f_2) & \ln(B_2) \\ 1 & \ln(f_3) & \ln(B_3) \end{bmatrix} \begin{bmatrix} \ln(k) \\ \alpha \\ \beta \end{bmatrix}$$

As can be seen in Figure 3.13, curves were generated that fit manufacturer data points over a reasonable range. Figure 3.14 shows the error of calculation from the provided data. From this, there is a range of frequency and magnetic flux density that can be tested with reasonable confidence in matching losses with Steinmetz parameters.

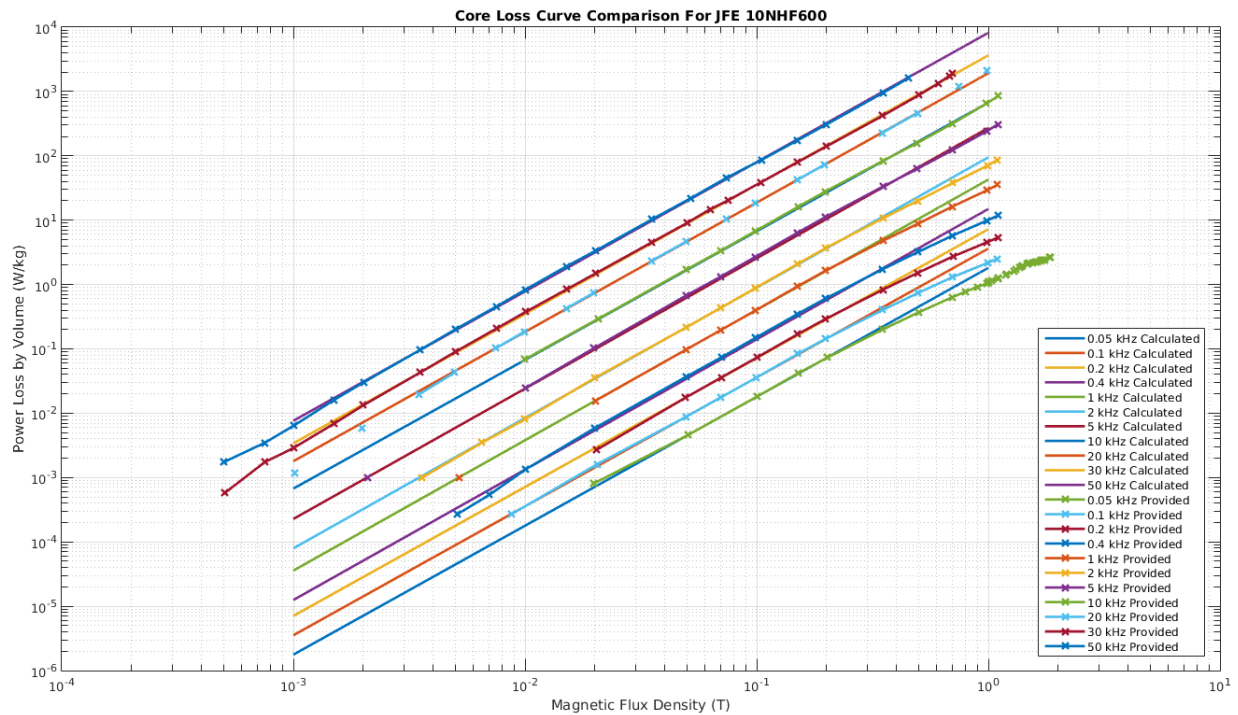


Figure 3.13: Manufacturer and Steinmetz Calculated Core Loss Curves for 10JNH600.

It was found that no single set of parameters adequately mapped the core loss profiles. This possibility is confirmed in [51]. Below, in Table 3.1, the calculated parameters for a particular frequency range are shown. Further work could create more parameters that better match the provided data over a wider range but this was outside the scope of this work.

Table 3.1: Steinmetz Parameters for JNHF Using Nine Point Method.

Frequency Range	$k$	$\alpha$	$\beta$
50Hz - 200Hz	36.1694	.9992	2.0035
400Hz - 5kHz	42.7696	1.148	2.0258
10kHz	16.8987	1.6	2.0
20kHz - 50kHz	16.8987	1.58	2.01

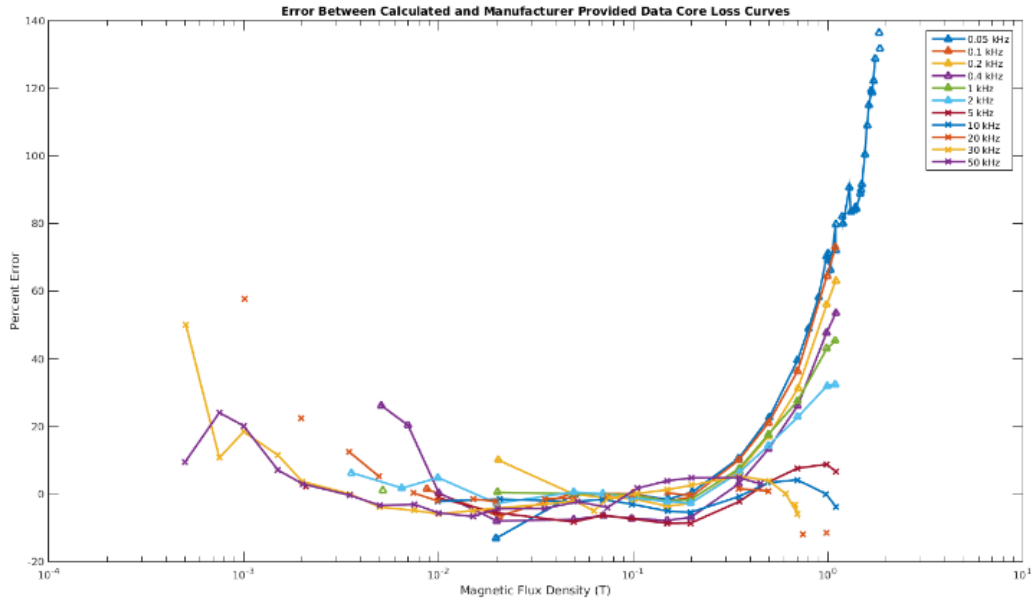


Figure 3.14: Error Between Calculated and Manufacturer Provided Data for 10JNHF600.

A linear regression fit model was shown in [7], where multiple data points can be used. With the matrix that is defined by 1s and the log of flux density and frequency defined as  $A$ , the Steinmetz fit can be found using (3.12).

$$(3.12) \quad X = (A^T A)^{-1} A^T \ln(P)$$

### 3.3.2 Software Surface Fitting

Another method of extracting coefficients is to use a surface fitting tools such as Matlab's *cftool* function. This method allows users to seed a fit function with unknown constants. Matlab then uses best fit algorithms to determine the most accurate coefficients for the entire loss map. However, grouping over ranges of conditions would have to be performed manually by separating the surfaces.

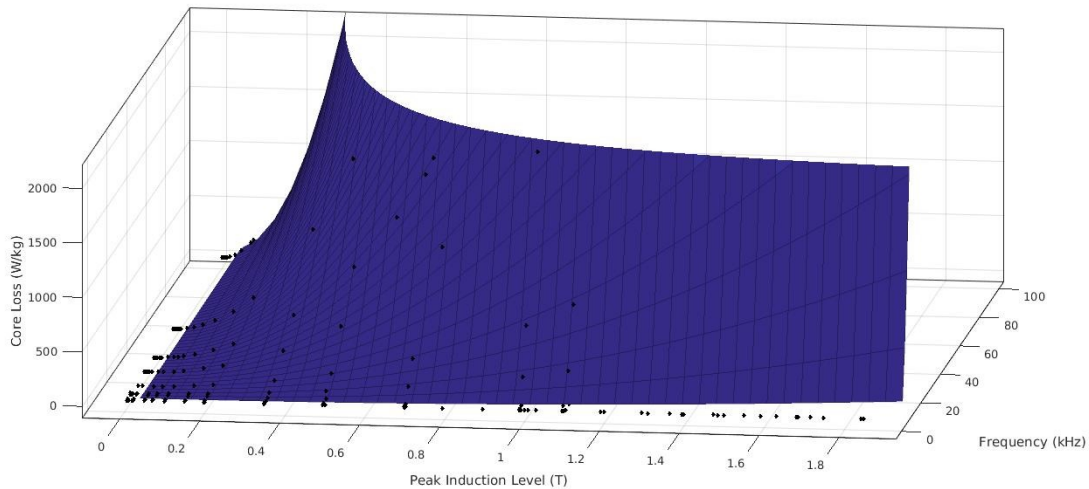


Figure 3.15: Surface for Steinmetz Loss Fitting.

Table 3.2: Steinmetz Coefficients from Surface Map

Frequency Range (kHz)	$k$	$\alpha$	$\beta$
10 – 100	16.16	1.629	2.2

### 3.4 Other Parameters of Interest

There are of course numerous other factors that can have an impact on the behavior of the magnetic core. A practical test bed would need to consider the impact of the following just to name a few, core cutting, core misalignment, permeability variability due to operating and environmental conditions, and mechanical stresses. Other parameters such as magnetostriction, resistivity and permittivity are of interest as well but beyond the scope of this work. For these parameters, it usual to map the interlinked behavior. Curve fitting can then be utilized as well for predictive modelling. This work will incorporate these various impacts for a holistic design approach.

### 3.5 Minimizing Error

One of the principal difficulties in this study is the multitude sources of error that can lead miscalculation of core loss. The relatively small component of core loss in the applied apparent power becomes increasingly problematic in low and medium permeability core

materials but can also impact measurements on high permeability materials. That is, the inductive component causes a significant amount of reactive power to be delivered by the exciting converter. This requires higher rated sensors which likely have less resolution. With small amounts of core loss, the exact measurements can get lost or become less apparent. This makes it difficult to generate accurate results and loss maps.

### 3.5.1 Sensor Approaches to Minimizing Error

It is important to discuss the issue of measuring current for magnetic core tests. As mentioned above, there are several current sensor options. However, because the phase between voltage and current distinguishes between magnetizing reactive power and core loss power, careful selection of the sensor is needed. In [38], the authors used a low inductance resistive shunt and measured the voltage across it. This can be an effective solution to a small testing window at low power. However, as higher power tests are performed, the shunt options become less appealing. Rather, an induction based current sensor is preferred with a wide range.

In order to accurately characterize a material, it is essential to identify and minimize non-core variations. Specifically, measured core losses can be influenced by a variety of sources most notably measurement errors, and core harness induced losses. First we must understand that the error introduced by the current sensor is due to the delay of the current sensor. For any given signal, this error is shown below in (3.13) [80]. Here,  $\delta$  is the actual angle of measurement while  $\phi$  is the angle error introduced by a sensor delay and  $E_{Tol}$  is the maximum tolerance of the particular sensor.

$$(3.13) \quad E_T = 100 \frac{\cos(\delta+\phi) - \cos(\delta)}{\cos(\delta)} + E_{Tol}$$

Given the frequency range and  $\Delta B$  of test, transformer parameters and losses at those particular test points, a profile the current sensor errors can be developed. The values  $\delta$  can be

determined from (3.14). Here the equivalent core resistance,  $R_c$ , and reactance,  $X_m$ , can be calculated by (3.15) and (3.16) respectively. In (3.15),  $N_p$  is the number of primary turns,  $\mu$  is the permeability,  $l_m$  is mean magnetic path length and  $A_c$  is the core area. In (3.16),  $P_{loss}$  is found using the core loss curves.

$$(3.14) \quad \delta = \text{atan}\left(\frac{R_c}{X_m}\right)$$

$$(3.15) \quad X_m = \frac{2\pi f N_p^2 \mu_r \mu_0 A_c}{l_m}$$

$$(3.16) \quad R_c = \frac{V_{rms}^2}{P_{loss}} = \frac{\left(N_p A_c 2\pi f \left(\frac{\Delta B}{2\sqrt{2}}\right)\right)^2}{P_{loss}}$$

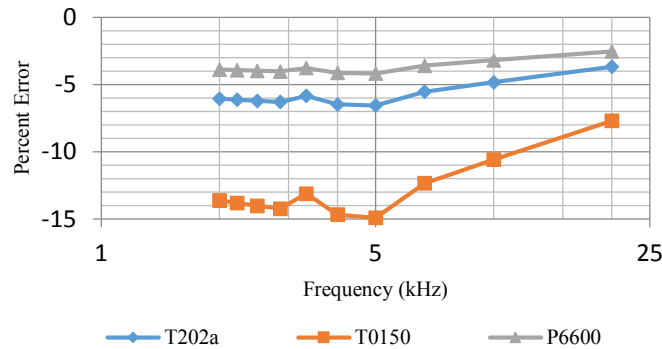


Figure 3.16: Maximum Error for Different Current Probes' Delay and Tolerance  
T is Tektronix and P is Pearson Brand Sensors.

It is clear from Figure 3.16 that the Pearson current sensor is the best choice. With the Pearson 6600, the current measurement error is within  $\pm 5\%$ . However, if DC current is desired, an active probe such as the Tektronix would be required as the Pearson probes are passive.

### 3.5.2 Circuit Based Techniques to Minimize Error

In very low loss cores or cores of a very small volume, the sensor error may be irreconcilable. A very small delay in these tests would result in significant error. The authors of [55] presented a method to eliminate the magnetizing power of a core and thus only measure the real power losses. Instead of studying a single core material with one excitation winding and one sense winding, they explore two sets of windings on a core material and an air core. The two

excitation windings are connected in series and configured additively while the two series sense windings are configured to be subtractive. While this is quite effective for low permeability materials, the size of the air core cancelation transformer becomes prohibitively large with high permeability core materials.

In [81], the author shows how to only partially cancel out the reactive power for improved sensitivity in the real power measurement. This approach requires multiple steps to determining core loss. Principally it uses the scope deskew to force a skewed measurement. The partial cancelation allows for a wider range of a testing window with the same reactive power reference.

### **3.6 Preliminary Laboratory Setup**

To begin basic material characterization, a H bridge circuit was constructed, Figure 3.17. This circuit is good for baseline testing and general understanding. However, there are limitations and a new circuit is proposed to overcome these limitations. This new circuit is discussed in section 3.8. Custom transformer were assembled for characterization. The right of Figure 3.17 shows an example of four 10JNHF600 I cores from JFE steel prepared for both triangular excitation and DC premagnetization characterization. These cores were bracketed in a fiberglass and steel rod frame. For material characterization, the primary and secondary turns are the same to ease analysis. The maximum number of turns is limited by the desired required voltage at the peak frequency and flux density set point

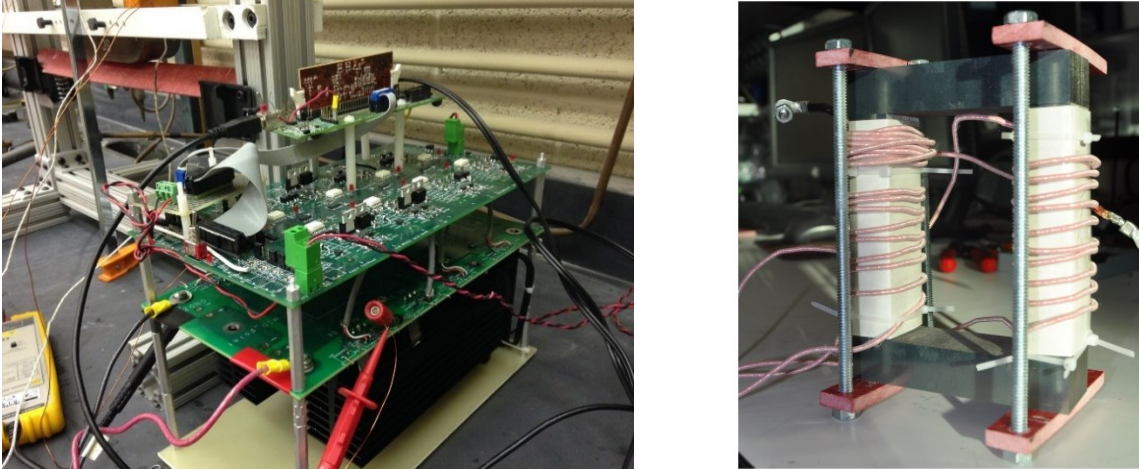


Figure 3.17: First Generation Experimental Test Bed (Left) and Example Material Characterization Setup (Right).

It is important to note, that the coils where medium frequency power was applied were spread out to limit intertwining capacitance. An initial design had nice and compact windings that had a low leakage inductance but capacitance witch ended up causing resonant ringing during tests, making results very noisy and difficult to analyze.

Table 3.3, below, describes example equipment used for a typical study. [38] was used as a reference to validate equipment and testing procedures. First, the core under test (CUT) is subjected to a triangular field as would be occur if a square voltage is applied to the CUT. The next test, applies a medium frequency sinusoid to the primary coil while DC is injected in a tertiary coil.

Table 3.3: Test Equipment and Important Figures of Merit.

Device	Model Number	Tolerance	Rise Time
DC Source	TDK 400-25 Gen		
Sinus AC Source	Chroma 61602		
Triangular AC Source	Custom SiC H Bridge Inverter		
Current Sensor	Pearson 6600	$\pm 1\%$	5ns
Current Sensor Alt	Tektronix 202A	$\pm 1\%$	<7ns
Voltage Sensor	Tektronix 0200		<2.3ns
Oscilloscope	Tektronix MSO2024		2.1ns

A voltage controlled DC power supply is needed to provide the core excitation power. For this test bed the Keysight 8937A 15kW DC supply was used. This power supply is able to

provide the necessary excitation power. The built in current limit functions also provide a level of safety during testing.

One additional consideration for the DC supply is voltage stiffness. While the power supply may have sufficient power rating, and only loss power is being consumed, the voltage may dip during transitions. This is because the converter must supply both loss current and reactive current necessary to magnetize the core. Because this current is cyclic, it will not register in the DC power supplies current reading but it can cause voltage ripples. In order to improve the stiffness and illuminate the spurious ripple, an additional external capacitor bank was added to the output of the supply. This was a capacitance of 3.6 mF. At rated voltage of the converter, 1200V, this gives an inertia constant (3.17), of 0.17s. This is much greater than the 0.0015s of the supply without the additional capacitance.

$$(3.17) \quad H = \frac{1}{2} C_{DC} V^2 = \frac{1}{2} L_m I^2$$

### 3.7 New Core Testing Harness

This section will describe the construction of a magnetic core harness that allows for material characterization with minimal error. The emphasis on characterizing materials suitable for medium frequency, high power converters. With the rapid availability of new magnetic materials and even more options in post-processing techniques such as field and strain annealing [82], full property maps of materials and final fabricated components are needed for proper system design. This is especially critical in modern wide bandgap power electronics based converters where medium switching frequencies are used to deliver high power. In these systems, the magnetic design has a significant impact in the overall losses. The magnetics constitute a majority of the losses and magnetic properties have a defining influence on the overall systems, e.g. available power flow and soft switching regions. A new lossless structural

harness that allows easy testing of cores and the development of property maps is presented. The harness also enables the testing of mechanical variations such as gapping and clamping pressure on the core. Next an example characterization for a Finement core with transverse annealing will be presented.

The test bed consists of three primary entities. First, a harness is needed to enable an appropriate testing domain for the desired material. The harness should allow impact studies of additional environmental factors on the core behavior as well. The second component of the test bed is a DC power supply. This power supply is separate from any necessary control power and should have a sufficient power rating for the excitation energy. Finally, power electronics converter capable of producing the desired excitation waveform is needed. It is important to ensure that this converter has a sufficient power rating necessary to fully energize the core material under test over the extent of the testing domain.

### **3.7.1 Core Harness**

The main purpose of the harness is to provide a platform for controlled and repeatable testing conditions for the magnetic core under test. Figure 3.18 is a photograph of such a core harness. There is no conductive material in the harness that is in contact or near the core in this harness. The loss errors this can introduce are discussed in the next section. The core is stabilized in both the vertical and horizontal axis. A slotted extruded aluminium superstructure is used to mount all fiberglass stabilizing brackets.



*Figure 3.18: Magnetic Core Testbed Harness.*

The primary method of holding the core in place is the two horizontal pieces of red GPO3 fiberglass angle. This angle is reinforced with fiberglass bar. GPO3 is preferred for core surface contact because of its superior electrical and temperature ratings of standard fiberglass [83]. With the higher rating, the test domain is expanded. The fiberglass angle is in contact with the core on its corner to maximize holding strength and minimize core surface coverage. This allows more core surface for natural thermal convection.

Eight fiberglass screws are used for horizontal support. These stabilize and ensure proper cut core alignment. The screws are tapped and threaded into the white fiberglass bar seen in the center of Figure 3.18, ensuring holding pressure. These screws safeguard from shifting in the horizontal plane. Furthermore, they enable fine-tuned controlled of the cut pieces of magnetic core to ensure proper alignment. Once aligned, the screws prevent the effects that fringing fluxes would have in forcing the core to twist and break out of alignment. The top fiberglass bars have quick release handles enabling easy and rapid test core changes. These screws provide the

necessary horizontal position control while minimizing the core surface that is covered. This enables positioning without increased thermal penalties.

Another feature of the harness is the ability to produce consistent and controlled mechanical clamping force on the core under test. There are two calibrated springs that provide the backing for the bottom vertical support angle. A screw clamp is used to apply compressive forces on the core. Then top vertical support is locked in place. The applied compression force is easily measured by determining the compression distance of the springs and using the known spring constant. The compressive force is distributed along the top and bottom of the core. Care must be taken that neither top nor bottom brackets deflect under high compressive forces as this will lead to non-uniform force distribution on the core.

With the variability of support bracket location, the harness provides a flexible platform for a variety of magnetic material tests. There is ample space for various tests such as winding configuration, bobbin design and others. The core surface is exposed as much as possible to ensure good cooling either through forced air or natural convection. Vertical compression enables consistent mechanical studies and provides the flexibility of air gap testing. The presented harness provides the physical framework for producing accurate and repeatable material characterizations while controlling for numerous environmental parameters.

### **3.7.2 Stray Eddy Losses in Harness**

One concern for core characterization is the error that can be introduced by stray eddy currents induced in the harness itself. As mentioned above, great care has been taken to ensure that nonconductive material is the only aspect of the harness in contact with the core. The aluminium super structure is present however and could be such a source of error. Below in

Figure 3.19, finite element analysis (FEA) verifies that the aluminium frame is sufficiently far enough from stray flux lines.

Figure 3.19 shows the FEA results for the worst case leakage flux at low excitation levels. This occurs when the core has an air gap and the core is excited at high frequencies. Even in this extreme case no flux lines cross into the aluminium of the core harness so it does not contribute to inflated loss measurements.

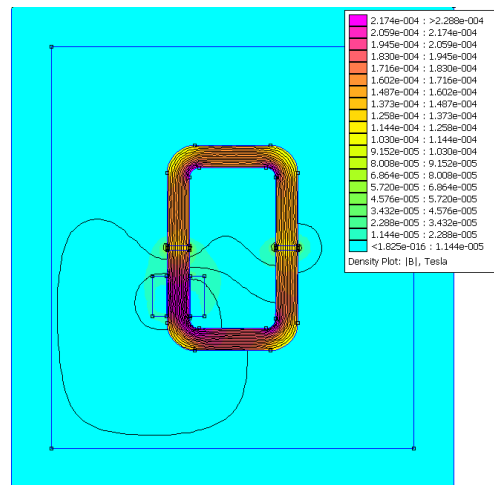


Figure 3.19: *Medium frequency, Low Excitation Core Harness FEA.*

### 3.7.3 Material Characterization Example

To demonstrate the effectiveness of this magnetic testbed an example characterization is presented below. This results show various parameters extracted from Finemet race track core as seen pictured in Figure 3.18. Table 3.4 below lists some of the physical parameters of the core provided by the manufacturer.

*Table 3.4: Physical Properties of Test Core.*

Property	Value	Units
Magnetic Length	28.0614	in
Stacking Factor	0.78	
Effective Cross sectional Area	1.5223	in <sup>2</sup>
Weight	11.657	lb.
Annealing	Transverse	
Inner Corner Radius	0.5	in
45° Beveling Width	0.038	in
Rated Core Loss	5.0	W/lb. at 20kHz

It is clear from the above information provided by the manufacturer that only an incomplete picture is provided. As such the full parameter map should be determined using the proposed test bed. Baseline parameters will be determined using single cycles and allowing full core cool down. Steady state parameters will be investigated after the core has reached thermal steady state.

### 3.7.3.1 Baseline Material Properties

As mentioned above the baseline parameters are determined near room temperature. Three steps were taken to ensure that the core temperature did not vary significantly during testing. First, fans were used to provide forced air cooling. Second, the excitation was applied only for a short duration. Finally, the core temperature was measured using K type thermocouples at the air gap, a corner of the inner bend, at center of the primary winding and at the geometric center of the flux path on the face of the core. During the tests the temperature was held within 5° C and tests were halted if the core became hotter.

Using (3.1), (3.2), (3.3), and (3.4) over a broad frequency and induction testing domain the property maps of Figure 3.20 and Figure 3.21 were developed. During testing, the supply voltage was adjusted to reach desired induction using (3.18) where  $k$  is the wave shape factor. Using the pulsing profile of Figure 3.2, this leads to  $k=1$ .

$$(3.18) V_{DC} = 4kfA_cN_pB_{ref}$$

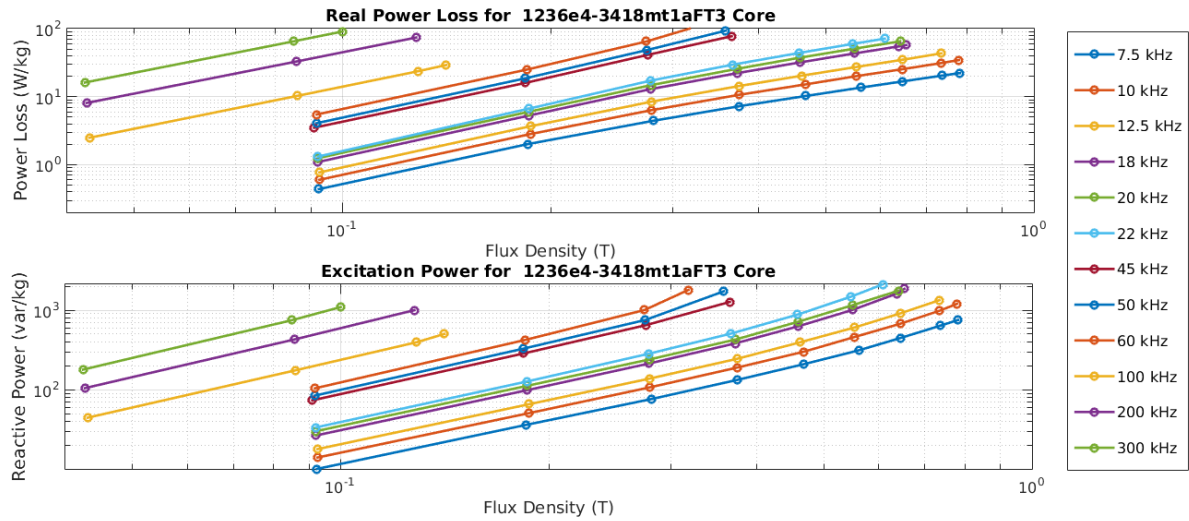


Figure 3.20: Core Loss and Excitation Energy at Room Temperature.

With this loss profile it is easy to curve fit the losses into the Steinmetz form (2.25) through either the linear or the surface methods mentioned in the previous section. It is important to reiterate that the constants extracted, are valid for the specific excitation only, e.g. triangular, sinusoidal. While triangular losses are proportional to sinusoidal losses [59], this method of producing the constants does not allow direct scalability. The relative permeability is also calculated according to (3.3) and plotted against both flux density and excitation force over the test domain as seen below.

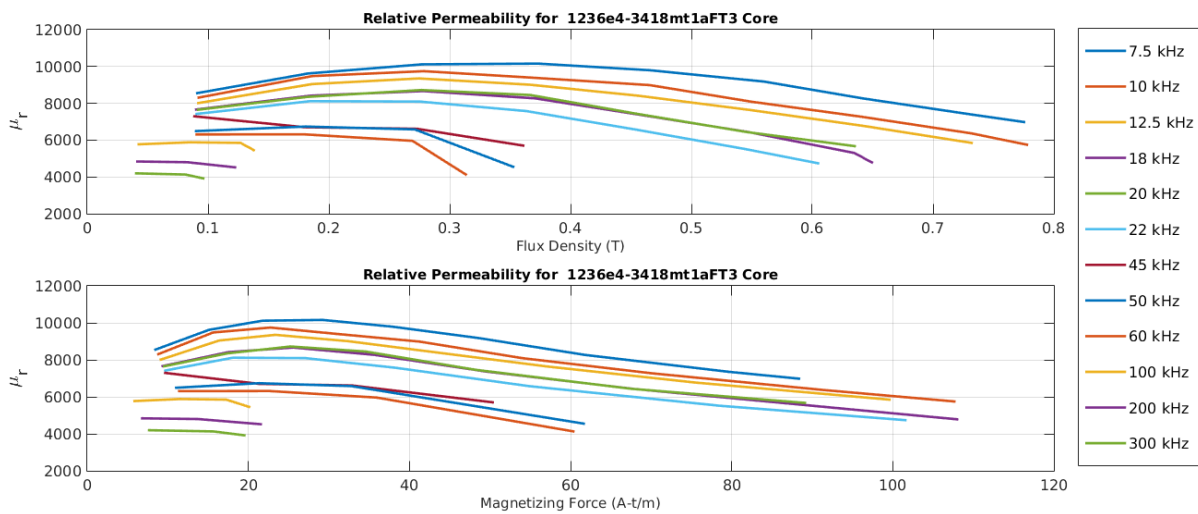


Figure 3.21: Relative Permeability vs. Flux Density and Magnetizing Force at Room Temperature.

Finally, the core was tested at a 10 kHz excitation frequency for various air gap lengths. In Figure 3.22 below the measured core loss and excitation power are shown. Excitation power increased dramatically as expected due to the reduction in effective magnetizing inductance with the increased air gap. Interestingly, the core loss remained very close to non-gapped predicted values shown by the red trend line. This implies minimal impact from fringing flux or other air gap non-idealities associated with the gap with respect to core loss. In other words, any penalty due to gapping is present once the core is cut and does not change with increasing gap.

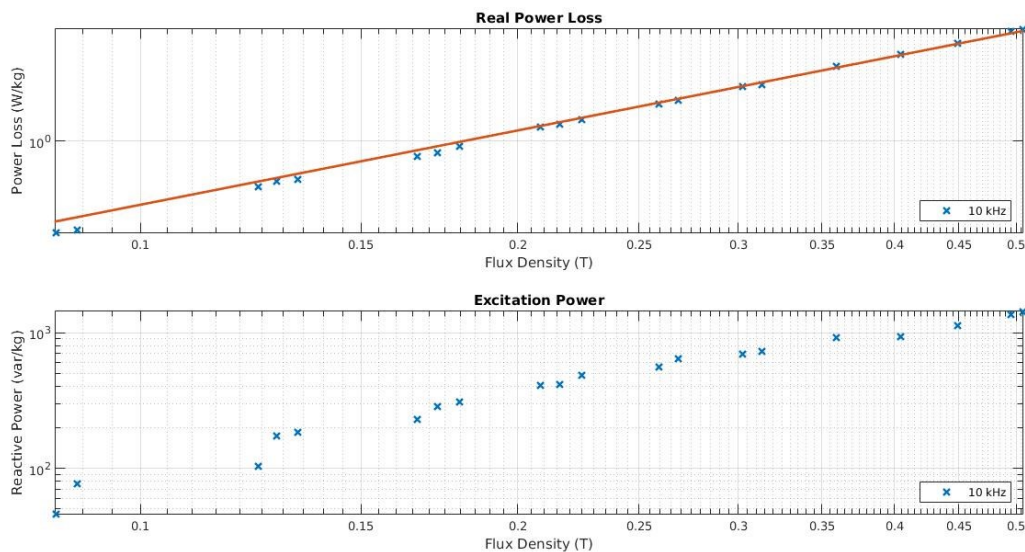


Figure 3.22: Core Loss, Magnetizing Power for Various Air Gaps at 10 kHz.

Once the base line properties are established it is possible to create the first iteration of design. However, a complete design would consider the steady state effects and not rely on parameters established in such an environmentally regulated test.

### 3.7.3.2 Practical Material Properties

A practical design will consider the thermal effects on core parameters. The results presented in this test are for a single excitation profile of 10 kHz and 0.6 Tesla flux density. The

system was allowed to run for 3 hours until thermal steady state was achieved. The excitation was then disabled to naturally cool the core. There was no forced air convection for these tests.

The thermal profile is shown below in Figure 3.23. Snapshots of the primary current and induced voltage were taken at consistent intervals during the test. The face temperature at the geometric center of the magnetic path was used for analysis. The temperature at the gap was much higher but this was a local effect and therefore not indicative of the magnetic core temperature. A similar argument is made for the inner bend temperature which is cooler due to the increased surface area exposed to cooling.

By repeating the analysis approach used in the baseline tests the thermal impact can also be studied. Figure 3.24 shows the loss and excitation with respect to temperature. Interestingly, the losses are weakly coupled to temperature variation. The total change in room temperature to the steady state was less than 6%. There is a small decrease in losses due to increased resistivity reducing eddy currents and associated losses; however, it is difficult to extract these effects as the loss variations are near the sensor tolerances.

The exciting power increases dramatically, however. This is due to the change in relative permeability caused by increasing temperatures. This is verified by comparing the BH hysteresis plots of the cold temperature and steady state temperature in Figure 3.25. Figure 3.26 shows the change of relative permeability as calculated over the entire thermal range.

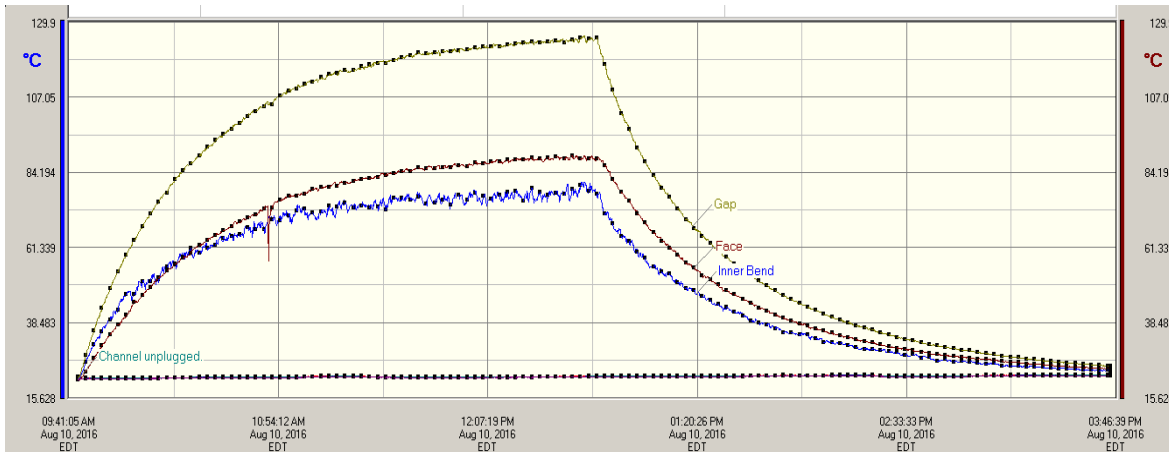


Figure 3.23: Magnetic Core Temperature Over Time Profile.

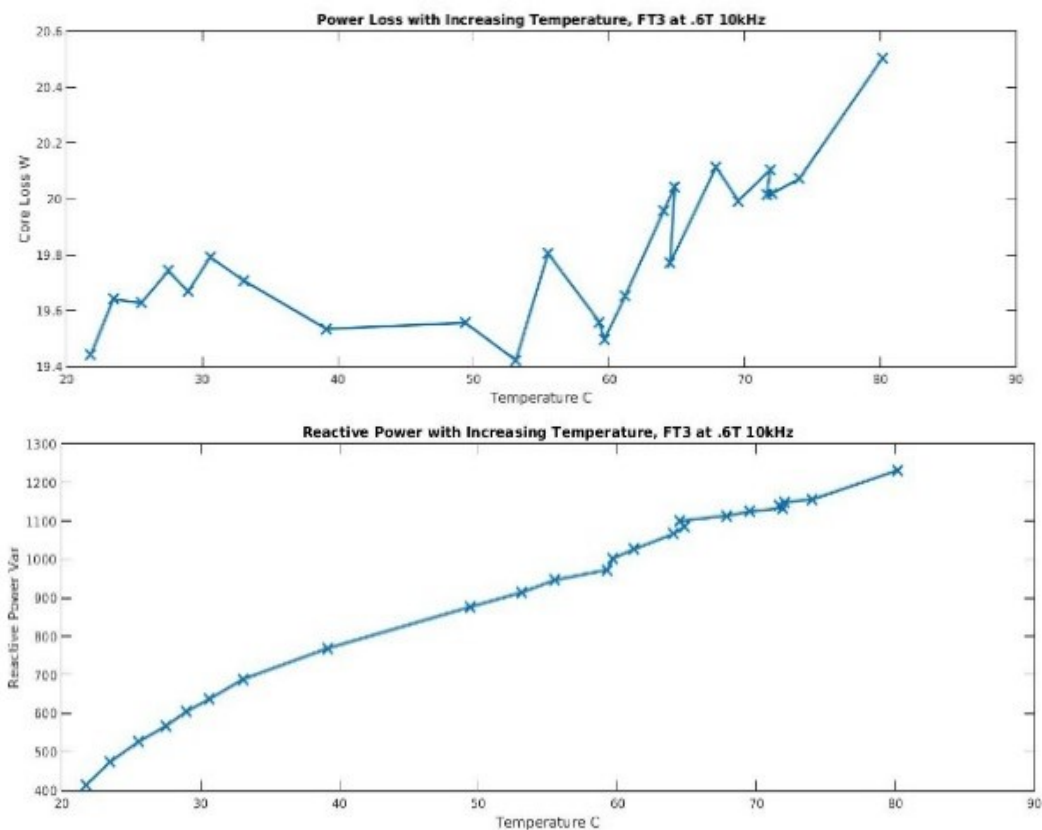


Figure 3.24: Core Loss and Exciting Power with Respect to Face Temperature.

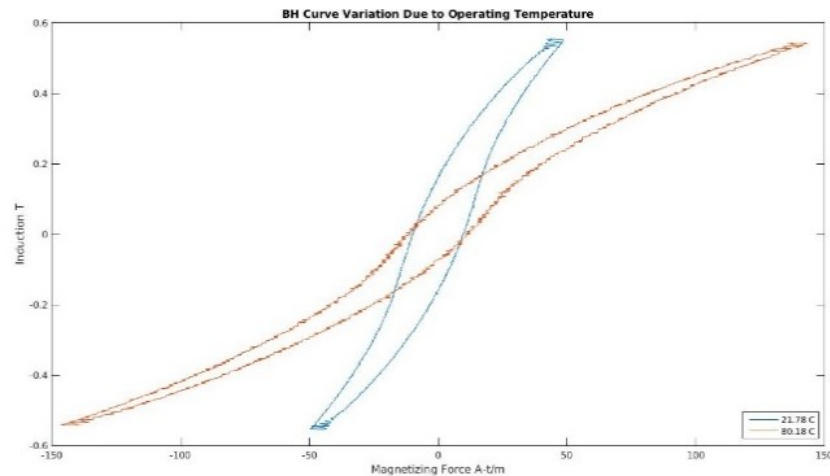


Figure 3.25: *BH Loops at Various Temperature.*

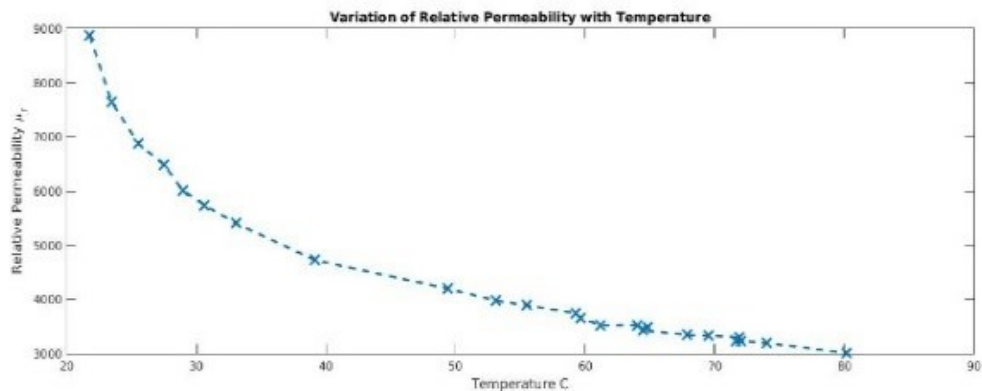


Figure 3.26: *Temperature Induced Permeability Decay.*

The permeability decay in a practical application presents many design issues. If, as in many designs, the exciting coil covers an extensive region of the core a positive feedback loop is created. That is, as the core heats up and permeability decays due to watt loss, the magnetizing inductance will drop. This will cause an increase in the reactive power delivered to the core and consequently increase the current through the coil. This causes an increase in the conduction losses with the square of current. The increased conduction losses can act as a heat source further increasing the core temperature. This results in further permeability decay, and can result in a thermal runaway situation. Careful design must be made to ensure there is enough cooling or thermal stability in the final design.

### **3.7.3.3 Mechanical Stress effects**

While all of the current tests have been made with consistent mechanical clamping force. Future work can incorporate a deflection map like that of the thermal change to allow engineers to extrapolate baseline parameters to their specific application. This can be achieved using the loaded springs of the harness.

### **3.7.3.4 High Temperature Characterization**

A high temperature core harness prototype is shown below in Figure 3.27. This new harness leverages many of the operating principals of the previous design except only high temperature materials are used. The core is suspended using nonconductive ceramic tubes which can be finely tightened by adjusting nuts and set screws in the extruded aluminium. This harness also holds the magnetic device forward of the super structure to enable easier access to various core surfaces. As shown in the next chapter, this also reduces the potential effects of leakage flux. More suspension arms or ceramic plates can be added if the clamping pressure needs to be more evenly distributed than the three prong approach shown below. Importantly this harness can withstand very high temperatures that enable magnetic testing for extreme conditions.



*Figure 3.27: High Temperature Core Harness Prototype.*

### **3.8 New Core Excitation Circuit**

#### **3.8.1 Introduction**

Dual active bridges (DAB), proposed in [61], are a well-known and widely utilized converter topology, Figure 3.28, providing many benefits. As their popularity has increased, many researchers have worked to optimize different aspects of the circuit [62] and [63]. Further work has proposed advanced switching techniques that operate the DAB with three level voltages instead of the traditional two [64] and [65]. One of the key elements in the optimization of the DAB is the medium frequency transformer. In order to achieve the optimization, characterization of the transformer loss is paramount.

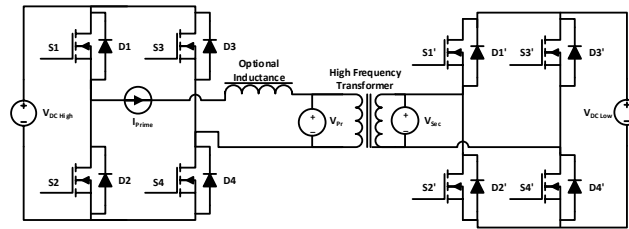


Figure 3.28: Typical Circuit of Dual Active Bridge.

For control stability and increased operating range and frequency, an optional inductance may also be added in series with the medium frequency (HF) transformer [66] and [67]. In [68], an auxiliary transformer is added in series to provide a controllable inductance. These additionally inserted magnetic components will also experience trapezoidal excitation. If there is a mismatch in the leakage inductance in the HF transformer due to a large turn ratio, there is also a two slope trapezoid excitation [69]. The pronounced voltage mismatch leads to non-zero voltage when both ends of the DAB are supply voltage. This also occurs if there is a mismatch in the turns ratio and the voltage ratio. As an example, the connection of a battery bank of 24-48V and a DC bus off 380V has many solutions where the HF transformer turns ratio do not perfectly match the voltage ratio.

Trapezoidal excitation in magnetic material is not exclusive to the standard DAB either. The three phase DAB has pronounced trapezoidal excitation over most design scenarios [13]. Other converters subject the magnetics to trapezoidal excitation e.g. DC motors and flyback converters [70] and [71].

As mentioned previously existing circuitry and approaches for characterizing magnetic is limited and insufficient for trapezoidal characterization. In order to overcome some of these limitations, a novel dual voltage source converter is presented. The operation of the circuit is described and a laboratory prototype is demonstrated. Finally, the implications for material behavior and performance as well as future tests are discussed.

### 3.8.2 Dual Voltage Source Converter

In order to achieve the desired induction profile, high current must flow through the medium frequency transformer with low to zero voltage. This implies the need for a second, low voltage source converter connected to the transformer. The ramp of the induction profile is generated by a non-zero applied voltage. This means that the medium frequency transformer needs both a high voltage source and a low voltage source converter to generate the desired induction profile. Figure 3.29 below shows such a parallel connection with the traditional voltage source converter on the left and the additional low voltage source converter on the right. In order to facilitate this parallel connection and prevent the high voltage excitation from flowing through the freewheeling diodes of the low voltage converter, reverse diodes are added to the low voltage converter connection.

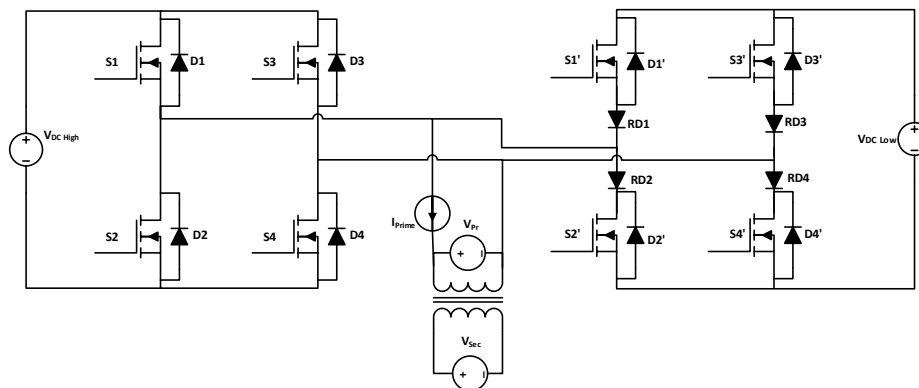
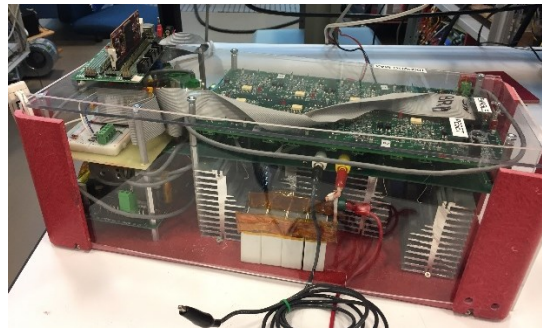


Figure 3.29: New Dual Voltage Source Converter Topology.

The transformer primary is connected to both converters and the secondary is left as an open circuit. This allows direct analysis of induction,  $B$ , and magnetizing force,  $H$ , as discussed previously in (3.1) and (3.2). Core loss,  $P$ , by core volume,  $V_c$  can then easily be calculated by (3.4). Permeability is a more complicated concept as the trapezoidal hysteresis curve has lossy discontinuities. This means that (3.3) is no longer a valid calculation of relative permeability. The trapezoidal characterization section will provide further insight into this topic. The core loss

is measured without the impact of any power flow through the transformer. All power loss measured is transformer core loss when the secondary voltage is used.

This new excitation generating topology applies two voltage levels to an exciting coil, Figure 3.31. In order to apply the two levels, two drive circuits are connected in parallel. Two H bridges are utilized to introduce the desired excitation waveform where the high voltage H bridge is a standard topology and the low voltage H bridge has anti-series diodes. The proposed test circuit leverages the advantages of existing open secondary tests. In this way, only one coil is used to excite the magnetic material and the second coil is used to measure the induced voltage. This allows the continued use of equations (3.1) and (3.2) when analyzing magnetic core materials. The left H bridge applies high voltage and provides the high  $di/dt$  ramp of the desired exciting waveform. The right H bridge applies a lower voltage and can range from flat top, zero  $di/dt$ , to very close to the initial high  $di/dt$ . Careful gating enables continuous current conduction without the use of any freewheeling diodes.



*Figure 3.30: Dual Voltage Source Core Tester Laboratory Prototype*

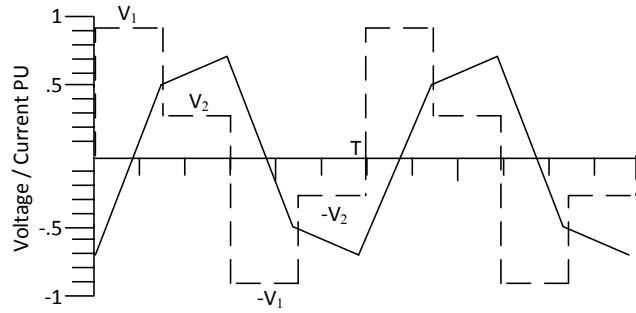


Figure 3.31: Ideal Trapezoidal Excitation.  
Dash = Voltage, Solid = Current.

In order to verify the proposed topology, a 2 kVA test bed prototype was assembled in the lab, Figure 3.30. This circuit is connected with separate DC supplies. Cores were tested to verify the test circuit performance and capabilities. It is essential to determine the applied induction level in order to properly relate the results and meaningfully compare them to other loss maps. Following the same derivation procedure used to determine the sinusoidal (AC) induction level (3.19), the induction levels for both bipolar square, triangular (T) induction (3.20) and two level square, trapezoidal (TP) induction (3.21). The full section will provide graphics of the applied voltage waveforms with variable definitions.

$$(3.19) \quad B_{AC} = \frac{\sqrt{2}}{2\pi ANf} V_{rms}$$

$$(3.20) \quad B_T = \frac{1}{4ANf} V_{DC}$$

$$(3.21) \quad B_{TP} = \frac{1}{2ANf} \left( DV_{High} + \left( \frac{1}{2} - D \right) V_{Low} \right)$$

### 3.8.3 Switch Gating of Proposed Converter

With the proposed dual topology, a new gating scheme is needed to achieve the desired induction profile. An arbitrary trapezoidal induction profile can be generated by understanding that the voltage sourced converter provides relatively high ramp to the induction profile shape and the low voltage source converter provides relatively low ramp to the profile. It is clear from the time derivative of induction that the two ramp rates are governed by the applied voltage to the transformer. For an example, the first half of a flat top trapezoid is generated first by

applying a positive voltage and then a zero voltage. Therefore, the voltage source converter is gated for a duration needed to achieve the desired peak induction as seen in (3.22). Then the low voltage source converter is gated on to provide a zero or low voltage current path. The applied voltage and corresponding gating signals is shown in Figure 3.32 top and Figure 3.32 middle respectively. Figure 3.32 bottom shows the resulting current excitation.

$$(3.22) \quad \Delta T = B_0 + \frac{\Delta B N_s A_c}{V_{Tx}}$$

This equation can be used for determining the on time at any point in the excitation.  $B_0$  is the induction level at the start of the time period.  $N_s$  is the number of turns and  $A_c$  is the core cross sectional area.  $V_{Tx}$  is the applied voltage level.

#### 3.8.4 Simulation Verification of Gating

The new converter is studied using Plecs magnetics with switching components that include parasitic elements extracted from the datasheets. In Figure 3.32 it is clear that a near ideal flat trapezoidal induction achievable. In this simulation the results were achieved by matching the low voltage source voltage,  $V_{Low}$ , to the parasitic voltage drop. Figure 3.32, right, shows an induction profile consistent with a DAB where the transformer turns ratio that does not match the voltage ratio. This was achieved with a low voltage level higher than the parasitic drop. This shows the flexibility of the converter to provide desired induction profiles. Table 3.5 provides a description of the switch gating times as well as the voltage and current stress seen by each device.

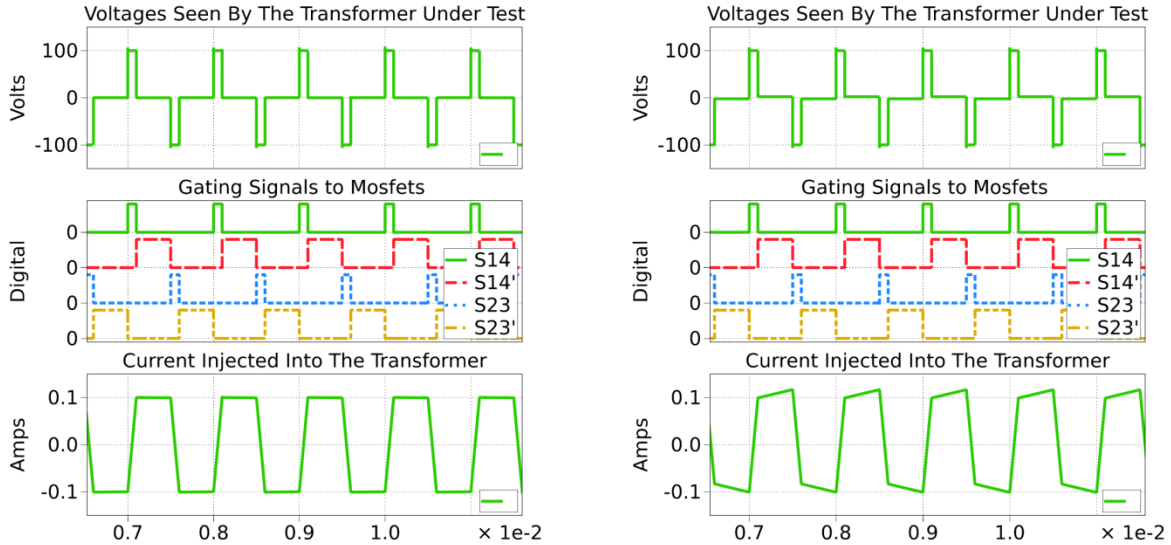


Figure 3.32: Waveforms of Dual Voltage Source Core Tester.  
 $V_{Low}$  Matching (Left) and  $V_{Low}$  Greater Than (Right) the Parasitic Drop.

In order to achieve the desired excitation shape the, the time the device is on and the delay after which it is energized is listed in Table 3.5. Based on the simulation, the voltage and current stresses are also shown below in Table 3.5.

Table 3.5: Dual Voltage Source Converter Switch Timing and Stresses.

Switch	On Time	On Delay	Voltage	Current
$S_1, S_4$	$\Delta T$	0	$\frac{1}{2} V_{High}$	$I_{Pk}$ Ramp 1
$S_2, S_3$	$\Delta T$	$180^\circ$	$\frac{1}{2} V_{High}$	$I_{Pk}$ Ramp 1
$S_1', S_4'$	$\frac{1}{2} T_{prd} - \Delta T$	$\Delta T$	$\frac{1}{2} V_{Low}$	$I_{Pk}$ Ramp 1
$S_2', S_3'$	$\frac{1}{2} T_{prd} - \Delta T$	$\Delta T + 180^\circ$	$\frac{1}{2} V_{Low}$	$I_{Pk}$ Ramp 2
$D_{Reverse}$	$\frac{1}{2} T_{prd} - \Delta T$	S' Time	$\frac{1}{2} (V_{High} - V_{Low})$	$I_{Pk}$ Ramp 2
$D_{Body}$	$T_{Deadband}$	$\frac{1}{2} T_{prd}$	$\frac{1}{2} V_{High}$	$I_{Pk}$ Ramp 2
$D_{Body}'$	0	Never	$\frac{1}{2} V_{Low}$	0

### 3.8.5 Switching Progression for Trapezoidal Excitation

In order to further clarify and explain the operation of the proposed converter, Figure 3.33– Figure 3.37 show the switching progression for a positive half cycle to the negative half cycle. In these figures, the dark path is used to highlight the operating components. That is, the

mosfets are gated on, the wires are conduction and the diodes are forward biased and conducting. The light components are specifically not conducting.

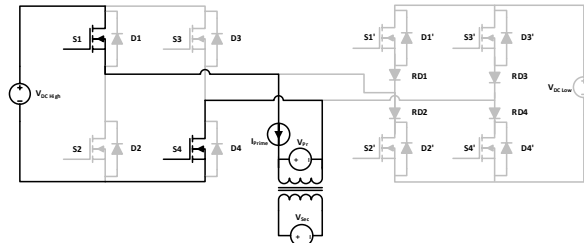


Figure 3.33: Positive High Voltage Applied to the CUT Through Mosfets S1 and S4.

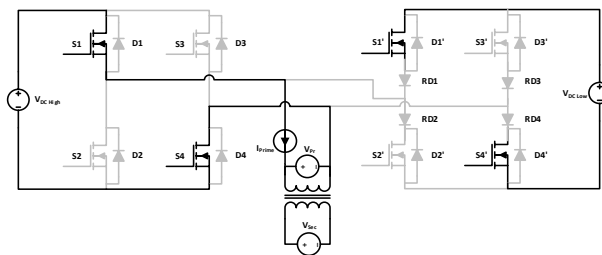


Figure 3.34: Mosfets S1' and S4' are Pre-Gated On for Overlap Time.

One unique aspect of the switching procedure in this dual topology is to prematurely gate on the low voltage mosfets for a desired overlap time, Figure 3.34. This will be explained further in the next section with hardware results. This pre-gating enables the transition of conducting exciting current from the high voltage converter to the low voltage converter with only the turn on delay of the reverse diodes. While the high voltage converter is on, the diodes are reverse biased and blocking any shoot through current between the two converters. Once the high voltage converter is gated off, the reverse diodes become forward biased and conduct, Figure 3.35.

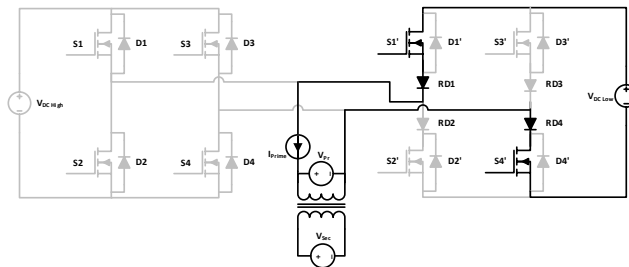


Figure 3.35: Low Voltage Excitation Through Mosfets and Reverse Diodes Conduction.

Once the desired induction level is achieved through the second ramp of current, negative excitation is needed. As such, it is ok that there is an applied negative voltage resulting from conduction through the freewheeling diodes as seen in Figure 3.36. However, this negative voltage is greater than the desired negative voltage (3.23) and should be minimized by gating on the proper mosfets, Figure 3.37.

$$(3.23) \quad V_{TX} = -(V_{DC} + 2V_{on}) + i(t)R_{cu}$$

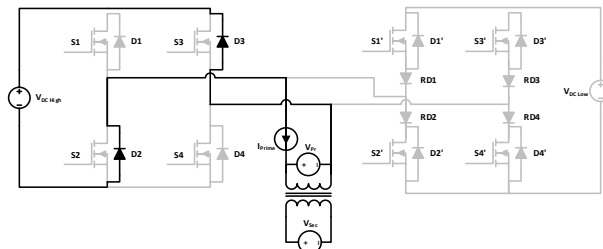


Figure 3.36: Freewheeling Diodes Conduction: Positive to Negative Voltage Transition.

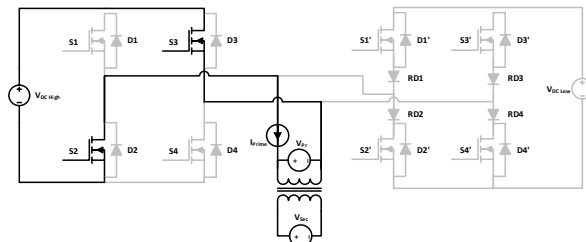


Figure 3.37: Negative High Voltage Applied to the Core Under Test Through Mosfets.

It is clear from these circuit diagrams that desired excitation current can be applied to a magnetic core under test. This converter can apply two separate voltage levels while continuing to supply positive current within the positive half cycle of a desired waveform.

### 3.8.6 Switching Noise Reduction

In both presented waveforms and in all other recorded data, there is a negative  $di/dt$  during the high positive to low positive transition. This negative slope exists despite never applying negative voltage to the core under test. In order to verify that this is not a circuit artifact, the current contribution of the two separate converters is analyzed separately and added

together to determine the total current injection. Figure 3.38– Figure 3.40 show the focus of this study.

First, the mosfet gating on time of the low voltage converter is adjusted to study the impact of the switches transition. In Figure 3.38 where Ch. 1: Blue = Current into Exciting Coil, Ch. 2: Cyan = Primary Voltage, Ch. 3: Purple = Secondary Voltage, Ch. 4: Green = Low Side Current Ch. 3 and Ch. 4 are on the same vertical with no zero crossing, the low voltage mosfets are gated on immediately after the high voltage mosfets are gated off with no deadband. It is clear from the current contribution of the low voltage converter, Ch. 4, that this turn on time results in a significant resonant ringing of several MHz. This results from the discharge of switch capacitances and the parasitic inductance of traces and conductors. With this much switching noise, the current injected into the core under test, Ch. 1, inherits some of this ringing which in turn shows on the measured secondary voltage, Ch. 3. The applied voltage, Ch. 2 has some small ringing as well. It is important to note that the voltage is always positive and yet the current measured into the transformer has a negative  $di/dt$  period during the transition.

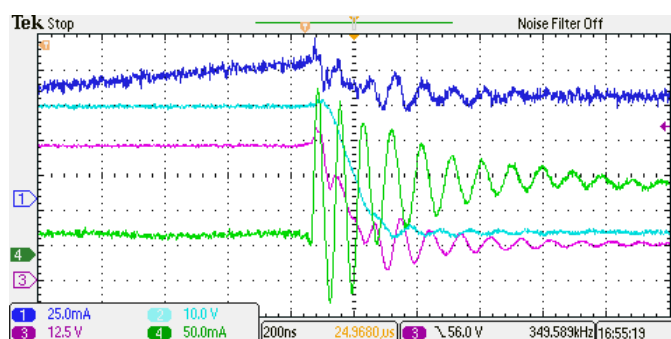


Figure 3.38: Time Zoomed Positive Transition From 50V to 12.5V.

Ch. 1: Blue = Current into Exciting Coil, Ch. 2: Cyan = Primary Voltage, Ch. 3: Purple = Secondary Voltage, Ch. 4: Green = Low Side Current.

As mentioned in the previous section, it is best to pre-gate the low voltage side mosfets. This negative deadband is shown below in Figure 3.39. Now the current contribution from both converters is measured summed to determine the exciting current. It is clear that a significant

reduction in switching ripple is achieved now that only the capacitance of the anti-series diodes must be discharged.

Again, the exciting current shows a negative  $di/dt$ . The magnetizing inductance is calculated during the steady state positive voltage with positive  $di/dt$  period. Using this inductance and the negative  $di/dt$  measured in Figure 3.39 one would expect a negative voltage of 3.5 kV.

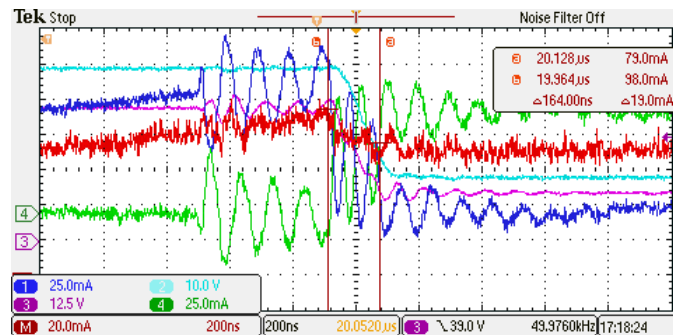


Figure 3.39: Time Zoomed Positive Transition From 50V to 18V.

Ch. 1: Blue = High Side Current, Ch. 2: Cyan = Primary Voltage, Ch. 3: Purple = Secondary Voltage, Ch. 4: Green = Low Side Current Math: Red = Current into Exciting Coil.

In order to further reduce the switching noise, the mosfet switch speed was slowed down. This was achieved by increasing the gate resistance from 10  $\Omega$  to 25  $\Omega$ . It is clear from Figure 3.40 below, that approach of slowing the mosfet gating time and applying specific overlap time does provide reduced ripple.

In the construction of the prototype, emphasis was placed on constructing the circuit from a modified platform. As such, the design does not optimize for minimal parasitic inductances. Future iterations will bring this approach into the design to further reduce switching ripple. However, it is clear from the presented figures that the switching ripple primarily oscillates between the two converters. The impedance path of the core under test is much higher than the other converter. This switching ripple, while present, has little impact on the resulting magnetic core characterization.

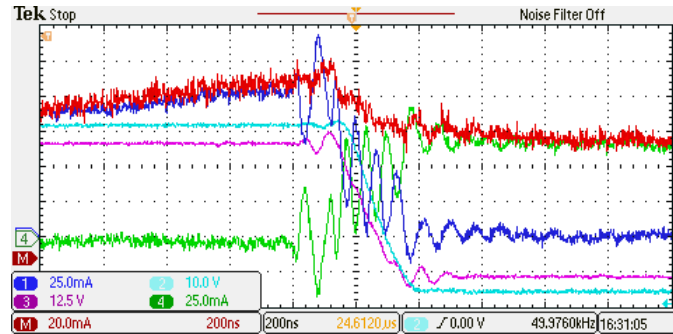


Figure 3.40: Time Zoomed Positive Transition From 50V to 18V with Reduced Ringing. Where Ch. 1: Blue = High Side Current, Ch. 2: Cyan = Primary Voltage, Ch. 3: Purple = Secondary Voltage, Ch. 4: Green = Low Side Current Math: Red = Current into Exciting Coil.

### 3.8.7 Confirmation of Magnetic Core Behavior

With the unexpected behavior of opposite signed  $di/dt$  despite consistently signed applied voltage, it is important to verify that this phenomenon is in fact a magnetic core behavior and not a circuit error or induced behavior. First, an air core inductor is constructed and the new circuit applies the two level excitation. As can be seen below in Figure 3.41, when a lossless inductor is applied with the two level excitation the current slope follows the expected slope transition of an ideal inductor. Next, a high silicon steel core is inserted into the air core area to provide a lossy magnetic core to the inductor. Figure 3.42 shows the unexpected  $di/dt$  behavior.

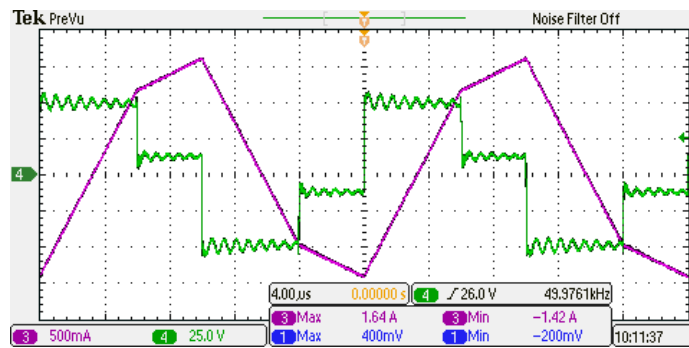


Figure 3.41: Air Core Inductor at Reference Excitation.

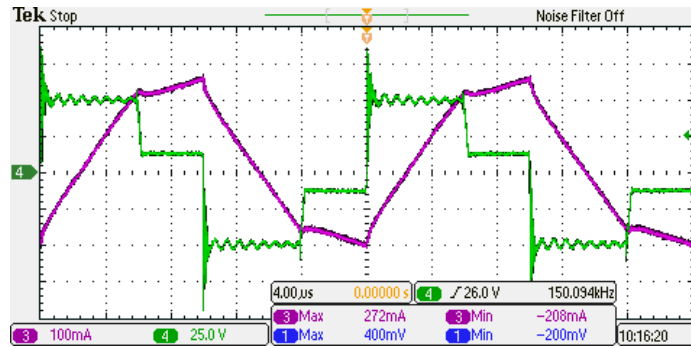


Figure 3.42: A Lossy Core Material at Reference Excitation.

The overall level of current decreases because there is less reactive power going to the coil, the inductance has increased. However, the notching in the current that occurs between the current slope transitions is unexpected in a lossless inductor and can be attributed to core loss.

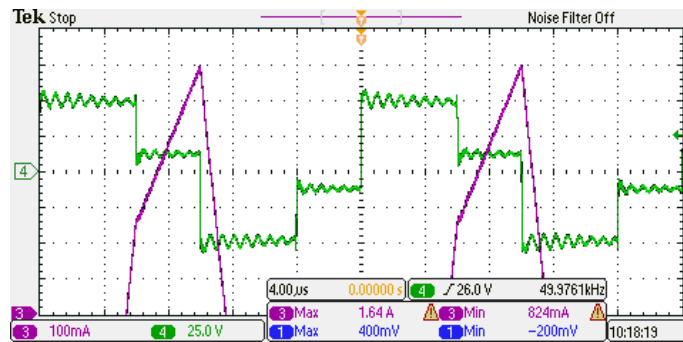


Figure 3.43: Air Core Inductor at Reference Excitation and Lossy Core Scale.

In order to verify there were no sensor errors, the lossy core is removed and the air core inductor current is reexamined at the zoomed in levels of the previous case, Figure 3.43. It is clear that the notching is no longer present, reaffirming that the notch is core loss.

Further verification is seen in the hysteresis loops of the two inductors. The air core inductor is seen with zero enclosed area meaning that no energy was lost to transition around the loop, Figure 3.44. The lossy core inductor has enclosed area, Figure 3.44, right. The near vertical current transitions seen in Figure 3.42 translate to horizontal transitions in the lossy BH loop, giving the loop width and thus enclosed area. From this reasoning, it is clear that the losses of the core material appear in the excitation waveforms vertical jerks.

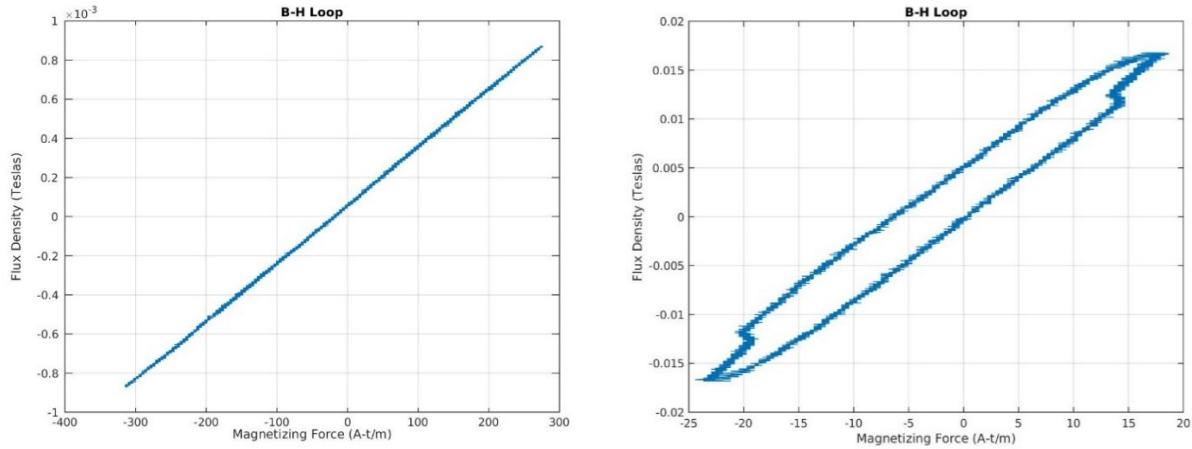


Figure 3.44: *BH Loops for Dual Voltage Source Core Tester Verification*  
*Lossless Air Core BH Loop (Left) and Lossy Core BH Loop (Right).*

As mentioned previously, many authors work has focused on bringing loss fitting techniques, Steinmetz Equation, closer to the fundamental physics. Specifically, they have followed the idea that losses depend primarily on the time rate of change of flux density,  $dB/dt$ . With some simple substitution we can see that this equates to losses depending primarily on the applied voltage (3.24) and (3.25).

$$(3.24) \quad V = -\frac{d\phi}{dt}$$

$$(3.25) \quad V = \frac{\phi}{A}$$

However, as can be seen in the following figures, there is a dominate loss component when Voltage changes or losses depend heavily on  $d^2B/dt^2$ . This will expand the knowledge in origination of magnetic core losses and could lead to better modelling and prediction of losses.

### 3.8.8 High Power, Low THD Sinusoidal Excitation

On major advantage of the proposed topology is the near unlimited flexibility in parallel connection. Below, Figure 3.45, a configuration of three converters with the voltage evenly split among them is able to generate a six level sin like wave. In this configuration, the  $N$  converters generate a  $2N$  level sin wave. The control gating is rudimentary at the moment and just based on comparison with a sin wave. One big advantage to this circuit is the elimination of deadband in

the gating signals. Since a different converter conducts the next level voltage and is protected with an anti-series diode, you do not have to have protection delaying the turn on of the power mosfets. This enables higher switching frequencies and smoother excitations at high power, Figure 3.46.

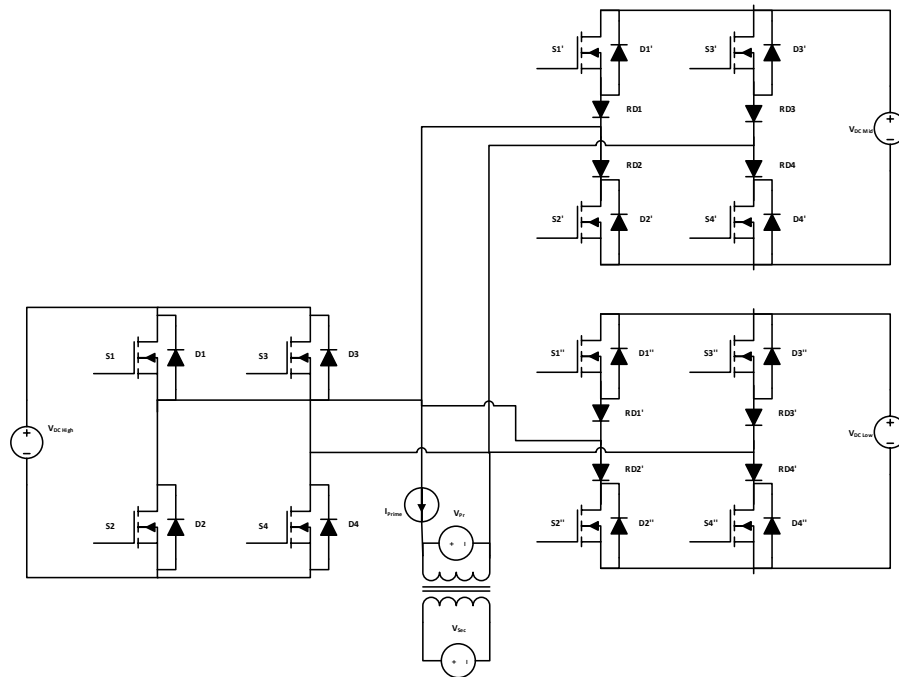


Figure 3.45: Three Level Sinusoidal Configuration.

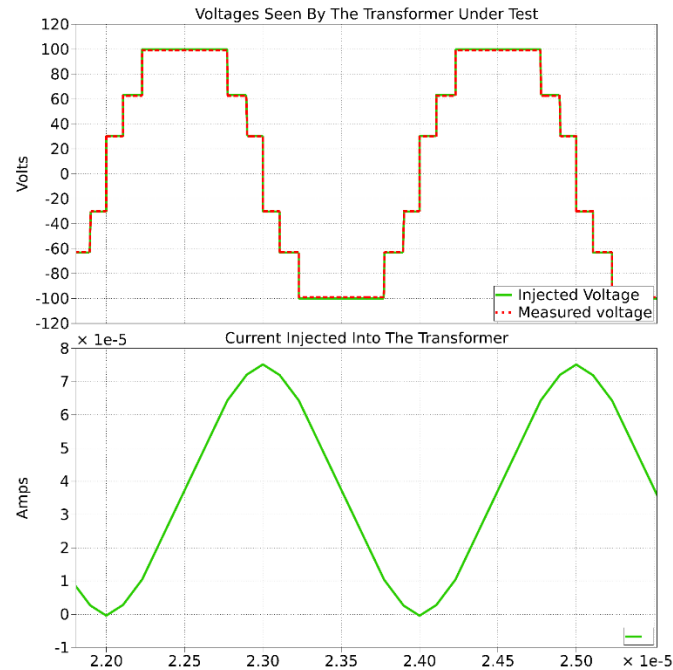


Figure 3.46: Output Waveforms of Multilevel Voltage Source Core Tester. Top: Applied Voltage, Bottom Injected Current.

### 3.8.9 High Power Dielectric Testing

Generating the medium frequency sinusoid or any other arbitrary voltage waveform makes this converter ideal for dielectric testing. This converter is able to subject sample dielectrics to practical power levels and practical  $dv/dt$  that typical impedance or LCR meters cannot. A simple copper pressure plate harness was constructed in order to perform these types of tests Figure 3.47. A high power excitation, a 900V Square wave at 100 kHz was applied to several sample dielectrics Figure 3.48. These waveforms were then returned to collaborators for in depth material analysis. They found that there were significant differences between the dielectric properties after the power test that were not appearing with their low power test equipment.



Figure 3.47: *Prototype Dielectric Testing Harness.*

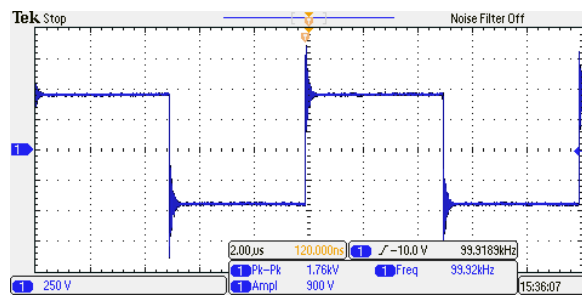


Figure 3.48: *High Power Dielectric Test Waveform.*

### 3.8.10 Alternative Uses of New Converter

Another potential design using this converter is a monodirectional inverter. If the DC bus is very high and it is parsed with series capacitors, this converter topology could connect to each capacitor to provide an output. Importantly it is not bi-directional but it could be a means to connecting to very high DC voltage as the switches would only need to withstand the capacitor divided voltage. Similarly, it could monodirectionally source multiple isolated DC sources. This could be beneficial for applications such as PVs. Each string of PV would be connected to a DC terminal of this converter. Then, each terminal could manage the PV string mpp voltage independently. If there was partial shading of a string, it could still source power without forcing other strings to reduce voltage.

### 3.9 Trapezoidal Induction Study

#### 3.9.1 Analysis of Excitation Levels in Active Bridge Transformer

The expectation is for the slope of the current to stay the same sign yet decrease following Ohms law for an inductor. However, as can be seen in Figure 3.42, there is a distinct change in current sign. From the electrical modelling perspective, current behaves less like the circuit shown in Figure 3.49, also known as the cantilever model. Importantly, the observed behavior cannot be recreated by the model with the loading resistor  $R_m$  is in series with the magnetizing inductance  $L_m$ . Only when  $R_m$  is in parallel does the resistor provide the high speed current change path when voltage changes.

In order to better understand voltages seen in the dual active bridge MF transformer it is useful to investigate the pi model of the transformer, Figure 3.49. For this analysis, all impedances are reflected to the same side and normalized. The two voltages are ideally equivalent, i.e. the volts per turn are the same on either HF transformer port,  $k = 1$ . If there is a voltage mismatch, then  $k \neq 1$ . There are two important periods of applied voltage when there is a phase shift and the voltages are opposite sign and when the phase shift is over and the voltages are the same sign. The resulting magnetizing voltage for the two periods is shown in (3.26) and (3.27) respectively.

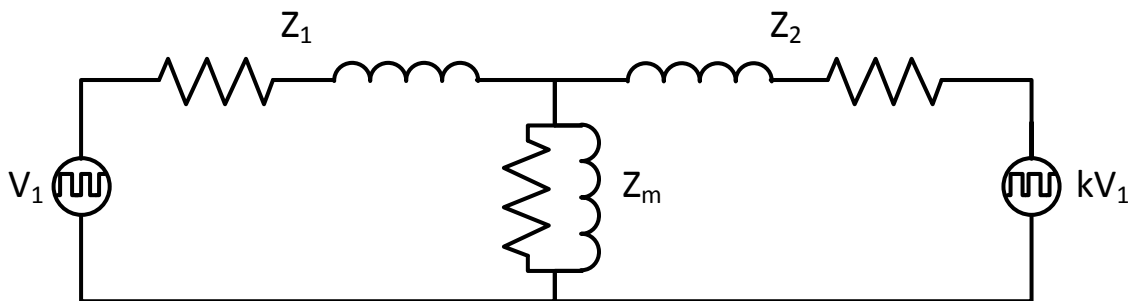


Figure 3.49: Pi Model of MF Transformer

$$(3.26) \quad V_{m-PS} = \frac{-kZ_1Z_m + Z_2Z_m}{Z_1Z_m + Z_2Z_m + Z_1Z_2} V_1 \quad (3.27) \quad V_{m-NS} = \frac{kZ_1Z_m + Z_2Z_m}{Z_1Z_m + Z_2Z_m + Z_1Z_2} V_1$$

This approach can also be used for studying the leakage path losses. However, it should be noted that the voltage necessary to emulate the leakage paths is the sum of  $V_I$  and  $kV_I$ . It is evident from this analysis that under all but the most ideal situations the voltage applying to the magnetizing branch exhibits two levels during the half cycle. This is a more complex waveform that is achievable with the new testing circuit.

### 3.9.2 Preliminary Trapezoidal Excitation Results

A sample of the amorphous AMCC core tests is shown in Figure 3.50. In particular, the low voltage side is tuned to provide a flat top trapezoidal excitation. Parasitic capacitance between the exciting turns, the sensing turns, and with the core introduces some secondary voltage ringing during the voltage transitions. However, this ringing is not present in the applied primary voltage. Figure 3.50 right, shows the hysteresis loop that results from this excitation.

A sample of the HTX core tests is shown in Figure 3.51. In these results, a large excitation difference between the two positive levels is shown. Furthermore, in these results the capability of providing two separate slopes of exciting current is shown. Again, some parasitic capacitances introduce voltage ringing on the measured secondary voltage. However, this ringing is not present on the applied primary voltage. Figure 3.51 right shows the hysteresis loop that results from the excitation and induction of Figure 3.51 left. The current slip that was evident in the first set of results is more pronounced in these with the higher transition range of applied voltage. This slip exists despite no application of negative voltage that would satisfy the negative  $di/dt$ .

In all cases, Ch.1, blue, is the primary current energizing the exciting current and Ch.2, cyan, is the applied voltage. It is evident from these results that trapezoidal excitation is

achieved. Figure 3.50 shows the results for a representative amorphous material, AMCC excited at 10kHz. Figure 3.51 shows the results for a representative nanocrystalline material, HTX at 50kHz.

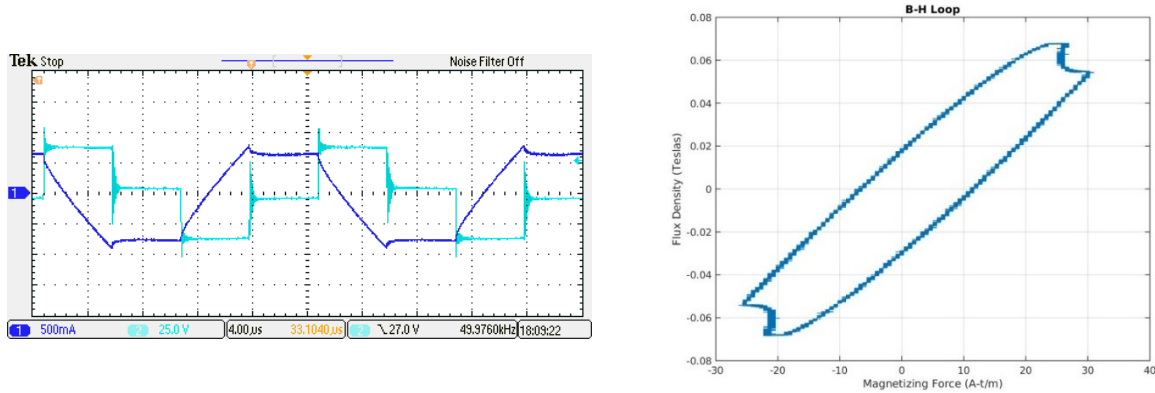


Figure 3.50: Flat Top Trapezoidal Excitation of AMCC Amorphous. Electrical Waveforms (Left) and Hysteresis Loop (Right).

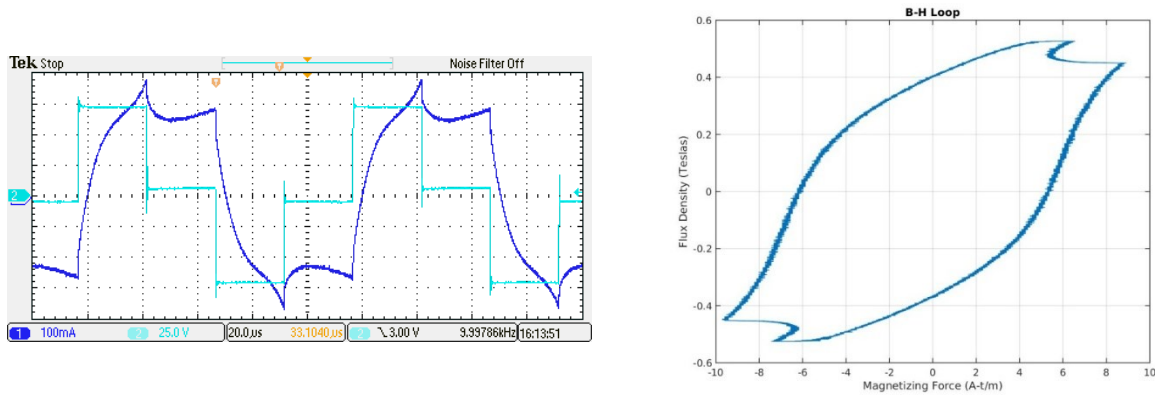


Figure 3.51: Dual Slope Excitation of HTX Nanocrystalline Core. Electrical Waveforms (Left) and Hysteresis Loop (Right).

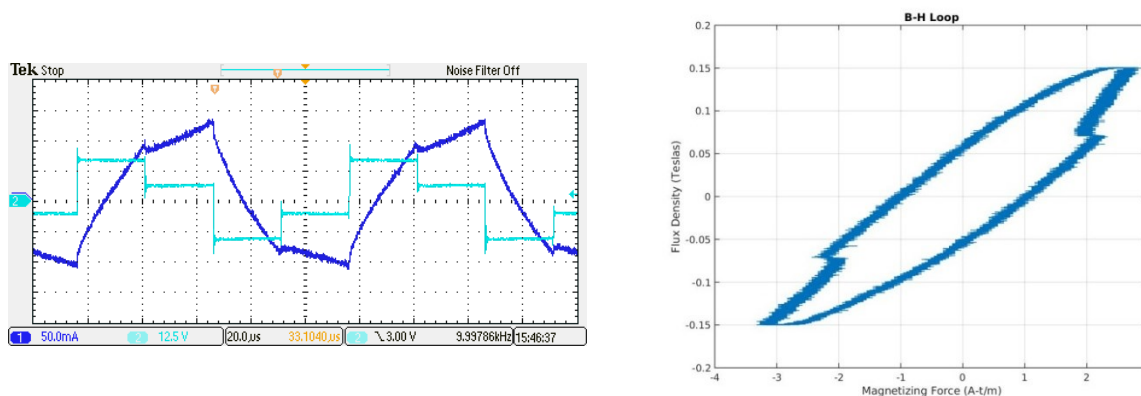


Figure 3.52: Verification of  $-di/dt$  Despite All Positive Voltage. Electrical Waveforms (Left) and Hysteresis Loop (Right).

### 3.9.3 Test Conditions

One of the key issues in this type of testing is the phase discrepancy between the current sensor and the voltage sensor [80]. While the authors present useful calculations and methods to correct for this error more modern testing equipment can also be utilized. In this case, a Teledyne 1 GHz, 12-bit, 4ch HDO 6000 oscilloscope is used. By using the DCS015 deskew kit, the phase difference between the active current probe, CP031A, and differential voltage probe, HVD3206, can be reduced to a few picoseconds. This significantly improves the accuracy of the testing with the limitations now being the probe accuracy itself.

As mentioned before, a cobalt rich nanocrystalline core that is similar to Finemet was used for the test verification. The core is 0.49 kg and uncut in a race track geometry. Five turns were used to excite the core and ten turns were used for sensing the induction level. Both coils utilized 12 awg litz wire. While this is not critical, it ensured that the exciting coil had low losses and contributed little to no external heating to the core. In the same sense, a Hioki temperature logger was used measure multiple core locations' temperature. This ensured that testing was repeated for the same thermal conditions with only 2°C variation allowed. Equations (3.20) and (3.21) were used to set the DC source voltages for a desired induction level. Due to parasitic

drops of the converter and exciting coil there is some discrepancy in the desired induction level and the actual measured level. However, this is accounted for in the analysis and the testing could be improved with updates to (3.20) and (3.21) that account for these drops in the applied voltage.

### **3.9.4 Test Results**

The test procedure presented in this paper for the core is to subject it to three different types of excitation waveforms. The aforementioned characterization equations were used to, estimate the necessary applied voltage, analyze the resulting waveforms, and extract relevant parameters. Sinusoidal data was provided by Carnegie Mellon through the use of a commercial core tester. First, the core was subjected to triangular excitation with square voltage. Next, trapezoidal excitation was explored in two variations. The second test subjected the core to a half period of half high voltage and half low voltage. The third test swept the high voltage on time from 5% to 25%, half of a half period. These tests are presented in the in the following three subsections.

### **3.9.5 Baseline Triangular Excitation**

In this set of tests only the high voltage side converter was used. As such there was a deadband time when freewheeling diodes conducted. However, this period was short. There could be some advantages in also gating the low voltage side but this possibility has not been explored. The induction levels were swept between 0.1 T and 1T. Frequencies between 2.5 kHz and 50 kHz with that induction range were tested. An example of one of the tests in this set is shown in Figure 3.53. The resulting loss map and permeability map are shown in Figure 3.54 and Figure 3.55 respectively.

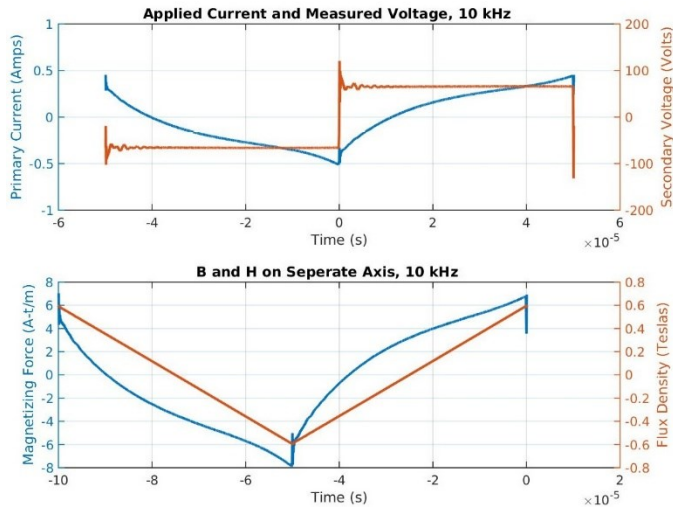


Figure 3.53: Triangular Excitation Waveforms. Measured Current and Induced Voltage (Top), Calculated Magnetizing Force and Induction Level (Bottom).

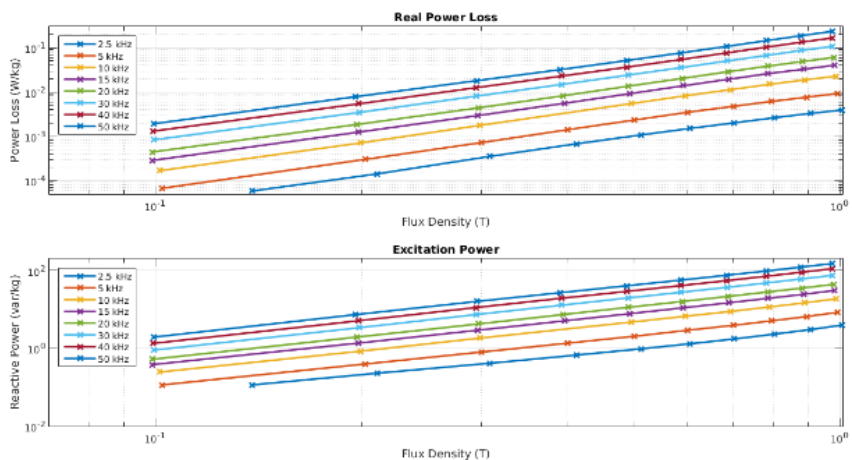


Figure 3.54: Triangular Excitation Power Map. Core Loss (Top) and Excitation Power (Bottom).

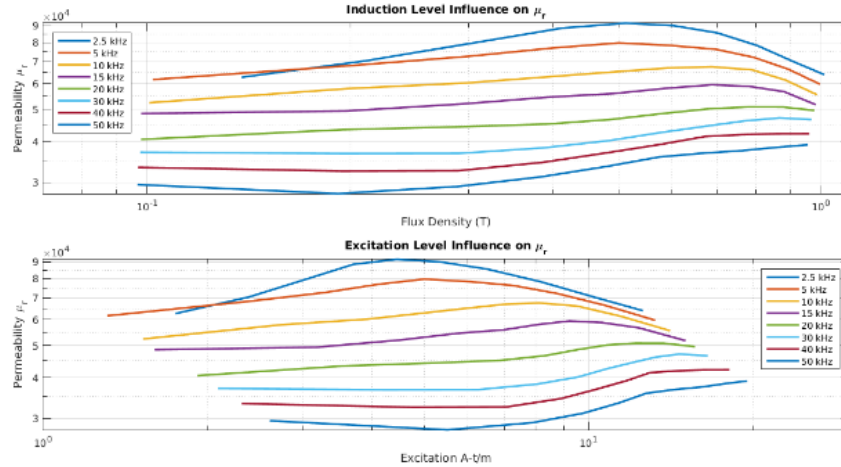


Figure 3.55: *Triangular Excitation Permeability Variation. w.r.t. Flux Density (Top) and Excitation Force (Bottom).*

### 3.9.6 Dual Slope, Quarter Duty Cycle

In these tests the high voltage was applied for a quarter, half of the positive half period. The low voltage was held constant at 10V. This voltage was chosen to ensure that no ‘apparent’ negative voltage was applied during the low voltage on time. The high voltage was adjusted with this in mind to reach the desired induction level between 0.1 T and 1 T. The frequency was swept from 5 kHz to 50 kHz. Certain test points were not tested because it would require a high voltage setting lower than the low voltage. Again, an example of the waveforms is shown in Figure 3.56. The summary plots of power and permeability are shown in Figure 3.57 and Figure 3.58 respectively.

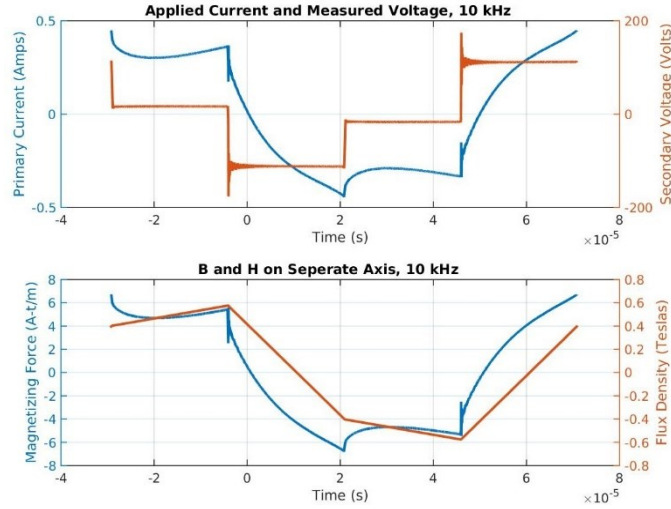


Figure 3.56: Trapezoidal Excitation Waveforms. Measured Current and Induced Voltage (Top), Calculated Magnetizing Force and Induction Level (Bottom).

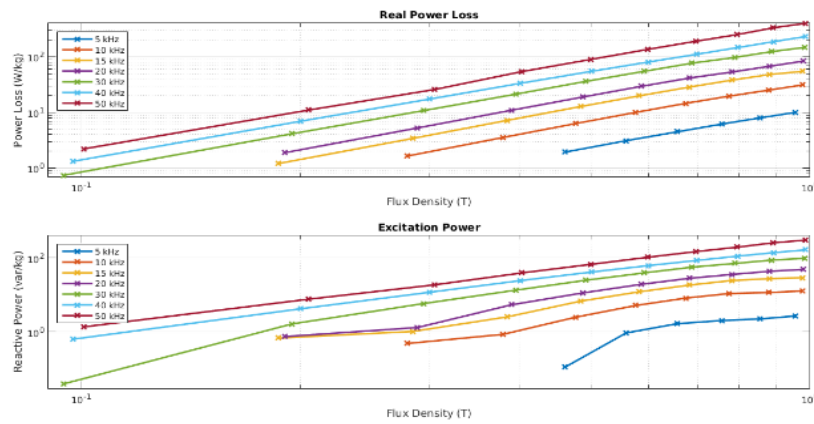


Figure 3.57: Trapezoidal Excitation Power Map. Core Loss (Top) and Excitation Power (Bottom).

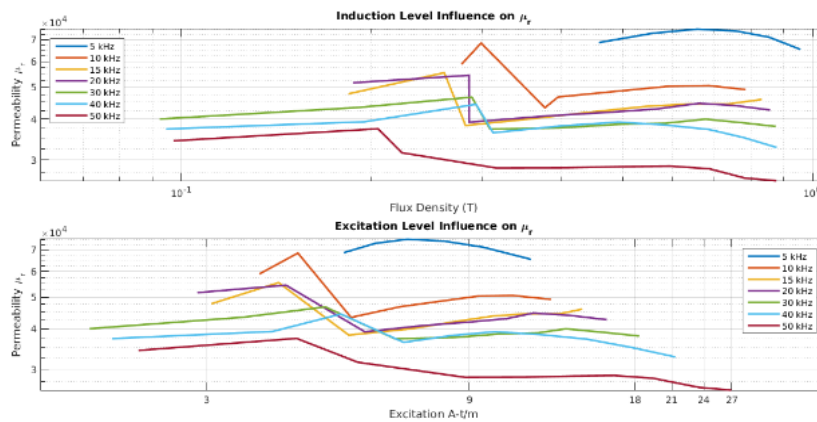
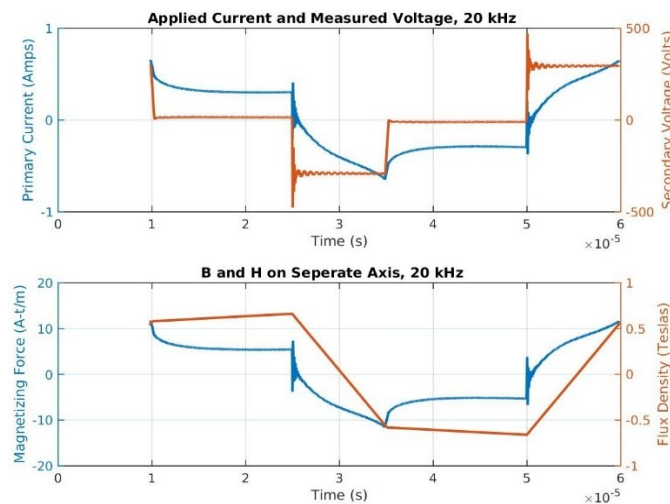


Figure 3.58: Trapezoidal Excitation Permeability Map. W.r.t. Flux Density (Top) and Excitation Force (Bottom).

### 3.9.7 Dual Slope, Duty Cycle Sweep

The third set of tests explores variations in the on time of the high voltage. The on time was swept from 25% to 5% with a constant low voltage of 3V. The low voltage was chosen to provide as flat of a trapezoidal current as possible. This is representative of the phase shift voltage in an ideal DAB. These tests put strain on the converter, which in its second version has an undesirable amount of switching ripple. This noise caused issues in the gating circuitry and controller that limited the scope of testing. Here the frequency was swept from 15 kHz to 50 kHz. An example waveform is shown in Figure 3.59 and the summary power and permeability maps are shown in Figure 3.60 and Figure 3.61.



*Figure 3.59: 20% Duty Cycle Excitation Waveform. Measured Current and Induced Voltage (Top), Calculated Magnetizing Force and Induction Level (Bottom).*

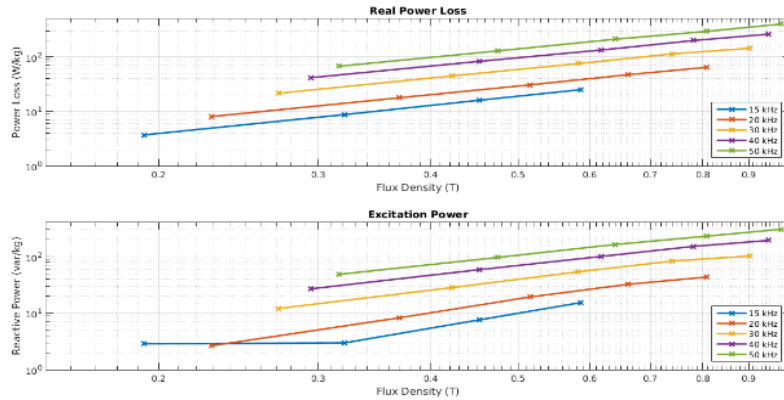


Figure 3.60: 20% Duty Cycle Power Map. Core Loss (Top) and Excitation Power (Bottom).

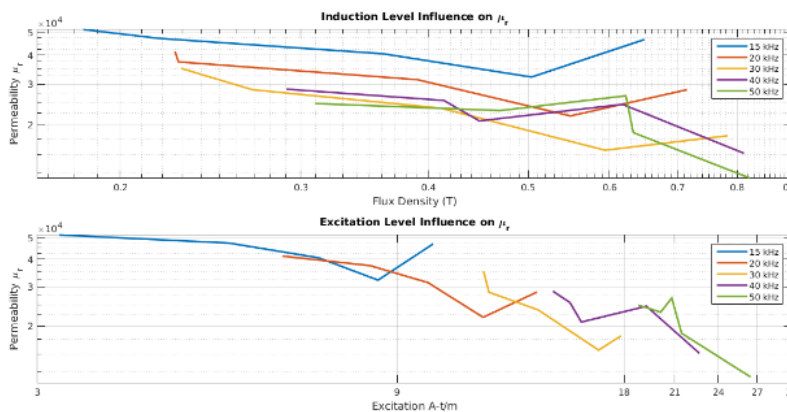


Figure 3.61: 20% Duty Cycle Permeability Map. W.r.t. Flux Density (Top) and Excitation Force (Bottom).

### 3.9.8 Comparison of Excitations

As demonstrated in the above loss maps, the excitation pattern has a significant impact on the effective performance of the core material. As such, it is important for engineers and designers to understand and predict these variations. One of the simplest methods for comparing the loss maps of a given excitation waveform is to use curve fitting to provide a representative equation for performance change behavior. Conveniently, the form of the Steinmetz equation, (2.25), can be used to represent the loss maps regardless of the excitation waveform. Table 3.6, shows the variations in Steinmetz's constants where Matlab's curve fit tool was used to fit the loss surface, and maintain a high R value. While this method is useful for comparison it has limitations in predictive utility as the fit parameters are only valid for the exact excitation pattern.

While generalized loss models can be more useful for predicting loss variations between excitation patterns, this approach provides the ability of direct comparison between record losses.

*Table 3.6: Waveform Dependent Fit Parameters Using Classic Steinmetz Equation.*

Mode	K	$\alpha$	$\beta$	Mode
Sin	0.4525	1.672	2.129	Sin
Triangular	0.7685	1.474	2.181	Triangular
Half Duty	0.4563	1.739	2.201	Half Duty
Duty Sweep	0.5812	1.68	1.572	Duty Sweep
Mode	K	$\alpha$	$\beta$	Mode

Similarly, the recorded loss data can be compared on the same plot. This is useful for understanding what penalties can be expected from different excitation patterns. An example comparison between triangular and trapezoidal excitation is shown in Figure 3.62. It is important to note insights that can be gleaned from this type of comparison, e.g. low frequency triangular and trapezoidal losses are nearly identical but higher frequency losses can have the same impact as increasing the frequency by 25% as in the case for 40 kHz excitation. This gives greater insight into the system design limitations and enables better and more generalized predictions.

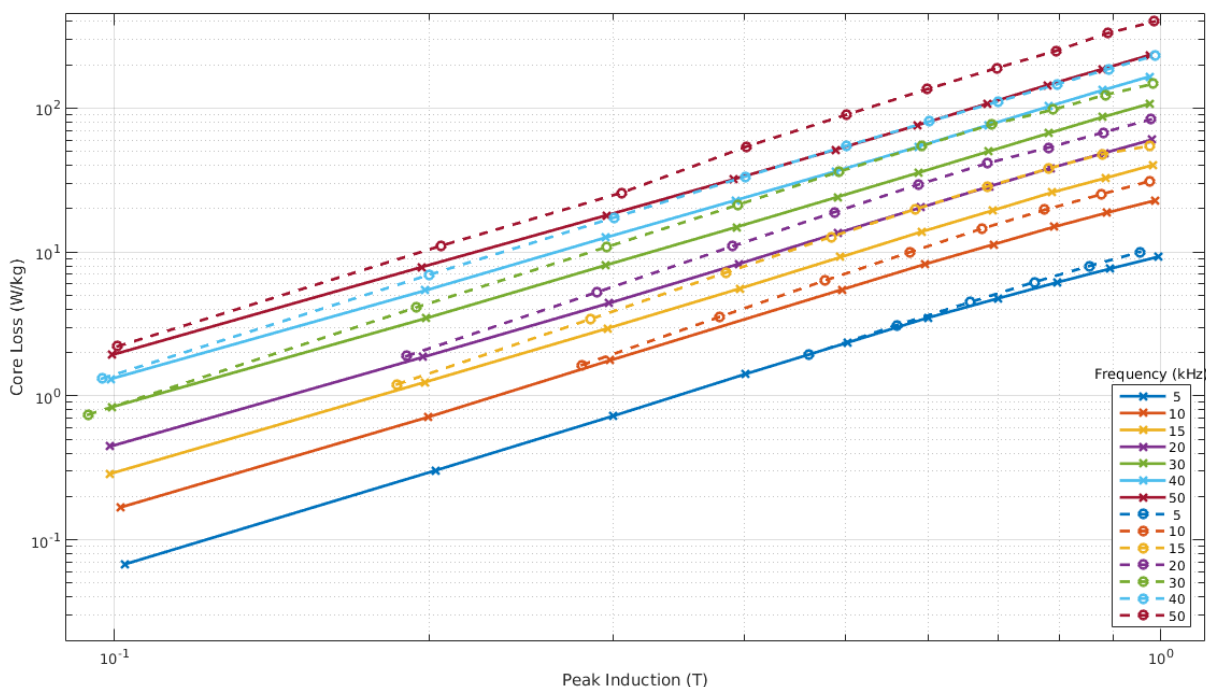


*Figure 3.62: Excitation Dependent Core Loss Comparison Map. Triangular Excitation (Solid) and Dual Slope, Half Duty Cycle, Excitation (Dashed).*

A third approach to better understanding the magnetic material's response to excitation is a direct comparison of the hysteresis loops that the excitation pattern develops. As an example, the hysteresis loops for the excitation pattern shown in Figure 3.53 and Figure 3.56 is compared in Figure 3.63. Alternatively, all three excitation patterns, triangular and trapezoidal not shown and Figure 3.59 of duty sweep, can be compared as in Figure 3.64. While this allows the three mode comparison, some of the finer details are lost due to the crowded graph area. What is clear, from both the loss map comparison and the hysteresis loop comparison, is the 'apparent' frequency increase due to waveform shape. This manifests in the increase in the coercive force,  $H_c$ , where the hysteresis loop crosses the  $X$  axis. The remnant flux density,  $B_r$  may also be increasing, but where apparent and not obfuscated by the loop pattern, these effects seem less pronounced than the coercive force increase.

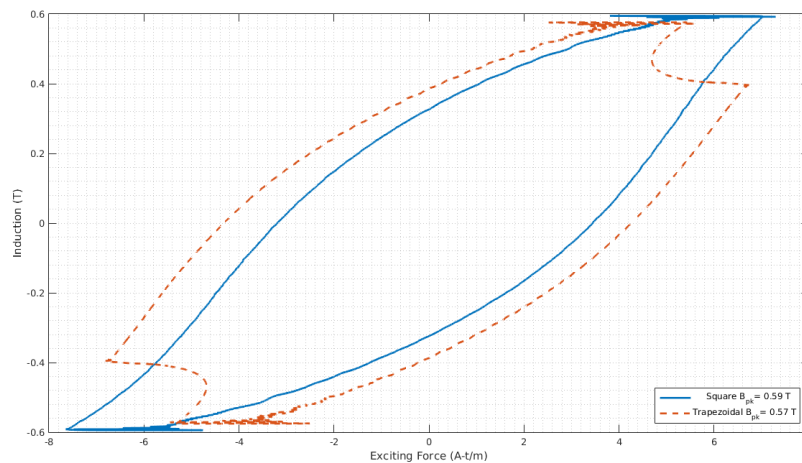


*Figure 3.63: 10 kHz, 0.6 T Hysteresis Loop Comparison. Triangular (Solid) and Dual Slope (Dashed) Waveforms.*

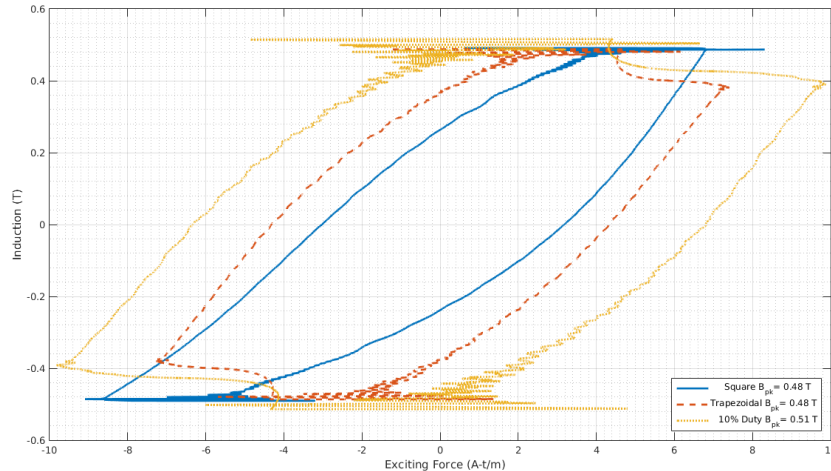


Figure 3.64: 20 kHz, 0.6 T Hysteresis Loop Comparison. Triangular (Solid), Half Duty (Dashed), 20% Duty (Dotted).

### 3.10 Conclusions and Future Work

This section presented a magnetic material test bed that enables engineers and designers to evaluate materials over a wide range of operating and environmental parameters. This test bed is focused on the high power medium frequency domain space and utilizes wide bandgap mosfets to achieve practical power converter profiles. The need for this multi-parameter testing is confirmed by showing the parameter extraction and mapping for a metal amorphous nanocrystalline core. The data presented provides a more complete picture of the material than the information presented by the manufacturer. With this information, more optimal designs are achievable without the need for multiple iterations.

An interesting phenomenon occurs during the transition from a high voltage to low voltage level of the same polarity. Despite no significant sign change in the applied voltage, there is still a negative  $di/dt$ . In order to verify that this is not an artifact of the converter and switching ripple, the low voltage level was increased to maintain no voltage sign change even with switching ripple. The negative  $di/dt$  is still present and must be a material property. This behavior further highlights the need for this testing circuit to accurately characterize magnetic materials with trapezoidal excitation. A third circuit version is forthcoming with improved

performance that will expand the testing window and decrease the switching ripple that is currently present.

This new magnetics test bed allows researchers to explore in depth variations that were previously uncontrollable or partially evaluated. While full results and parameter maps were shown for a nanocrystalline material, initial studies have shown similar behavior in both ferrites and amorphous cores. Since this work and [81] shows the effect in Ferrite materials, it is unlikely to be an eddy current effect alone. Alternatively, tests with air core magnetics have not shown similar effects. With high  $dv/dt$ , it is possible the drop is associated with effects normally neglected in kHz range studies of magnetic materials. Rather, higher frequency effects need to be considered and investigated such as those described by [84].

This will enable targeted research that further advances the understanding better refines models. Where there are differences in the current modelling techniques and the measured material performance, new models can be proposed. It is through the results generated by this testing apparatus that the new models and modifications to existing models will have a targeted effect. This enables a better alignment between the physical behavior and the performance model. These results lead to a better understanding of the fundamental nature of magnetic core loss. As mentioned in the first chapter, effects such as magnetic relaxation, viscosity or traditional loss mechanisms could be at play. Future work will need to utilize the presented novel converter to isolate these effects for future study.

## CHAPTER 4: LEAKAGE FLUX AND OTHER PARASITIC ELEMENTS IN LAMINATED MAGNETIC CORES

### 4.1 Motivation

In traditional transformer design, the magnetizing inductance is generally the primary constraint. The magnetizing inductance is chosen with a maximum magnetizing current and the transformer flux density in mind. Similarly, the leakage inductance is minimized to enable maximum power flow through the transformer [85]. However, in modern isolated power converters, the leakage inductance is a critical energy storage element for switching devices [86]. Similarly, the leakage inductance can be a part of a resonant impedance that enables soft switching [62], [87]. As such, the design of the leakage inductance must be carefully design and generally not minimized. There are other physics that come into effect that influence parasitic models of the transformer such as series resistances and capacitances that are critical for high performance designs. Groups such as Dartmouth and ETH Zurich have devoted considerable research resources to these topics and so this chapter will only provide a brief overview. The main focus of this chapter will be the design of leakage inductance and the implications this inductance has for transformers constructed of MANC ribbon cores.

### 4.2 Introduction

There are three primary parasitic components in magnetic devices, leakage inductance, capacitance and winding resistances. Numerous authors and researchers have reported several models for parasitic capacitances and resistances. Similarly, leakage inductance models have been introduced for various geometries and configurations. However, these leakage inductance models do not consider additional losses associated anisotropic materials such as ribbon or tape wound magnetic cores. As these losses have been reported to contribute seven to ten times

additional losses, new models will be critical for proper medium frequency magnetics design. This chapter will focus on the estimation of leakage inductance and associated losses. It will mention some of the capacitance models have already been developed by various researchers as these models are critical design aspects for high power medium frequency magnetics. With the high voltages and the relatively high fundamental frequencies, both series and shunt parasitic capacitances will influence designs and as such will be presented in this chapter. Finally, the winding resistance model will also be included as part of a complete medium frequency transformer model.

A main focus of this chapter will be leakage inductance and associated losses. These losses are a unique phenomenon that has had little reporting. [88] observed and reported losses but came short of fully explaining the effects. In traditional magnetics designs of low frequency or high frequency magnetics, stray flux in the form of leakage, fringing, or other non-magnetizing flux has not been considered a lossy component. That is, low frequency devices using laminated magnetic cores do not have a high enough frequency for stray flux to cause losses. High frequency devices using ferrite material can also neglect eddy currents associated with stray fluxes as ferrites have a high resistivity isotropically. As low frequency transformers grew both physically and in power rating, leakage based losses became a concern. A capacitor, resistor and voltage source network model that is influenced by geometry was proposed to model the higher order magnetic equivalent circuit of laminated plates in iron transformers [89]. Similarly, researchers used an array of search coils to determine the radial flux in a large prototype transformer [90]. With this data, they provided a curve fitting for both losses and temperature rise that is applicable to these large transformer cases. The authors of [91] combined these works and found agreement with the magnetic flux between the network model and the

search coil measurements. However, loss predictions are only marginally accurate and are limited by measurement equipment. Rather, the losses are inferred from thermocouple measurements. A similar issue is with very high power magnetics that also have significant stray fields. These fields can introduce losses with the case. Groups of researchers have explored stray eddy currents in low frequency magnetics structures [92], [93], [94] and have sought advanced FEA modelling techniques.

At medium frequencies, and high powers where laminated materials are used, the stray flux paths must be considered and understood to contribute to losses. In order to improve designs of these materials, this chapter will provide insight into this stray loss calculation. These new flux models along with models of other parasitic elements will enable researchers to design magnetic systems in the high power medium frequency solution space.

### **4.3 Leakage Flux**

#### **4.3.1 Flux Path at the Interface of Materials**

Leakage flux and leakage inductance are inherently difficult to calculate due to the three dimensional space that the magnetic field exists in. Particularly, magnetic flux will flow through a volume that depends not only on the volume's magnetic permeability but also any interface with other volumes. Following the derivation presented in [95] we can determine the deflection of flux between two materials, A and B of relative permeability of  $\mu_A$  and  $\mu_B$  respectively. By first investigating the tangential component of field intensity, we enclose a loop around the interface of two materials, of length  $l$  and thickness  $t$ , left of Figure 4.1. It is important to note that the thickness approaches zero and no externally applied current is enclosed in the loop. Similarly, following Ampere's law (4.1), (4.2) shows the relationship between tangential fields. From this equality (4.3) shows how the tangential component of the magnetic flux behaves at the interface

of the two materials. This is appropriate for an arbitrary area,  $A$ , that goes into the page arbitrarily and is along the thickness  $t$ . Then, (4.4) shows the ratio of tangential components between the two interfaces is simply the ratio of the permeability of the two materials. Next, the normal component of magnetic flux can be determined by examining the right of Figure 4.1, there is an enclosed volume with thickness,  $t$ , that approaches zero. The volume has a depth of  $d$  into the material. Using Maxwell's equation (4.5) and understanding that no flux enters the sides of zero thickness, (4.6) and (4.7) shows the equivalency of the normal flux component between the two interfaces.

$$(4.1) \quad \oint H \cdot dl = I_{enc} \quad (4.2) \quad H_{TA} = H_{TB} \quad (4.3) \quad \frac{\phi_{TA}}{A\mu_r A \mu_0} = \frac{\phi_{TB}}{A\mu_r B \mu_0}$$

$$(4.4) \quad \frac{\phi_{TA}}{\phi_{TB}} = \frac{\mu_r A}{\mu_r B} \quad (4.5) \quad \oint B \cdot ds = 0 \quad (4.6) \quad B_{NA} = B_{NB}$$

$$(4.7) \quad \phi_{NA} = \phi_{NB}$$

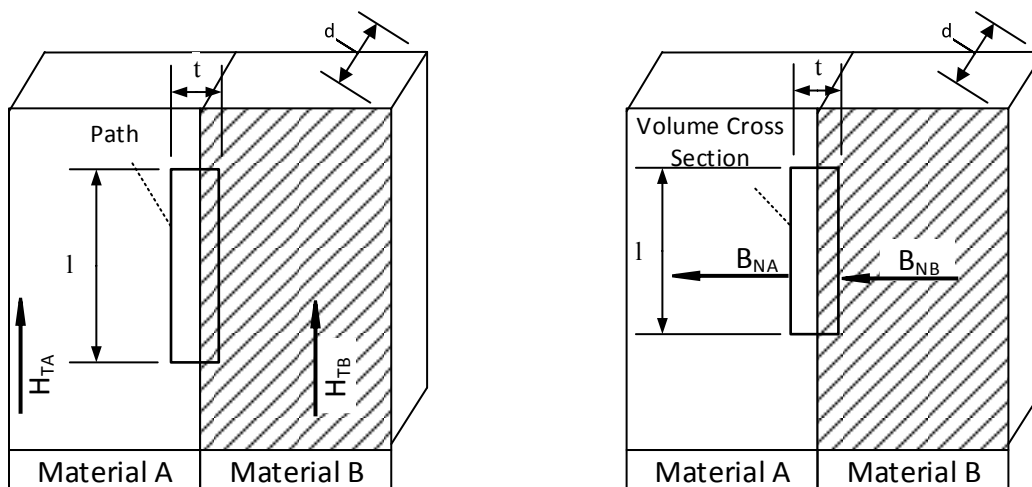


Figure 4.1: Tangential Component of Magnetic Flux at Material Interface (Left) and Normal Component of Magnetic Flux at Material Interface (Right).

It is clear from Figure 4.2 that for even low permeability ratios, the only a small portion of the horizontal flux transitions from the high permeability material to the low permeability

material. A conservative assumption is then to assume that all flux crossing air to magnetic core is perpendicular to the core surface. As an example of a practical permeability ratio,  $\mu_r = 5000$ , an angle of approach of only  $1^\circ$  translates to an  $89.3^\circ$  exit at the material interface or 99.9925% of the flux magnitude being normal to the surface.

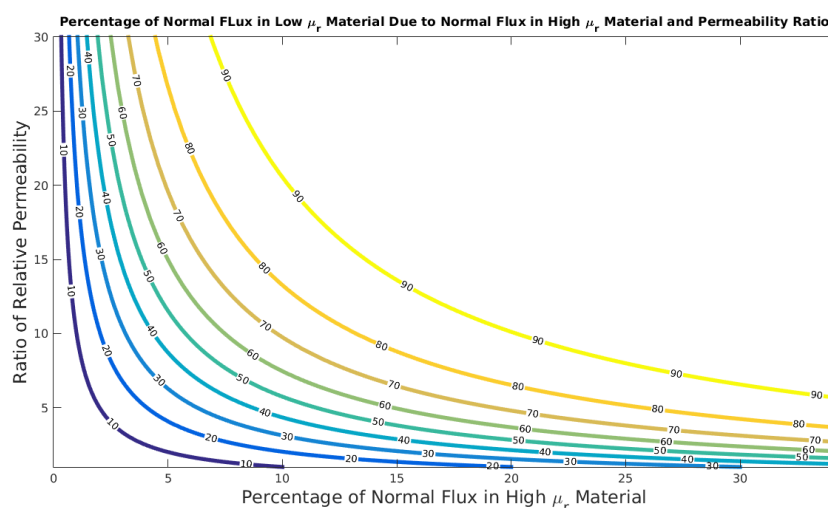


Figure 4.2: Angle of Flux Between Two Materials.

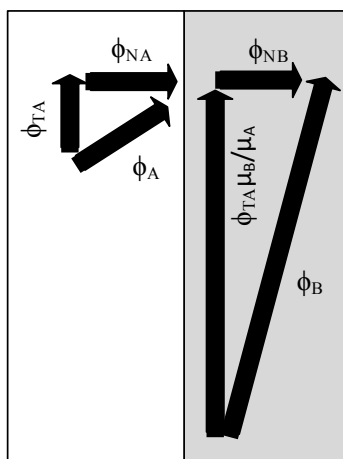


Figure 4.3: Flux Components At Material Interface,  $\mu_B \gg \mu_A$ .

Instead of the previous assumption where no enclosed current was considered, now the derivation considers the induced eddy currents due to the normal component of the flux density the tangential component changes. Following Amperes law, the tangential field intensity is related to the enclosed eddy current. Figure 4.4 demonstrates the impact of the induced eddy

currents on the flux path at the interface of two materials. For simplicity, let us assume that only meaningful eddy currents exist in material  $B$ . Now both the tangential and normal flux components are affected by the induced current. Specifically, the tangential component is adjusted to (4.8) and the normal component to (4.9). The sign of the eddy current contribution in (4.8) depends on the model set up. It is clear however that given a small permeability ratio with low eddy currents, as in well-designed magnetic cores, the horizontal component that persists across the boundary is very small. If the material is highly conductive, and the eddy currents are significant, the horizontal component can provide significant distortion. However, a worst case design can neglect the induced eddy current impacts and assume that all of the flux traversing a low to high permeability region will approach the interface perfectly normal. In reality there will be some small angle contribution to the tangential and some small reduction in the normal to cause a real implementation that is less lossy than the estimate.

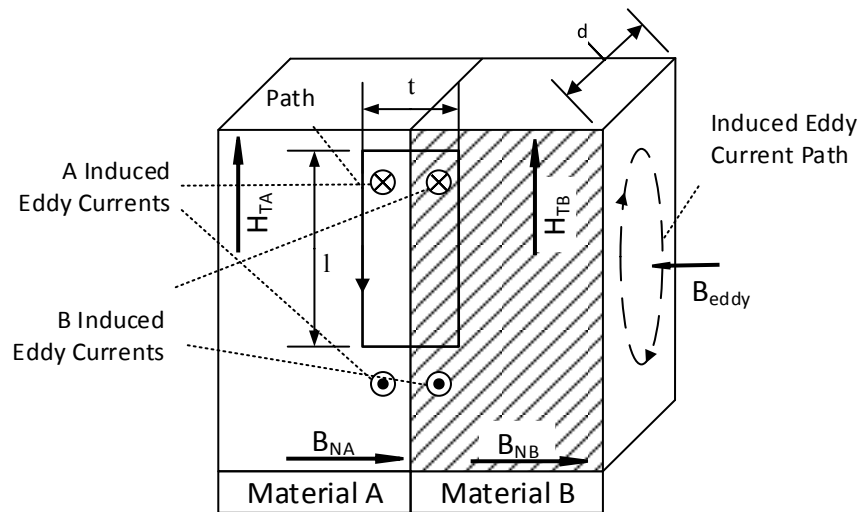


Figure 4.4: Induced Eddy Current Impact on Tangential and Normal Flux At Interface.

$$(4.8) \phi_{TA} = \frac{\mu_{rA}}{\mu_{rB}} \phi_{TB} - \mu_0^2 \mu_{rB} \text{Depth} I_{eddy}$$

$$(4.9) B_{NA} = B_{NB} - B_{eddy} = B_{NB} - \frac{\mu_0 \mu_{rB} I_{eddy}}{t_{lam}}$$

### 4.3.2 Permeance for Gap Fringing

With the assumption that the flux enters a magnetic core from air normal, it is possible to derive the flux paths near core gaps. This permeance can be included in a magnetic circuit using Hopkinson's law to determine the leakage flux. The inclusion of these paths into the magnetic equivalent circuit enables direct prediction of fringing flux. The permeance path can be determined by investigating two methods of determining the energy in a coil. The permeance of the leakage path is  $P$ . First, coil energy as a function of coil current,  $I$ , and turns,  $N$ , is shown in (4.10). Then, using (4.11), the stored energy is described as a volume integral function of the magnetic field,  $H$  [95]. Using these equations and geometric parameters, as shown in Figure 4.5, The various fringing permeance paths can be determined and are shown in (4.12) for the outside path, (4.13) for the inside path, and (4.14) for the two paths that enter the core front and back face.

$$(4.10) \quad E = \frac{1}{2}PN^2I^2$$

$$(4.11) \quad E = \frac{1}{2}\mu_0\int H^2dV$$

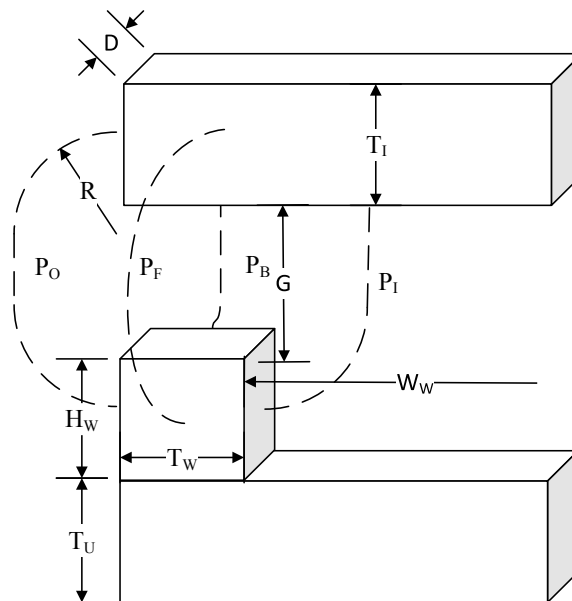


Figure 4.5: Fringing Permeance Paths for Half of a UI Core Geometry.

$$(4.12) \quad P_O = D \frac{\mu_0}{\pi} \ln \left( 1 + \frac{\pi}{G} w \right) \Big|_{w=\min(T_I, H_w + T_U)}$$

$$(4.13) \quad P_I = 2D \frac{\mu_0}{\pi} \ln \left( 1 + \frac{1}{2} \frac{\pi}{G} w \right) \Big|_{w=\min(T_I, \frac{W_w}{2})}$$

$$(4.14) \quad P_F = P_B = T_w \frac{\mu_0}{\pi} \ln \left( 1 + \frac{\pi}{G} w \right) \Big|_{w=\min(T_I, H_w + T_U)}$$

### 4.3.3 Permeance for Leakage Flux

While there are many published models for determining the leakage inductance, e.g. [95], [96], [97], the method demonstrated in [98] is convenient for identifying and isolating different sub paths of the total leakage flux path. This method analyzes the total device flux by assembling constitutive geometries to interface with the core material and encompass an excitation coil. These geometries have a defined magnetic permeance that accounts for the magnetic permeance in the region. In order to determine which geometries are relevant, a Comsol FEA model of the test core is developed. Modelling anisotropic cores at medium frequencies and with eddy currents is a nontrivial task. [99] compares homogenization techniques to account for anisotropic conductivity. It should also be noted that the vertical and horizontal core blocks have different tensors. The rounded corners also a unique tensor and they reference a cylindrical coordinate system. Comsol componentizes this coordinate system into Cartesian coordinates. However, the overall core anisotropy is easily verified with analysis of magnetizing flux. Despite these advances, it is particularly challenging to develop FEA models that properly define all relevant physics for high power medium frequency magnetics. Therefore, these models were used as qualitatively to identify behavior and performance trends. They are not to be relied on for exact calculation but the models still provide significant insight.

Three of the most common transformer winding configurations were explored in FEA. These windings are adjacent, Figure 4.6, abutting, Figure 4.7, and concentric, Figure 4.8. There

are other winding configurations possible such as interleaved, shell or axial but these will be left to future work. The advantage of the chosen three designs is their ease of manufacturing and their relatively low parasitic capacitance. This makes them well suited for use in high power medium frequency applications. Due to the aforementioned difficulties in modelling, levels of various parameters were normalized to highlight relative magnitudes and hot spots.

The surface of the cores in the FEA results is colored to show the magnitude of normal flux on the surface. An anisotropic permeability tensor was used to model a core permeability in the ribbon directions and ribbon, air stack in the normal direction. Contour lines on the core show the induced current density. Here, a diagonal conductivity tensor was used to model material conductivity on the ribbon and no conductivity between ribbons. Finally, the colored streamlines show the paths of leakage flux in air. The thickness of the lines corresponds to the relative magnitude of the leakage flux density. The colors of these streamlines is chosen to highlight where on the core physically the described leakage inductance enters the core. The red streamlines intersect the outside broad ribbon surface while magenta intersects the inside, window, broad ribbon surface. Orange lines show the relatively low loss flux streams that enter the face of the core. These paths are low loss because the available eddy current path is constrained by the thinness, several micrometers, of the magnetic ribbon.

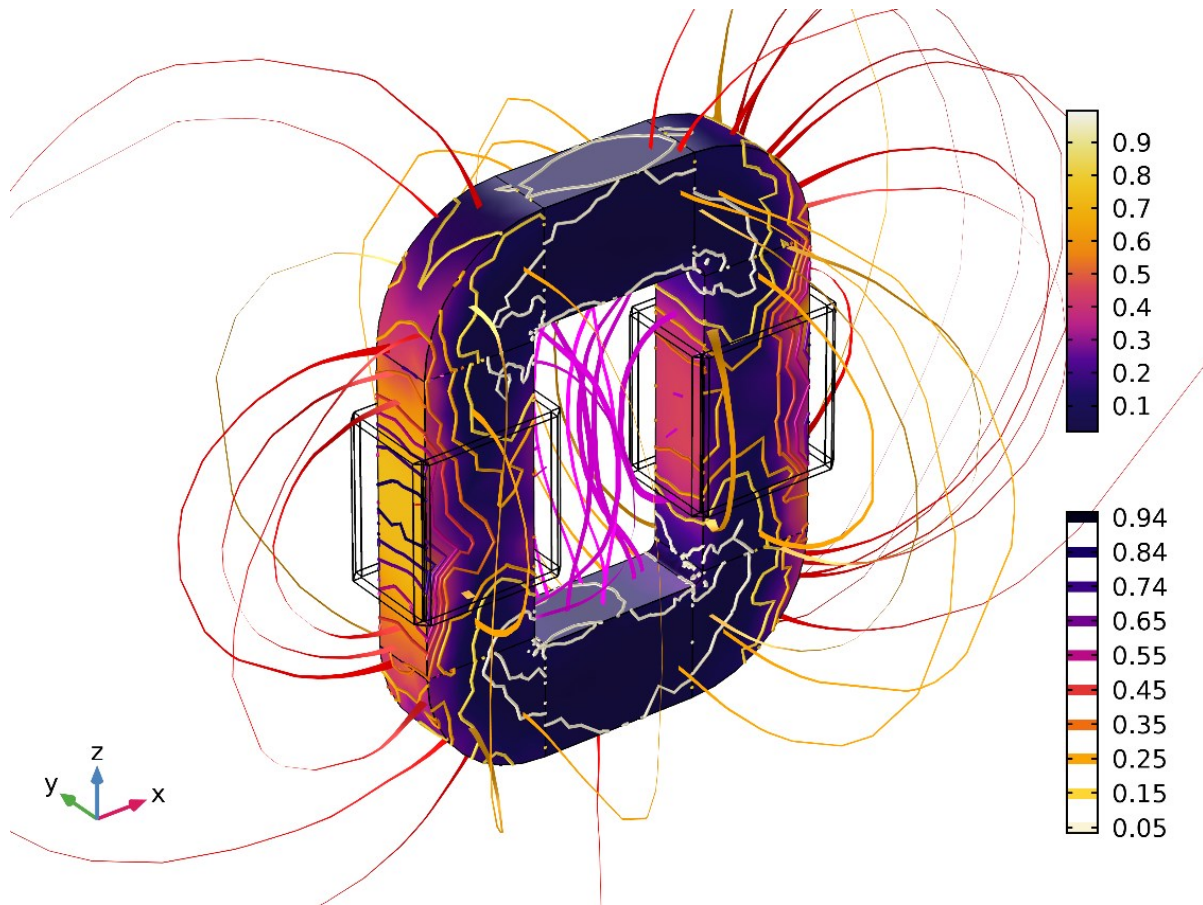


Figure 4.6: *Adjacent Winding Configuration Leakage FEA.*  
 Surface =  $|B|_{\hat{n}}$  Normalized; Contour =  $|J_i|$ ; Streamers Leakage Flux: Red = Outside, Magenta = Inside,  
 Orange = Face.

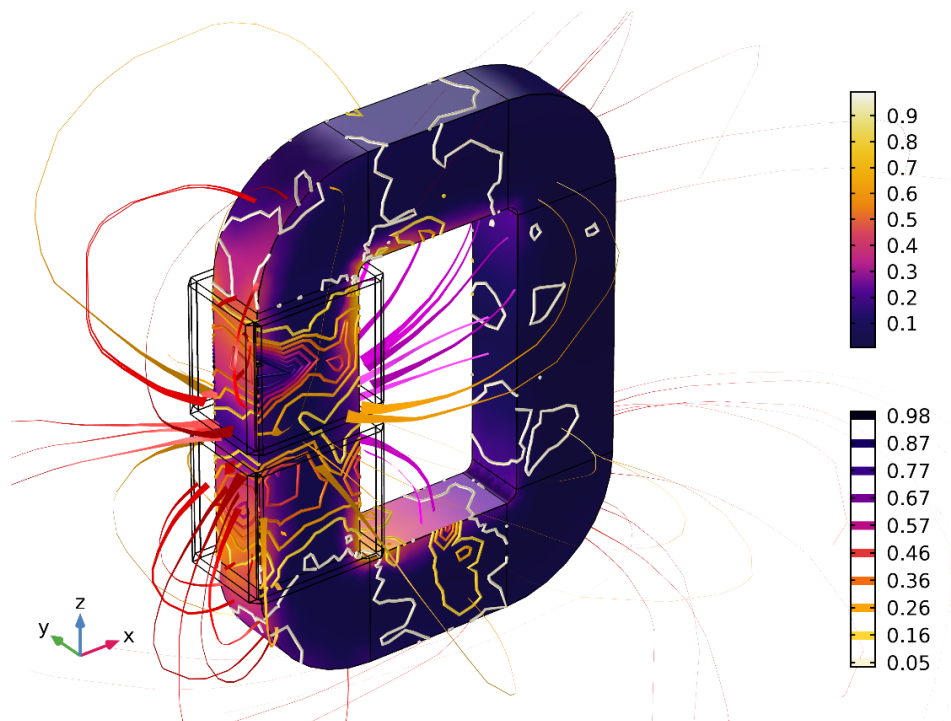


Figure 4.7: *Abutting Winding Configuration Leakage FEA.*  
 Surface =  $|B|_{\hat{n}}$  Normalized; Contour =  $|J_i|$ ; Streamers Leakage Flux: Red = Outside, Magenta = Inside,  
 Orange = Face.

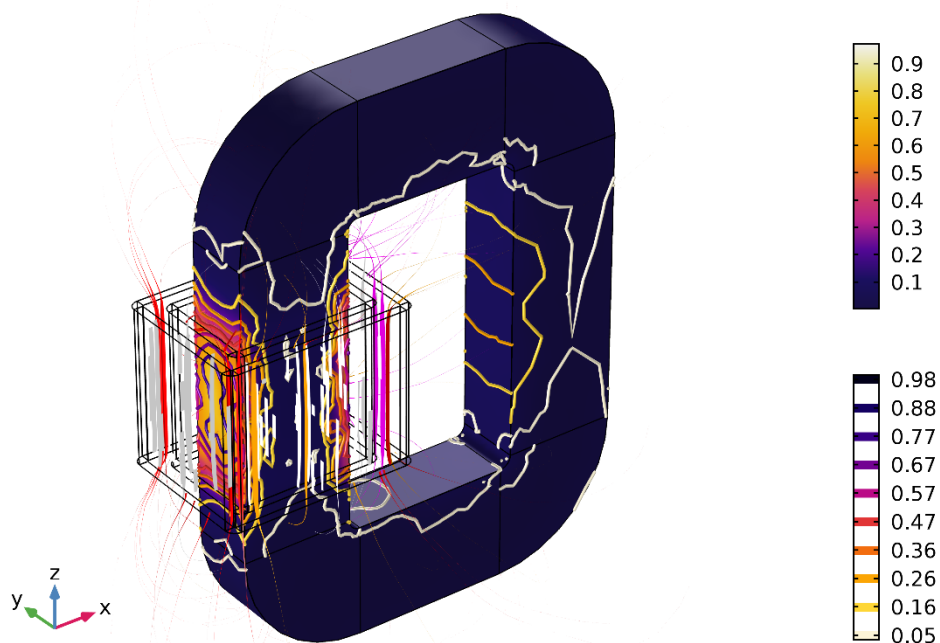
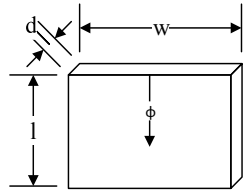
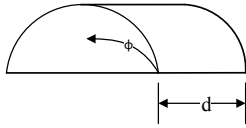
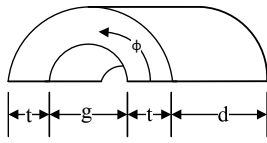
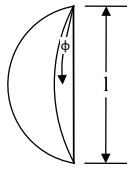
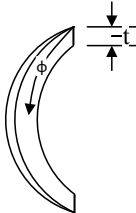


Figure 4.8: *Concentric Winding Configuration Leakage FEA.*  
 Surface =  $|B|_{\hat{n}}$  Normalized; Contour =  $|J_i|$ ; Streamers Leakage Flux: Red = Outside, Magenta = Inside,  
 Orange = Face.

It is clear from the above FEA figures that there are five primary stray flux paths. These paths are boxes, half cylinder slices, half annuli, spherical slices and quarter rounds. Using FEA to identify the paths increases the certainty of the 'Probable Flux Paths' demonstrated in [98]. The different flux paths will be grouped based on where they enter the core, corresponding to the above flux path colors. This will be useful when accounting for losses as the different groups of paths enter into different parts of the core with different geometries and different loss coefficients. The general permeance,  $\hat{P}$ , equations for the five paths are shown below in equations (4.15) to (4.19) in Table 4.1. These equations are taken by determining a probable flux regions volume and mean path. Thus the geometric term of permeance, area by length is the same as volume by length squared. A practical example of this partitioning and leakage flux calculation is shown below using the adjacent winding transformer.

Table 4.1: Permeance Equations for Constitutive Geometries.

Shape	Connection Rule	Permeance	General Shape
Box	Surface - Surface	(4.15) $\hat{P}_B = \frac{\mu d w}{l}$	
Half Cylinder Slices	Edge - Edge	(4.16) $\hat{P}_C = \frac{\mu \pi d}{8 * 1.22^2}$	
Half Annulus	Surface - Surface	(4.17) $\hat{P}_N = \frac{\mu d}{\pi} \ln \left( 1 + \frac{2t}{g} \right)$	
Spherical (45° Sector)	Edge	(4.18) $\hat{P}_Q = \frac{\mu \pi l}{48 * 1.3^2}$	
Spherical Shell (45° Sector)	Edge - Edge	(4.19) $\hat{P}_S = \frac{\mu t}{8}$	

Using the above permeance equations enables two necessary steps in estimating the losses associated with the stray fields. First, the geometries can be used to decompose the paths of the stray flux around an exciting coil. Then, by observing where the constituent paths intersect with the core, the degree to which the path causes losses can be determined. This is done by determining if the path intersects the broad surface of the magnetic ribbon, a high loss path, or the stack of magnetic ribbon edges, negligible to low losses. Other paths that do not intersect with the core, e.g. between to concentric windings, do not cause any induced eddy current losses. An example of this path counting for simple geometries, Table 4.2, is shown below in Table 4.3.

Table 4.2: Common Ribbon Core Assemblies.

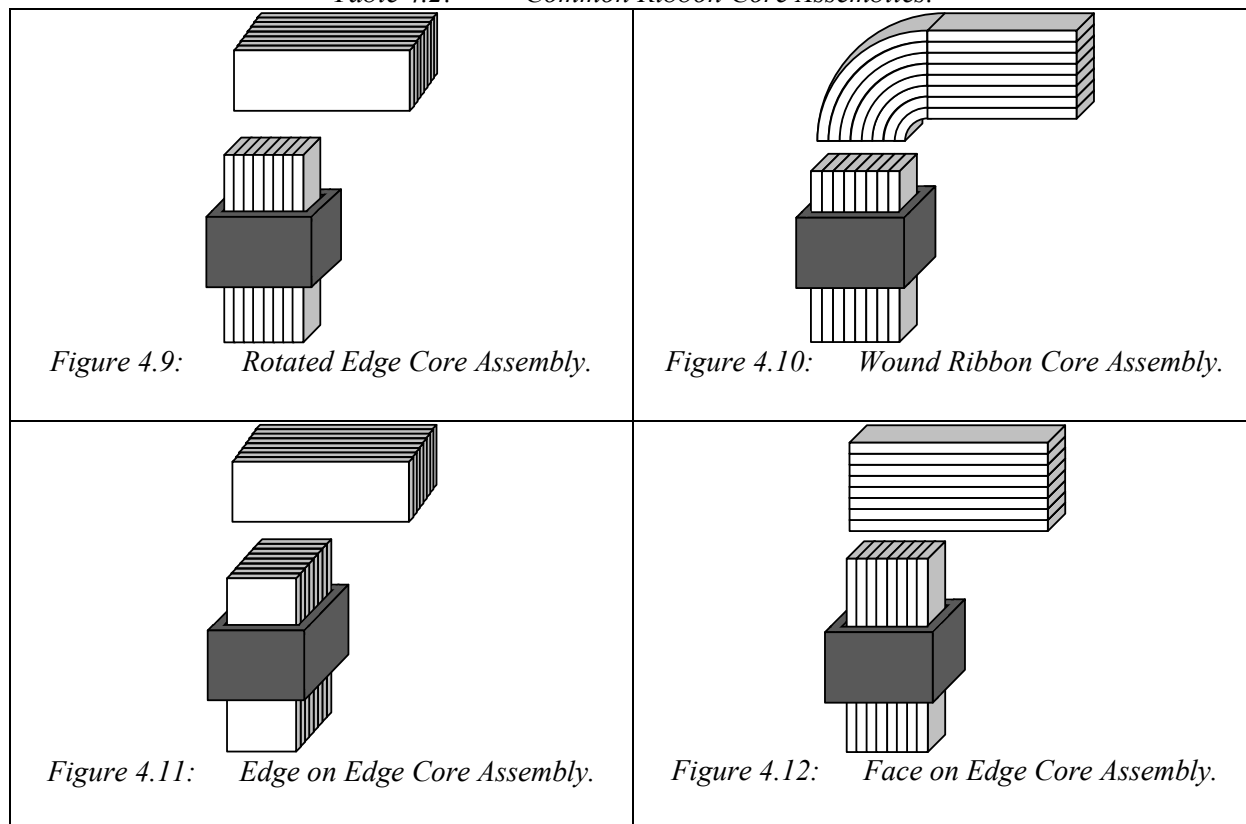


Table 4.2 shows a winding bundle in dark gray relative magnetic ribbon layers assembled in a core. It also shows different orientations available if an air gap is desired. It is important to note that while the geometry of Figure 4.12 is physically possible, it should be avoided. As can be seen in Table 4.3, the magnetizing flux crosses a broad surface of the core ribbon. This will induce significant eddy currents at the junction and result in excessive losses. Table 4.3 shows which magnetizing, leakage, and fringing, if a gap is used, paths that enter into the broad surface of the core ribbon. The ribbon edge surfaces are not counted as the induced eddy current loss will be negligible because the available eddy current path is very small.

Table 4.3: *Number of Broad Surfaces Normal Flux Encounters for Various Core Connections and Flux Path Region.*

Core Connection	Magnetizing Flux	Window Leakage	Outer Leakage	Page Leakage	Inner Fringing	Outer Fringing	Page Fringing
Rotated	0	2	2	0	1	2	1
Wound	0	4	2	0	2	2	0
Edge on Edge	0	0	0	2	0	0	2
Face on Edge	1	4	2	0	2	1	0

#### 4.4 Modelling Leakage Flux and Losses

The first step in the design process is to determine the different leakage flux paths. A simplified geometry of a practical core assembled of wound ribbon, Figure 4.10, without any gaps is shown below in Figure 4.13. Symmetric dimensions are left unlabeled. This geometry simplifies some of the discrepancies in core curvature and dimensional mismatches due to construction. Figure 4.14 shows the breakdown of permeance paths. This is done using the geometries of Table 4.1. These paths are assembled to complete leakage flux torus around the excitation coils. The paths are color-coded based on the rules of Table 4.2 and Table 4.3. Paths that are red and magenta are high loss and intersect the outside and the inside of the core respectively. The paths that intersect the thin ribbon face of the core are color coded with orange and provide a minimal contribution of induced eddy current losses. For the sake of simplicity these losses will be neglected. Another point of interest is the corners of the core. While one may reasonable assume that these paths do not enter the core at all or at most enter a negligibly small corner of the core, this is not the case. As shown by the flux streamers Figure 4.6, the flux ‘bends in plane’ around to enter core material in the normal vector. This again agrees with Figure 4.2 given that the corner of a core is not an easy path for flux to enter. Now that the leakage flux paths have been determined and componentized, the next step is to develop a new magnetic equivalent circuit to further understand how the flux path contributes to leakage flux induced eddy current losses.

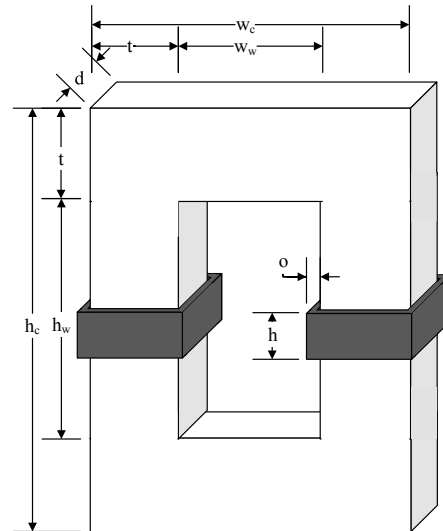


Figure 4.13: *Simplified Geometry for Adjacent Winding Transformer.*

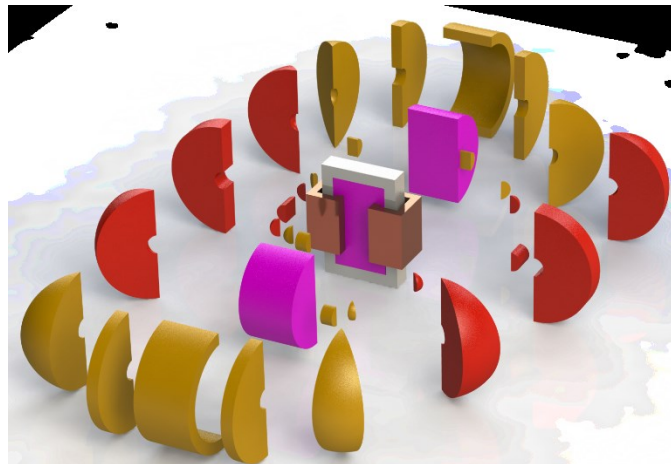


Figure 4.14: *Flux Path Segmentation of Adjacent Winding Transformer.*

Development of the magnetic equivalent circuit requires some assumptions and a nuanced understanding of the likely paths of flux. In general, the total permeance of a path is the series combination of the air permeance and a core permeance. A first assumption is that the permeances of the three segmented paths does not share the same core path nor influences the flux of the others. The inner and outer leakage paths do not share any core material with each other. However, the face path shares core material with both inside and outside. This is neglected as the face path has significantly more core region to use in between the regions used by the inside and outside paths. Similarly, it is assumed that none of the leakage flux passing through

core material exceeds a flux density that would cause saturation. This may not be the case for the outermost ribbon layers due to their thin cross sectional area. However, if the ribbon layer saturates, another is nearby to take the remaining flux. There are many other flux paths but their permeance is either very high or very low and can be simplified as open or short circuit paths.

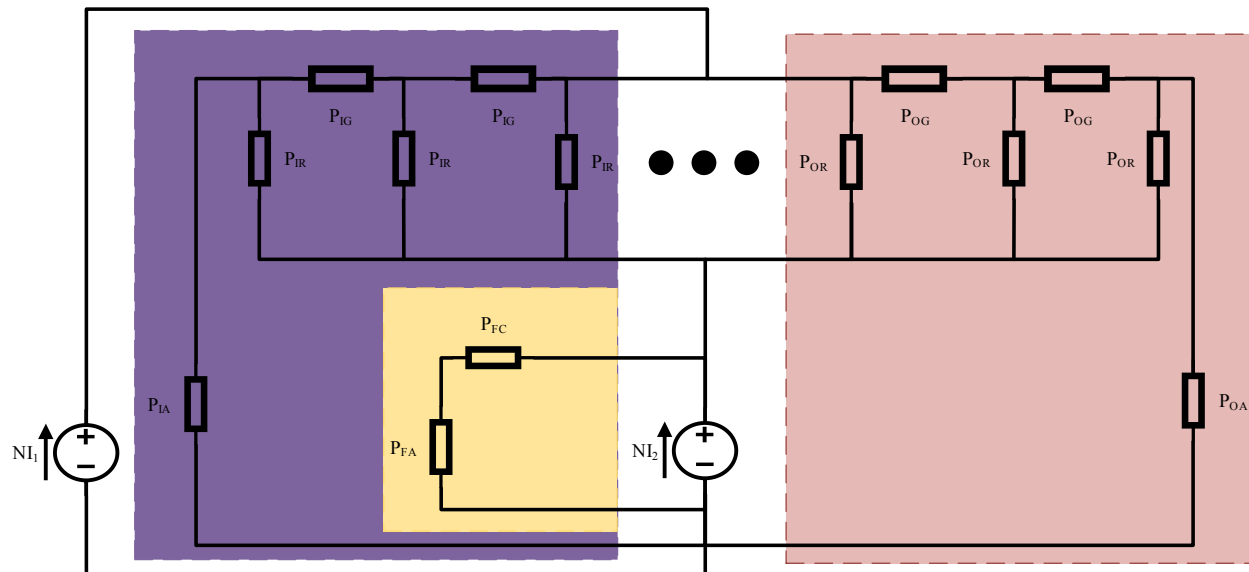


Figure 4.15: Magnetic Equivalent Circuit Considering Componentized Leakage Paths.

The simplest flux path to define is the face path. This path consists of two permeances, the permeance through air and a much lower permeance through the core. The total permeance is shown below in (4.20). The outside and inside permeance paths also include an air and core combination. However, the flux enters the broad surface of the ribbon. Due to the nature of the geometry there is a high permeability path to return to the coil but it has a very thin cross sectional area. This means that as flux enters the first ribbon layer, some will return to core. However, a significant amount of flux will pass through the gap between layers to the next layer. This results in a latter permeance network where shunt permeances are the ribbon layers represented by  $R_R$  and the space between layers is a series permeance  $R_G$ . The ratio between core ribbons and total core area is the fill factor,  $F$ . The core has a mean magnetic path of  $l_e$  and

effective cross sectional area of  $a_e$ . The ribbon has a thickness of  $t_R$ . It is also assumed that the permeance path includes 1/3 of the winding height.

$$(4.20) \quad \hat{P}_{Face} = \hat{P}_{FA} + \hat{P}_{FC} = 2 \left( \hat{P}_N + 2(\hat{P}_{N2} + \hat{P}_C + \hat{P}_S + \hat{P}_Q) \right) \parallel \hat{P}_{FC} =$$

$$2 \left( \frac{\mu_0 w_w}{\pi} \ln \left( 1 + \frac{t}{h_w} \right) + 2 \left( \frac{\mu_0 t}{\pi} \ln \left( 1 + \frac{3h_c - h}{2h} \right) + \frac{\mu_0 \pi t}{8 * 1.22^2} + \frac{\mu_0 (3h_c - h)}{48} + \frac{\mu_0 \pi w_h}{192 * 1.3^2} \right) \right) \parallel \frac{l_e}{\mu_r \mu_o a_e}$$

The outer and inner flux paths can be derived similarly. The inner flux path is shown below in (4.21) with  $\hat{P}_{LIC}$  being the effective permeance of the latter network. It should also be noted it is assumed that a half cylinder on either side of the window is a flux path where the flux bends to enter the surface inside the window. Where  $\hat{P}_{IG}$  and  $\hat{P}_{IR}$  are described in (4.22) and (4.23) respectively. The outer flux path is shown in (4.24) with  $\hat{P}_{IG}$  and  $\hat{P}_{IR}$  in (4.25) and (4.26).

$$(4.21) \quad \hat{P}_I = \hat{P}_{IA} + \hat{P}_{LIC} = (\hat{P}_B + 2\hat{P}_C) \parallel \hat{P}_{LIC} = \left( \frac{\mu_0 w_w d}{h_w} + \frac{2\mu\pi d}{8*1.22^2} \right) \parallel \frac{\hat{P}_{IR} + \sqrt{\hat{P}_{IR}^2 + 4\hat{P}_{IR}\hat{P}_{IG}}}{2}$$

$$(4.22) \quad \hat{P}_{IG} = \frac{\mu_0 2(h_w + w_w)d}{\left(\frac{1}{F} - 1\right)t_R}$$

$$(4.23) \quad \hat{P}_{IR} = \frac{\mu_r \mu_o t_R d}{2(h_w + w_w)}$$

$$(4.24) \quad \hat{P}_O = \hat{P}_{OA} + \hat{P}_{LOC} = 2 \left( \hat{P}_N + \hat{P}_C + 2(\hat{P}_S + \hat{P}_Q) \right) \parallel \hat{P}_{LOC} =$$

$$2 \left( \frac{\mu_0 t}{\pi} \ln \left( 1 + \frac{3h_c - h}{2h} \right) + \frac{\mu_0 \pi t}{8 * 1.22^2} + 2 \left( \frac{\mu_0 (3h_c - h)}{48} + \frac{\mu\pi w_h}{192 * 1.3^2} \right) \right) \parallel \frac{\hat{P}_{OR} + \sqrt{\hat{P}_{OR}^2 + 4\hat{P}_{OR}\hat{P}_{OG}}}{2}$$

$$(4.25) \quad \hat{P}_{OG} = \frac{\mu_0 2(h_c + w_c)d}{\left(\frac{1}{F} - 1\right)t_R}$$

$$(4.26) \quad \hat{P}_{IR} = \frac{\mu_r \mu_o t_R d}{2(h_c + w_c)}$$

Using the above permeance equations it is now possible determine the proportion of total flux that is associated with each of the three primary paths for the adjacent winding, magnetic ribbon core. Similarly, the fundamental geometries can be used to assemble the permeance paths and examine the leakage flux division of the other three winding configurations presented in Figure 4.6, Figure 4.7, or Figure 4.8 or any other winding configuration. Exotic magnetics

geometries may need new constitutive shapes. However, the process of determining the shapes volume and dividing by the mean magnetic path to determine the effective cross sectional area enables limitless designs.

A comparison of the flux breakdown is shown in Figure 4.16. These charts tie together the simple geometry permeance models with the geometrically precise Comsol FEA models presented previously. This shows the efficacy of the approach and enables designers to identify the paths that could lead to issues. With these tools, it is easy to take targeted, corrective actions to limit the amount of flux that is on a path that would enter a broad surface of the ribbon.

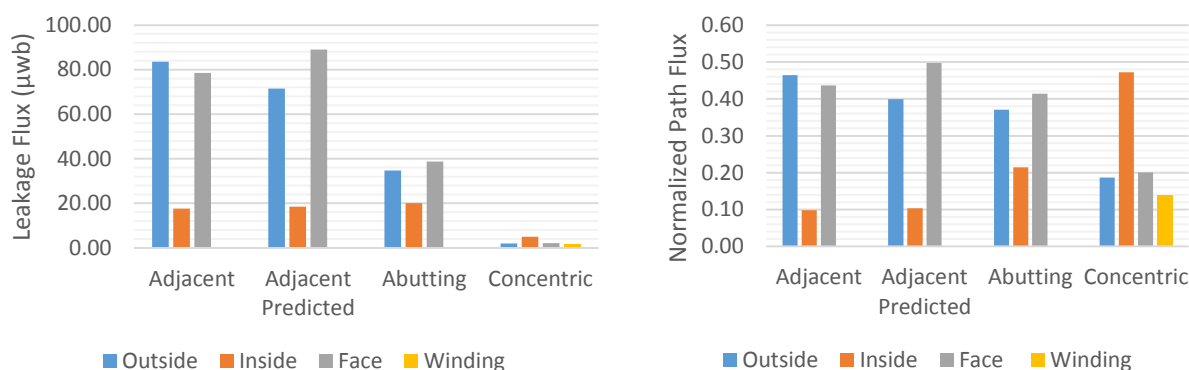


Figure 4.16: Magnitude (Left) and Path Proportion (Right) of Winding Configuration Dependent Total Surface Leakage Flux.

#### 4.5 Induced Eddy Currents in Ribbon

As shown above different physical regions of the magnetic core have different levels of leakage flux approaching the surfaces. It was also shown that for practical cores, all but a minute amount of flux enters the ribbon perfectly normal. It is then essential to determine the induced eddy currents and resulting power losses for each of these regions. Continuing with the adjacent winding core geometry, it is clear that there are six eddy current loops that could have significant losses. There are negligible loops on the front or back face of the core as the thin profile of the ribbons presents a high resistance path. The first two loops are the top and bottom surfaces of the

window. The other four loops are the top and bottom of both the left and right outside surfaces of the core. If the excitation coils are producing flux in the positive  $z$  direction, up, then the leakage flux exits from the top window surface and enters the bottom surface. It also exits from the top half of the two outer surfaces and returns by way of the bottom two outside surfaces. Due to symmetry, the six surfaces can be represented by two different eddy current resistances. The outer surfaces can be represented by  $R_{eo}$  and the inner surfaces by  $R_{ei}$ . This section will derive these impedances using the geometric dimensions shown in Figure 4.13. By definition, the eddy current resistance is (4.27), where  $\sigma_R$  is the conductivity of the magnetic ribbon that is used in the core. The eddy current path area,  $A_e$ , for both eddy current loops is shown in (4.28) where  $k$  is the percentage of ribbon width that is utilized by the induced eddy currents,  $d$  is the core depth, ribbon width, and  $t_R$  is the ribbon thickness. The induced eddy currents generate a magnetic flux in opposition to the leakage flux, (4.9). This opposing flux reduces the changing flux in the center of the ribbon and can result in minimal eddy currents in this region. As such, the eddy current path must be windowed from the total which is served by the  $k_w$  term. It has been found that  $4^{-1} \leq k_w \leq 3^{-1}$ . The eddy current length of the two path geometries is the two resistances diverge. It is important to note that while the flux entering the ribbon is shaded by the excitation coil, the induced eddy currents in the ribbon are not. It is then assumed that the eddy current loop length exists over the entirety of the top or bottom half surface. This assumption is verified in the Comsol FEA models as well. The outer and inner path lengths are shown in (4.29) and (4.30) respectively. Figure 4.17 illustrates the paths of the stray flux induced eddy currents in magnetic ribbons.

$$(4.27) \quad R_e = \frac{l_e}{\sigma_R A_e}$$

$$(4.28) \quad A_e = k_w d t_R$$

$$(4.29) \quad l_{eo} = h_c + 2d(1 - 2k_w)$$

$$(4.30) \quad l_{ei} = 2(w_w + h_w + d(1 - 2k_w))$$

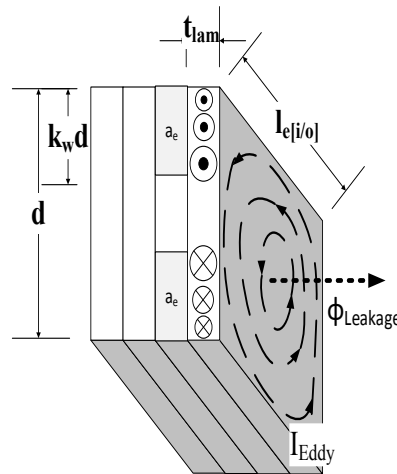


Figure 4.17: Eddy Current in Magnetic Ribbon Paths.

The voltage that is induced in a region by the stray flux into a surface is shown below in (4.31) where  $\phi_{lr}$  is the leakage flux for the inner and outer regions determined by the magnetic equivalent circuit defined previously. Thus the power loss caused by the induced eddy currents for a particular region is (4.33). For a triangular leakage flux of peak value  $\phi_{pk}$ , the total leakage induced losses are shown in (4.33). The variables  $\hat{P}_i$  and  $\hat{P}_o$  are the percentage of total leakage flux that enters region, e.g. Figure 4.16, and  $n_l$  is the number of layers of magnetic ribbon material that are involved in this loss mechanism. The number of layers involved has been experimentally determined to be between 1% and 2% of the total core thickness.

$$(4.31) \quad \epsilon_e = \frac{d\phi_{lr}}{dt}$$

$$(4.32) \quad P_{er} = \frac{\epsilon_e^2}{R_{er}}$$

$$(4.33) \quad P_{e-leakage} = n_l \delta \left( \frac{2\hat{P}_i^2}{R_{ei}} + \frac{4\hat{P}_o^2}{R_{eo}} \right) \phi_{pk}^2 f^2$$

#### 4.6 Modified Transformer Electrical Model

A more nuanced transformer equivalent circuit is now needed such that the presented concepts can be included. The definition of the leakage paths enables the total homogenized leakage inductance to be separated into several leakage inductances that correspond to a path.

The induced eddy current losses associated with these paths are then modelled as resistors in parallel with the path specific inductance. An example of this modelling is shown below in Figure 4.18. The different regions are again color coded for clarity and are consistent with other color coding in this chapter.

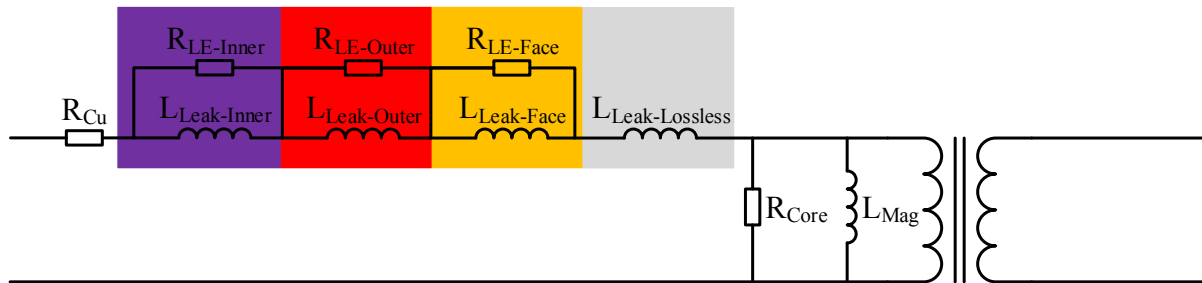


Figure 4.18: Modified Transformer Electrical Equivalent Circuit.

This new model can incorporate any configuration by weighting the inductances and resistances with the procedures presented. Continuing with the adjacent winding, wound ribbon example, the inner, outer and face zones would be used while the lossless inductor would be omitted as this geometry has no lossless paths e.g. between two concentric windings. One advantage of this new model is that the nuanced leakage model can include several new layers of specificity without impacting other aspects of the model. Similarly, the paths and regions that lead to the most losses can be easily identified as those with a high inductance and a low resistance. Once identified, the problematic zones and paths can be mitigated by solutions presented in the next section.

#### 4.7 Leakage Flux Control and Loss Mitigation

Careful magnetic design can be used to manage the leakage flux once the critical leakage paths are identified and the degree to which the total leakage flux is shared among the paths is determined. There are three primary principals that can be employed to manage and mitigate stray flux induced losses. The first is to limit the magnitude of eddy currents that are generated in

the core material by increasing the resistivity. Another principal is to limit the amount of normal flux that enters the material by reducing the ratio of permeability between the core material and air. The third, and focus of this section, is to limit the magnitude of leakage flux that enters any ribbons.

Increasing the resistivity of the core is fundamentally a materials problem. Ongoing research into core chemistries, processing continues to improve the resistivity of magnetic ribbons [100], [101]. However, these improvements are marginal and MANC magnetic ribbons still have relatively low electrical resistivity. One effective way of increasing the resistivity is by crushing the ribbon into a powder and forming a composite magnetic core of binding agents and the crushed material. However, this results in a significantly lower relative permeability because the fill factor of bulk core to crushed powder is very low as there is effectively a distributed air gap [102]. This makes powdered cores poor choices for transformer applications. Ferrites are another core material that is a viable candidate with high resistivity and a relatively high permeability. However, ferrites have a low saturation magnetic flux density and maximum operating temperature. This makes ferrite designs difficult in the high power medium frequency design space. Therefore, increasing the resistivity alone is not a viable solution and in most cases introduces new difficulties in the magnetic component design.

The second approach is to minimize the amount of flux that enters the ribbons normal. This can be achieved with a low permeability gradient as shown in Figure 4.2. All of the leakage flux must complete a loop around the excitation coil. As the flux approaches a low relative permeability core layer, it can enter the core layer at an angle. By entering the core at an angle, only a limited amount of the flux contributes to induced eddy currents. Some of the flux is able to use this low, but higher than air, permeance ribbon to return to the coil. This has the potential

for significantly lowering induced eddy current losses. Conceivably, a necessarily large region could have a gradient of permeability that enables enough flux to return to the coil before it reaches higher permeability material [7]. However, if magnetic ribbons are used, this gradient is impossible as between each layer of ribbon there is an air layer. Thus, regardless of the layer to layer ratio of permeability, there will be a high ratio of permeability between a ribbon and air. A gapless material with graded permeability or a large section of all low permeability layers could be sufficient. An example of this is shown below in Figure 4.19. The layer to layer permeability ratio is only 8. However, the layer to air ratio is  $n8$  where  $n$  is the layer index from the outside layer. The initial layer allows some angled flux but this flux turns normal as soon as it reaches higher boundary ratio layers. Furthermore, the low perm layers are not sufficient to return the leakage flux to the coil and thus the flux penetrates to much higher permeability ratio ribbon layers.

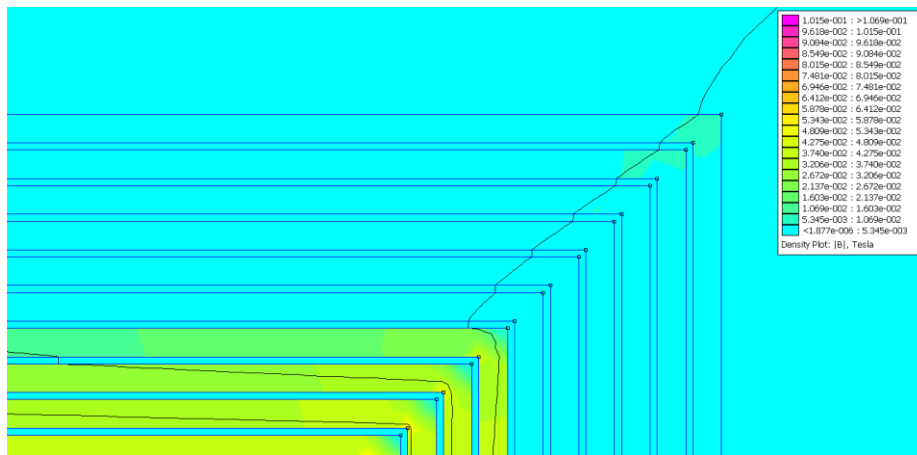


Figure 4.19: Graded Permeability Based Normal Leakage Flux Reduction.

Alternatively, a highly conductive layer e.g. copper can be used to shield the leakage flux. Rather than minimizing eddy currents, this maximizes the eddy currents such that an opposing flux prevents the leakage flux from passing through, Figure 4.20. Losses are reduced proportionally with very low resistivity with the penalty of higher a  $I_{eddy}^2$ . This approach can

result in lower losses with careful design but the loss reduction is minimal. Importantly, the leakage inductance is significantly reduced because the leakage path must make the entire loop in air instead of partially through the core. This minimizes the practicality of this approach as the leakage inductance is often a necessary design limit.

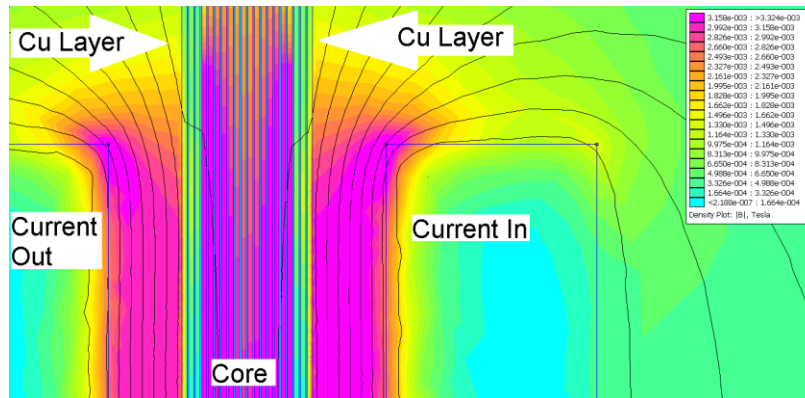


Figure 4.20: High Conductivity Based Normal Leakage Flux Reduction.

A third way to minimize the losses associated with leakage flux induced eddy currents is to minimize the amount flux that enters magnetic ribbons while keeping it in a high resistivity material. This approach is similar to efforts used in [92] where shielding limits stray flux related losses in the transformer metal housing. Other shield like approaches include [103] and Minimizing the flux entering the ribbon can be achieved by introducing two new permeances to the magnetic equivalent circuit as part of a flux shield component. The first, is a high permeance path that allows flux to return to the excitation coil directly from a leakage path. The second permeance should be low and in series between the magnetic ribbons and the leakage path. This combination of permeances is shown below in Figure 4.21 as a single shield component. The higher permeance path,  $P_T$ , is tangential to the axis of excitation and the low permeance path,  $P_N$ , is normal to the core and axis of excitation. It should be noted that the normal flux can be further reduced by having a space between the shield and the ribbon core. This space is represented by  $P_O$  and can simply be an air space. Given that the shield must handle both tangential and normal

flux, it is recommended to use an isotropic material. Ferrite is an ideal material in that it is both isotropic and it has a high resistivity. This allows the leakage flux to return to the excitation coil, without entering the magnetic ribbon cores, in a high resistivity region. If we assume that the magnetic core offers an infinite permeance path, the reduction in leakage flux that enters the core is presented in (4.34).

$$(4.34) \quad \phi_{red} = 100 \left( 1 - \frac{P_{ST}(P_{SN}+P_O)}{P_{SN}P_O+P_{ST}(P_{SN}+P_O)} \right)$$

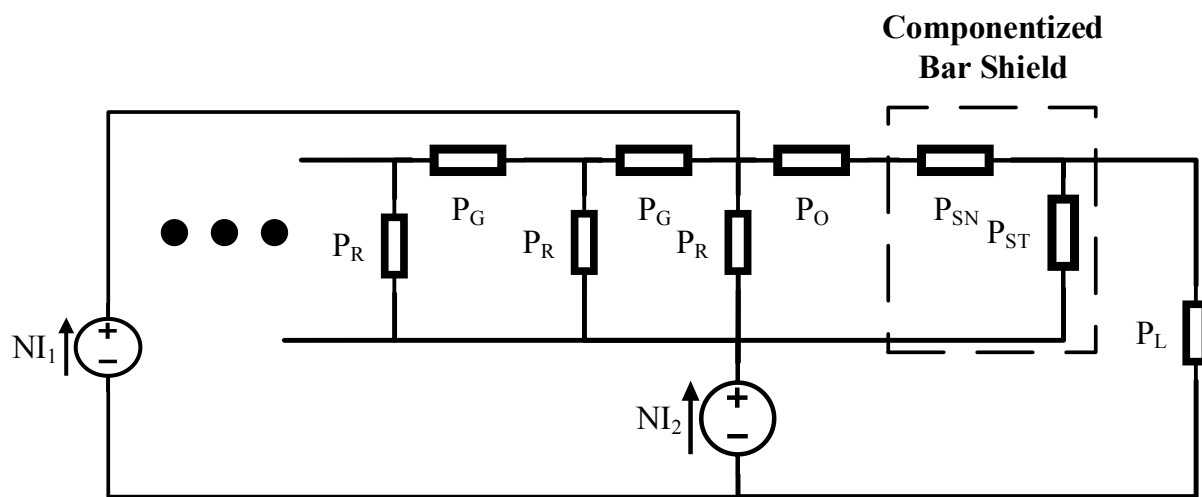


Figure 4.21: Permeance Paths with Leakage Flux Bar Shield.

The first approach available to designing the leakage flux shield introduces minimal change to the overall leakage inductance. This is achieved by using a bar geometry shield. The permeance paths through air remain mostly unchanged. There is the potential for a slight increase in leakage inductance as the bar can shorten the air path, increase the permeance, of the flux at curved corners. A design recommendation is to cover as much of the height of the core as possible. The space between the ribbon core and the shield material should be maximized within volume constraints. Thus the two permeances of the shield and the offset permeance are shown below in (4.35), (4.36), and (4.37).

$$(4.35) \quad \hat{P}_{SN} = \frac{\mu_r \mu_0 h_{sh} d_{sh}}{w_{sh}}$$

$$(4.36) \quad \hat{P}_{ST} = \frac{\mu_r \mu_0 w_{sh} d_{sh}}{h_{sh}}$$

$$(4.37) \quad \hat{P}_O = \frac{\mu_0 h_{sh} d_{sh}}{l_o}$$

The depth of the shield,  $d_{sh}$ , should be at least as deep as the core depth,  $d$ . Small variations are ok but qualitatively larger  $d_{sh}$  is better. Similarly, the height of the shield,  $h_{sh}$  should be as tall as the core height,  $h_c$ . If the shield is placed in the inside window, it should cover as much of the side surfaces as possible,  $h_w$ . The shield width is flexible and must only be great enough to ensure that the shield does not saturate. Dimensional tuning will aid in shielding performance by decreasing  $\hat{P}_{SN}$  and  $\hat{P}_O$ , and increasing  $\hat{P}_{ST}$ .

An FEA model of the bar shield is shown below in Figure 4.22. The surface and contour lines show the normal flux density and induced eddy current density which is normalized to the unshielded case. The reduced peak values of the scales show reduced normal flux and consequently induced eddy currents due to the application of the shield. The nearly lossless flux that interface with the shield are shown with blue stream lines.

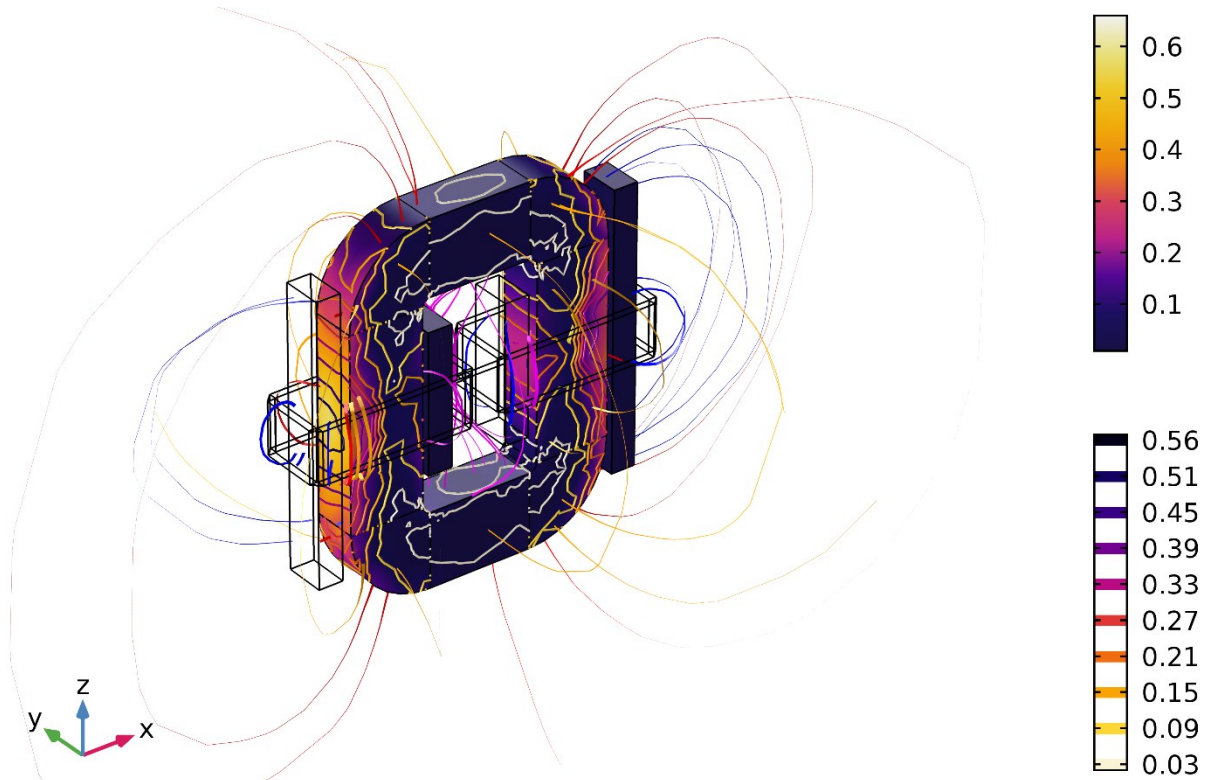


Figure 4.22: 3D FEA Model of Bar Shield.

If designers need to increase the leakage inductance or have geometrically independent control of the leakage inductance, a wing shield design can be used. This method of leakage flux shielding fundamentally changes the design process transformers. Now, the magnetizing inductance and leakage inductance are designed independently. This significantly expands the options and design choices of MANC core materials. Now, the design process will tend towards the following principles. Magnetizing cores should have high relative permeability to proportionally increase the magnetizing inductance. Similarly, the magnetizing core should be uncut to maintain the high permeability and limit layer misalignment induced losses where flux is forced to cross ribbon layers. This misalignment will result in eddy currents at the cut location even if no meaningful gap is present. The Shield cores should have a relatively large and specifically tuned gap or a tuned permeability. This limits magnetizing flux in the leakage core and enables greater range of leakage inductance values. If the leakage core is gapped, it should

have a high resistivity and preferably use an isotropic to accept several incident vectors of leakage flux without excessive induced eddy currents. An exciting new opportunity for strain annealed, [82], materials is a low perm leakage core without any air gaps or cutting. This contains the leakage flux entirely in the additional core and offers a very wide range of tunable leakage inductances.

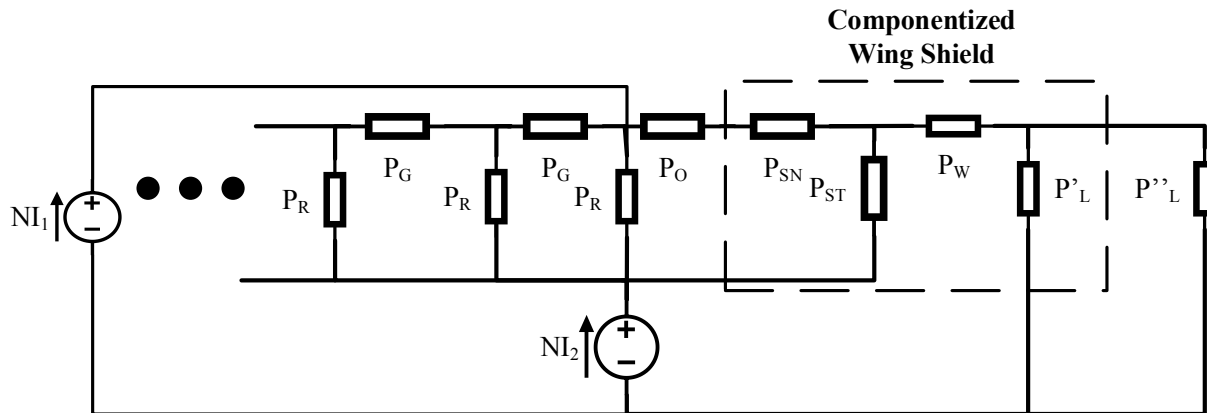


Figure 4.23: Permeance Paths with Leakage Flux Wing Shield.

Figure 4.23, the magnetic equivalent circuit, shows that the wing shield design principal is to again create a high permeance path that does not include the magnetic ribbon of the main core. However, now there are three new permeances that can be tuned for optimal performance. The first is,  $P_w$ , the permeance of the wings of the shield. As can be seen in, (4.38) the high relative permeability of the core easily creates a high permeance proportional to the cross sectional area of the wing,  $h_w d_w$ , and inversely proportional to the width of the wing,  $w_w$ . If the shield has a gap or does not encircle the excitation coil, there is a new air permeance, (4.39). This Permeance depends on the geometry of the wings and wing shield and is the sum of the constitutive geometry permeances,  $\hat{P}'_{CG}$ , that are incident with the shield. A third permeance,  $\hat{P}''_L$ , is also assembled of constitutive geometries and accounts for the air space around the

shield. This permeance should be very low as a good wing shield will take up much of the likely flux path space.

An FEA model of the wing shield is shown below in Figure 4.24. The surface and contour lines again show the normalized normal flux density and induced eddy current density. However, these values are normalized to the unshielded case. Therefore, it is clear that the shield reduces the peak values by the maximum values of the scale. The blue stream lines are flux paths that interface with the shield are effectively lossless paths.

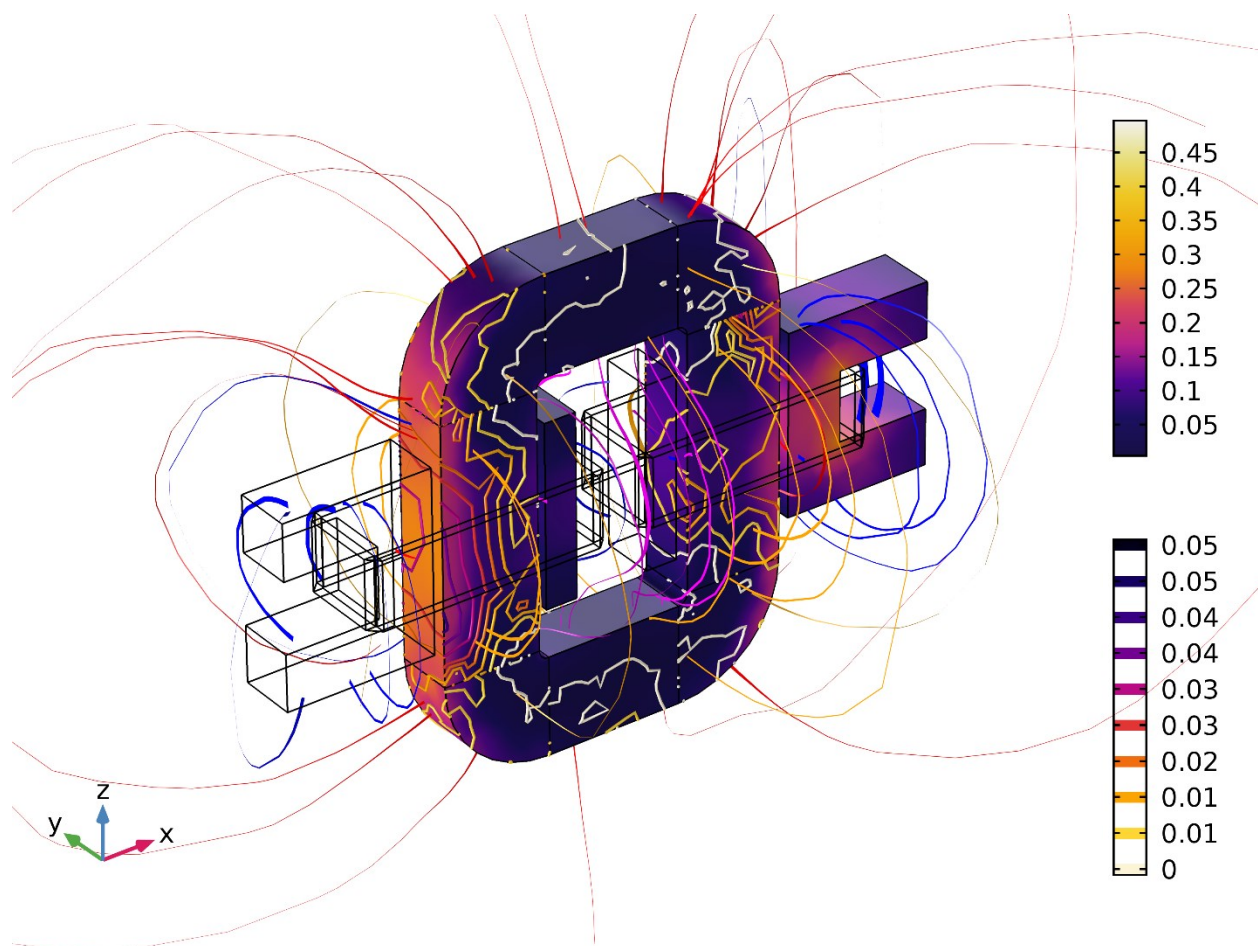


Figure 4.24: 3D FEA Model of Wing Shield.

If an uncut strain annealed shield material is used,  $\hat{P}'_L$  is the constituent geometries around the face of the shield core and  $\hat{P}''_L$  would be minimal. The independent design of magnetizing inductance and leakage inductance could be achieved by (4.41) and (4.42)

respectively where the magnetizing core has relative permeability of  $\mu_r$  and the strain annealed core has a relative permeability of  $\mu_{SA}$  and  $\mu_r \gg \mu_{SA}$ .

$$(4.38) \hat{P}_W = \frac{\mu_r \mu_0 h_w d_w}{w_w}$$

$$(4.39) \hat{P}'_L = \Sigma \hat{P}'_{CG}$$

$$(4.40) \hat{P}''_L = \Sigma \hat{P}''_{CG}$$

$$(4.41) L_{mag} = N^2 \hat{P}_{core} \propto \mu_r$$

$$(4.42) L_{leak} = N^2 \hat{P}_{SA} \propto \mu_{SA}$$

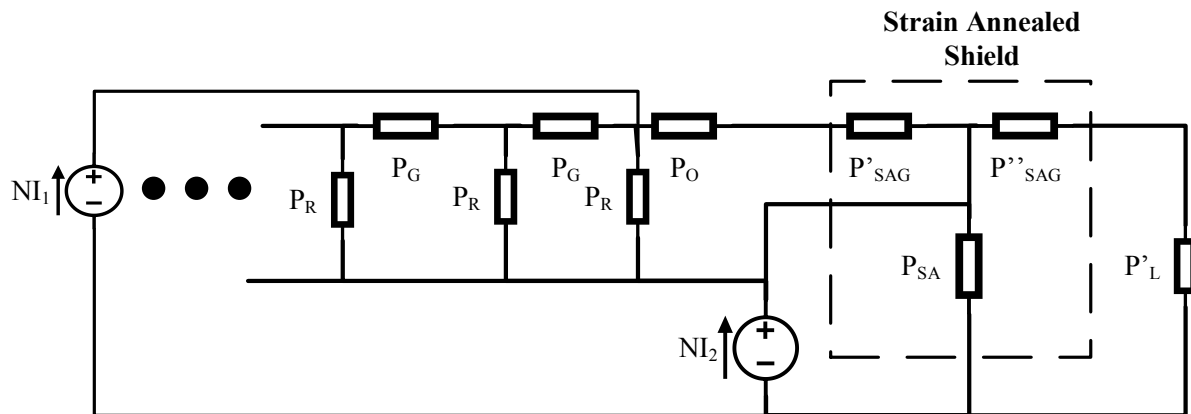


Figure 4.25: Magnetic Equivalent Circuit of Componentized Wing Shield.

This approach to integrated leakage inductance design is advantageous over [88]. This is because in all cases, the leakage flux flows along an easy axis. In [88], the flux was redirected within the ribbon leading to a hard axis flux flow. At this connection point, the low permeance joint causes behavior similar to that of an air gap leading to stray and fringing fields. Furthermore, this solution and derivation analytically determines where leakage flux is most problematic and proposes targeted solutions.

#### 4.8 Leakage Flux Shield Penalties

While the leakage induced eddy currents constitute a significant loss that is mitigated by shielding approaches, this solution is not without loss penalties. There is a small increase in the copper resistance due to the increased perimeter of the core and shield. This proportionally increases the excitation coil conduction losses. However, utilizing an uncut magnetizing core

with a high saturation flux density, like most magnetic ribbon materials, allows for a low number of necessary turns. This means that the unshielded design excitation resistance is minimal and the increase due to shielding will also be relatively small. With shielding materials there is also an increase in magnetization losses. These losses will also be low because of low levels of flux in the flux path. The flux density does increase in flux concentrating designs such as the wing shield but further research is needed to determine if this is also the case for the bar shield. Intuitively, the bar shield would result in negligibly higher magnetizing losses as the fundamental path of the leakage flux is not changed. The only difference is paths is traveling through magnetic ribbon core material or shield material. The flux concentrating effect would lead to higher magnetizing losses in the shield. However, these increases in losses are minimal compared to the reduction in leakage flux related losses.

#### **4.9 Experimental Results**

It is difficult to directly observe eddy currents and transformer localized losses. Rather, indirect methods such as thermal imaging allow observers to see the effect of localized losses. Due to the thermal anisotropy of the core, discussed further in the next chapter, thermal gradients can local hot spots can aid in identifying local losses. An example of this is shown below in Figure 4.26. The middle of Figure 4.26 shows the thermal profile of standard open secondary test used in core characterization as discussed in the previous chapter. As expected, the hottest part of the core is in innermost ribbon layers. This is due to the concentration of magnetizing flux in the high permeance path. The right of Figure 4.26 shows the thermal results of the same transformer when the secondary is shorted. This short circuit test forces the vast majority of the magnetic flux through the leakage paths of the transformer. In both cases the time and excitation current level were held constant. Figure 4.26 highlights the leakage flux induced eddy currents as

observed by heating of the outer most layers. Magnetizing flux is not present in these layers as the mean magnetic path reduces the permeance compared to the inner most layers.

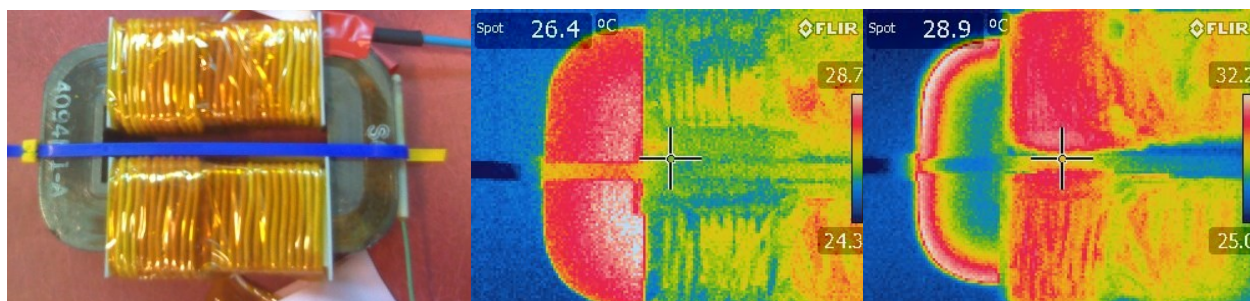


*Figure 4.26: Comparison of Magnetizing and Leakage Test Thermal Profiles. Typical Medium Frequency Transformer (Left), Magnetizing Test (Center), Leakage Test (Right).*

#### 4.9.1 Fiber Optic Thermal Mapping

A similar result using an advanced fiber optic line scan sensing technology is shown below. This sensor overcomes some of the limitations of thermal imaging of shiny metallic surfaces as the sensor does not rely on emissivity. Rather, the thermal energy causes distortions in the optical properties of the fiber optic cable which in turn change the backscattering profile of the sensing light. This can then be interpreted as changes in temperature from the ambient temperature. Another MANC magnetizing core was subjected to open and shorted secondary tests with a length of fiber optic cable woven around various locations on the core. Importantly, the cable wrapped around both the outside and inside layers of the core. Figure 4.27, left, shows the magnetizing result tests. Again, the inside layers of the core are hottest. Figure 4.27, right, shows the results of the short circuit test. Now the outside layers are the hottest. Again the losses associated with the leakage paths are isolated and confirmed.

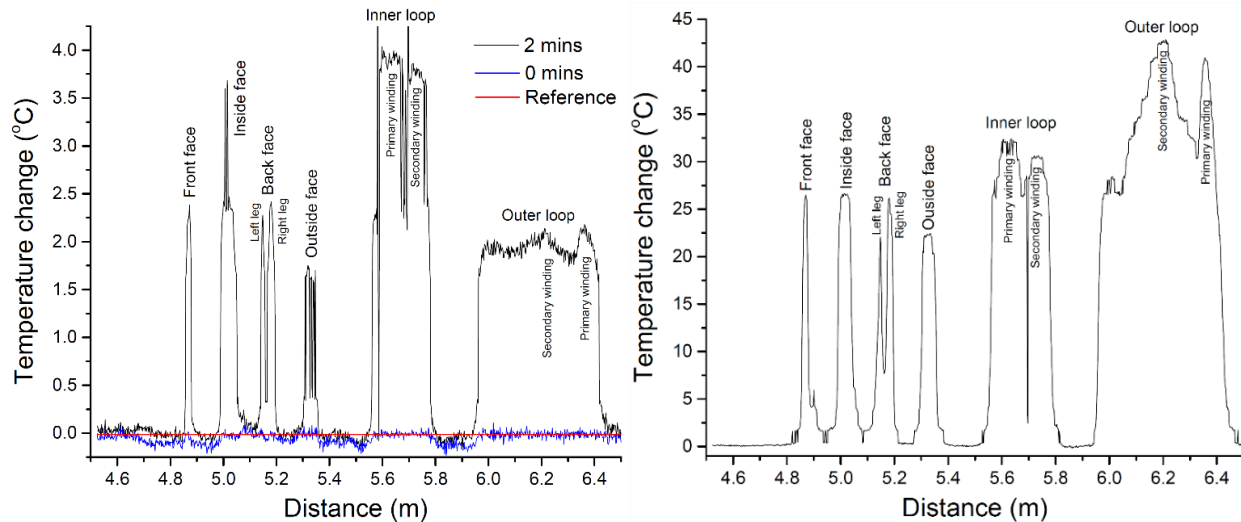


Figure 4.27: Optical Line Scan Measurement of Transformer Thermal Profile. Magnetizing Test (Left) and Leakage Test (Right).

#### 4.9.2 Three Dimensional Flux Mapping

As shown in the FEA models, the flux emanates from the excitation coil like a catenoid. This shape and the idea that all flux entering magnetic material from air enters normal to the magnetic material need to be observed. In order to do this, a three axis location meter was assembled. This involves fixing the location of the magnetic core and then measuring the two offset from this point to achieve a coordinate in the XY plane. The location in the Z dimension was determined using a height gauge. In order to enable measurements inside the window of the core, the sensor arm was adjustable on a single axis. A three dimensional leakage flux map, Figure 4.28, was developed using a three axis flux meter from GMW. In this test, the core was subjected to 0.1 T at 10 kHz in a short circuit test. Measurements were taken in the upper right octant of the transformer. In the figure below, two regions are clear. The first region, existing in the width between 0 and 20 mm, depth

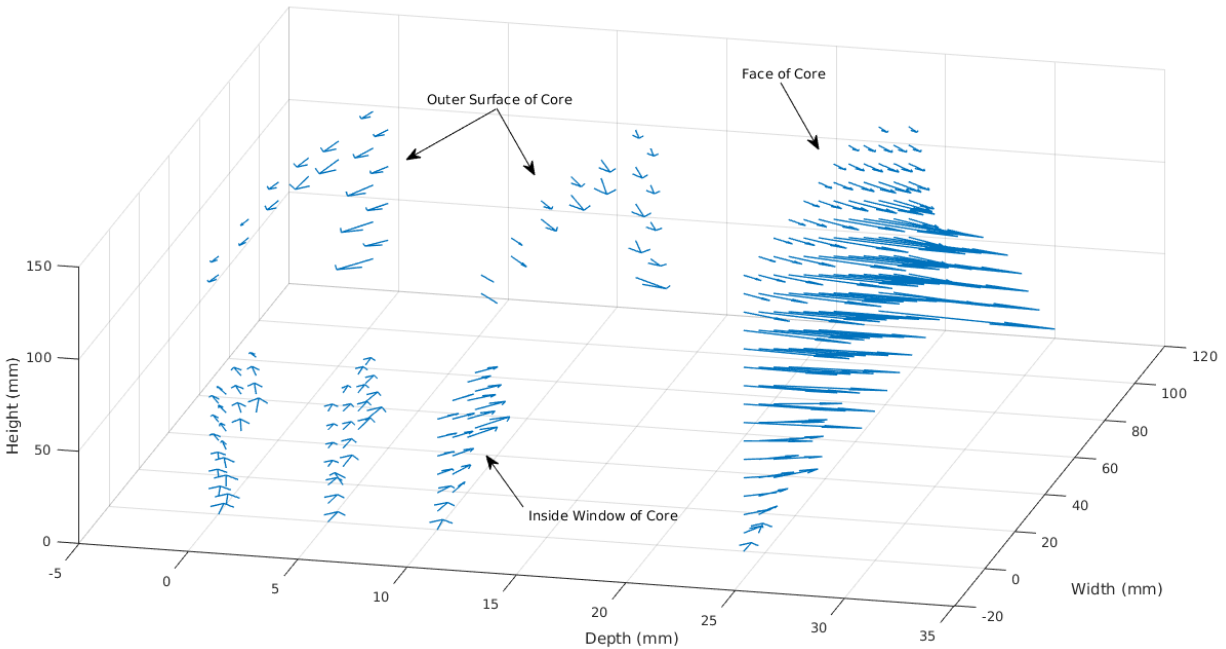
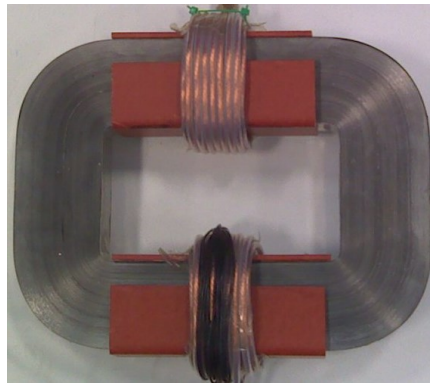


Figure 4.28: Measured Leakage Flux Field Around Transformer Upper Right Octant .

### 4.9.3 Adjacent Winding Case Study

An example case study will be presented with the model development and testing of a transformer design that could be used in a dual active bridge. For this example, the transformer is chosen to have a fundamental switching frequency of 10 kHz, a peak operating power of 10 kW and a peak operating voltage of 355 VDC. Some design aspects are deliberately chosen as non-optimal in order to highlight the leakage flux based losses and improve understanding. An off the shelf nanocrystalline Finemet FT-3TL core was chosen as the magnetic core with no additional manufacturing processes. The product code for the specific geometry is F1AH1171 and specific dimensions and values can easily be found in product literature. This analysis will use generic symbols as much as possible to improve the usability of this example. Figure 4.29 shows the unshielded 15:15 turn, adjacent winding configuration, similar to Figure 4.6, used in this case study. By these design, parameters, the traditional analysis would observe that the transformer operating point is at a maximum of 0.53T, resulting in 86.2 W of loss or a 99.2% efficient

design. This is not in the highest realm of efficiencies but is within the realm of reason. Furthermore, the leakage inductance of  $157\ \mu\text{H}$  and  $12\ \text{mH}$  magnetizing inductance is in the range typical of dual active bridge designs for the aforementioned specifications. A photograph of this transformer is shown below in Figure 4.29. The thermal image of this core in the open secondary test is shown in Figure 4.30. This thermal image was taken after 15 minutes of exciting the core at  $0.2\ \text{T}$ . Then, the excitation level and frequency was swept over a range of  $0.1\ \text{T}$  to  $1\ \text{T}$  and  $10\ \text{kHz}$  to  $50\ \text{kHz}$ . The excitation level was curtailed at higher frequencies due to limitations of the DC power supply. This same core was tested with the secondary shorted. In this test a thermal image was taken after 15 minutes of exciting the core at  $0.2\ \text{T}$ . However, this magnetic flux was through the leakage paths. In this case, it is clear that the outer most layers and the inner most layers of ribbon are contributing to losses. This is expected as this design is similar to FEA models above where there are significant amounts of leakage flux entering the outside ribbon layers and in the window of the transformer.



*Figure 4.29: Unshielded 10 kW DAB Transformer.*

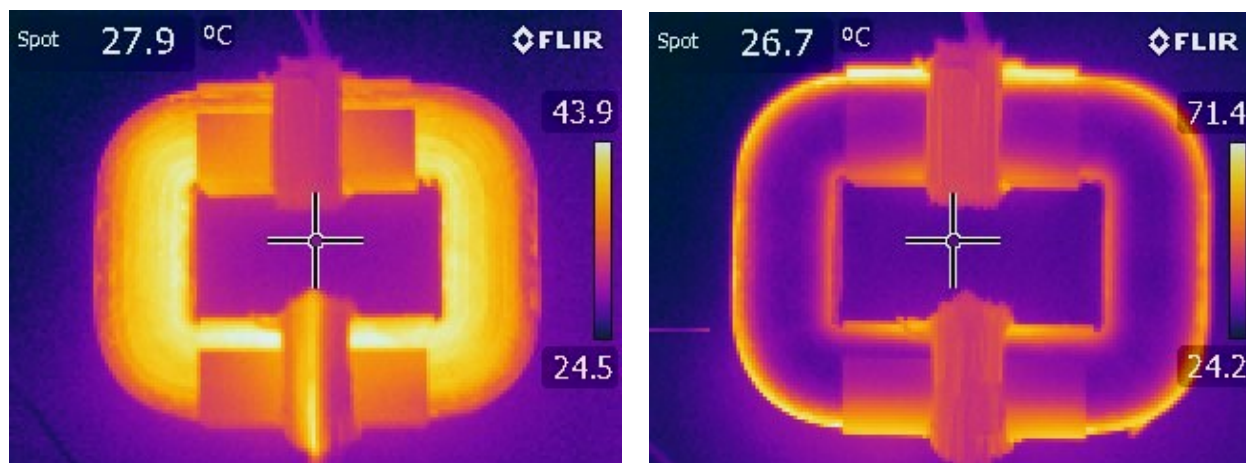


Figure 4.30: 10 kW Unshielded DAB Transformer Thermal Profiles. Magnetizing (Left) Leakage(Right).

Figure 4.31 highlights the magnetizing flux thermal profile. It is clear from these images that the interior of the core is the hottest. Similarly, there are losses distributed throughout the core. This is because magnetizing flux is exciting all of the magnetic ribbon layers, leading to excitation loss.

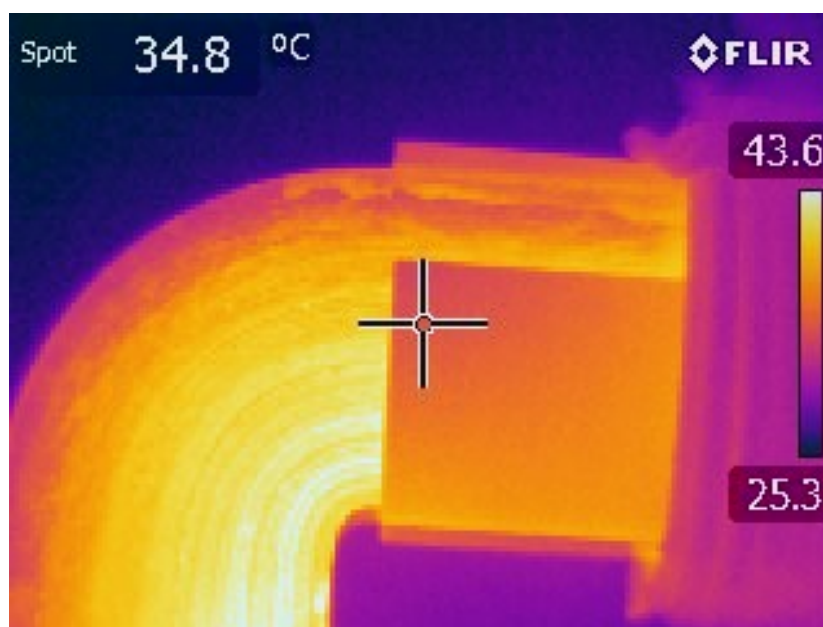


Figure 4.31: Zoomed 10 kW Unshielded DAB Transformer Thermal Profile.

Observing the thermal profile of the side of the transformer also yields interesting results. The top view, showing the broad surface of the ribbon is shown in Figure 4.32. It can be seen

that the hottest regions of this outermost layer are along the edges. It is also clear that the very top is cooler than the surfaces closer to the windings, top of the thermal image. These effects correspond to the concentration of eddy currents around the perimeter of the surface, accounted for with the  $k_w$  term that affects the area of the eddy current path in equations (4.28), (4.29), and (4.30). This is really accounting for the second order effects of flux cancellation as described in (4.8) and (4.9).



*Figure 4.32: 10 kW DAB Transformer Case Study, Unshielded Top View. Photograph (Left) and Leakage Test Thermal Profile (Right).*

A summary of the recorded magnetizing and leakage losses is shown below in Figure 4.33. Measured data is recorded as points, ‘x’ for leakage and ‘o’ for magnetizing. First the magnetizing losses were recorded following the procedure in the previous chapter. Second, a current loss lookup table was created for the conduction losses of the primary coil. The leakage losses were determined by taking the average power of the instantaneous voltage and current in the primary winding. Then the conduction loss,  $I^2R$ , and magnetizing loss for that excitation level were subtracted out. It is clear from both the measured data and the fit lines that leakage inductance based losses are significantly higher than the magnetizing losses, 20 to 30 times higher. These newly characterized losses represent a significant loss mechanism that greatly limits the ability to successfully design high power medium frequency transformers. As power is

transferred through the leakage path, the induced eddy currents will introduce a previously unaccounted for power loss that will dramatically lower system efficiencies.

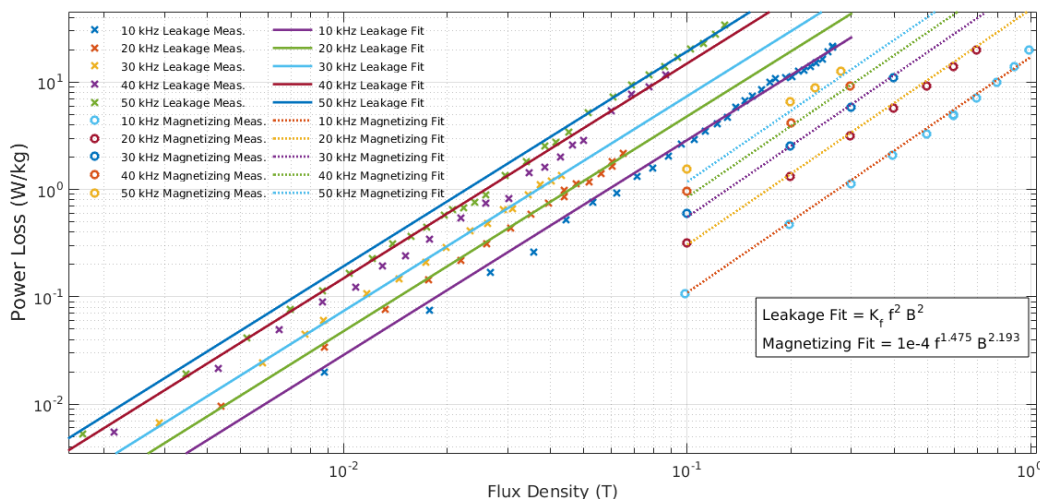


Figure 4.33: Loss Map for Magnetizing and Leakage Losses of F1AH1171 Core.

The bar shield is a simple approach to minimizing leakage flux losses that has a minimal impact the overall core performance and design. In fact, the bar shield can be a first solution to existing designs that are found to have excessive losses. An example bar shield was assembled using Ferroxcube 3c95 ferrite 'I' cores, Figure 4.34. Two cores were connected together to form the outer shield while a single bar forms the interior. As a laboratory prototype, off the shelf bars were used. In a formal design, specific dimensions that fit the core would have better performance. It is clear from the magnetizing thermal image, Figure 4.35, that the bar shield has minimal impact to the magnetizing behavior of the transformer. However, in the leakage test, the transformer runs significantly cooler. Rather than the edges of the core being the hottest spots as is the case in the unshielded design, the bar shield enables the transformer core to stay cooler than the exciting coils. It is clear that the bar shield is redirecting leakage flux away from the magnetic ribbons and is thus minimizing stray flux induced eddy currents. This reduction of eddy currents is clearly shown in the reduced losses shown below in Figure 4.39.

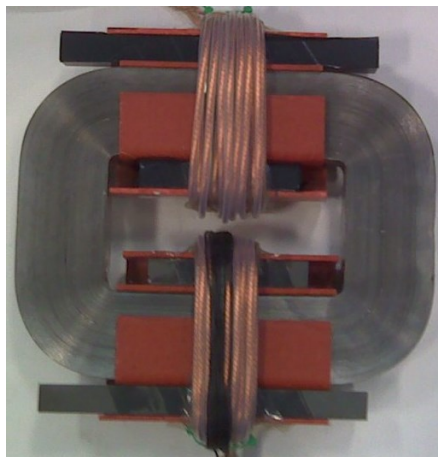


Figure 4.34: 10 kW DAB Transformer Case Study, Bar Shielded.

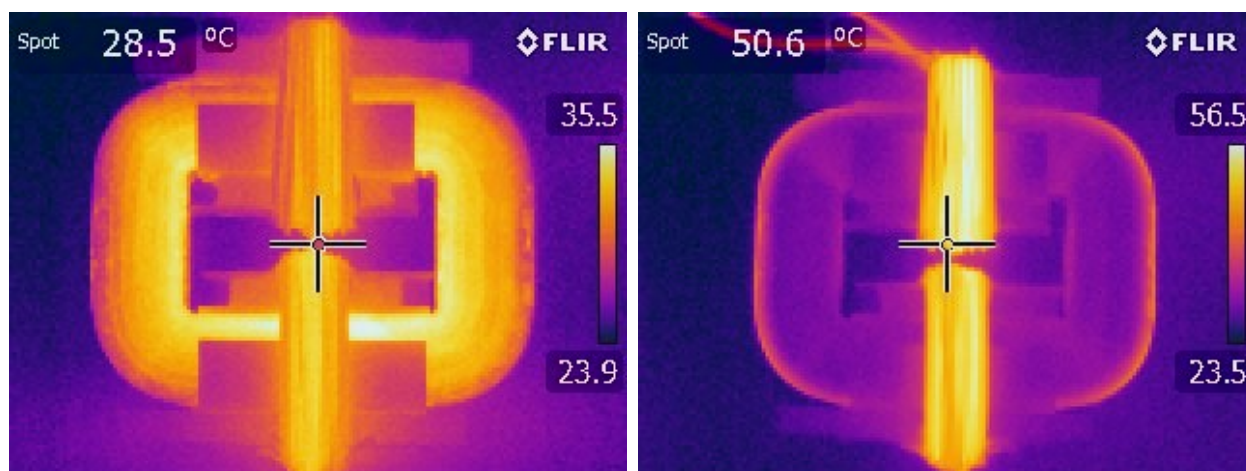


Figure 4.35: 10 kW Bar Shielded DAB Transformer Thermal Profiles. Magnetizing (Left) Leakage(Right).

It can also be seen that the top layer of the core is running cooler, Figure 4.36. The core is coolest closet to the shield where minimal flux is entering the ribbon. Away from the shield, the core is hotter and exhibits a hot edge around the perimeter, similar to the unshielded case.



*Figure 4.36: Bar Shield Leakage Top View Thermal Profile.  
10 kW DAB Transformer.*

The next shielding design presented is the wing shield, Figure 4.37. The bar shields remained Ferroxcube 3C95 however only C cores of 3C90 were available in suitable dimensions. The wings used extend nearly 3x the winding thickness. There is still a significant air gap however and the extension length could be shortened with a shorter air gap design. Again, this would take a custom core design that is beyond the scope of this proof of concept. This design was also subjected to a 10 kHz leakage and magnetizing loss measurement sweep.

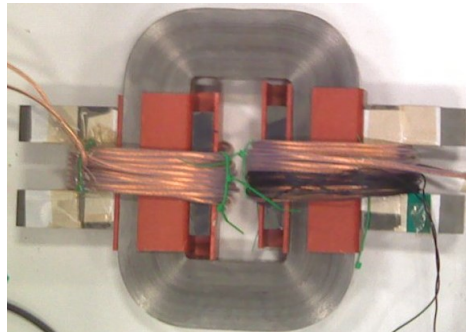


*Figure 4.37: 10 kW DAB Transformer Case Study, Wing Shielded.*

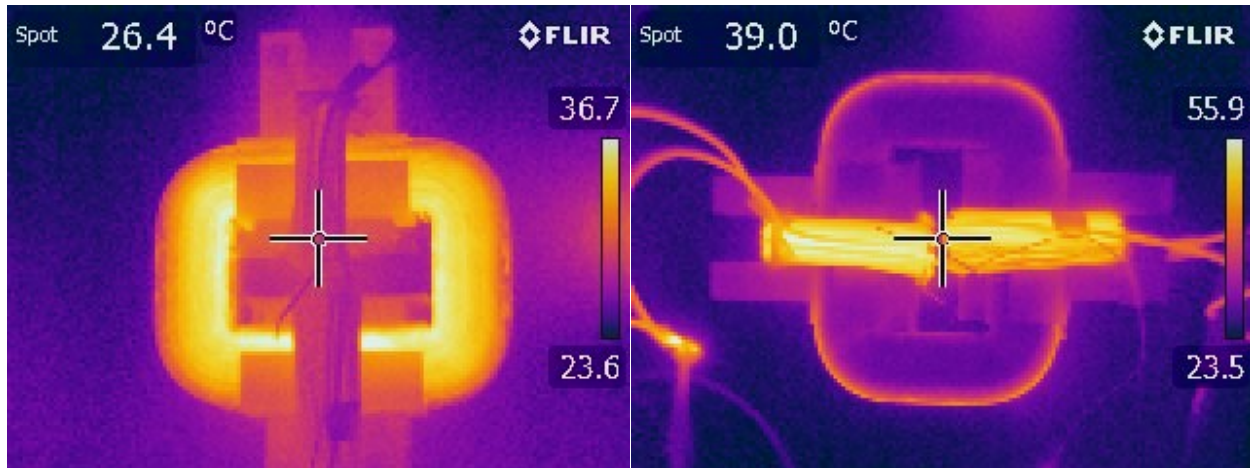


Figure 4.38: 10 kW Wing Shielded DAB Transformer Thermal Profiles. Magnetizing (Left) Leakage(Right).

The wing shield shows similar thermal results to the bar shield. The magnetizing test, Figure 4.38, shows minimal, if any impact to the magnetizing test thermal profile. The leakage test shows a significant reduction in outer and inner ribbon heating. This thermal profile proves that the wing shield is a viable solution to increasing the transformer efficiency while gaining independent leakage inductance design flexibility.

The loss measurements for the three design cases, unshielded, bar shielded and wing shielded are shown below in Figure 4.39. The three fit lines for the leakage losses were all found to fit the expected form for classical eddy current losses. The three magnetizing tests resulted in nearly identical measurements and so only one fit line is presented. This line also fits nicely with a Steinmetz like equation. It should be noted that the magnetizing loss coefficients are not the traditional Steinmetz coefficients because the core was subjected to triangular excitation.

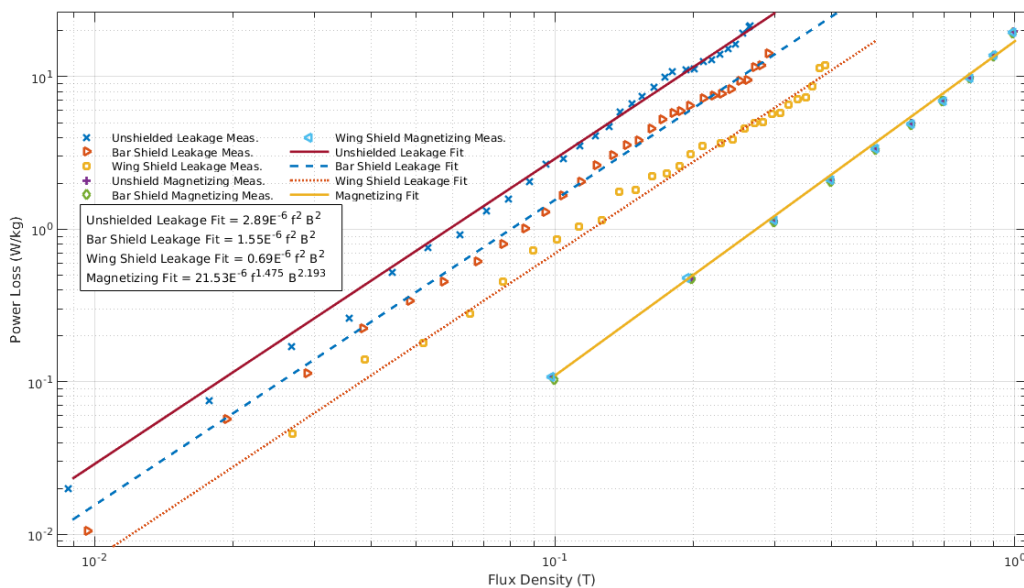


Figure 4.39: 10 kW, 10 kHz Unshielded / Shielded Loss Map.

It is evident that the shielding approaches provide a significant reduction in leakage losses. These leakage losses are still higher than the simple magnetization losses. However, more deliberate shield design with specially designed ferrite geometries could reduce these leakage losses even further. In these shield designs, the shield was found to reduce the amount of flux into the ribbon by nearly half. Further geometry and design improvement could reduce this stray field even further thus potentially providing core designs that are as efficient through the leakage path as the magnetizing path. However, these proof of concept designs were able to reduce the leakage losses by roughly 45% and 75% for the bar and wing designs respectively while minimizing the impact on the magnetizing losses, Figure 4.40. Loss variations less than 5% are within the sensor tolerances. A similar solution comparison is the reduction of  $k$  value for the different shields and frequencies. This comparison is shown in Figure 4.41 where it is clear that both the bar and wing shield provide a significant loss reduction over a design with no shield.

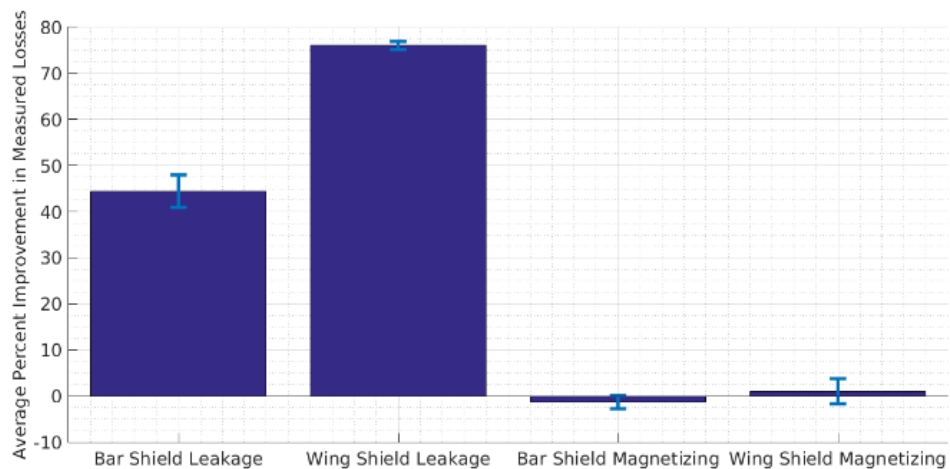


Figure 4.40: Shielded vs Unshielded Loss Reduction.

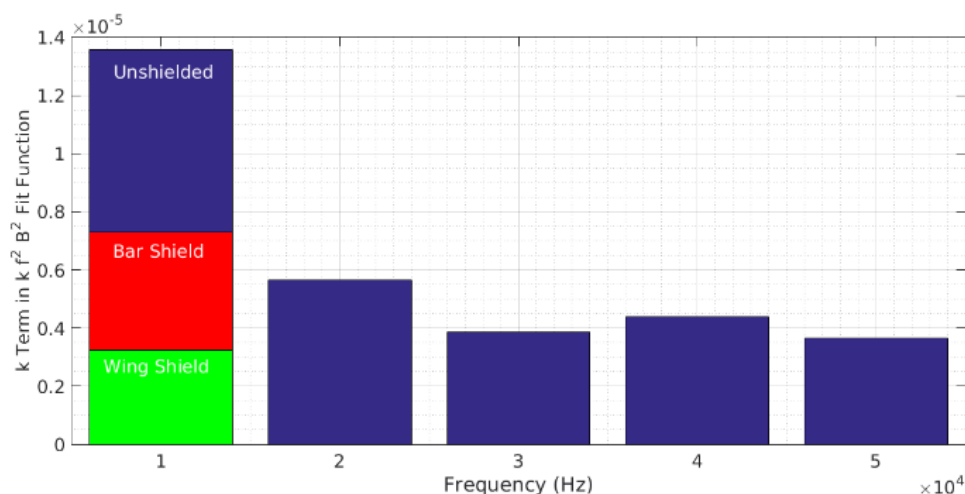


Figure 4.41: Variation in Leakage Loss  $k$  Term.

The reduction of  $k$  values through shielding is convenient for comparison between designs and curve fitting. However, what the shields are actually doing is reducing the amount of flux generated by the excitation coil that enters the broad surfaces of the ribbon. Therefore, an alternative way to look at the wing shield efficacy is by the effective ribbon flux reduction. This is shown in (4.43) where  $k_{none}$  is the  $k$  term of the unshielded induced eddy current loss fit line. The  $k$  term for either the bar or wing or some other future shielded loss fit function is  $k_{sh}$ . Using this analysis, the bar shield reduces the apparent normal flux by 27% and the wing shield reduces the flux by 51%.

$$(4.43) \quad \phi_{PR} = 100 \frac{\left( \sqrt{\frac{k_{none}}{k_{sh}}} - 1 \right)}{\sqrt{\frac{k_{none}}{k_{sh}}}}$$

It is also important to inspect how the shielding changes the leakage and magnetizing inductances. Figure 4.42 shows this impact to permeability. It is clear that the bar shield has a minimal impact on both leakage and magnetizing inductances enabling it to be a direct addition to a current magnetics design. The wing shield however, significantly increases the leakage inductance. This increase leads to the idea that by utilizing wing shields, shields with gaps or strain annealed ribbon shields, the leakage inductance can be tuned independently of the magnetizing inductance. This enables significant design simplification where a tight leakage inductance design is needed such as in the active bridge converter.

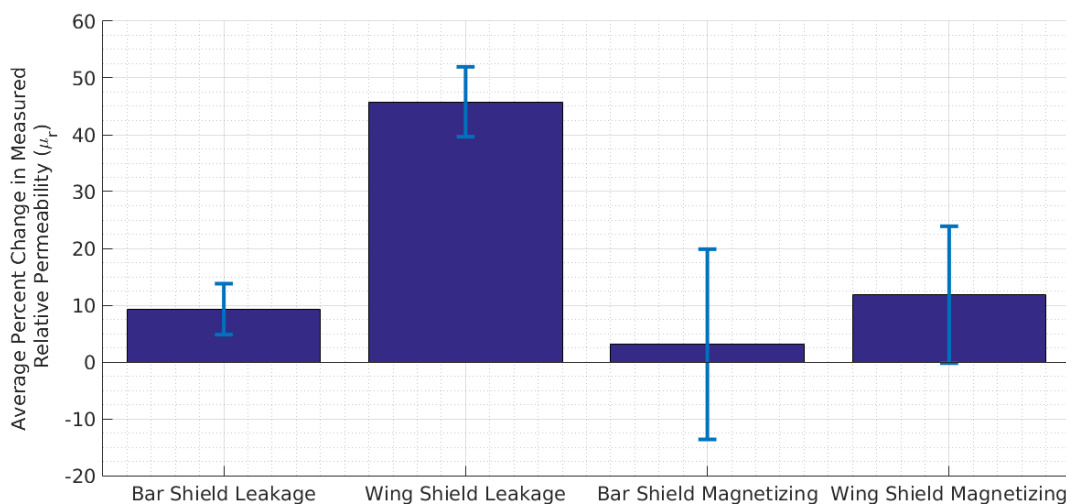


Figure 4.42: Change in Effective Permeability Due to Addition of Leakage Shielding Component.

This case study has shown the importance of leakage and stray flux induced losses. These losses can be significantly higher than the typical loss models for magnetic components predict. Design tools were presented that utilize a magnetic equivalent circuit model that segregates the different flux paths into lossy and lossless paths. The permeances for these paths are constructed from simple constituent geometries that relate to the magnetic component construction. A

method of shielding the magnetic flux was proposed whereby the flux is directed away from the wide surfaces of the magnetic ribbon and through a high resistivity ferrite core. Both a bar and wing geometry were proposed with magnetic equivalent circuits and general design guidelines. The shields greatly reduced the measured leakage losses while having minimal impact on magnetizing losses. Using the wing shield geometry, it is clear that the transformer leakage inductance can be tuned independently of the magnetizing core and general transformer geometry. This independent leakage and magnetizing design represents a significant advancement for high power medium frequency magnetics and enables new solutions for advanced applications.

#### **4.10 Stray Capacitance models**

Parasitic capacitance is an important element in the medium voltage transformer. In the typical construction, there are several capacitive paths that must be considered. Series capacitances such as winding capacitance represent a low impedance path for high frequency, common mode currents [104], [105]. This capacitance can also impact the operating range converters by reducing the soft switching region [106]. The capacitance between winding sets and the core is discussed in [107] and [108] provides a broad overview of winding capacitive paths.

In general, the capacitance between windings is determined by the energy to voltage,  $V$ , relationship (4.44). The capacitance between windings is  $C_o$ . The winding layout, standard or flyback, Figure 4.43, influences the total capacitance. The excitation coil is constructed of  $K$  layers. The capacitance between layers depends on the winding layout. Windings can either be orthogonal, Figure 4.44 left, or orthocyclic, Figure 4.44 right. While [108] shows many methods

of estimating capacitances, this section will highlight those that were found to have the closest agreement with measured results.

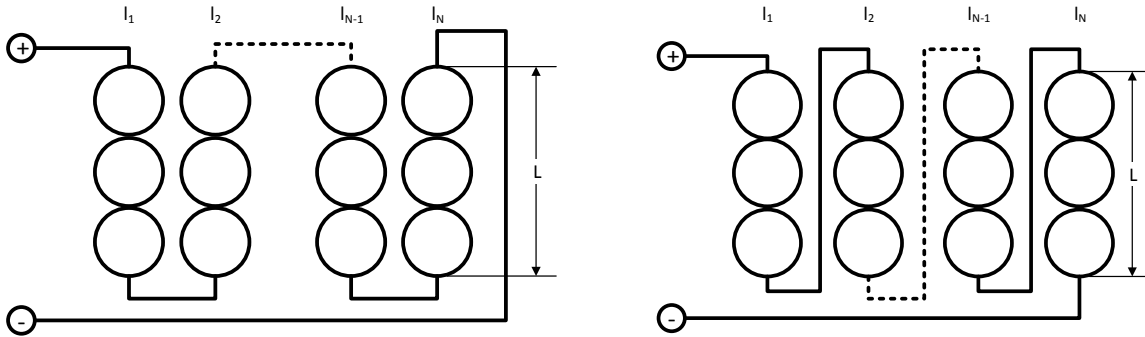


Figure 4.43: Winding Layout for Magnetic Devices. Standard (Left) and Flyback (Right)

$$(4.44) \quad W = \frac{C_o}{2L} \int_0^L V^2(x) dx = \frac{1}{2} C_{Layer} V^2$$

The layer of windings is treated as an equipotential surface for the nominal capacitance calculation. From (4.44), and the winding geometries, it is clear that equivalent layer to layer capacitor,  $C_{Layer}$ , is  $C_o/3$  for the standard winding and  $C_o/4$  for the flyback winding. The local effects of the crossover wire of the flyback winding configuration are neglected. Next it is important to determine the capacitance between windings. As mentioned above this depends on how the individual wires are arranged. For orthogonal windings, of  $N$  turns per layer of  $d_w$  wide wire, a cylindrical capacitance model was found to provide the most accurate results. Simplifies the derivation by modelling the windings as two concentric sheets of inner and outer radii of the winding layers,  $R_I$  and  $R_O$  respectively. The capacitance for orthogonal windings is (4.45) for the winding layout of Figure 4.44, left.

$$(4.45) \quad C_{o-orthogonal} = N \frac{\epsilon_0 \epsilon_{rw} 2\pi d_w}{\ln\left(\frac{R_O}{R_I}\right)}$$

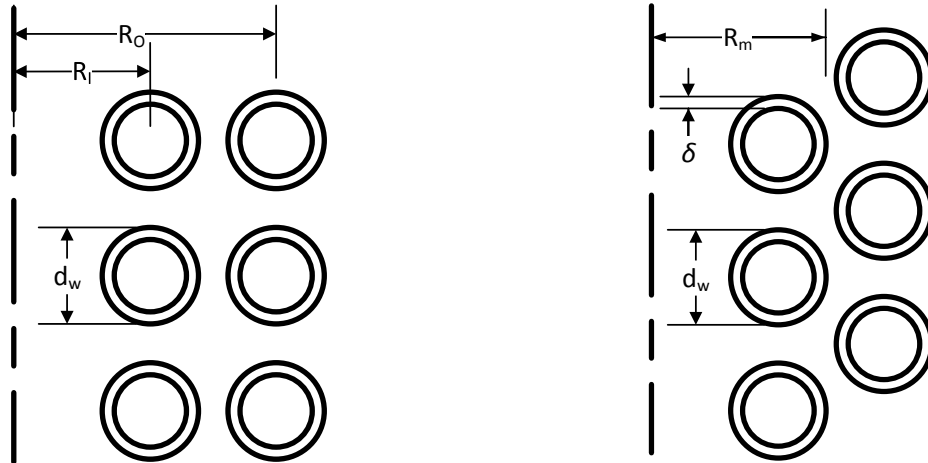


Figure 4.44: Turn to Turn Winding Alignment.  
Orthogonal (Left) and Orthocyclic (Right).

Researchers needed a more nuanced model to determine orthocyclic winding capacitance. This model assumes that electric flux lines emanating radially from a winding's center and intersect with the radial line of an incident winding. The electric field strength is determined from the flux lines and is used to calculate the stored electric energy. Equation (4.46) is the layer capacitance for orthocyclic windings, Figure 4.44 right, of mean layer radius  $R_m$ . Two simplifications are shown in (4.47) and (4.48). A unique permittivity is shown in (4.49).

$$(4.46) \quad C_{o-orthocyclic} = 4N\epsilon_o\pi R_m \left[ L + 2\delta \frac{d_w - \delta}{\epsilon_i d_w^2} M \right]$$

$$(4.47) \quad L = \frac{1}{2} \int_0^{\frac{\pi}{6}} \frac{\cos^2(x) - \cos(x) \sqrt{\cos^2(x) - \frac{3}{4} - \frac{1}{2}}}{\left( \cos(x) - \left(1 - \frac{\delta}{\epsilon_i d_w}\right) \sqrt{\cos^2(x) - \frac{3}{4} + \frac{1}{2}} \right)^2} dx$$

$$(4.48) \quad M = \frac{1}{2} \int_0^{\frac{\pi}{6}} \frac{\sin^2(x) - \cos(x) \sqrt{\cos^2(x) - \frac{3}{4} - \frac{1}{2}}}{\left( \cos(x) - \left(1 - \frac{\delta}{\epsilon_i d_w}\right) \sqrt{\cos^2(x) - \frac{3}{4} + \frac{1}{2}} \right)^2} dx$$

$$(4.49) \quad \epsilon_i = 2.5 + \frac{0.7}{\sqrt{d_w - 2\delta}}$$

Accommodating Litz wire or partial layers is a matter of scaling factors. The authors of [109] explore the variations between solid wire and Litz wire equivalent capacitances. To handle

a partial layer of  $x$  turns beside a full layer of  $z$  turns, the partial layer capacitance (4.50), is added to the other layers capacitance. The capacitance between a coil and the core is also well researched.

$$(4.50) \quad C_{part} = \frac{4C_o(N-1)(z^2+x^2)}{((N-1)z+x)^2}$$

The capacitance to the core is also easily determined. Low power transformers or very high frequency transformers using ferrite model the core as a dielectric, [107]. However, most core materials of interest for the high power medium frequency operation, MANC, amorphous etc., have a relative permittivity near 1 and a high conductivity meaning they can be modelled as an equipotential conductor, [110]. For these types of materials, the core is grounded to eliminate possible discharge. Therefore, windings next to the core have a parasitic capacitance to ground. One method of reducing the effects of this parasitic capacitance to ground is to had a resistive layer between the winding and the core for a lossy controlled path [111].

These important models aid the holistic design of a transformer. The parasitic capacitances are a penalty to adding more turns for a given design. This penalty can lead to oscillatory behavior and common mode current. In some designs, this oscillation can be harnessed for a resonant switching approach. However, this requires very careful design and requires a complete understanding of parasitic capacitance paths.

#### 4.11 Winding Losses

There are three primary effects that introduce additional loss components in a transformer model. The most obvious is the low frequency resistance of the wire. As the coil is subjected to higher frequencies, two other effects become more dominant, the skin effect and the proximity effect. Many researchers have explored these effects. Notably, the research group at the Dartmouth Magnetic Component and Power Electronics Research Lab has advanced the

understanding of these topics for many specialized applications. This section will provide a brief overview of the basic models, available in many textbooks, [112], of these effects and their implications for high power, medium frequency magnetics. It will also summarize some of the more advanced work that can be used for refined modelling and informed design decisions.

The first and most obvious loss component of windings is the low frequency resistance. This is shown in (4.51). This resistance depends on the resistivity of the conductor,  $\rho$ , and the total length of the of the wire used to construct the coil,  $l_w$ . This resistance also depends on the cross sectional area of the conductor,  $A_w$ .

$$(4.51) \quad R_{DC} = \frac{\rho l_w}{A_w}$$

At higher frequencies, a phenomenon known as the skin effect also contributes to losses. The skin effect is when, at high frequencies, the current in a conductor drifts towards and concentrates in the outer perimeter of the wire. A solid wire carrying medium frequency current that is experiences the skin effect behaves more like a hollow tube carrying the same magnitude of wire. The skin effect ultimately is reducing the cross sectional area of the conductor. The depth of conductor that the current can penetrate is known as the skin depth, (4.52). This effectively reduces the area of the conductor and leads to a higher resistance. While approximate for round wires, this increased resistance is shown in (4.53).

$$(4.52) \quad \delta = \sqrt{\frac{\rho}{\pi \mu f}}$$

$$(4.53) \quad R_{AC} = \frac{\rho l_w}{\pi(r^2 - (r - \delta)^2)}$$

More appropriate designs will use conductors which have an area that is tuned to the specific skin depth. That is, the wire diameter will be no more than two skin depths. This is the basic principal behind Litz wire where a bundle of very thin, individually insulated, conductors is woven together to form a high current conductor. A procedure for optimal Litz wire design and selection is proposed in [113].

The third principal is the proximity effect. This effect accounts for the crowding of current in a conductor due to the influence of the magnetic field. This magnetic field can come either from stray fields as previously mentioned or from a local field of an adjacent winding. This effect is much more difficult to characterize and several sources have provided various models to account for design variabilities [114], [115]. Dowels equation provides for the increase in a sectors resistance due to adjacent layers. However, it is important to apply this to a practical coil of layered windings. This procedure was presented for  $N$  layers of Litz wire, in [116] and reshown below in (4.54). The Litz wire is made of  $s$  strands and has a conductor fill factor  $F_w$ . The strand diameter,  $d_o$ , must be less than the skin depth.

$$(4.54) \quad R_{AC} = R_{DC} \left( 1 + \frac{\pi^2 s F_w d_o^4}{3072 \delta^4} (16N^2 - 1 + \frac{24}{\pi^2}) \right)$$

There are other aspects that influence the proximity effect such as the magnetic fields near a gap or window leakage flux crossing windings. In order to estimate these effects, refer to [117] and [118]. One of the approaches to minimizing the gap induced losses is to construct a larger gap of many, smaller, gaps know as a distributed gap or to use large section of low, but higher than air, permeability material [119]. Rearranging the windings within the core window also helps reduce gap based losses, [118]. However, with MANC and other ribbon cores, it is not recommended to gap due to the flux entering the ribbon normal. Therefore, it should not be necessary to calculate the proximity effects due to fringing flux. Processes such as strain annealing should be used to specifically tune a relative permeability to desired levels instead of gapping.

The winding of a magnetic device introduces ohmic losses to the component. Higher frequency currents do not utilize as much of a conductor's area as DC. The skin effect accounts for this underutilization and should be considered when choosing wires. Litz wire enables larger

effective areas of conductors and should be used in high power medium frequency applications. The magnetic fields from nearby wires also leads to higher losses. All of these effects must be considered when optimizing a magnetic device. One advantage of the high saturation flux density and relative permeability of ribbon cores is the need for less turns to achieve a desired inductance at a flux density. This ultimately leads to lower conduction losses than a similar ferrite design with a higher number of turns.

#### 4.12 Conclusions and Future Work

This chapter has shown three elements of high power medium frequency magnetics that are generally considered parasitic, leakage inductance, capacitance and conduction resistance. In the case of leakage inductance however, it is often a system design requirement. This design aspect requires careful thought as it was shown that the leakage flux can introduce significant new losses in ribbon core transformers. These losses are many times larger than magnetizing losses and depend heavily on the core geometry and winding arrangement. Importantly, these losses are proportional to  $(fB)^2$  where the scalar is based on the core material and geometry as well as the breakdown in flux paths. New design tools that break down these paths and distinguish lossy paths from lossless paths were introduced to aid design decisions. In order to mitigate the leakage flux losses, a new flux redirection shield was introduced that enables leakage flux to return to an exciting coil while staying in a high resistivity material, minimizing eddy currents.

Future work will explore these eddy currents and losses in the wider ribbon cores that have recently come into production. Similarly, second order models that account for flux cancelation in center of the ribbon are needed for a refined understanding. Currently, there is also good agreement with a power loss curve fit that is proportional to  $f^{1.5}B^2$  implying that the skin

effect is possibly influencing the power loss due to normal flux induced eddy currents [120]. Future work will determine the efficacy of this approach and what assumptions need modification from the current model development.

Work will continue with shield development and understanding as well. One unique opportunity is a core design with 100% MANC materials. The magnetizing core would be a traditional material and leakage cores will use new strain annealed ribbons. This design approach would be mechanically robust with a minimal amount of movable components. It would also provide a very tunable design where the magnetizing inductance and leakage inductance are independent. This enables many more design solutions and allows the geometry to be tuned for thermal or volumetric optimizations.

## CHAPTER 5: STRAIN ANNEALED CORE ANISOTROPIC THERMAL MODELLING

### 5.1 List of Symbols

The use of the advanced manufacturing technique of strain annealing for nanocomposite magnetic ribbons enables control of relative permeabilities and spatially dependent permeability profiles. Tuned permeability profiles enable enhanced control of the magnetic flux throughout magnetic cores, including the concentration or dispersion of the magnetic flux over specific regions. Due to the correlation between local core losses and temperature rises with the local magnetic flux, these profiles can be tuned at the component level for improved losses and reduced steady-state temperatures. We present analytical models for a number of assumed permeability profiles. This work shows significant reductions in the peak temperature rise with overall core losses impacted to a lesser extent. Controlled strain annealing profiles can also adjust the location of hot spots within a component for optimal cooling schemes. As a result, magnetic designs can have improved performance for a range of potential operating conditions. This chapter contains many complex equations with subtle nuances in variables. As such a list of symbols is provided to aid readers below in Table 5.1.

Table 5.1: List of Variables Used in CHAPTER 5

Symbol	Description
$a$	Area of a material for thermal impedance
$\alpha$	Frequency dependent loss exponent
$B$	Magnetic flux density
$B_{avg}$	Average flux density over toroid profile
$\beta$	Magnetic flux density loss exponent
$B_z[a, b]$	Incomplete Beta function
$c$	Exponent in exponential permeability profile
$C$	Circumference of a circular path
$C_c$	Thermal capacitance of toroid core
$f$	Frequency of excitation waveform
$F$	Core fill factor, ratio of total material thickness to core thickness
$g$	Ratio between slope and offset magnetic permeability terms
$h$	Height of magnetic ribbon in the z direction
$I$	Current flowing through excitation coil
$K$	Power loss scalar term
$k_t$	Thermal conductivity
$k_c$	Thermal conductivity of the magnetic ribbon
$k_G$	Thermal conductivity of the gap between magnetic ribbon layers
$\lambda$	Ratio between outer and inner radius of toroid
$L$	Magnetic inductance of wound toroid
$l$	Length of a material for thermal impedance
$\lambda$	Ratio between outer radius and inner radius of a toroid core
$L_r$	Length of ribbon
$l_r$	Length of ribbon to apply strain for a given radius
$l_G$	Length of region between ribbon layers
$l_{Gz}$	Length of region between ribbon material and external free space
$L_n$	Layer number of a wound toroid
$\mu$	Magnetic permeability of core material
$\mu_0$	Magnetic permeability of free space
$\mu_1$	Magnetic permeability following the graded with offset profile
$\mu_c$	Magnetic permeability following the constant profile
$\mu_e$	Magnetic permeability following the exponential profile
$\mu_s$	Slope term for the graded and offset graded profiles
$N$	Number of turns of excitation coil
$N_L$	Total number of layers of ribbon for the full toroid core
$n$	Ribbon layer number between 1 and $N_L$
$\bar{P}$	Permeance of magnetic core
$\phi$	Magnetic flux
$P$	Power loss due to magnetic core excitation
$P_{loc}$	Power loss in the local region of the core
$Q$	Heat injection into the core
$r$	Radius of layer of inspection for toroid core
$r_i$	Inner radius of toroid core
$R$	Thermal impedance
$R_t$	Tangential thermal impedance
$R_r$	Radial thermal impedance
$t$	Magnetic ribbon thickness
$T$	Temperature of magnetic core
$T_{amb}$	Ambient Temperature
$V$	Volume of magnetic material

## 5.2 Motivation

Fully understanding the losses for a magnetic component is critical for optimal design in power electronics applications. It is also important when determining the necessary cooling systems for a particular design. There are multiple authors and publications that explore the variations in core loss due to the excitation waveform[1], [14], [40], [43]. However, all of these

prior investigations base their loss models on assumptions of uniform flux density within the core. These models either use the maximum of average flux density or the overall peak flux density. While this can be useful for predicting the losses as a function of excitation waveforms enforced by the electrical circuit, it does not account for core geometry, flux concentration and pinching, and other material effects. Permeability engineered cores with significant variations in relative permeability and resulting flux density profiles will be further susceptible to errors in loss estimations in the previously mentioned approaches and these modeling approaches cannot provide guidance to the optimal magnetic core designs in cases where permeabilities can be readily adjusted throughout a given magnetic core.

In [121], the author derives and highlights the differences in estimated total losses using the local peak flux density associated losses against the rational approach using a single global flux density. The solution space explored is useful for small components but does not explore some of the design possibilities that are needed for the high power applications of interest. Similarly, [122] utilized similar analysis to recommend variations to the magnetic core cross section. Here the motivation was, as is true in this analysis, minimizing thermal variation over the core profile. Unlike this papers approach, utilizing variations in effective permeability, the author of [122] recommended varying heights along the toroid radius. As the author mentions, this is problematic for manufacturability. Furthermore, the author fell short of a complete analysis and did not fully analyze the variation in core losses due to the improved flux density profile. Finally, the author was only able to explore solutions in finite element analysis. There is ample room for continued analysis and analysis that considers newly proposed post processing techniques.

Thermal modelling has also been shown by others, [123]. However, the complete, electro-thermal model as not yet been presented. As shown previously, as the magnetic material temperature changes the core parameters can change dramatically. Furthermore, advancements in materials processing enable the design of materials with spatially variable properties that need to be considered with the spatial distribution of heating. The thermal model presented in the chapter will focus on the nuances of magnetic ribbon wound. This will provide the details necessary for thermal models to make medium frequency transformers.

### **5.3 Introduction**

Passive device designs must meet the stringent requirements brought about by the continued increase in capabilities and adoption rates of wide bandgap power semiconductors. Specifically, magnetic component designs need to consider new operating spaces and to take advantage of new soft magnetic materials and material processing. Generally, power converter controls and topologies are moving towards very high efficiencies through soft switching techniques that greatly reduce the losses associated with the switching devices. This in turn means that a dominant loss component of a power converter will be the passive devices and specifically the magnetic components [124], [125], [126]. Further, magnetic components will continue to play a critical role in power converters due to their energy storage and isolation capabilities. The high reliability and wide design envelope of magnetic devices also makes them critically important elements of any power converter design. It is because of the aforementioned factors, that both magnetic design techniques and the components used need to be fully characterized and improved.

Analytical predictions will enable improved screening and optimization of magnetic designs in order to reduce the number of designs that require careful characterization and more

detailed optimization through experimental prototype efforts and/or more computationally intensive applied electromagnetics tools such as finite element based modeling. Furthermore, analytical expressions can be developed to incorporate new materials and new material processing strategies. By determining estimations for currently unavailable materials or magnetic cores, this approach can also help to guide the research and development goals for new alloy development as well as advanced manufacturing process optimization techniques. That is, the magnetic core research and development can be refocused on the realization of a subset of candidate designs that have shown promise through analytical expressions and have been confirmed by finite element modeling techniques. Such an approach is particularly useful in understanding the role and performance potential of magnetic cores that are post-processed with strain annealing techniques in which the permeability can be readily tuned along the length of the ribbon. The utility of an analytical design approach is in determining which strain annealing profiles are most useful such that the material and process development can focus on optimized designs. Similarly, the analytical approach can better define what baselines provide a meaningful comparison.

Due to the myriad of factors that influence the design of a power electronics converter, it is important to characterize and provide predictions for magnetic designs using similar methodologies to that of semiconductor device characterizations. That is, magnetic devices need to be characterized for all operational sensitivities, e.g. temperature, loading,  $dV/dt$  etc. in a particular solution space [127]. This research focuses on two of the more influential aspects of magnetics design, namely the direct relationship between the local temperature rise and core magnetizing losses. It is noted that for some power electronics converter designs leveraging amorphous and metal amorphous nanocomposite (MANC) ribbon based core materials,

additional loss contributions have been determined to be significant and even dominant in some cases as a result of eddy current losses generated within the ribbon plane due to flux leakage from the magnetic core. While we do not specifically discuss that source of losses in this work, similar techniques are relevant to address those challenges and are the subject of on-going research activities. It is also important to note that new post processing techniques such as strain annealing, [128], [129], [130], [131], [132], [7] and field annealing, [133], are enabling new material characteristics. These materials could lead to improved designs and alternative solutions. However, without full characterization and analytical screening of the post-processing dependent performance of these materials, their development is not able to successfully transition into applications and components for which they can have the most significant impact on overall performance. The characterization of magnetic designs and materials under operationally relevant conditions is paramount to continued success and improvements in magnetics design.

This paper will highlight the improved capabilities in power magnetics component level performance enabled by the strain annealing post processing techniques. It will first provide a brief overview of the state of the art as motivation to provide deeper insight into thermal modelling and loss predictions of traditional materials. These loss predictions are strongly coupled to thermal performance and can provide insight for the thermal profile of the magnetic ribbon cores. An observed gradient in temperature is due to the flux density concentration and the anisotropic core. This anisotropy is represented in the proposed thermal model. Finally, an example is explored with a comparison of physical cores designed for high power inductor applications.

#### 5.4 Heating from Magnetizing flux

For clarity, it is important to first define the variations in flux density representations. The local flux density is the typical flux density that is derived using the relationship between current and magnetic field using Ampere's law (5.1). Typically, the relative permeability,  $\mu$ , is the product of the constant relative permeability of the core material under investigation,  $\mu_r$ , and the permeability of free space,  $\mu_0$ . However, because strain annealing will enable an arbitrarily variable profile of relative permeabilities, it is left as a function of the toroid radius,  $r$ , assuming that the permeability varies only as a function of core radius but is otherwise equal along the core height and circumferential direction. Such a permeability profile is readily produced using strain annealing techniques through a monotonic variation in applied tension during the strain annealing process followed by standard core winding and fabrication processing techniques. The flux density is scaled by the number of turns,  $N$ , and the excitation current,  $I$ , regardless of excitation shape. This flux density is valid in the applicable range of  $r$  between the inner radius,  $r_i$ , and the outer radius, where  $\lambda$  is used to define the ratio between the outer radius and the inner radius. The average flux density in a toroid is shown in (5.2).

$$(5.1) \quad B(r) = \frac{\mu(r)NI}{2\pi r} \Big|_{r_i \leq r \leq \lambda r_i} \quad (5.2) \quad B_{avg} = \frac{NI}{2\pi r_i(\lambda-1)} \int_{r_i}^{\lambda r_i} \frac{\mu(r)}{r} dr$$

Below in Figure 5.1, an example toroid is drawn with the top view and a cutout side view of one of the ribbon layers. This drawing illustrates some of the physical and construction parameters. Similarly, the dimensions shown in this drawing will enable the detailed definition of various thermal impedances as described in the next section.

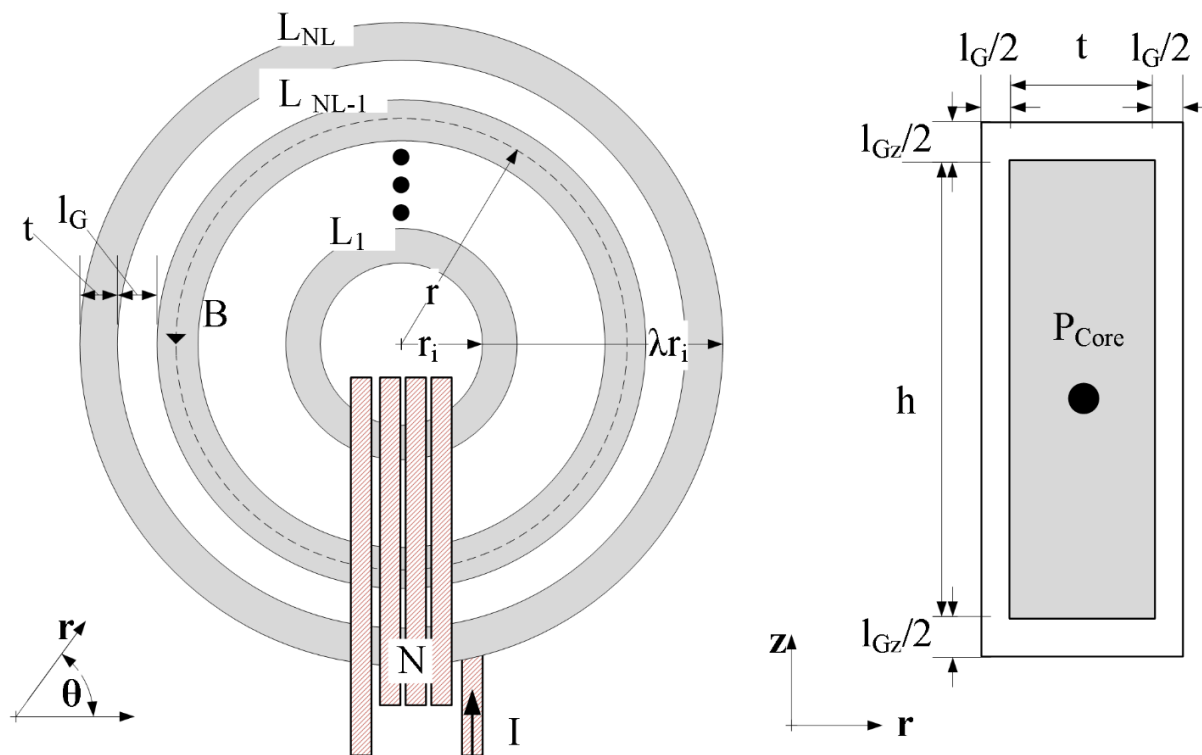


Figure 5.1: Toroid Geometry with Dimensions.

## 5.5 Heating from Normal Stray Flux

As discussed in the previous chapter, there is a loss phenomenon associated with stray flux, leakage and fringing and others. This loss predominately affects the edge layers of ribbon on the outside and inside, window, of the core. As such, a heat injection,  $Q_{stray}$ , that depends on leakage and stray fluxes and the core geometry should inject heat at the edge layers of the thermal model. The specific heat injection depends on the exact construction of the core, if shielding is present and the various flux paths as discussed in CHAPTER 4. Solutions for minimizing these losses and subsequent heating have already been discussed. This chapter will focus on the magnetizing losses and thermal management through the use of strain annealing enabled magnetizing flux control.

## 5.6 Anisotropic Thermal Model

Given the above defined flux density profiles a proper thermal model is needed to account for the anisotropic nature of the ribbon wound magnetic cores. A model can be represented as an equivalent circuit of thermal impedances, thermal capacitances and heat flow with resistances, capacitors and current injections respectively as described [134]. Other researchers have followed a similar approach of modelling power magnetics by either using isotropic materials or averages of bulk materials, [135], [136] and [137]. In [138], the authors model anisotropic cores but do not consider variations in heat injection due to a flux density profile. In order to account for this localized heat injection due to localized losses, it is necessary to have a localized thermal model. This proposed model is shown below in Figure 5.2. This model discretizes the spiral of a wound magnetic tape into several concentric ring layers of one ribbon thickness. Given that many ribbon cores have a high electrical conductivity, the thermal conductivity will also be high, [139]. This enables the ring of the core to be represented in two dimensions as it is a reasonable assumption that each discretized ring will be an isotherm and temperature will only vary in the radial direction. Given this symmetry of the ring, the model can be broken into the radial and height dimensions using the subscripts  $r$  and  $z$  respectively. The thermal model is treated as an electrical analogue using common relationships behaviors between physical processes, [140], [141], [142], and [143]. The subscript  $n$  is the discretization variable. Each ring has a thermal capacitance,  $C_c$ , corresponding to its effective ring mass and material's specific heat capacity. However, this capacitance need only be considered for thermal transients. At steady state temperatures, the thermal mass capacitance can be neglected. The heat injected is directly attributed to the local losses, represented by the current injection  $P_{core}$ .

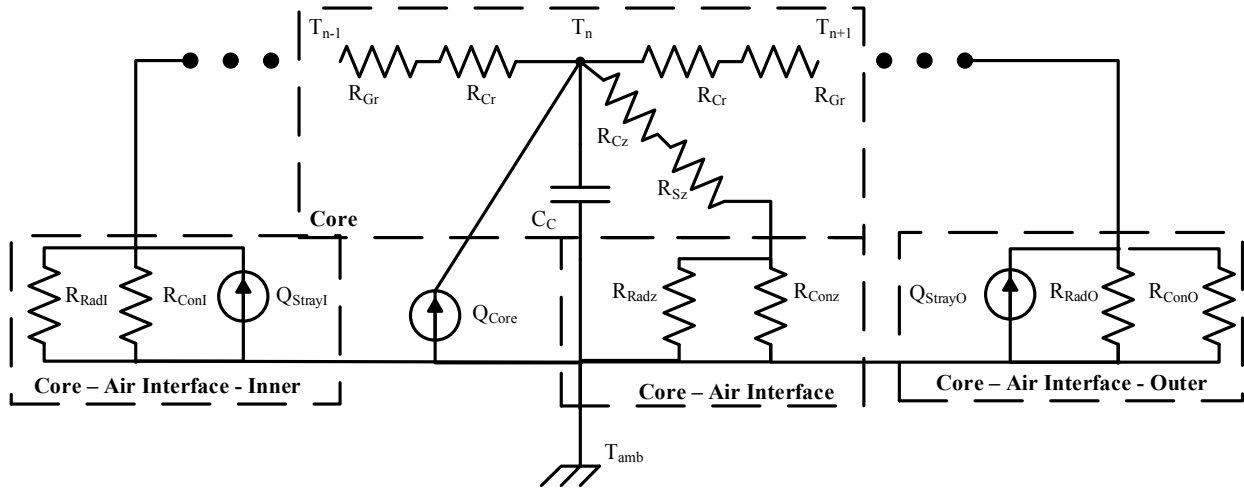


Figure 5.2: 2D Thermal Model for Anisotropic Magnetic Ribbon Cores.

In order to define the above model, the heat flow processes of convection and radiation are also treated as impedances of the form shown in (5.3). The components of (5.3) for all of the thermal impedances of Figure 5.2 are described in Table 5.2.

$$(5.3) \quad R_{thermal} = \frac{l}{k_t a}$$

Table 5.2: Description of Thermal Impedances for Anisotropic Core Model.

Subscript	Description	Dimension	Length (l)	Area (a)	Thermal Conductivity ( $k_t$ )
$G_r$	Gap conduction	radial	$l_G/2$	$2\pi R_n h$	0.6 – 1.4 w/mk
$C_r$	Core conduction	radial	$t/2$	$2\pi R_n h$	5 – 10 w/mk
$G_z$	Gap conduction	height	$l_G/2$	$2\pi R_n t$	0.6 – 1.4 w/mk
$C_z$	Core conduction	height	$h/2$	$2\pi R_n t$	5 – 10 w/mk
$C_{onz}$	Convection	height	1	$2\pi R_n t$	5-500+
$C_{onl}$	Inner convection	radial	1	$2\pi R_l t$	5-500+
$C_{onO}$	Outer convection	radial	1	$2\pi R_l (l_G+t)$	5-500+
$R_{adz}$	Edge radiation	height	$T-T_{amb}$	$2\pi R_n t$	$\epsilon\sigma_s(T-T_{amb}^4)$
$R_{adl}$	Inner radiation	height	$T-T_{amb}$	$2\pi R_l (l_G+h)$	$\epsilon\sigma_s(T-T_{amb}^4)$
$R_{adO}$	Outer radiation	height	$T-T_{amb}$	$2\pi R_l (l_G+h)$	$\epsilon\sigma_s(T-T_{amb}^4)$

Values for constants are easily found in various textbooks and research and are presented from [144], [145], [146]. The core is assembled of  $N_L$  layers such that  $R_n$  is the radius at the center of a ribbon of the  $n^{th}$  layer. The  $G$  region is the gap between two ribbon layers and  $t$  is the thickness of a ribbon layer. The dimension  $l_G$  can also be used to account high thermal impedance materials between ribbon layers and between the ribbon and air. This can be used to represent thin oxidation layers or epoxies. The radial  $G$  effect can be estimated by using the

thermal impedance of air, oxidation, or epoxy with the core fill factor. High fill factors would have low  $G$  region impedances while low fill factor cores would have a high anisotropy in the tangential and radial dimensions. The thermal anisotropy varies significantly with the bulk magnetic core fill factor. The ratio of thermal conductivity between the tangential and radial directions of toroid is shown in (5.4) where  $F$ , the fill factor, is the ratio of the core thickness,  $t$ , and the sum of the ribbon thickness and the gap thickness,  $G$ . This ratio can be near five for typical fill factors, around 80-85%, ribbon thicknesses, and fill materials. This assumes the ribbon and  $G$  region have thermal constant conductivities of  $k_c$  and  $k_G$  respectively.

$$(5.4) \quad \frac{k_t}{k_r} = \frac{(k_g G + k_c t) \left( \frac{G}{t} + \frac{k_g}{k_c} \right)}{(G+t) \left( \frac{k_g G}{t} + k_G \right)} = F^2 \left( 2 - \frac{k_c^2 + k_G^2}{k_c k_G} \right) + F \left( \frac{k_c^2 + k_G^2}{k_c k_G} - 2 \right) + 1$$

The effective thermal impedance for convection is determined using Newton's law of cooling. The variation in the  $k_{[c/G]}$  value, replacing the traditional symbol  $h$ , for the coefficient of convective heat transfer in this impedance is due to the different cooling methods ranging from natural, unforced air convection to higher performance forced liquid cooling. The thermal impedance modelling radiation utilizes Stefan's law and reorganizes the law into the form of a typical thermal impedance. In these impedances,  $T$  is used to represent the core layer temperature and  $T_{amb}$  the ambient temperature.

In the above Figure 5.2, the basic model most properly represents interior layers of the ribbon. For the innermost and the outer most layers a slight modification is needed. Specifically, the model region defined as *core-air interface* connects to both the  $z$  dimension and the radial dimension. These augmentations to the radial thermal impedance account for the convection and radiation associated with the exposed broad surface of the inner and outer most ribbon layers. These are represented by the two edge regions of *core-air interface inner* and *outer* respectively.

This model is then connected to other radial models to represent the different tangential zones of the magnetics. Three examples of zones are uncovered, covered with heat sink material, and covered with heat injection component. Uncovered zones can be represented by the above model without any modifications. The two covered zones both effect the  $z$  dimension thermal resistances and while a covered with heat injection component could potentially add to the heat injection. That is, a heat sink material adds its own thermal model between the edge, inner, or outer impedances depending on its physical connection to the core. Alternatively, a heat injection component has several aspects to consider for complete thermal modelling. A prime example of a potential external heat injection component is the excitation coils in a magnetic component. One of the simplest modifications is modelling the use of a thermal insulator between the excitation coil and core. With this scenario, the effected region does not have significant heat flow paths to ambient and thus all model connections to the sink can be removed. However, if a thermal conductor is used, one must consider the heat injection caused by the heating of the excitation winding. The thermal path from the core to the thermally conductive bobbin to the excitation coil does have a path to free space and thus the thermal resistances to ambient of convection and radiation can be included.

With a complete thermal model of the transformer we can see that the local loss profile has a significant impact on the temperature profile of the core. The thermal anisotropy between the radial and tangential dimensions further couples the temperature profile to the local losses. Where the thermal body be isotropic, the temperature profile would normalize somewhat but still be heavily dependent on the heat injection profile. The thermal impedances in the  $z$  dimension have some variations between the layers due to varying surface areas but it is minimal. The exception to this trend is the inner most and the outermost layers and the layers where the broad

surfaces are exposed to ambient temperatures. Thus, the radiative and convective impedances at these two layers allow significant heat flow and ultimately a steady state temperature nearer to ambient. This effects closely adjacent layers due to the larger temperature difference.

### **5.6.1 Heating Impact**

The heating of the core has several impacts. The core must remain below certain temperatures, e.g. the Curie or impregnated epoxy breakdown temperatures, with safety margins that would affect fundamental core properties. However, in most practical power magnetics designs there are even lower critical temperatures that are important to avoid such as the thermal limits of insulating epoxies or plastics.

While these limits exist, one may wish to have designs that further limit the maximum core temperature. The temperature impacts on the operating performance of cores is generally material specific with [52] providing some polynomial approaches to account for the variations in ferrites. An example of a ferrite material that has a wide range of variation due to heating is L material [147]. Nearly all performance metrics have varying sensitivities to operating conditions including permeability, core loss and saturation flux density. While ferrites have shown this variability it is not always the case for nanocrystalline [127]. In that study, cores were shown to have minimal variation in measured core losses over a reasonable temperature range. However, the effective relative permeability of the core changed significantly. In operating up to 80°C, the effective relative permeability of the core dropped roughly 300%. This resulted in a much lower transformer magnetizing inductance. In a practical converter this could result in up to a nine-fold increase in conduction losses as a result of a 3x increase in the required magnetizing current. This increase in current would also have to be accounted for in determining the system maximum current rating and the selection of winding gauge. However, this increase in

magnetizing current could be used advantageously as certain converters utilize magnetizing current to increase the window for which semiconductor switching losses are minimized. The authors in [148] and [77] showed how so-called soft switching of converters can utilize magnetizing current for improved operation. Thus, regardless of the design, it is important to have a firm grasp of the overall operating temperature and to understand the implications that this temperature has on the magnetic core performance.

### **5.7 Strain annealing profiles**

As mentioned above, applying mechanical strain as a post-production process to the magnetic ribbon causes variations in the relative permeability. By applying an arbitrary strain profile along the length of the ribbon, a core with an arbitrary relative permeability between various layers of ribbon in the radial direction can also be manufactured. While the ultimate profile achievable could be arbitrary, four fundamental profiles are presented here for their logical and practical utility as well as their manufacturability during the strain annealing process without the need for highly sophisticated process controls. These profiles are constant strain, ramped strain, ramped strain with initial strain, and exponential strain. These profiles will be discussed in further detail in the respective subsections. In this analysis, there are a myriad of variables to explore and potentially many local inflection points in relative performance. As such, this analysis is meant to provide an initial overview and to allow further in-depth study for specific cases. For all of the presented design cases, the core permeance was held to be the same. In this way, the comparison of strain annealing approaches is for magnetic devices with the same inductance, as inductance is equal to the permeance times the turns squared. Each strain annealing profile is analyzed to present the average flux density, permeance, loss estimation

based on the average flux density, the heat injection, and finally the loss calculation based on the local flux density.

The profiles are presented in terms of the core radius to easily apply the proposed permeability to the definition of flux density. However, this radially defined profile does not provide insight into the strain profile. For this, we must determine the length along the ribbon for which the strain should be applied. While the toroid is constructed as an Archimedean spiral, a simplified approximation yields adequate results. The length function is then presented in (5.5). The layer number,  $L_n$ , is determined by (5.6). Once a desired permeability profile is chosen, the length for which the strain should be applied,  $l_r$ , given a desired radius location,  $r$ , is easily determined in (5.7).

$$(5.5) \quad L_r = \pi L_n \left( 2r_i + \frac{t}{F} (L_n - 1) \right) \qquad (5.6) \quad L_n = \frac{F(r-r_i)}{t}$$

$$(5.7) \quad L_r = \pi \left( \frac{Fr^2}{t} - \frac{Fr_i^2}{t} - r - r_i \right)$$

### 5.7.1 Assumptions used in Analysis

As with any numerical analysis and modelling of physical systems, certain assumptions must be made. There are three primary assumptions used in this analysis. The first is that the loss term,  $\beta$ , does not change with the strain and permeability or temperature. Future work will verify this assumption or provide functions and curves to account for the impact. The initial samples under investigation have not shown significant variations. Another simplification is that the core height,  $h$ , or strain annealed ribbon width is constant. While applying strain, the ribbon stretching causes elongation in the axis of the applied strain and shrinkage in the other axes. This can result in a reduction of the thickness of the ribbon and the width of the ribbon. The cross sectional area is consequently reduced. This could lead to a slightly higher than predicted flux density in the

ribbon required due to the reduced area. The third assumption is that the magnetic and electric properties of the core material will not change with temperature. While it has been shown to have significant effects, [127], incorporating the full impact requires a specific core thermal model. Furthermore, the initial core parameters will remain sufficiently unaffected while the core temperatures remain low. It is with the understanding of the variations and the assumptions that the forthcoming analysis remains adequate for the understanding of strain annealing effects on the total core losses of a finished magnetic core. For this analysis, the loss term and the ribbon width, core height, and thickness terms were assumed constant and unvarying with temperature.

In the forthcoming analysis, the relative permeability, scaled by the permeability of free space,  $\mu_0$ , is represented by  $\mu$ . The subscript denotes the type of strain annealing profile. The differential volume of the toroid reduces to the circumference at that radius multiplied by the differential radius volume. The ratio between inner radius,  $r_i$ , and outer radius is denoted with  $\lambda$ . As shown in [128], a set of Steinmetz parameters  $k$ ,  $\alpha$ , the frequency,  $f$ , and loss component,  $\beta$ , can be used to fit the loss curves for an arbitrary excitation using the Steinmetz equation, (2.25). As mentioned in a previous section, the authors in [149] showed how a map or surface of measured losses can be fitted using (2.25) for several common excitation waveforms. In the following analysis, accurate parameters are assumed to have been measured and fitted. The scaling factor,  $k$ , has a wide range of values and can be used to modify the equation to handle parameters extracted for either 1000's of Hz or kHz. In other words,  $k$ , could be different by a factor of  $1000^\alpha$  depending on if frequency,  $f$ , is analyzed in Hz or kHz. The frequency factor,  $\alpha$ , is typically in the range of 1 - 3 while the flux density term,  $\beta$ , is between 2 - 3.

### 5.7.2 Constant Permeability

This strain annealing profile has no profile variation from the permeability of traditional cores. However, reducing the permeability of the core by applying strain could eliminate the need of air gaps or achieve some other specifically desired relative permeability. In this application, a constant strain is applied to the ribbon to result in a constant permeability for the entire ribbon. Thus the radially dependent permeability is a constant (5.8). As a wound toroid core, this strain annealing profile would result in a magnetic flux density profile that is like any other core of the same constant permeability. As such, this approach will be used as the baseline for comparison of other strain annealing profiles.

$$(5.8) \quad \mu(r) = \mu_c$$

By averaging the radially dependent flux density over the boundaries of the core it is clear that the average flux density is (5.9), where  $N$  is the number of turns in the exciting coil and  $I$  is the exciting current. The resulting core permeance for a core of height,  $h$ , is derived from the flux and is shown in (5.10). These dimensions can be seen below in Figure 5.1. By using the flux density averaged over the entire core and the total core volume in Steinmetz loss equation we can see that the losses based on the average flux density is shown in (5.11).

$$(5.9) \quad B_{avg} = \frac{NI\mu_c \ln(\lambda)}{2\pi r_i(\lambda-1)}$$

$$(5.10) \quad \hat{P} = \frac{\phi}{NI} = \int_0^h \int_{r_i}^{\lambda r_i} B(r) dr dz = \frac{h}{2\pi} \mu_c \ln(\lambda)$$

$$(5.11) \quad P(B_{avg-\mu_c}) = V k f^\alpha B_{avg}^\beta = k f^\alpha h \pi r_i^2 (\lambda^2 - 1) \left(\frac{NI}{2\pi}\right)^\beta \left(\frac{\mu_c \ln(\lambda)}{r_i(\lambda-1)}\right)^\beta$$

For understanding the heat injection profile, it is useful to investigate the local power loss (5.12). This is equivalent to the heat injection,  $Q$ , in the thermal model. Here the volume is the local slice of volume.

$$(5.12) P_{loc-\mu_c} = Q = kf^\alpha hC(r)tB(r)^\beta = kf^\alpha ht2\pi r^{1-\beta} \left( \frac{\mu_c NI}{2\pi} \right)^\beta$$

Finally, an estimation of the losses using the local flux density is presented in (5.13). This method of loss calculation applies the Steinmetz equation to small slices of the core. As such, the differential volume is needed. This volume is equivalent to the circumference of the infinitely thin slice and is represented by  $C(r)$ . The height of the core is a scalar to the volume and is independent of the radius.

$$(5.13) P(B_{loc-\mu_c}) = kf^\alpha h2\pi r \left( \frac{NI}{2\pi} \right)^\beta \frac{\mu_c^\beta r_i^{2-\beta} (\lambda^{2-\beta} - 1)}{2-\beta}$$

With two estimations for losses, one based on the average flux density and the other based on the summation of local losses, a comparison of differences between the two can provide insight into the design cases for which the numerical simplification of using  $B_{avg}$  is valid (5.14). A surface of this ratio is shown below in Figure 5.3. It is important to note that all constant permeability design cases result in less than a 10% variation in estimation. It is only when ratio between inner and outer radii,  $\lambda$ , is high and the loss term,  $\beta$  is low that the estimation difference is at its greatest. However, using the average flux density to predict magnetic core losses obfuscates the thermal impacts by considering the losses as a whole and not as a profile. Furthermore, this loss estimation will miss the loss impacts of different strain annealing profiles with the same permeance.

$$(5.14) \frac{P(B_{avg-\mu_c})}{P(B_{loc-\mu_c})} = \frac{\ln(\lambda)^\beta (\lambda^2 - 1)(2 - \beta)}{2(\lambda^{2-\beta} - 1)(\lambda - 1)^\beta}$$

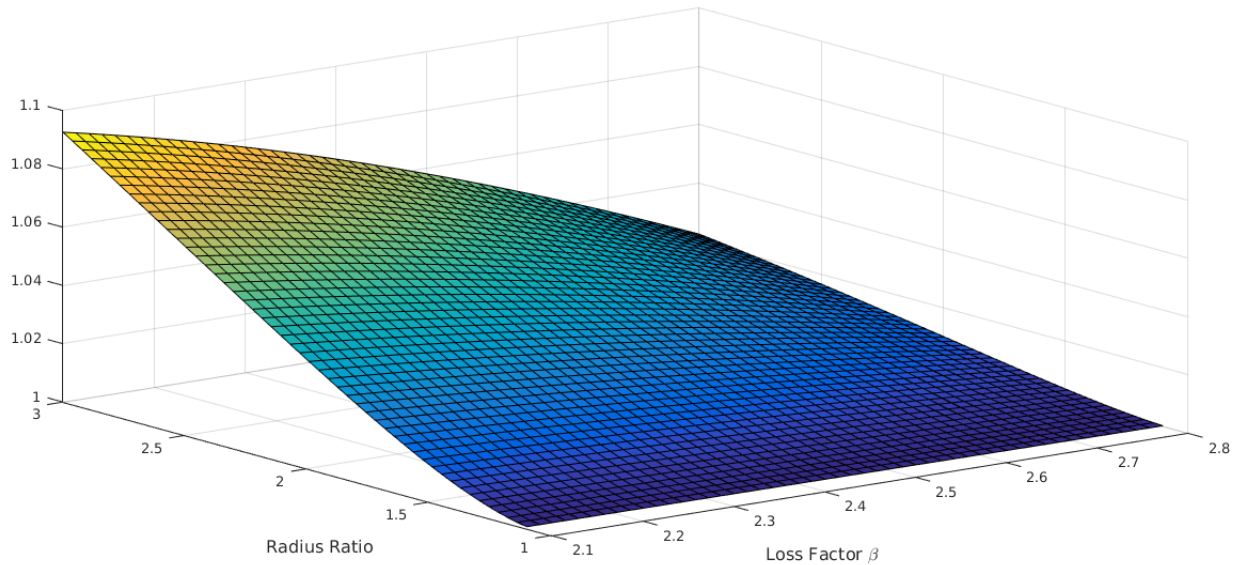


Figure 5.3: Ratio of Loss Calculation Methods Surface.

Using (5.13), loss contours for the general design space for power magnetics can be established. Specifically, the local losses can be studied under four different scenarios. This would be the combination of low and high inner radii and low and high permeability. In this case, the low inner radius is 10mm and the high inner radius is 100mm. The relative permeability is chosen with the focus of power inductors where low permeability is generally ideal. In this case, the permeabilities studied are  $10\mu_0$  for the low permeability case and  $100\mu_0$  for the high permeability case. The values of the contour are loss scalars that reflect division of common variables. These common variables are shown below in (5.15). For all of the strain annealed permeability profiles, the contours in Figure 5.4 will be used as the baseline to compare the impact of a strain annealed induced permeability profile on the toroid's magnetization losses. These curves show the scalar term of a constant permeability design local loss. In other words, a constant permeability design total losses could be determined by multiplying (5.15) by a point of the curve corresponding to the chosen design.

$$(5.15) \quad kf^\alpha h 2\pi \left(\frac{NI}{2\pi}\right)^\beta \mu_0^\beta$$



the same strain and results in the same permeability over the layer. This profile has the minimum variation between maximum and minimum flux density as they should, within manufacturing tolerances, be the same. The permeability function is shown below in (5.16).

$$(5.16) \quad \mu(r) = \mu_s r$$

This permeability profile effectively forces each ring of the toroid to be the same reluctance. This results in an even distribution of magnetic flux. Other researchers have proposed other solutions to achieve the same goals, [150]. However, since these approaches required changing the physical cross section of the core, they create numerous manufacturing difficulties. With the inline nature of strain annealing, the same effect can be achieved with minimal increases in manufacturing processes.

The average flux density and permeance for a graded permeability profile are shown below in (5.17) and (5.18). As mentioned above, the flux density profile is flat such that it is equivalent to the average flux density along the entire core profile. Therefore, the flux density is no longer dependent on the core radius. The power loss due to the average flux density, (5.17), is shown below in (5.19). Again, the basic Stienmetz estimation is used for losses.

$$(5.17) \quad B_{avg-\mu_s} = \frac{NI}{2\pi} \mu_s \qquad (5.18) \quad \hat{P} = \frac{h}{2\pi} \mu_s r_i (\lambda - 1)$$

$$(5.19) \quad P(B_{avg-\mu_s}) = kf^\alpha h\pi r_i^2 (\lambda^2 - 1) \left(\frac{NI}{2\pi}\right)^\beta \mu_s^\beta$$

The local losses are calculated for this profile in (5.20). It is interesting to note that despite the flat flux density profile, the heat injection profile along the core is not flat. This is because the volume of the core rings increases with the increasing radii of the discrete ring.

$$(5.20) \quad P_{loc-\mu_s} = kf^\alpha h t 2\pi r \left(\frac{\mu_s NI}{2\pi}\right)^\beta$$

Finally, the total losses, calculated locally, is shown in (5.21). The percent change in losses are shown below in Figure 5.5. In these design comparisons, the slope factor,  $\mu_s$ , is chosen to ensure that the linearly graded permeability results in the same core permeance as the constant permeability core permeance.

$$(5.21) \quad P(B_{loc-\mu_s}) = kf^\alpha h 2\pi r \left(\frac{NI}{2\pi}\right)^\beta \frac{\mu_s^\beta r_i^2 (\lambda^2 - 1)}{2}$$

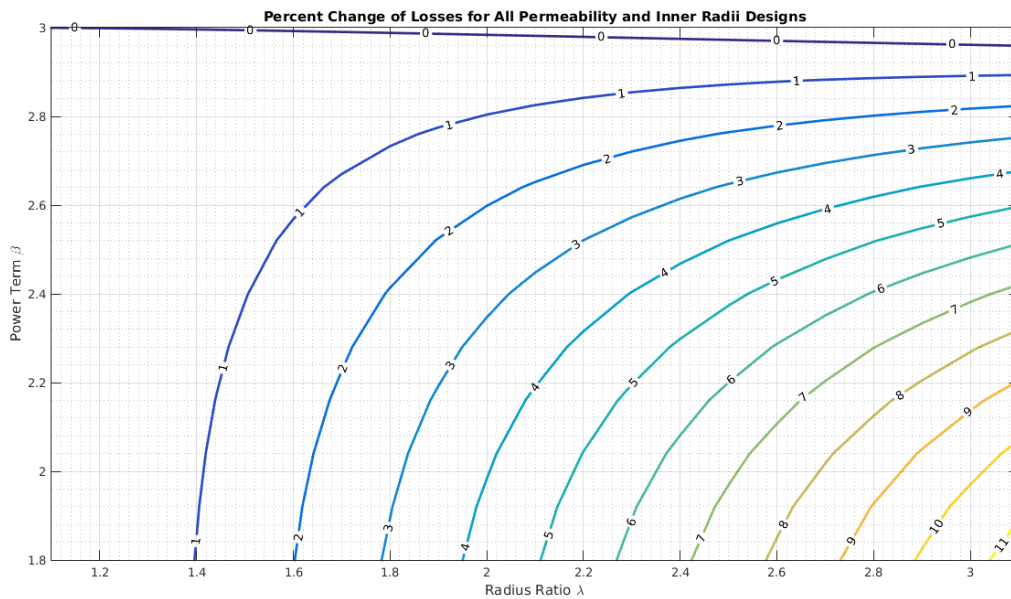


Figure 5.5: Graded Permeability Toroid Magnetization Loss Percent Change.

Interestingly, when designed to match the permeance of the constant permeability profile the linearly graded permeability, flat flux density profile, design has the same loss increase for all four design cases. In fact, it is easily shown that the loss ratio reduces to (5.22) which is equivalent to (5.14). Again, using the common radius ratio and loss term for power magnetics of 2 and 2.4 respectively we can observe that there is a 2.8% additional loss for this profile and design point.

$$(5.22) \quad \frac{P(B_{loc-\mu_g})}{P(B_{loc-\mu_c})} = \frac{\ln(\lambda)^\beta (\lambda^2 - 1)(2 - \beta)}{2(\lambda^{2-\beta} - 1)(\lambda - 1)^\beta}$$

To generalize, the change in losses is independent of the inner radius and the effective constant permeability that the graded permeability design is replacing. The increase in losses is lowest for high flux density loss terms and low radii ratios. The highest increase in losses is for low loss terms with high radii ratios, however this increase is less than a 10% increase. In general, there is a minimal penalty of increased losses in magnetic losses for this strain annealing profile. The benefit of reducing the peak flux density differences along the core geometry may be more important than the costs of slightly increased losses for many designs if they are observed in practice.

#### **5.7.4 Linear Graded Permeability with Offset**

Logically the next straining profile to investigate is a linearly graded permeability that has a non-zero y intercept. For this permeability function, the permeability when the radius is chosen as zero is nonzero, in contrast to the previously mentioned linear graded permeability profile. This profile could account for two common scenarios. First, the magnetic ribbon does not have the mechanical strength to withstand the peak strain forces needed for the linearly graded permeability. With a lower permeability slope applied, the effective permeability at the low end must be increased to ensure that the permeance matches the base case of constant permeability. Similarly, the magnetic properties of the ribbon at the beginning and end permeabilities could be significantly worse than nominal. To ensure that the magnetic ribbon performances is not too far degraded, an operational window of permeabilities could be enforced. This minimum and maximum allowable permeabilities would then define ribbon start and end permeabilities with a linear slope applied between the two. Functionally, the permeability profile is described below in (5.23). One point to note, the subscript for the offset

permeability is chose as 'l' instead of the letter 'o', for 'offset', to avoid confusion between the strain annealed permeability profile and the permeability of free space,  $\mu_0$ .

$$(5.23) \quad \mu(r) = \mu_1 + \mu_s r = \mu_1(1 + gr)$$

In order to simplify the analysis, the offset permeability,  $\mu_l$ , is extracted from the slope permeability such that the functional permeability is equivalent to the right most form of (5.23). The benefits of this are apparent in investigating the average flux density, (5.24), where the offset permeability is treated as scalar to two types of permeability functions, constant and linearly graded. Permeance is shown in (5.25). The estimated losses using the average flux density is shown below in (5.26).

$$(5.24) \quad B_{avg-\mu_1} = \frac{NI}{2\pi} \mu_1 \left( \frac{NI}{r_i(\lambda-1)} + g \right)$$

$$(5.25) \quad \hat{P} = \frac{h}{2\pi} \mu_1 (\ln(\lambda) + gr_i(\lambda - 1))$$

$$(5.26) \quad P(B_{avg-\mu_1}) = kf^\alpha h\pi r_i^2 (\lambda^2 - 1) \left( \frac{NI}{2\pi} \right)^\beta \left( \mu_1 \left( \frac{\ln(\lambda)}{r_i(\lambda-1)} + g \right) \right)^\beta$$

The local power, heat injection, for the strain annealed profile that is linearly graded with an offset is shown below in (5.27).

$$(5.27) \quad P_{loc-\mu_1} = kf^\alpha ht2\pi r \left( \frac{NI}{2\pi} \mu_1 \left( \frac{1}{r} + g \right) \right)^\beta$$

The total power loss due to this strain annealing profile is shown below in (5.28). It should be noted that  $B_z[a, b]$ , is the incomplete beta function [151]. The derivation from the basic local power loss equation to (5.28) is provided in Appendix A. Again, the utility of extracting the offset permeability from the slope permeability is shown through the simplification in the derivation of (5.28). Specifically,  $\mu_l$  is able to be removed from the integrand.

$$(5.28) \quad (B_{loc-\mu_1}) = kf^\alpha h 2\pi r \left(\frac{NI}{2\pi}\right)^\beta (-g)^{\beta-2} \mu_1^\beta (B_{-g\lambda r_i}[2-\beta, 1+\beta] - B_{-gr_i}[2-\beta, 1+\beta])$$

There are now at least two types of linearly graded permeability with an offset that could be compared to the base case. In order to solve for the necessary offset permeability for this analysis, two types of permeability slope gains,  $g$ , were chosen of 5 and 50 and are represented with dashed and solid lines respectively. The percent change in magnetization losses are shown below in Figure 5.6 for different geometric and profile design cases. Analytically, the loss ratio is shown in (5.29).

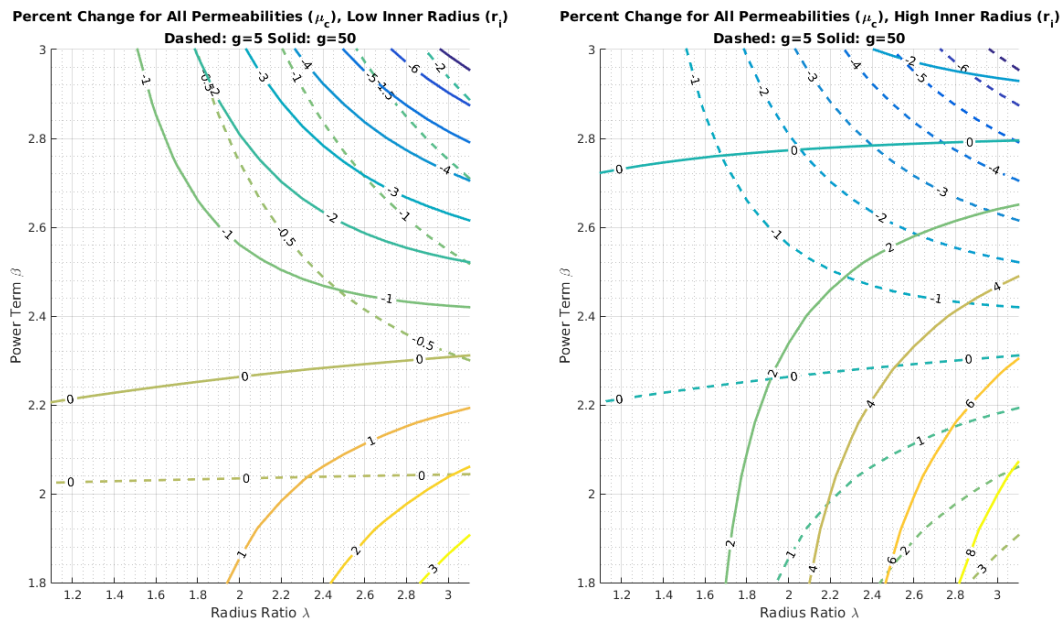


Figure 5.6: Graded with Offset Permeability Toroid Magnetization Loss Percent Change.

$$(5.29) \quad \frac{P(B_{loc-\mu g})}{P(B_{loc-\mu c})} = \left(-\frac{r_i g \ln(\lambda)}{\ln(\lambda) + g r_i (\lambda - 1)}\right)^\beta \frac{(2-\beta)(B_{-g\lambda r_i}[2-\beta, 1+\beta] - B_{-gr_i}[2-\beta, 1+\beta])}{(-g r_i)^2 (\lambda^{2-\beta} - 1)}$$

From the above figure and (5.29), there are several interesting conclusions to make. The first being that a low slope gain of permeability can provide some improvements in the magnetic core losses over most of the design space. While these improvements are small, they are

nonetheless significant compared to the linear graded permeability with zero offset where all designs had incurred penalty of higher magnetizing losses. Furthermore, the high slope gain also shows some loss improvements. However, these improvements are limited to low inner radius designs with high power terms. For high inner radius designs, the improvements exist in a much smaller design space with penalties that more closely reflect those of the zero offset designs. It is also important to note that all of the trends exist independent of the level of the baseline constant permeability.

Again, the common design of a radius ratio of 2 and loss term of 2.4 is chosen as an example. For low inner radius designs, a low  $g$  of 5, results in a negligible loss reduction of 0.2% and for high  $g$  of 50, the loss reduction is marginally better at 0.4%. For high inner radii designs, the loss reduction for low gains is still small at 0.4% however there is penalty at high gains with a 1.8% loss increase.

### 5.7.5 Exponential Permeability

The fourth and final strain annealed permeability profile examined in this analysis is a profile that changes exponentially with the core radius. There is a scalar term defined as  $\mu_e$  and the exponent is the variable  $c$ . This profile is defined in (5.30). One motivation of this profiles is to effectively invert the flux density concentration in a core. This would shift the heat injection to the outer edges of the core where the natural thermal impedance to convection and radiation is lower. Similarly, shifting the hotspot to the exterior of a core enables easier access and more surface area for application of cooling through a heat sink or other active measure.

$$(5.30) \quad \mu(r) = \mu_e r^c$$

The average flux density and core permeance are shown below in (5.31) and (5.32) respectively.

$$(5.31) \quad B_{avg-\mu_e} = \frac{NI\mu_e r_i^c (\lambda^c - 1)}{2\pi c r_i (\lambda - 1)}$$

$$(5.32) \quad \hat{P} = \frac{h}{2\pi} \frac{\mu_e r_i^c}{c} (\lambda^c - 1)$$

The estimation for power losses using the average flux density is presented in (5.33). The local heat injection due to localized losses is shown in (5.34).

$$(5.33) \quad P(B_{avg-\mu_e}) = kf^\alpha h \pi r_i^2 (\lambda^2 - 1) \left(\frac{NI}{2\pi}\right)^\beta \left(\frac{\mu_e r_i^c (\lambda^c - 1)}{c r_i (\lambda - 1)}\right)^\beta$$

$$(5.34) \quad P_{loc-\mu_e} = kf^\alpha h t 2\pi r \left(\frac{\mu_e r^c NI}{2\pi r}\right)^\beta$$

Finally, the losses calculated by using the local flux density is shown in (5.35). The percent change in losses of the exponential permeability profile are compared to the baseline of constant permeability below in Figure 5.7 with the corresponding ratio shown in (5.36).

$$(5.35) \quad P(B_{loc-\mu_e}) = kf^\alpha h 2\pi r \left(\frac{NI}{2\pi}\right)^\beta \frac{\mu_e^\beta r_i^{\beta(c-1)+2} (\lambda^{\beta(c-1)+2} - 1)}{\beta(c-1)+2}$$

$$(5.36) \quad \frac{P(B_{loc-\mu_e})}{P(B_{loc-\mu_c})} = \left(\frac{c \ln(\lambda)}{\lambda^c - 1}\right)^\beta \frac{(2-\beta)(\lambda^{\beta(c-1)+2} - 1)}{(\beta(c-1)+2)(\lambda^{2-\beta} - 1)}$$

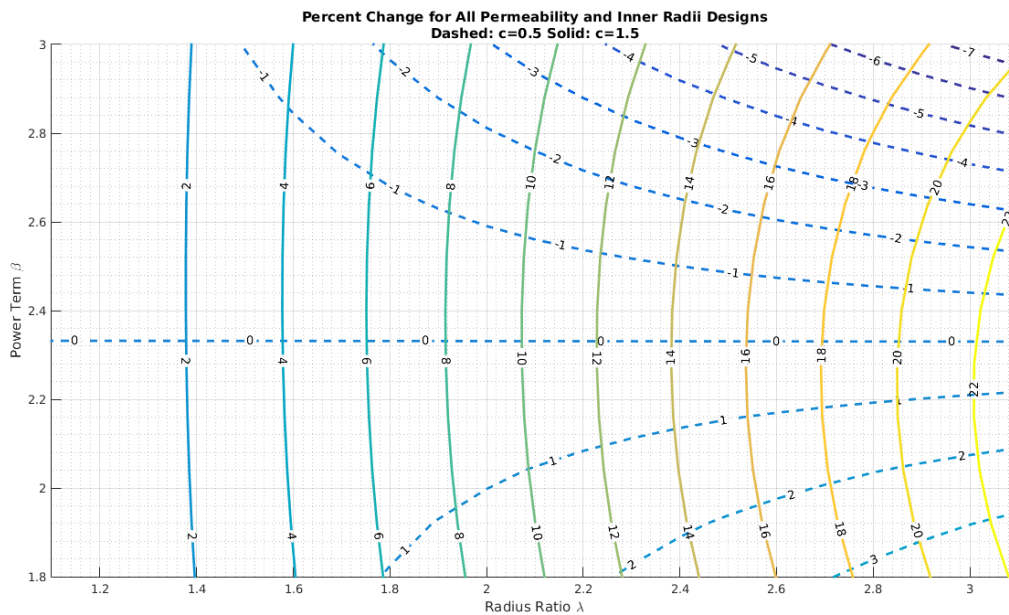
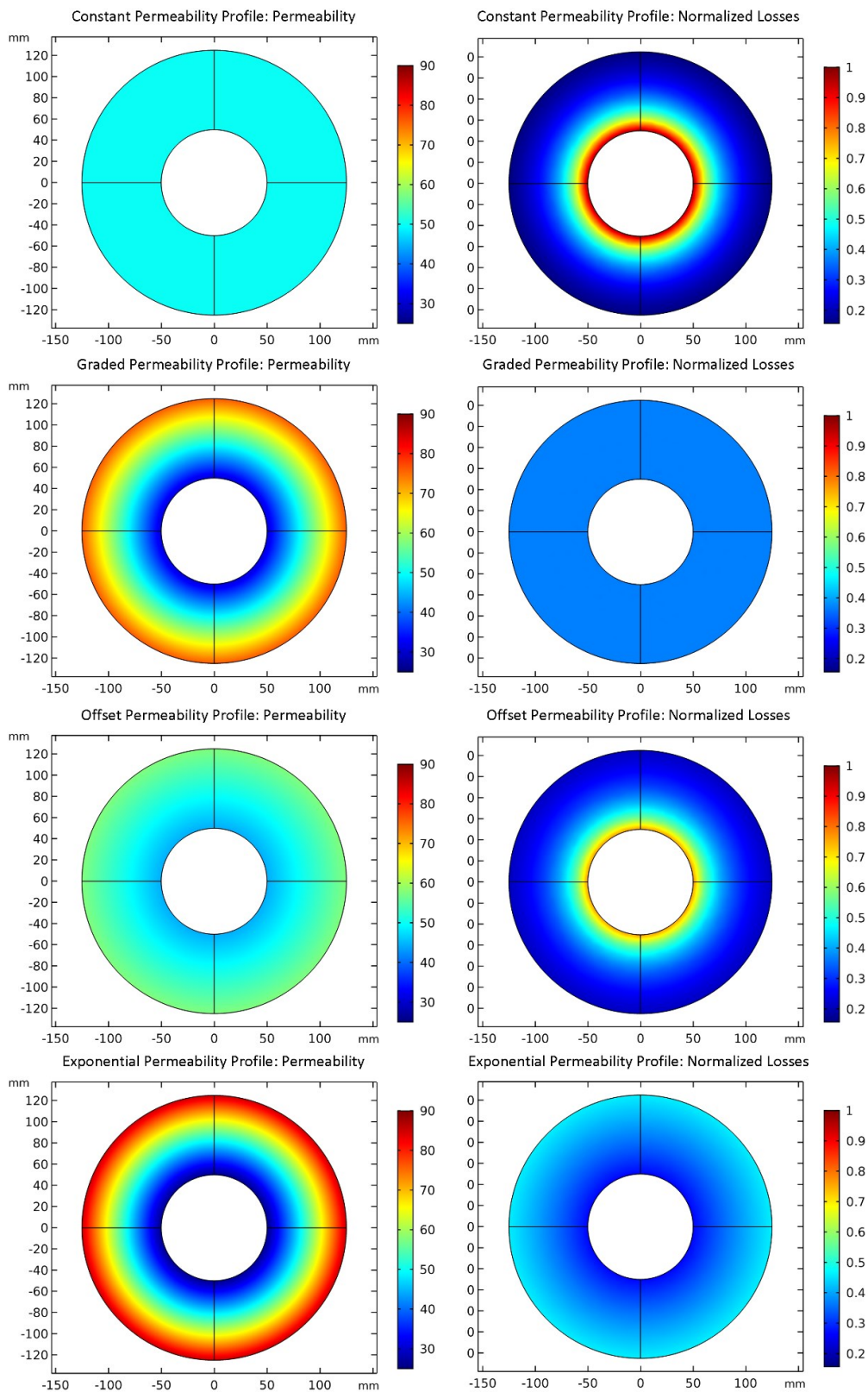


Figure 5.7: Exponential Permeability Toroid Magnetization Loss Percent Change.

The contours of Figure 5.7 show the general approach to the exponentially graded permeability profile. The first and foremost observation is that regardless of the inner radius level or the baseline permeability level the loss changes are the same for this profile when the permeance of the profiles is chosen to match the constant permeability permeance. For this permeability profile type, when the exponent is low, there are some small benefits in overall losses e.g. a loss reduction of 0.2% for the example core of a radius ratio of 2 with a power term of 2.4. Higher exponents result in higher losses and significantly higher losses as the radius ratio increases with a 9.1% increase in the example core. In fact, with high exponent values, the change in losses depends mostly on the radius ratio.

### **5.8 Example Comparison of Permeability Profiles**

The different strain annealed permeability profiles are compared in an example power inductor through Comsol FEA. This simple design comparison is used to explore the different permeability and core loss profiles for practical applications. The permeability profile and loss profile is shown further below in Figure 5.8. The left column of surface plots shows the relative permeability of the core for the different strain profiles. The right column shows the local loss profile which corresponds to the heat injection, ultimately reflecting core temperature rise due to the thermal anisotropy shown in Figure 5.2.



*Figure 5.8: FEA Analysis of Constant Strain Annealed Toroids. Descending: Graded, Graded with an Offset, Exponential; Left: Permeability Profiles; Right: Normalized Losses.*

For this example, the following variables were set with their corresponding values: with an inner radius,  $r_i = 50\text{mm}$ ,  $\lambda = 2.5$  for an outer radius,  $r_o = 125\text{mm}$ , the baseline constant permeability,  $\mu_c = 50$ , and the loss term,  $\beta = 2.5$ . In order to solve for the remaining variables in the offset permeability profile and exponential permeability profile, the values of  $g$  and  $c$  were set to 5 and 1.3. All free variables are solved to ensure that each strain annealed core has the same inductance as the constant relative permeability design.

The tabularized results of the flux density, normalized core loss terms and validity of above presented equations for this example, Table 5.3, show the significance of the controlled strain annealing approach to impacting the thermal profile of a magnetic core. For a given inductor, new thermal management regimes can be employed. For instance, all strain annealing approaches reduce the peak thermal injection by reducing the local losses in the core. This enables improved performance with minimal redesign. Alternatively, more improvement could be achieved by using either the graded or exponential approaches in this example that result in the toroid hot spots shifting to the outside. This translates to higher heat injection on the outside of the core from the inside. As discussed above, the outer layers of the core have reduced thermal impedances for heat flow to ambient. Additionally, the outside of the core is usually easier to access physically than the inside of the core. This means that an external heatsink, attached to the outside of the core can have a greater impact. The heating is now closer to the highest levels of heat injection into the core and thus can better sink heat away from the hotspot of the core.

*Table 5.3: Losses and Peak Flux Density for Various Strain Annealing Profiles.*

Strain Profile	$B_{\text{Peak}}$ (T)	$B_{\text{Peak}}$ Reduction	FEA Loss Scalar	FEA Vs. Calculated
Constant	0.081	0	1.0482	0.0010%
Graded	0.050	-38.13%	1.0992	0.0056%
Offset	0.072	-11.06%	1.0384	-0.0133%
Exponential	0.055	-31.79%	1.1596	0.0026%

These FEA results show that significant improvements in core performance can be achieved through strain annealing. Notably, the peak flux density can be significantly reduced

while maintain the same inductance. The temperature profile can also be tuned and controlled through strain annealing for application advantages. The presented analytical expressions show very close correlation with the FEA analysis and are proven to be valid.

## 5.9 Hardware Example

The controls and processing for managing continuous magnetic ribbon straining have very recently been completed to enable hardware testing. Two cores were manufactured from raw ribbon stock of a cobalt rich metal amorphous nanocomposite. The as cast relative permeability is around 80. From this stock material, the two cores were subjected to strain annealing to result in a core with a constant relative permeability profile and a graded with an offset relative permeability profile.

The constant permeability core was strain annealed to a permeability of  $\mu_c = 38.3$  and confirmed with thin strip testing. The linearly strained permeability is slightly more difficult to determine due to the nonlinear relationship between strain and resulting permeability. However, in this example, the range of strain results in a relatively constant and linear variation. Using strip testing on the beginning and the end of the ribbon the permeability function was interpolated to be  $\mu_g(r) = \mu_l + \mu_s r = 17.446 + 334r$ . The average flux density for the two cores of constant permeability,  $B_{avg\mu_c}$ , and graded permeability,  $B_{avg\mu_g}$ , is determined using the equations (5.9) and (5.24) from the analysis above. The ratio of power loss is then simply determined by comparing the ratio of power loss using Steinmetz equation and the respective average flux densities as presented in (5.29). Due to uncertainties in the final flux density loss term,  $\beta$ , an assumption was made that the two cores were the same  $\beta$  and then the result for a range of values was explored for,  $2 \leq \beta \leq 2.5$ . This resulted in a loss ratio of  $1.185 \leq \frac{P(\mu_c)}{P(\mu_g)} \leq 1.376$  for the

local flux density method and a loss ratio of  $1.22 \leq \frac{P(\mu_c)}{P(\mu_g)} \leq 1.329$  when the losses are calculated using the average flux density method. These ratios show a predicted reduction in losses by using the strain annealed profile. These analytical predictions match very close to the measured results where the constant permeability core produced 13.11 W of loss and the linearly graded with an offset produced 10.15 W of loss. This resulted in a 22.5% reduction in losses which agrees very well with the previously stated range of loss reduction.

In order to complete the comparison, it is important to confirm any variation in the resulting inductance, (5.37), due exclusively to permeance changes. Ultimately, the graded permeability core will be tuned to perfectly match a homogenous permeability core. However, at this initial stage, small variations in inductance due to high experimental manufacturing tolerances are acceptable. The variation for this experiment is shown below and is shown to be within a low tolerance.

$$(5.37) \quad \frac{L_{\mu_c}}{L_{\mu_o}} = \frac{\mu_c \ln\left(\frac{r_o}{r_i}\right)}{\mu_l \ln\left(\frac{r_o}{r_i}\right) + \mu_s(r_o - r_i)} = \frac{38.3 \ln\left(\frac{0.081}{0.031}\right)}{17.446 \ln\left(\frac{0.081}{0.031}\right) + 334(0.081 - 0.031)} = 1.0995$$

Figure 5.9 shows a thermal line plot of the temperature of the two cores along the radial dimension. These lines were developed using a FLIR thermal camera and the FLIR post processing software where several temperature measurement lines were taken. Figure 5.9 shows the average of all of the lines taken at different angles along the radial dimension. [152] further explores the creation, testing and processing of these cores. While there are obvious visual differences in temperature between the constant permeability core, and graded with an offset core, the total reduction in peak temperature is about 30% from nearly 91.6°C down to about 62.7°C. Furthermore, the losses measured using the open secondary test, demonstrated in [80], show a 25% reduction in core magnetization losses. These results correspond to the predicted

analytical results and represent a significant improvement core operation. Importantly, this is not a one to one comparison of cores as shown in Figure 5.8. Manufacturing limitations introduced variations in total inductance while Figure 5.8 and Table 5.3 compare designs of the same inductance. However, using the parameters of the constructed inductors to the presented analysis methods correlates very closely with measured results as shown in the analysis above.

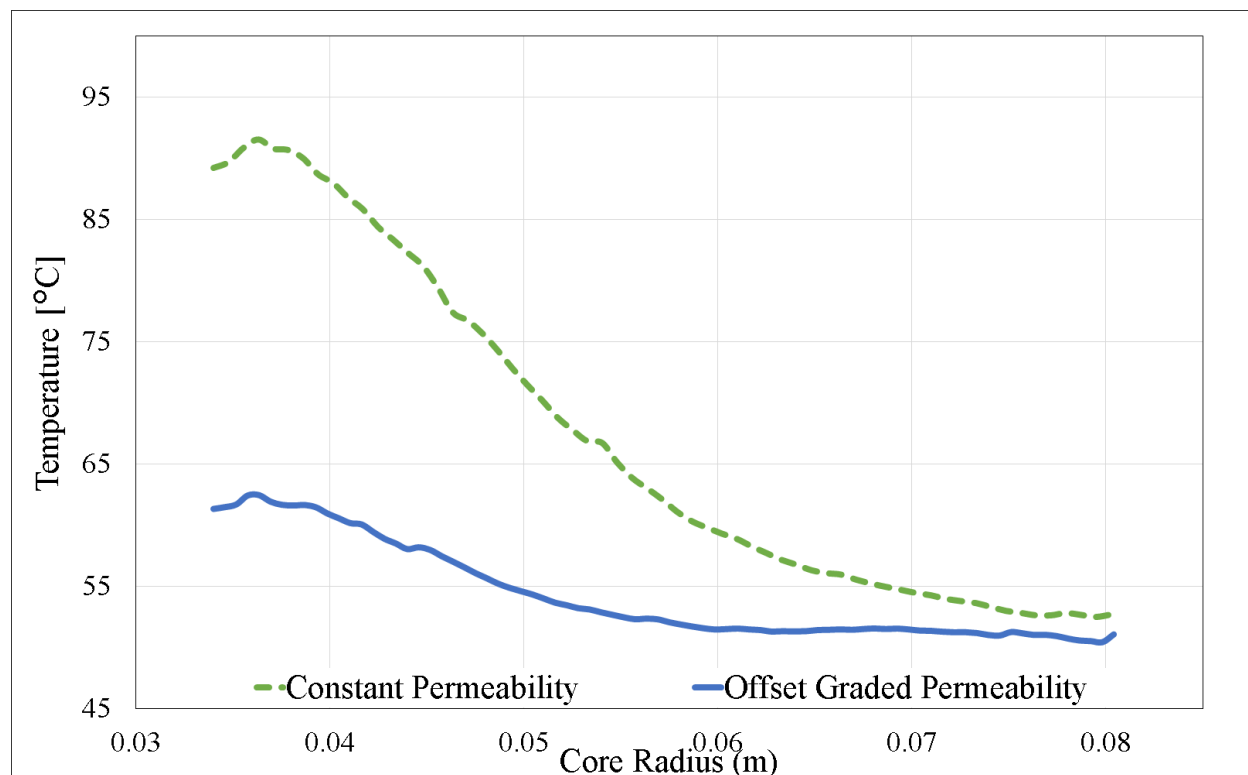


Figure 5.9: Comparison of Thermal Line Plots of Steady State Temperature. Constant Permeability Profile (Dashed) and Offset Permeability Profile (Solid) Toroids Along Radial Dimension.

A brief discussion is merited for the relationship between the thermal profiles and loss gradient profiles of Figure 5.8. From the loss profiles, one could reasonably expect a constant decay of temperature closely related to the decay of the local losses. However, the temperature near the inner and outer radii is strongly affected by the relatively low total thermal impedance in the radial direction. Specifically, the inner most and outer most layers have a very low impedance to ambient because of their exposed broad surfaces. This is shown by the two edge

resistive networks in Figure 5.2. These relatively cool layers act as sinks to adjacent layers resulting in core temperatures that are lower than one might expect given the heat injection profile. Another aspect of this that is not addressed in Figure 5.2, is the heat injection to the core from the exciting coils. This is noticeable by the slight increase in core temperature at the core edges.

### **5.10 Implications and Recommendations for Thermal Management**

As mentioned above the anisotropic nature of the thermal body enforces the local heating to follow the local loss with minimal transfer across ribbon layers. Because of this phenomena, it is an adequate assumption that the thermal profile and heat injection profile are proportional but follow the same general curve. As such, strain annealing can be used to deliberately assist magnetic core cooling. The following recommendations will provide uses and examples for each of the four presented strain annealed permeability profiles.

The constant permeability profile is the most elementary of the profiles. The manufacturing process is also the simplest as only a single constant tension force is needed. As such, the mechanical limits of the ribbon are less of a concern as the tension can be held within maxima for all designs. Its use and effect has the least variation from a traditional core. However, where the constant permeability core is most applicable is in replacing a magnetic component assembled with a core of higher standard relative permeability and an air gap. Now, the gap can be eliminated by using a strain annealed core that has the same effective permeability as the gapped core. This eliminates the additional losses, e.g. fringing and winding proximity, associated with the gap. Thus, a hot spot is eliminated whereby prior cooling is now unnecessary. However, because of the method of tuning for all of the other profiles this advantage is not unique to this profile.

Linearly graded permeability profiles offer the ability to shift the hottest point of the core to the outer edges. This has the advantage of working better with external heatsinks. This profile has some added complexity in the manufacturing and ribbon stress limits need to be carefully avoided. However, if properly implemented, the core is subjected to a uniform flux density along the radial direction. With increasing volume, this causes a linearly increasing thermal injection to the core. This reduces the thermal gradient to a constant over the entire core profile.

If there are mechanical or magnetic properties that limit full implementation of the linearly graded permeability, adding an offset provides a reliable solution. The resulting thermal profile is similar to the constant permeability case. However, the inner radius peak heat injection is significantly reduced and the outer radius injection is raised slightly. This approach offers one of the most practical design steps as it can accommodate the most constraints and tolerances while still providing the benefit of reduced peak temperatures and potentially reduced losses.

The exponential permeability profile is one of the more interesting cases. While having a minimal dependency on core inner radius and base permeability, this profile can provide three different approaches to heating profiles. Using a low exponent results in heat injection profiles similar to constant and offset permeabilities. Higher exponents have the ability to dramatically shift the heat injection to the outside of the core. This can result in more efficient external heat sink operation. Finally, by carefully choosing the exponent, the heat injection profile can be reduced to a constant. This uniformly heats the core and eliminates the radially dependent hotspots.

The ability to choose a permeability profile and specific variations in the profile offers a new tool in magnetics design. These variables enable new approaches to multi-objective

optimization. New optimization points and designs are available that can fit new operational spaces.

### **5.11 Future Work and Conclusions**

Future work will further quantify the magnetic ribbon variations due to strain annealing. This will allow the loss predictions to incorporate these dynamic impacts. Similarly, the loss model will be tightly integrated with the heat injection. This will provide further insight into the optimal strain annealing profiles to achieve final core temperature profiles. Similarly, more experimental results will be developed by assembling cores of the various profiles.

Fundamentally, the process of designing a magnetic core permeability profile through the use of strain annealing offers another tool in a magnetics designer toolbox. Four fundamental profiles were presented with analytical expressions for losses and heat injection. These heat injection terms can be coupled with the presented anisotropic thermal model to better predict a magnetic cores thermal profile and to anticipate potential hotspots. This prediction was verified using line scans of two experimentally verified toroid cores employing the constant permeability and linearly graded with offset profiles. Furthermore, the total losses measured were accurately predicted using the presented profile dependent loss equations.

The benefits of the strain annealing tool can come at the cost of increased losses depending on the desired design space. Sets of curves were presented to be used in the design screening process. It was shown that some profiles can reduce the toroid total losses while also providing the aforementioned thermal and flux control benefits. It is with these benefits in mind that new recommendations for a combined design process utilizing strain annealing and heatsink placement was provided for improved cooling performance. Thus, strain annealing a magnetic

ribbon core to provide a specific permeability profile represents a new paradigm in magnetic core design.

## CHAPTER 6: APPLICATION EXAMPLES

### 6.1 Motivation

This chapter will show the efficacy of the presented additions to the field of medium frequency magnetics. As discussed in the preliminary introduction, there are numerous applications where the presented techniques and models will provide optimized solutions. The following examples are meant to highlight various aspects of the modelling. Similarly, digital power concepts will be explored in this chapter through converter controller development. The designs will show how both the magnetics and the converter control design can be explored together for optimal systems.

### 6.2 Series DC Active Filter Coupling Transformer

#### 6.2.1 Introduction

Medium voltage DC (MVDC) microgrids are growing in popularity in a variety of fields [153], [154], [155]. The US Navy has proposed a MVDC testbed with stringent requirements, presented in Table 6.1. Figure 6.3 pictorial shows the waveforms and requirements described in Table 6.1. This platform is used to validate equipment for the next generation intelligent power system (NGIPS) for future warships with a roadmap seen in Figure 6.1 [156], [157]. Figure 6.2 is a photo of just such warship, the Zumwalt class destroyer. In these systems, it is desirable to use a high power medium voltage DC bus for energy distribution. Particularly with warships but also with remote DC grids, efficiency is paramount.

The MVDC amplifier provides a highly flexible test bed to help with the development of new technologies. It represents both a testing platform for MVDC systems as well as a highly capable MVDC Grid generator. This is critical in studying the unique electrical load structure of

onboard typical next-generation ships. In particular, the amplifier should be able to produce voltage steps of high slew-rate and minimal voltage excursions during a load step. An illustration of amplifier performance requirements is given in Figure 6.3 and the dynamic specifications for a 7.5 kV MVDC system, mentioned in [158], are provided in Table 6.1.

One high efficiency rectifier is a 12 pulse line commutated rectifier. However, this system produces a lot of voltage ripple and needs significant filtering. The DC Active filter has shown promise as a power converter that can provide both static and transient compensation, step flux injection, to a noisy medium voltage DC bus like 12 pulse active front ends (AFE). Most notably, the DC active filter is an integral part to achieving the performance specifications of the medium voltage amplifier, a system used to test the NGIPS when used as a DC bus filter with conventional thyristor rectifiers. Figure 6.4 shows how the DCAF can be connected with the rectifier. Depending on the connection type, the topology is either a series or parallel active filter. The active filter can be designed to work with a passive filter, a hybrid topology, or it can mitigate all of the ripple, active only. Table 6.2 shows the basic topology of the active filter based on its connection. One of the main drawbacks with the parallel active filter is that the coupling transformer must withstand all of the voltage of the DC bus. This requires the transformer to have significant amount of insulation, increasing size, weight and cost. As such, only series connected, series DC active filter (SDAF) topologies will be investigated.

In this medium-voltage dc amplifier system, the SDAF a series dc coupling transformer (SDCT) provides steady state filtering and improved dynamic response as well as an isolated coupling between the AFE and SDAF [159], [160], [161]. Others have shown topologies that do not provide isolation [162], [163]. This SDCT couples the DC active filter and the DC bus supplied by a thyristor rectifier, as seen in Figure 6.5. In the series topology, the primary side of

the transformer connects to the DC bus and the secondary side connects to the active filter. As such, the primary side of the SDCT carries the full load DC current. Without careful design, the transformer can easily saturate.

This application example investigates various DC active filter topologies and demonstrates a SDAF with a series SDCT. The section is organized as follows: the first section discusses the design and selection of passive components for both the DC bus low pass filter for hybrid topologies and the SDAF switching ripple filter. The next section provides an overview of general design requirements for the transformer construction and implementation. The following section provides an overview of design and control techniques that are critical to avoid core saturation with two techniques focused on in detail. The final section evaluates the designs in a 4 kVA, 380 V<sub>DC</sub> laboratory-scale test-bed, Figure 6.30.

Various design issues of the MVDC amplifier are presented in [158]. This section presents design considerations and the aspects of the SDCT based on which a design methodology is derived for the MVDC amplifier system. In what follows, first, design considerations for series dc coupling transformer are explained, and second, a design methodology for the transformer is presented. Design cases, preliminary transformer characterization and experimental results for the laboratory-scale evaluation of SDCTs are then provided. Finally, a summary of key points to consider in the design has been summarized with respect to experimental results.

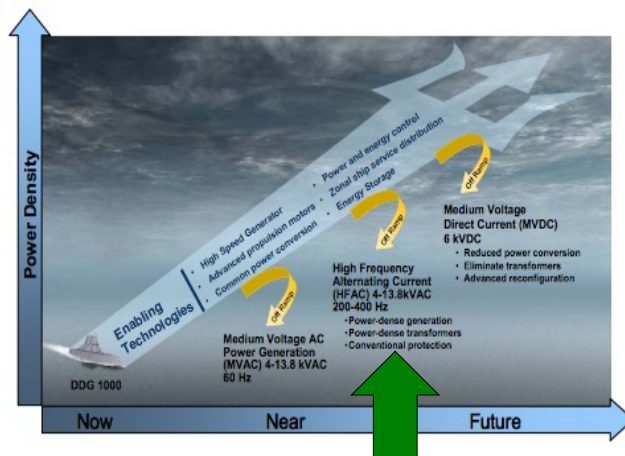


Figure 6.1: Navy NGPIS Technology Projection



Figure 6.2: Photograph of US Navy More Electric Ship: Zumwalt Destroyer.

Table 6.1: MVDC Performance Requirements.

Performance Metric	Value	Condition
Voltage Rise/ Fall Time	1.5 mS	.3 Step
Voltage Slew Rate	4.5 V/ $\mu$ S	.3 Step
Load Step Recovery Time	2.5 mS	.4 Step
Voltage Excursion	15 %	Max
Dead Time	0.2 mS	
DC Ripple	3 %	
DC Error	1.5 %	

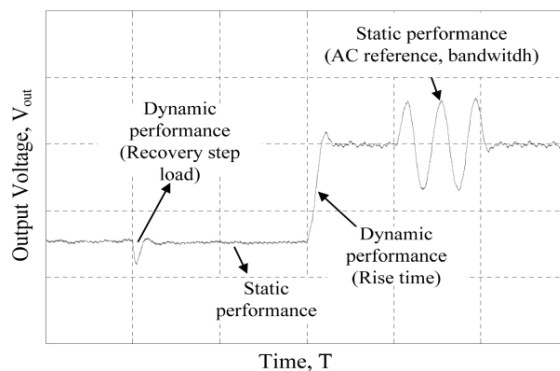


Figure 6.3: Illustration of MVDC Amplifier Performance.

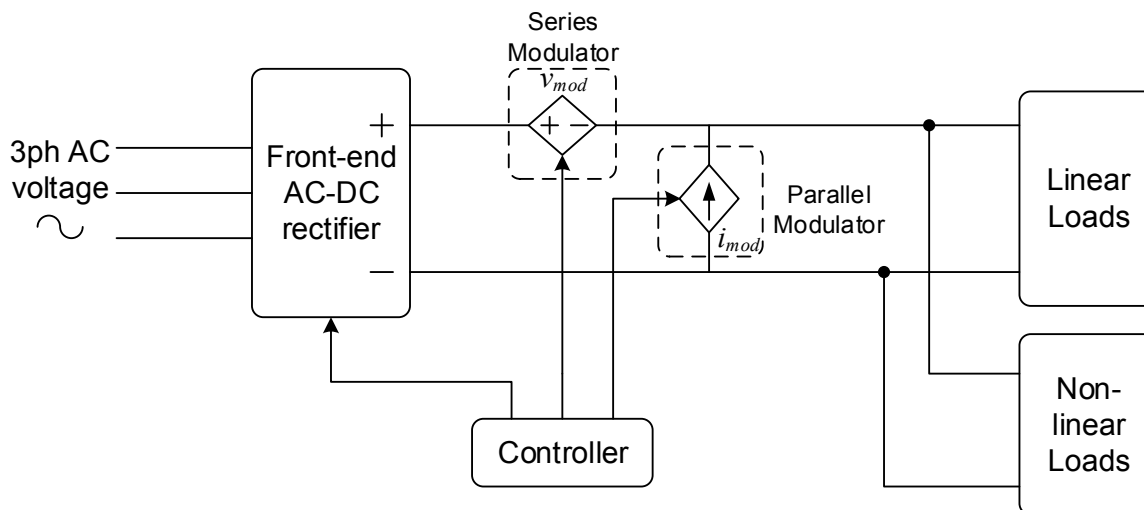


Figure 6.4: Connection of Rectifier with Filter Options.

Table 6.2: DC Active Filter Topology Variations.

	Series Connection	Parallel Connection
Hybrid Active		
Active Only		

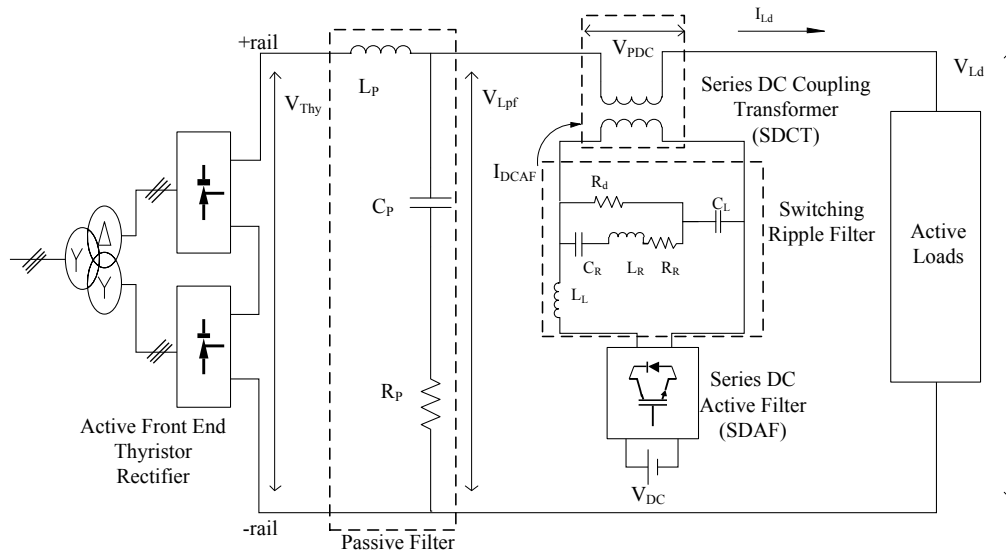


Figure 6.5: Topology of Thyristor Based MVDC with SDCT.

## 6.2.2 DC Bus Low Pass Filter

This low pass filter is designed to play two key roles in the MVDC amplifier system. First, this filter provides damping to higher order harmonics above the bandwidth of the SDAF. Furthermore, the inductance provides loading stiffness to the thyristor rectifier that improves stability as seen described in [164]. This low pass filter also provides a distinct measurement point for traditional SDAF control [165]. As such, this filter was designed for 2 kHz with the understanding that the SDAF would compensate up to the 24<sup>th</sup> harmonic or 1440Hz. However, as will be shown in the laboratory evaluation, adequate controls completely eliminated the need for the low pass filter at such low frequencies. In fact, only a low pass filter to assist in blocking any DCAF switching ripple is necessary and a simple inductor is sufficient.

## 6.2.3 SDAF Switching Ripple Filter Design

This section explores two passive filter types for attenuating the switching ripple from the SDAF. Because the converter switches using three level PWM, switching harmonics are twice the switching frequency. A resonant trap filter is recommended to eliminate this noise from the

SDAF injected current. Figure 6.6, shows a c type topology described in [166] and the frequency response of the individual passive components that make up the shunt branch and the SDAF voltage frequency response.

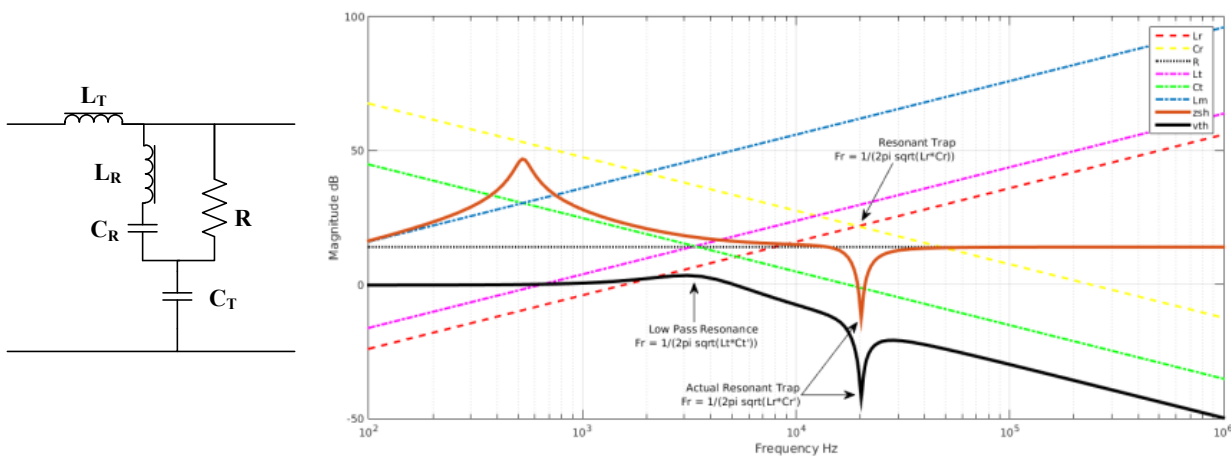


Figure 6.6: C-Type Topology Switching Ripple Filter with Resonant Trap. Topology (Left) and Frequency Response (Right)

$L_T$  and  $C_T$  establish the basic low pass filter with a cutoff frequency sufficiently higher than the rectifier ripples at the 24th harmonic.  $L_R$  and  $C_R$  are tuned to resonate at twice the switching frequency as mentioned above. In order to minimize the interaction between  $C_T$  and  $C_R$ ,  $C_T$  should be greater than 10x  $C_R$ . However, a low pass resonance at  $C_T$  where the series connection of  $L_T$  interacts with the parallel connection of  $C_R$ , and  $C_T$  dominates. In order to damp the low pass resonance, and increase the notch attenuation,  $R$  is introduced. Increasing  $R$  however, extends the corner frequency of the dominant low pass. Too much  $R$  allows the amplification resonance between  $L_T$  and  $C_R$  to become a factor. Therefore, careful consideration must be made to find a damping  $R$  that achieves adequate attenuation at the switching frequency while also providing sufficient damping of off frequency resonances. By placing the resonant branch and damping resistor in series with  $C_T$  the overall shunt impedance can be increased.

However, this series connection shifts the resonant notch to  $C_R'$ , the resonance of  $L_R$  with  $C_R$  and  $C_T$  in series. In order to aid in the design, the shunt impedance is shown below in (6.1).

$$(6.1) \quad Z_{shnt} = \frac{RS^3 + \frac{1}{C_T}S^2 + \frac{R(C_R + C_T)}{C_T C_R L_R}S + \frac{1}{C_T C_R L_R}}{S^3 + \frac{R}{L_R}S^2 + \frac{1}{C_R L_R}S}$$

An alternative topology and corresponding frequency response can be seen in Figure 6.7. Using the alternative design, similar damped low pass action can be achieved while also having the ability to independently tune the resonant branch. Simply having the resonant branch as a shunt introduces a significant amplification spike corresponding to the  $L_R$ ,  $L_T$  and  $C_R$  resonance. Furthermore, the damping resistor needs capacitance for DC blocking and higher low frequency impedance. This DC blocking is particularly important when active DC injection is implemented by the SDAF. Again, this shunt impedance is listed for clarity in (6.2).

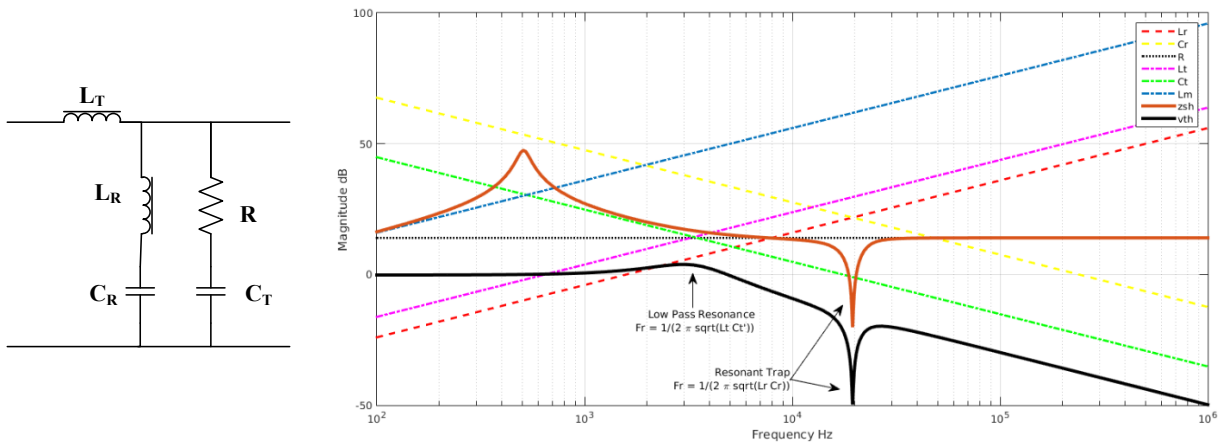


Figure 6.7: Parallel Shunt Switching Ripple Filter with Resonant Trap. Topology (Left) and Frequency Response (Right)

$$(6.2) \quad Z_{shnt} = \frac{RS^3 + \frac{1}{C_T}S^2 + \frac{R}{C_R L_R}S + \frac{1}{C_T C_R L_R}}{S^3 + \frac{R}{L_R}S^2 + \frac{C_T + C_R}{C_T C_R L_R}S}$$

It is clear from (6.1) and (6.2) that the two filters are similar however the key aspect is the differences resonant point and the sensitivity of those points to changing components.

The SDCT magnetizing inductance has some impact and should be designed considering [165] while also keeping a minimal number of turns to reduce copper loss. Both frequency responses include the magnetizing inductance and show the minimal impact it has on the overall filter performance. However, this minimal impact only holds while the magnetizing inductance,  $L_m$ , is sufficiently large. For both frequency plots, the components values are listed in Table 6.3 below with an adequate  $L_m$ . These values are those that are implemented in the laboratory test bed as well.

*Table 6.3: Switching Ripple Filter Component Values.*

Component	$L_R$	$C_R$	$R$	$L_T$	$C_T$	$L_M$
PU at 720 Hz	0.013	9.8	0.2	0.03	0.71	1.33

#### 6.2.4 General SDCT Design Considerations

The SDCT is a crucial and integral component of the amplifier system as shown in Figure 6.5. The transformer role is to couple the active filter to the amplifier by connecting it in series across the medium-voltage dc-bus and as such, it has to sustain a potentially large dc current bias under steady-state conditions. Further, it should be able to ride through dc current excursions during system transients. From the series active filter point of view, the transformer has to do both steady-state and dynamic volt-second, flux, injection in order to meet the system ripple factor and transient dynamic specifications [158].

Figure 6.8 shows the above mentioned facts through the simulated in the MATLAB/Simulink environment. It shows the amplifier response to a first-order target dynamic request. Therefore, the design of the transformer is driven by both the dc amplifier system and the active filter functional requirements. The system dc dynamics are affected by series connection of the SDCT and on the other, active filter performance and power rating are affected by magnetizing inductance of the SDCT [165]. Some important design considerations are

mentioned in the following sub-sections. The transformer should also work in the linear region over the entire operating range of the system which will be discussed in the next section.

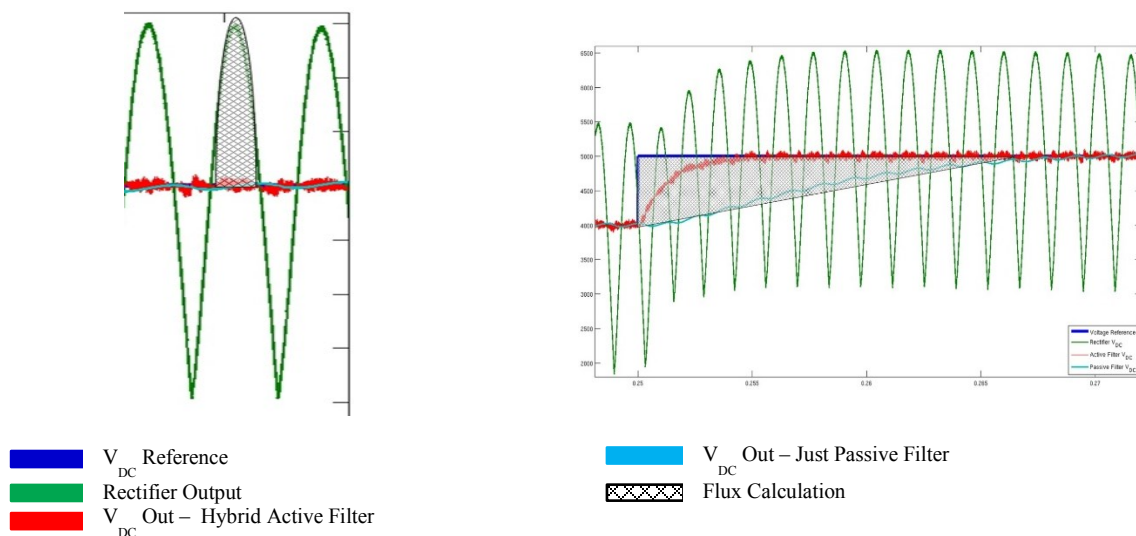


Figure 6.8: Compensation Requirement for the SDAF During Static Flux During Positive Half Cycle (Left) and Dynamic Flux During Step Request (Right).

#### 6.2.4.1 SDCT Magnetic coupling

The transformer should have strong coupling, which can be provided by magnetic materials with high permeability. This is to minimize leakage inductance that would degrade the voltage step response. The design will have to consider the necessary if an air gap is used to ensure the flux density,  $B_{max}$ , injected by the active filter is less than  $B_{sat}$  of the core. In this case, high permeability will give strong coupling but not necessarily high magnetic force,  $H$ , to  $B$  gain. Other saturation mitigation techniques could avoid the air gap and maintain a high gain.

#### 6.2.4.2 SDCT Size and Volume

Considering size and volume requires choosing a magnetic material with high maximum flux density,  $B_{sat}$ , to achieve low magnetic core cross sectional area and thus, smaller core dimensions. Another advantage to this choice is minimization of the perimeter of the core cross

section, an important parameter for influencing the conductor length and losses. Similarly, core properties such as stacking factor,  $sf$ , can maximize the magnetic material to total core cross sectional area ratio, thereby further reducing the overall volume. Reducing the overall core volume also reduces the total core loss for a given induction and frequency operating point.

The size and volume should also be reduced for economic reasons, less material and smaller profiles generally cost less. Due to magnetic and economic reasons, size and volume are necessary considerations in the optimization of design. Given the long term costs of losses, it is advisable to optimize the magnetic design to achieve maximum efficiency keeping the volume of core under a reasonable constraint.

#### **6.2.4.3 SDCT Copper loss**

This is an important factor as the transformer carries a large dc current in its primary winding. While the DC current is out of the designers' control, the winding resistance is. The winding resistance will mostly be influenced by the length of the wire but other parameters should be considered e.g. skin and proximity effects that are important with the active filters higher frequency components. Choosing a core material with a high  $B_{sat}$  will allow designers to use less turns and consequently less winding length. Since the magnetizing inductance is influenced by the turns squared, small increases in  $B_{sat}$  can lead to significant decrease in the required turns. Similarly, if the number of turns can be reduced significantly to enable a low number of winding layers, the penalty due to the proximity effect can be greatly reduced.

#### **6.2.4.4 SDCT Core Loss**

The active filter, with switching frequency of approximately 20 kHz, is injecting harmonics at multiples of ac-line frequency. Hence, the magnetic core should have low loss

characteristic. A typical design point is to develop the transformer from the copper loss to core loss ratio. Higher  $B_{\text{sat}}$  cores can have significantly higher core losses, minimizing the ratio.

One advantage to shifting the loss distribution to the core is the capacity for heat dissipation of the core relative to the copper windings. The core can and should have thermally efficient contact to heat sinks open to the outside environment. Similarly, the thermal mass of the core is higher due to the higher mass. Finally, heat in the windings has fewer avenues to dissipate. Therefore, sacrificing less optimal core losses can lead to more optimal and stable design.

It has been discussed in previous sections but it will be represented here for convenience. Steinmetz's equation provides a method for determining the power loss by volume for sinusoidal flux (2.25). An improved equation, described in [50], can incorporate arbitrary flux wave form with DC offset, (6.3).

$$(6.3) \quad \frac{P}{V} = \frac{1}{T} \int_0^T k_i \left| \frac{dB}{dt} \right|^\alpha (\Delta B)^{B'-\alpha} dt$$

#### 6.2.4.5 SDCT Core Magnetostriction

Similar to the core loss, magnetostriction is a quality of the transformer that leads to audible noise from the magnetizing force in the core. This force causes the core material to expand or contract as a solid body. This force will also cause expansion and contraction at joints in the core where the body is not rigid. Again, similar to core loss, magnetostriction follows a hysteresis loop from magnetic force  $H$ , from which the flexing of the material is seen. The flexing causes air displacement and thus audible noise.

The deformation of ferrous materials was described in [167] to have a hysteresis loop. Coupled with this property is the shift in the loop due to DC bias. It is therefore a key design point to determine the structural design of the core that minimizes joints, air gap regions, which

would lead to device movement. [168] describes building the transformer with step lap laminations that would improve the joint strength as the joint is now staggered along the lamination profile. This is different from the standard lamination where the gap lies on either side of joint center line. However, the step lap process requires higher grade steel and more precise manufacturing processes leading to a more expensive design.

Other options for reducing noise consider the transformer housing and installment. Stiff clamping can reduce the flexibility of gap joints. The clamping should focus on the direction of the flux path. However, due to fringing flux that would enter the core at oblique angles it is not always possible to constrain the core perfectly. Hence, it is recommended to clamp joint locations in as many surfaces/edges as feasible. Similarly, the bound core should be anchored to a sturdy base. The anchor should be sufficiently sized so as to reduce overall transformer vibration. This design is necessary for the series DC transformer due to DC bias and higher frequency flux.

#### **6.2.4.6 SDCT Insulation System and Requirements**

Insulation is obviously a significant requirement for the transformer design. In a practical system, the common mode DC voltage of the primary side can be as high as 24KV [158]. The AC voltage that the transformer will withstand is significantly less. Therefore the standard techniques recommended in [168] and common materials of [169] for low to medium voltage can be used to insulate between windings for this design. Disk winding of individual coils can minimize the gradient of voltage across the primary winding relative to the helical winding used experimentally. The proximity effect and increased winding length should be considered and reduced as much as possible while using disk winding techniques. An insulating bobbin is also a critical element in insulating the grounded core from the high DC voltages. Similarly, the

transformer can be submerged in oil based materials which improve the dielectric constant between windings and aid in cooling.

### 6.2.5 Overview of DC Bias Mitigation Techniques

There are four basic ways to design and control the DC bias flux in the series DC coupling transformer (SDCT). The most elementary, and typical of traditional high DC flux magnetic designs is to introduce an air gap in the transformer core. Since this is such a common procedure, it will be one of the focus designs of the SDCT. Two other options negate the DC bias flux with auxiliary flux sources. In the static case, a permanent magnetic is selected to provide a negative DC bias flux near the maximum expected DC bias flux from the load current. A more dynamic approach is to use a tertiary winding that tracks the load generated bias flux and actively tries to match it in a cancelling way. Finally, the dynamic DC bias flux cancellation can be integrated into the controls of the DC active filter (DCAF) to great effect with minimal cost. This final solution has several advantages and will be discussed in detail with a hardware design example. This overview will highlight the principal design method as well as provide an FEA analysis of the maximum DC load using FEMM and a lossless BH loop of the full system operation using Plecs Magnetics showing the efficacy of the approach. A summary of the study is presented below in Table 6.4.

*Table 6.4: Summary of Flux Mitigation Techniques.*

Mitigation Method	Air gap Required	BH Operating Points	External Flux Source	Experimental Model
Air gap	Yes, Designed	Positive and Negative Knee	No	Yes
Permanent Magnet	Yes, PM Length + Designed	Negative Knee to Positive Linear	Yes	[170], [171]
Auxiliary Winding	No	All Linear	Yes	[172]
Active DCAF	No	All Linear	No	Yes

#### 6.2.5.1 Fixed Air Gap DC Flux Mitigation

As mentioned above, introducing an air gap in the core is a common practice in magnetics that carry a high DC bias flux. This approach has the advantage of a simplified design

and construction. However, it is a static design and therefore difficult to scale for all designs. Furthermore, the air gaps in the core introduce mechanical joints that require increases in transformer superstructure for adequate housing. These joints also increase the core losses through fringing losses where the flux warps around the edge of the gap, introducing localized increases in eddy currents. An FEA analyses below, Figure 6.9, shows how the air gap can be used to prevent the core saturation during the worst case loading conditions. However, as seen in the simulated BH curve of this design, Figure 6.10, transient overshoots can drive the transformer into saturation. Furthermore, the transformer magnetizing permeability is effectively reduced requiring higher amp-turns to achieve the same induction levels. This design used four 1mm gaps at all four corners. The distributed gap approach reduces the fringing effects. A lapped gap design, using magnetic ribbon, could further reduce fringing with a highly distributed gap. Due to the nuances necessary in designing the transformer with an air gap for the SDCT despite the common use of air gaps, a hardware example is presented and demonstrated in a following section.

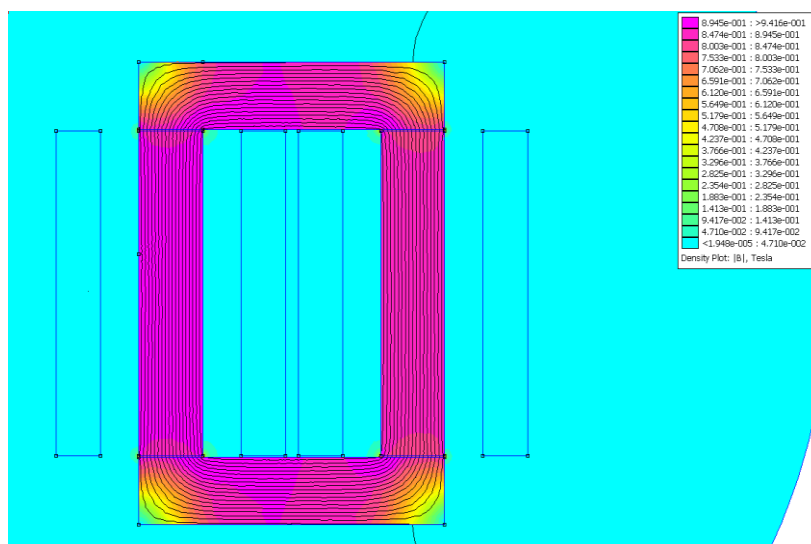


Figure 6.9: Gapped SDCT FEA.

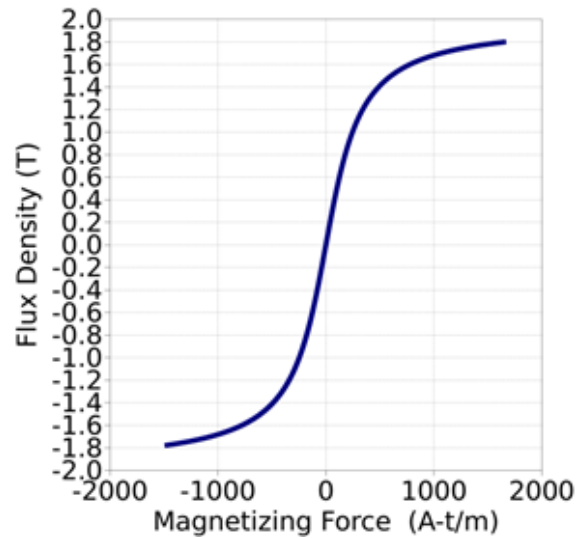


Figure 6.10: Gapped SDCT BH

### 6.2.5.2 Permanent Magnet DC Flux Mitigation

A permanent magnet (PM) provides a static DC flux in the core that can be used to neutralize the expected load current [170]. The air gap also acts as air gap if it is in line with the core material. This enables a compromise design between the length of air gap and effective DC flux injection of the PM. In [171], the authors provide a hardware example for a coupling transformer in their solid state transformer. Their coupling transformer carries significant DC current like the SDCT. While the demonstration below shows the PM in series with the core, [170], places the PM on the edges of the gap. While this solution is very effective at eliminating the DC bias at the designed load conditions, as studied in Figure 6.11, low load conditions and transients can be problematic. As seen in Figure 6.12, the core operating in the knee of the curve and effectively negatively saturated during the low load operation. The static design of the PM and the continued existence of an air gap has the same drawbacks as the air gap method mentioned above. Furthermore, the expense of the PM can be a factor as rare earth metals are costly components of PMs. This design can have benefits for high load conditions and depending upon the system operating times may be a suitable solution.

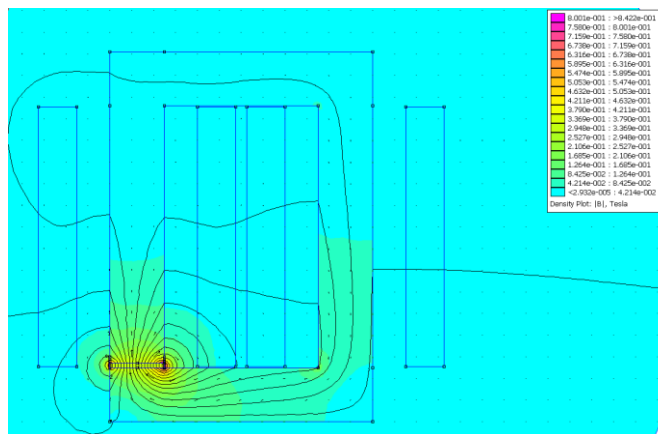


Figure 6.11: Permanent Magnet SDCT FEA

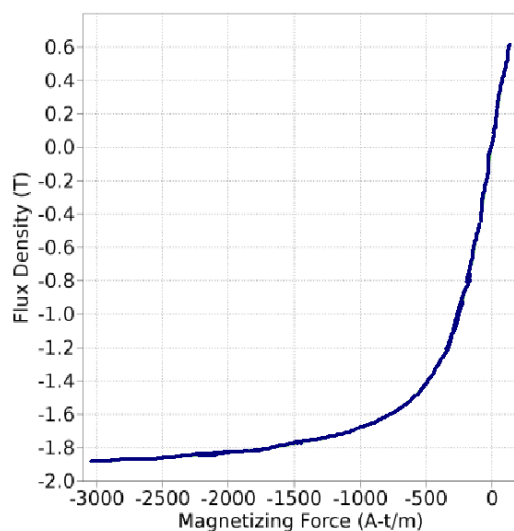


Figure 6.12: Permanent Magnet SDCT BH

### 6.2.5.3 Auxiliary DC Injection DC Flux Mitigation

A simple dynamic approach to mitigating the DC flux was presented in [172]. This approach requires an auxiliary converter and a tertiary winding. This auxiliary convert can be a simple DC-DC converter operating in current control mode. It then injects the necessary DC current into the tertiary winding to cancel the DC bias flux from the load. This has the advantage of completely following the DC bias flux during all operating points. However, it requires an auxiliary converter that requires a separate supply and so the costs are increased. A simplified model of this circuit is shown below in Figure 6.13. As seen in the FEA study in Figure 6.14, this

can effectively eliminate the load bias flux. However, the transformer needs to be designed with the space necessary to fit the tertiary winding. Given tight controls, the auxiliary converter can very effectively prevent saturation during all operating points, Figure 6.15. Furthermore, this design requires no air gap, allowing for a high B of H gain.

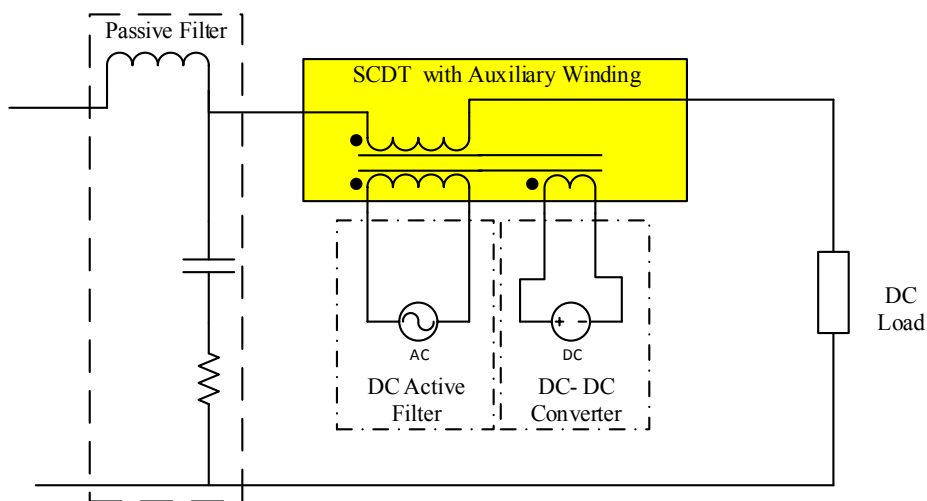


Figure 6.13: SCDT Auxiliary Converter for DC Injection.

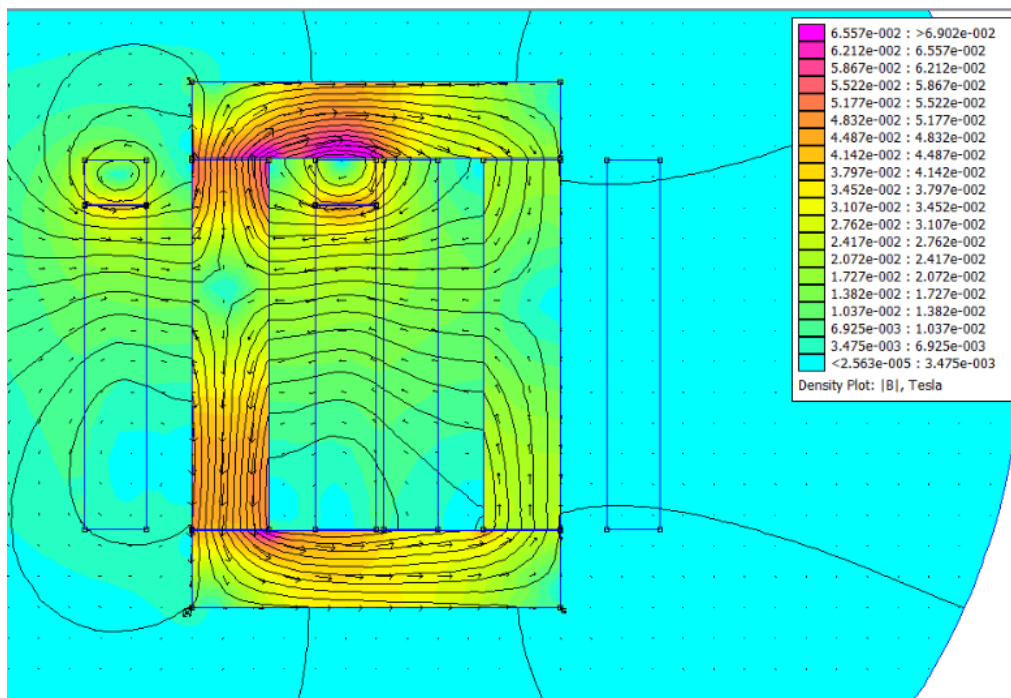


Figure 6.14: Auxiliary Winding SCDT FEA

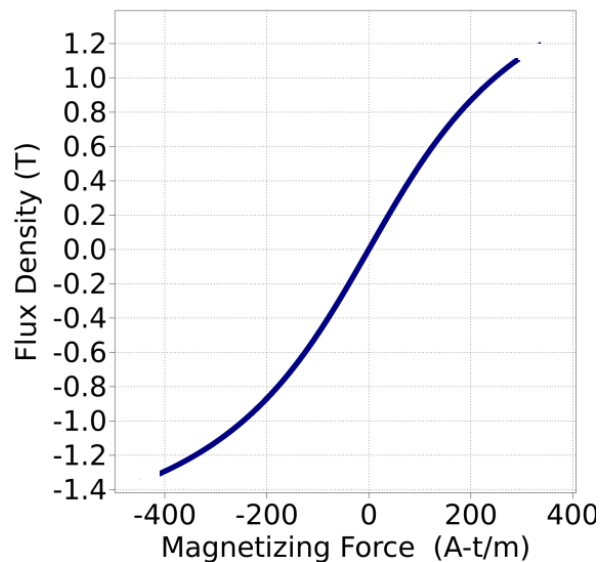


Figure 6.15: Auxiliary Winding SDCT BH

#### 6.2.5.4 Active Filter DC Injection DC Flux Mitigation

Another, dynamic solution is presented in [171]. This follows a similar approach to mitigating the DC load flux by actively injecting an opposing DC bias flux. However, it has the advantage over [172] by eliminating the tertiary winding and auxiliary converter. A simplified diagram of this method is shown in Figure 6.16. As can be seen in Figure 6.17 and Figure 6.18 this design also effectively eliminates the DC bias flux and allows the SDCT to stay in the linear region during all operating points of the SDAF. Interestingly, in comparing Figure 6.14 and Figure 6.17, less flux lines cross coils implying lower losses during DC transients. However, this would be a minimal contribution to overall efficiency. This design is discussed in detail in the hardware validation of this approach.

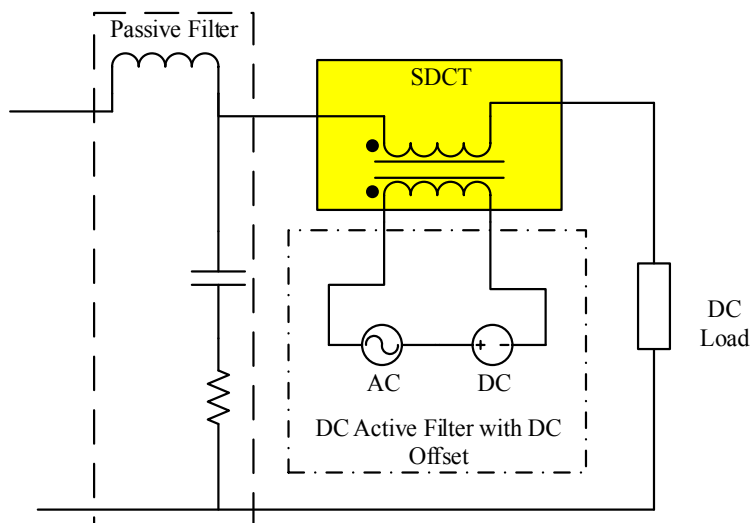


Figure 6.16: Proposed Circuit Topology for Active DC Injection.

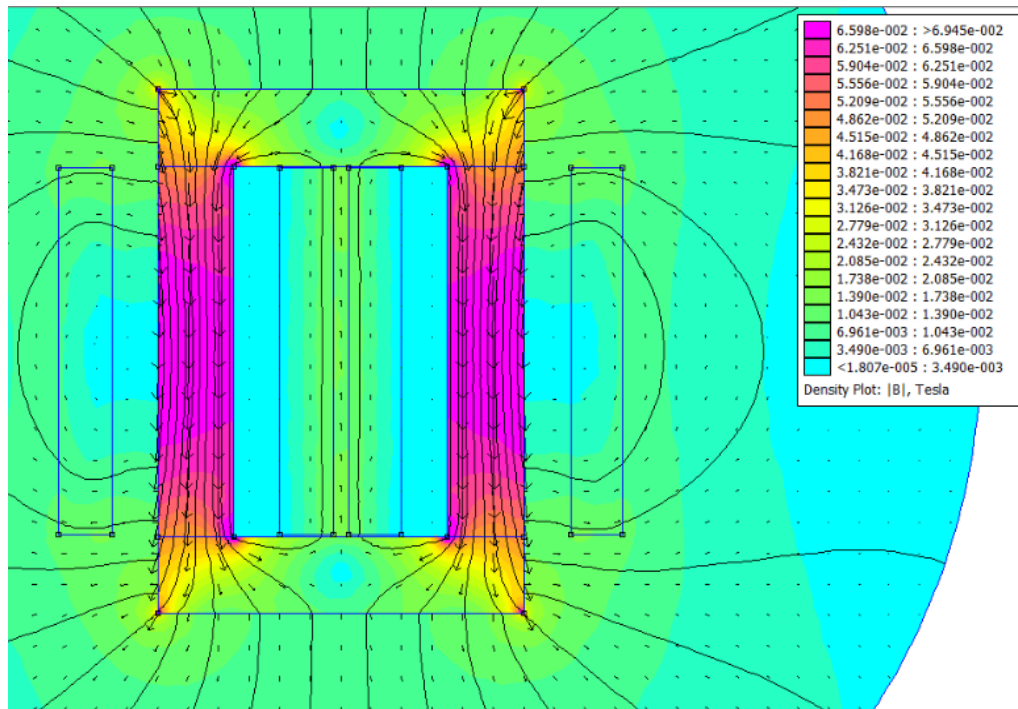


Figure 6.17: Active DC Injection SDCT FEA.

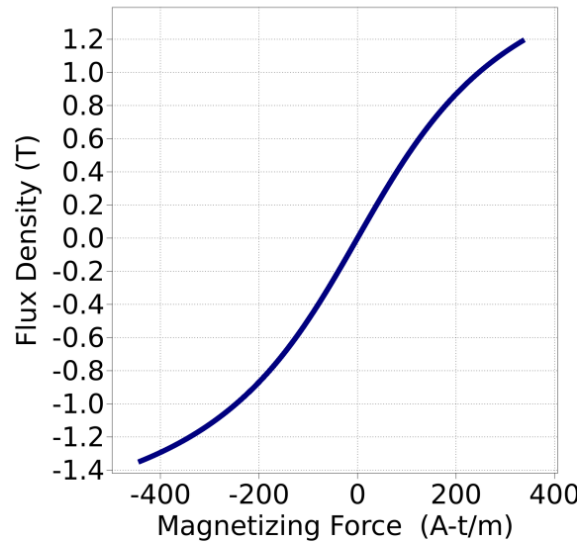


Figure 6.18: Active DC Injection SDCT BH.

## 6.2.6 Air Gap Flux Mitigation Design Methodology

### 6.2.6.1 Principal Design Constraint

The initial design procedure adopted here, results of which are reported in the following section, is for the laboratory-scale dc amplifier test bed. The design is carried out based on worst-case net flux linkage swing calculation. This ensures that the series DC transformer will not saturate under any active filter request. Two major components considered are the flux linkage swing caused by the maximum dc current flowing through the primary (dc-side) of the transformer, and the maximum volt-second (flux) injection on the secondary (active filter side) of the transformer. The sum of these two components should be less than the saturation flux density of the core. Therefore, the total flux linkage through core is shown in (6.4).

$$(6.4) \quad \lambda_c = \lambda_{c-dc} + \lambda_{c-ac}$$

Here  $\lambda_c$  is the flux density in the core with subscripts dc and ac representing the respective components. Expanding these terms and identifying their source for clarity leads to (6.5).  $\lambda_{c, Rec}$  is the flux linkage due to the DC load current through the primary winding and  $\lambda_{c, ac}$

$\lambda_{AF}$  is the flux linkage injected into the system by the active filter to diminish DC voltage ripple.

$\lambda_{c, dc-AF}$  is the flux linkage asked of the active filter to improve DC bus step response.

$$(6.5) \quad \lambda_{c-max} = \lambda_{c-dc-Rec} + \lambda_{c-dc-AF} + \lambda_{c-ac-AF}$$

Redefining the terms in (6.5) to system metrics presented in Table 6.1, leads to (6.6).

Here,  $V_0$  is the steady state DC voltage before a step response.  $\lambda_{c, ac-AF, max}$  is the flux of the AC ripple compensation by the active filter. This is found by taking the integral of a half cycle of the ripple voltage. An initial design can simply consider the fundamental ripple, 720Hz but a more accurate model would consider additional harmonics.

$$(6.6) \quad \lambda_{c-max} = \max \left( L_m I_{dc} + \frac{(V_{step-max} - V_0) \Delta t}{2} + \lambda_{c-ac-AF} \right)$$

$$(6.7) \quad \lambda_{c-max} < N_{pri} B_{sat} A_c$$

Finally, in (6.7), the flux injection is checked against the transformer design to ensure that saturation will not occur. Adding pessimistic assumptions throughout the process can provide a more robust design.

### 6.2.6.2 Optimal Core Design

Using (6.7) and fundamental equations considering geometry, a parametric sweep can be used to determine the optimal transformer design. One such sweep was performed for the two core materials investigated in this section. Due to the nonlinear and discontinuous nature of the optimization, developing a script is recommended.

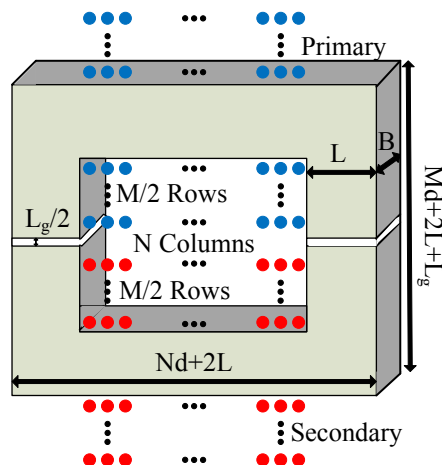


Figure 6.19: SDCT Winding and Core Geometry:  $M$  Rows and  $N$  Columns.

Figure 6.19 shows the understudied structure of the core and winding geometry. It has been assumed that the turns-ratio is equal to one. The first step then is to choose the width and height of the core for a chosen area  $A$  using (6.8) below. Where,  $L$  and  $B$  are the width and height of the core respectively. It is important to make sure that the choice of  $L$  and  $B$  are made such that the perimeter of the winding surface, (6.9), is of minimum length. Here,  $P$  is the perimeter of the winding surface. Using the above two equations and differentiating to get the minima we get (6.10) with solution (6.11).

$$(6.8) \quad A = LB$$

$$(6.9) \quad P = 2(L + B)$$

$$(6.10) \quad \frac{\delta P}{\delta L} = 2 \left( 1 - \frac{A}{L^2} \right) = 0$$

$$(6.11) \quad L = B = \sqrt{A}$$

This shows that for optimal design both width and height should be of same value. The window size has to be chosen such that both length of winding conductor and spatial volume of the core are optimal. This has been done to make sure that the volume of the core is constrained to avoid unreasonably costly shapes. This way the total copper loss is limited while limiting the core volume and weight at the same time. As shown in Figure 6.19 a method must be devised to come up with optimal values of  $M$  and  $N$  for a given number of turns,  $N_o$ .

### 6.2.6.3 Optimal Winding Length Design

It can be easily concluded that the total number of turns,  $N_T$ , the sum of both windings  $N_o$  (6.12), should be divided into a rectangular arrangement such that the product of  $2M$ , the number of rows, and  $N$ , the number of columns, is just larger or equal to  $N_T$ . To constrain the core dimensions, this rectangular arrangement should be the nearest rectangle to a square. Following these design goals, (6.13) and (6.14) should be used to determine  $M$  and  $N$ .

$$(6.12) \quad N_T = 2N_o$$

$$(6.13) \quad M = \lfloor \sqrt{N_T} \rfloor$$

$$(6.14) \quad N = \left\lceil \frac{N_T}{M} \right\rceil$$

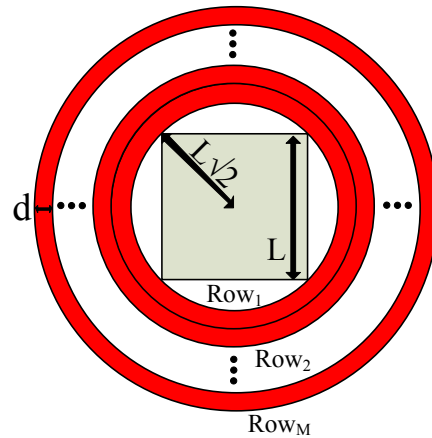


Figure 6.20: Slice View of Circular Winding Around a Core Leg.

The following method has been used to fix the geometry of this arrangement. As the winding surface has right angular edges, the windings would not completely wind around the surface without leaving air gap. A pessimistic approach of calculating winding length would be to consider them circular as shown in Figure 6.20. This way, the estimated loss would be slightly higher than experimental which is usually desired by manufacturers. Using a wire of diameter  $d$ , the radius,  $r$ , of each row,  $n$ , can be derived as in (6.15). The total length  $L_T$  of wire then is determined by (6.16).

$$(6.15) \quad r = \frac{L}{\sqrt{2}} + \frac{(2n-1)d}{2}$$

$$(6.16) \quad L_t = 2\pi r \sum_{N=0}^{0.5M-1} (N + N(N - 0.5M - 1))$$

The winding loss,  $P_{Cu}$  is closely coupled with the conduction current and the total winding length such that if the skin effect and temperature variations resistivity,  $\rho$  are neglected only (6.17) need be considered, understanding that this is a low estimate due to assumptions. Finally, the volume,  $V$ , of the core can also be derived as following as in (6.18). Here to present a more pessimistic value and thus be closer to the real design, the winding diameter is increased by 10% to account for non-ideal wrapping of the wire.

$$(6.17) \quad P_{Cu} = I_{DC}^2 L_T \rho_{wire} \qquad (6.18) \quad V = 4L^3 + 2.2L^2 d(N + M)$$

This optimization focused on the primary winding and core topology. In this case we assumed that an arbitrary cross sectional area and air gap could be utilized for construction. Similarly, we fixed the conductor parameters and did not attempt to oversize the conductor. In order to make meaningful comparisons, data is presented as a percentage of the maximum value.

#### 6.2.6.4 Optimization of AMCC and JFE Cores

A parameter sweep determines the geometry specific transformer copper loss, which is independent of core material. Using this data, designs utilizing the AMCC and the JFE cores can be explored. The AMCC and JFNHF core analysis results are shown in Figure 6.21. Both variation of normalized volume and copper loss has been shown. As expected both volume and copper loss increased with an increase in air gap length. However, with increasing number of turns, the copper loss increases while volume decreases. It should be noted that the variation of copper loss has several local peaks. This is due to the step-wise non-linear geometry selection mentioned in (6.13) and (6.14).

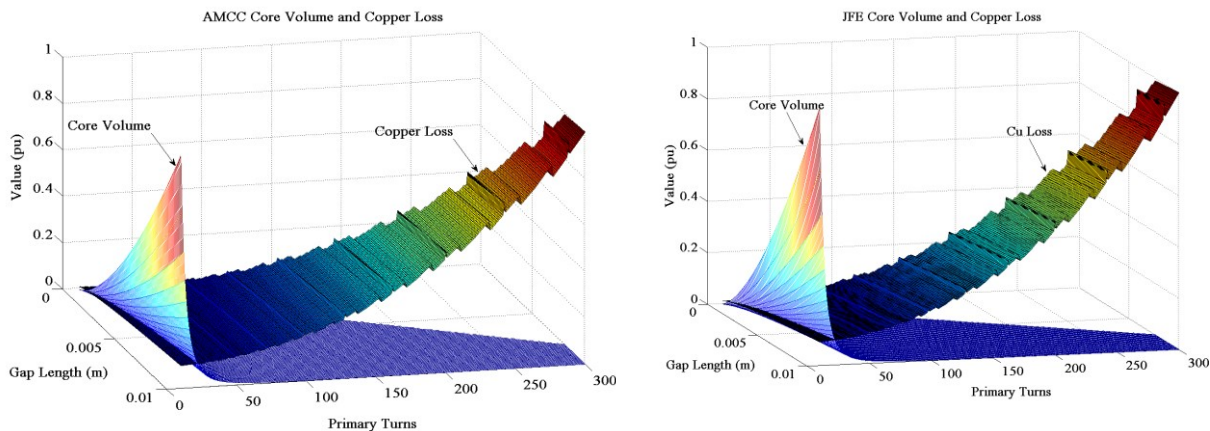


Figure 6.21: SDCT Normalized Volume and Copper Loss vs. Turns and Gap Length. AMCC Core (Left) and JNHF Core (Right)

It should be noted that owing to a higher  $B_{sat}$ , and larger stacking factor, JNHF cores have lower volume and more valid parameter selections. This is further illustrated in Figure 6.22 where the two SDCT designs are compared for an air gap of 4mm. As mentioned in earlier sections, the analysis presented in this section based on copper loss, neglecting core loss.

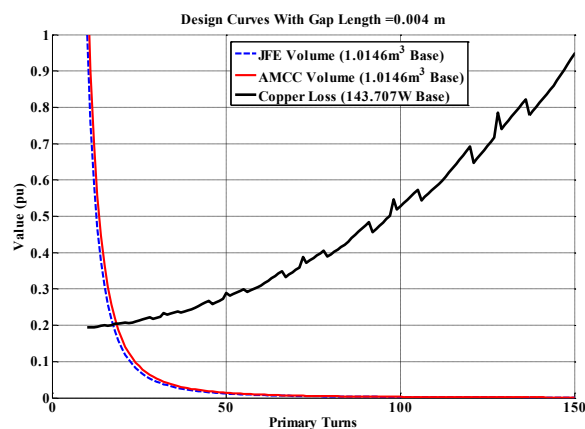


Figure 6.22: Volume and Loss Comparison of JFE and AMCC Cores gap = 4mm.

## 6.2.7 Active DC Flux Mitigation

### 6.2.7.1 Dynamic Saturation Mitigation SDAF Control

In this section, the design motivation for DC flux mitigation is described. The potential to use the controller for variable magnetizing inductance is also highlighted as an artifact of certain

material properties and the SDAF control of DC flux. Next, the controller structure with DC flux and ripple control is described. The controller is and DC flux cancelation is verified in Plecs magnetics domain and in FEA simulations.

### 6.2.7.2 Transformer Design Considering DC Flux

One of the key design issues of the SDCT is saturation avoidance. As with any magnetic component, the maximum flux density must be limited within the saturation flux density,  $B_{Sat}$ , unique to each material. In [173], the authors showed that this constraint is not trivial when considering the SDCT in the SDAF topology. Given the desired performance from Table 6.1, the SDAF subjects the SDCT to the core flux,  $\lambda_c$ , constraint as shown in (6.19).

$$(6.19) \quad \lambda_c = L_m I_{DC} + \frac{(V_{step} - V_0)\Delta t}{2} + \lambda_{AC} < N_{pri} B_{sat} A_c$$

Where  $L_m$  is the SDCT magnetizing inductance,  $I_{DC}$  is the DC load current in the primary,  $V_{step}$ ,  $V_0$ , and  $\Delta t$  are step time metrics and  $\lambda_{AC}$  is the flux injection needed to compensate ripple voltage.  $N_{pri}$  is number of primary windings;  $B_{sat}$  and  $A_c$  are transformer core properties. A common approach to satisfying this inequality is to introduce an air gap with a high  $B_{Sat}$  material. Introducing an air gap increases the transformer reluctance leading to a reduction in the magnetizing inductance  $L_m$  require an increase in turns to maintain the gapless  $L_m$ . However this limits the potential utility of a varying permeability as seen in Figure 6.23. This section proposes using active DC injection from the SDAF to match the DC flux biases through the primary winding. Incomplete matching enables controlled magnetizing force resulting in targeted permeability and magnetizing inductance. Designers can achieve up to 280% inductance changes for improved DC bus dynamics.

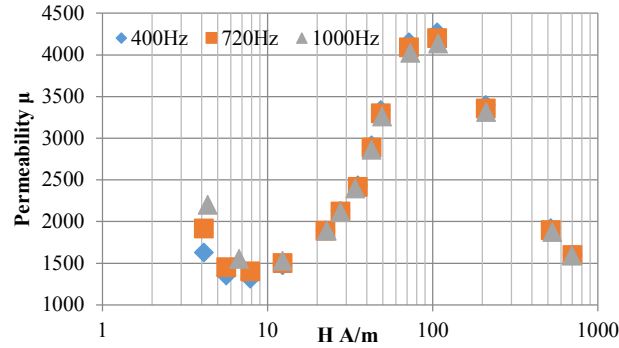


Figure 6.23: Variations in Magnetic Permeability for 10JNHF JFE Steel Core.

By dynamically following the DC current, the constraint, (6.19) becomes (6.20) where  $\beta$  is the DC compensation ratio. Complete DC flux can be mitigated or controlled to achieve an optimized target permeability. This enables a variable magnetizing inductance as a material property that is devoid of topological solutions.

$$(6.20) \quad \lambda_c = L_m(1 - \beta)I_{DC} + \frac{(v_{step} - v_0)\Delta t}{2} + \lambda_{AC} < N_{pri}B_{sat}A_c$$

In the case of JFE high silicon steel, permeability is not constant over the operating range, as seen in Figure 6.23. By using manufacturer provided data to interpolate the effective core permeability,  $\mu_r$ , it is clear that changes in the total MMF will change the SDCT  $L_m$ . For a fixed transformer, the SDCT  $L_m$  can vary 280% between peak  $\mu_r$  and minimum unsaturated  $\mu_r$ . This offers further control options and design flexibility minimizing or eliminating air gap. In this section and in the results that follow, the SDAF control targets 100% DC flux mitigation,  $\beta = 1$ .

### 6.2.7.3 SDAF Control Structure

Figure 6.24 shows the proposed control with a new current loop. The controller performance is verified using a Simulink and PLECS Magnetics model. The variable permeability,

Figure 6.23, is used to accurately model variable permeance in the simulations using a variable permeance block in the magnetics domain.

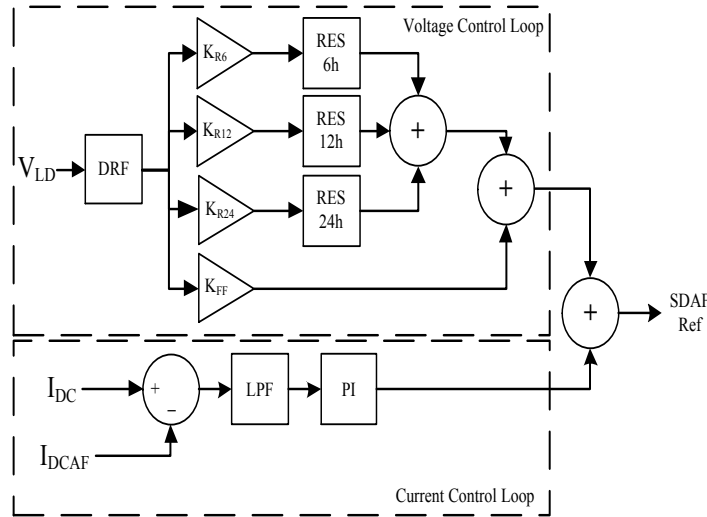


Figure 6.24: Resonant Voltage Control and PI Current Control for SDAF.

The controller utilizes PR control for the dominant harmonics due to the 12 pulse rectifier, 6<sup>th</sup>, 12<sup>th</sup>, and 24<sup>th</sup>. The feed forward branch enables the SDAF to compensate ripple that is not a part of the dominant harmonic. The input to both the feed forward and the resonant branches is the output load voltage,  $V_{LD}$ , pass through a DC removal filter as seen in [174] and shown below in (6.21) where  $a$  is close to unity. The integrators for the PR control follow the recommendations of [175] and are shown below in (6.22) given sample time  $T$  and resonant frequency,  $\omega_r$ .

$$(6.21) \quad DCF(z) = \frac{z-1}{z-a}$$

$$(6.22) \quad PR(z) = K_P + \frac{K_I T(z-1)}{(z-1)^2 + \omega_r T^2 z}$$

Figure 6.25 shows that DC flux mitigation techniques, both air gap and active DC flux injection, perform adequately in the aforementioned simulations. Figure 6.26 shows the B-H curves for both flux mitigation techniques. It is intuitive and evident from Figure 6.26, that when an air gap is used, the SDAF flux operates near the knee of the BH curve but under the  $1.98T B_{sat}$  in steady state. However, transient operation can bring the operating point into saturation. It is

also clear that a fixed air gap solution limits the utilization of the transformer core to half of the possible range at best because only slightly more H injection can saturate the core.

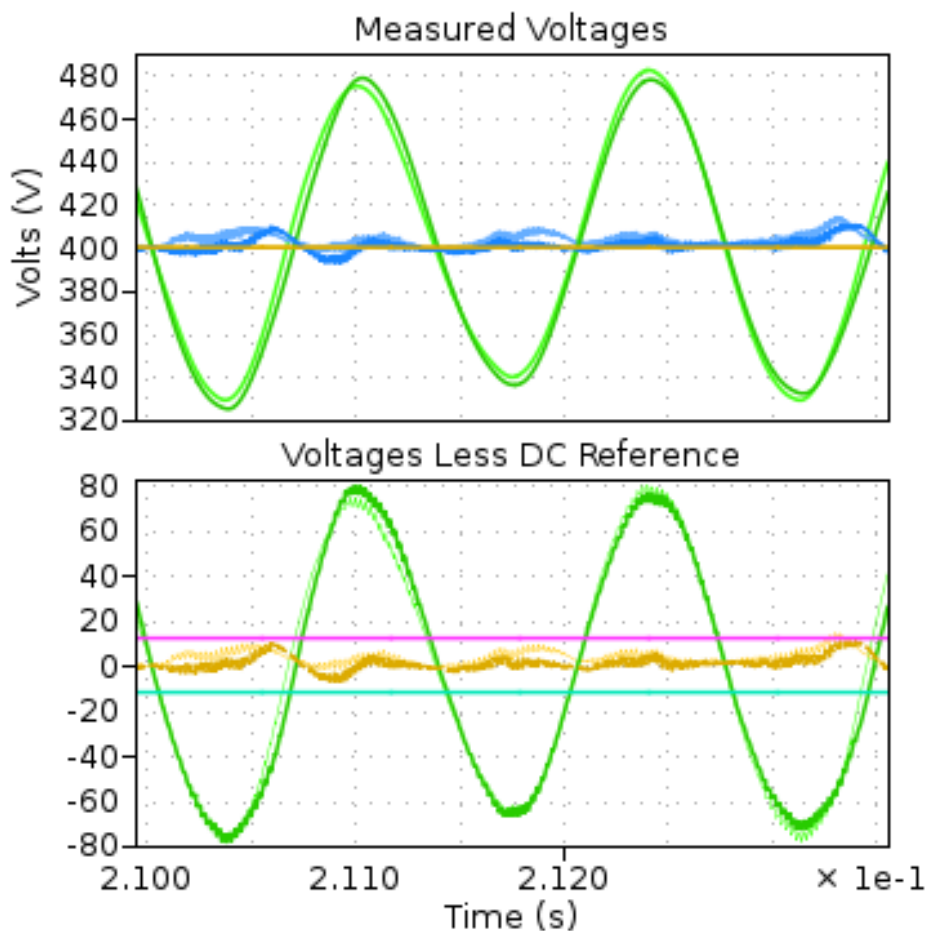


Figure 6.25: Simulated MVDC Amplifier Voltages for Air Gap (Light) and Active Injection (Dark) SDCT.

Top: Gold:  $V_{ref}$ , Blue:  $V_{LD}$ , Green:  $V_{LPF}$ ; Bottom Gold:  $V_{Ripple}$ , Green:  $V_{PDC}$ , Pink/Cyan: 3% Limit.

However, when active DC injection is used, the same AC Flux operates around the origin. This allows the entire B-H range to be utilized with AC injection for filtering. Transient operation is constrained under  $B_{Sat}$  as well because the SDAF injects DC current to follow load swings. This enables greater design flexibility and transformer utilization.

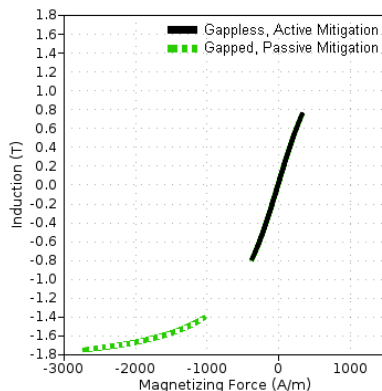


Figure 6.26: Pless Magnetics B-H Loop for Both Control Modes.  
Dash = Air Gap, Solid = DC Injection.

#### 6.2.7.4 FEA Verification of Simulations

In Figure 6.27 and Figure 6.28, FEA results show a comparison between the two DC flux mitigation techniques. Again the manufacturer data was imported into the software to ensure more accurate analysis. Figure 6.27 shows the analysis of the air gapped transformer with no active DC injection. Clearly, there is a maximum recorded flux density 0.9T in a majority of the core. When DC injection is utilized to mitigate the DC flux density with zero air gap, Figure 6.28, the maximum recorded is 0.066T resulting in a 93% reduction in DC flux density. As seen in the next section, this will have benefits towards reducing core loss.

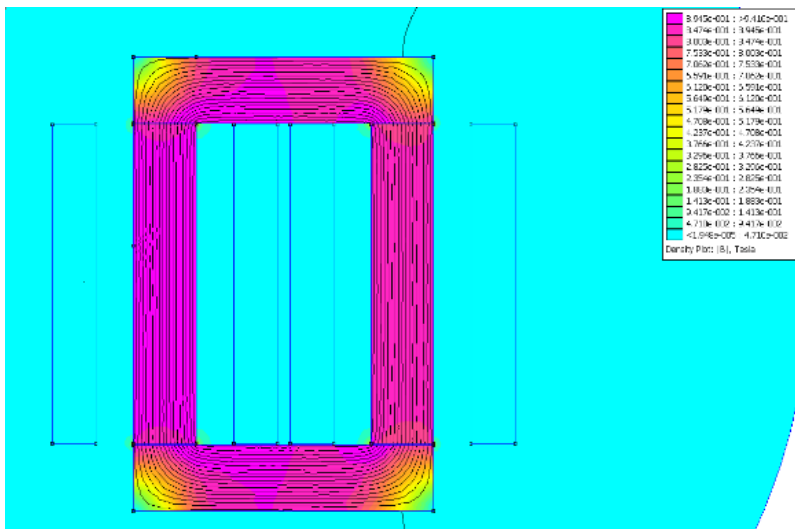


Figure 6.27: FEA Analysis for Air Gapped SDCT.  
 $B_{max} = 0.9T$ .

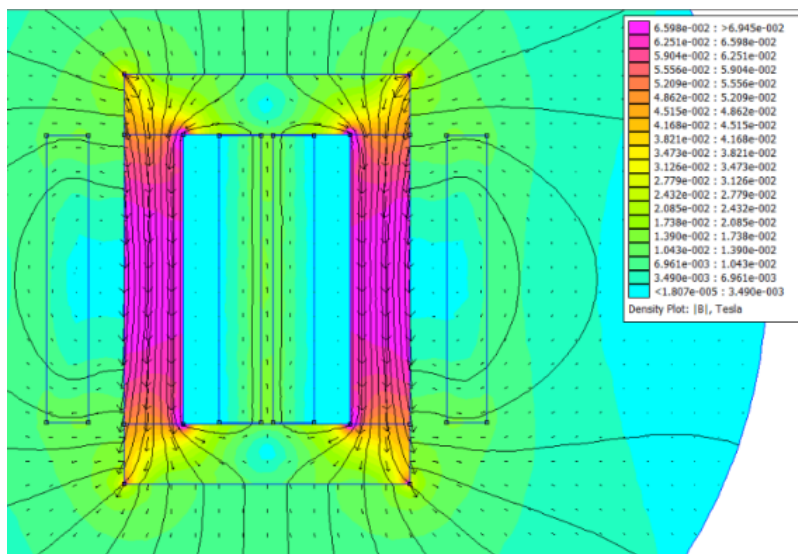


Figure 6.28: FEA Analysis of Active DC Injection SDCT.  
 $B_{max} = 0.066T$ .

### 6.2.7.5 Copper and Core Losses with DC Injection

It is important to point out that by eliminating the air gap, the total reluctance is greatly reduced. This reduces the number of necessary turns needed to generate the same magnetizing inductance for the SDCT. The number of turns needed for any particular magnetizing inductance is shown in (6.23) where  $\alpha$  is now the ratio between the length of the air gap and the length of the core material. The core properties of relative permeability and reluctance are  $\mu_r$  and  $R_c$

respectively. (6.24) shows the reduction in turns possible as air gap is reduced. A conservative estimate is to relate the winding resistance proportionally to the number of turns. However, this is only valid for a single layer of windings [173]. Since the SDAF filters relatively low frequencies, up to the 24<sup>th</sup> harmonic, high frequency effects can be neglected and (6.25) is sufficient for winding loss given a square core cross sectional area.

$$(6.23) \quad N = \sqrt{L_m \mathcal{R}_c (1 + \alpha \mu_r)} \qquad (6.24) \quad \%Reduction = 1 - \frac{1}{\sqrt{1 + \alpha \mu_r}}$$

$$(6.25) \quad P_{cu} = 8(I_{DC} + I_{AC})^2 N \sqrt{A_c}$$

The per volume core losses are predicted by the classic Steinmetz equation (CSE) (2.25) for sinusoidal flux where  $k$ ,  $\alpha$ ,  $\beta$  are core constants and  $f$  is the induction frequency of peak B. However, this does not adequately handle DC flux. [38] presented (6.26) for DC premagnetization. Following the procedure in [38] provides the modified Steinmetz parameters in Table 6.5. The results of these predictions are shown in Figure 6.29. Further efficiency improvements are gained by eliminating gap fringing effects and gap heating.

$$(6.26) \quad k_{new} = k \left( 1 + k_{DC} B_{DC} e^{\frac{-B_{AC}}{k_{AC}}} \right)$$

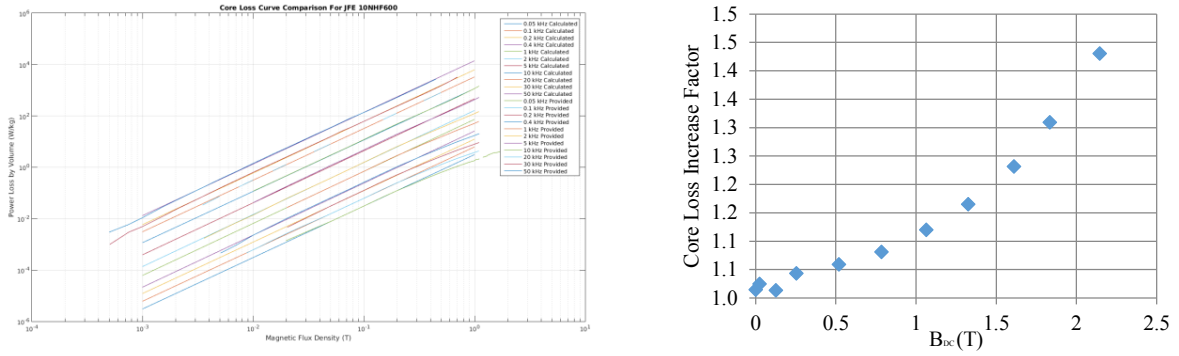


Figure 6.29: Loss Factors For JFE Steel Magnetic Core. AC Steinmetz Loss Map (Left) and Measured Core Loss Increase with DC Bias,  $B_{DC}=0.017T$  (Right).

Table 6.5: Frequency Dependent Steinmetz Parameters for 10JNHF JFE Steel.

Frequency Range	K	$\alpha$	$\beta$
50Hz - 200Hz	36.1694	.9992	2.0035
400Hz - 5kHz	42.7696	1.148	2.0258
10kHz	16.8987	1.6	2.0
20kHz - 50kHz	16.8987	1.58	2.01
$K_{DC}$	31.05	$K_{AC}$	4.75

In summary, the active injection of DC flux from the DCAF to mitigate saturation effects. There is a clear reduction in core volume and the number of turns needed. To adequately compare losses, designers can use the following two ratios (6.27) for copper losses and (6.28) for core losses.

$$(6.27) \frac{P_{cug}}{P_{cuu}} = \left( \frac{I_{AC}}{I_{ACDC}} \right)^2 \frac{N_g}{N_u} \sqrt{\frac{V_g}{V_u}}$$

$$(6.28) \frac{P_{cg}}{P_{cu}} = \frac{V_g}{V_u} (N_g I_{DC} \frac{\mu_0 \mu_r K_{DC}}{l_m} e^{-\frac{B_{AC}}{K_{AC}}} + 1)$$

In these ratios the subscripts  $g$  and  $u$  represent the gapped and gapless parameters respectively.  $V$  is the volume of the core and the core is assumed to be square. In (6.27), it is important to note that in the gapped SDCT, there is no DC current while there is DC current in the gapless design.

## 6.2.8 Hardware Realization of SDCT

### 6.2.8.1 Air Gap Design Cases

The series coupling transformers are tested in a laboratory scale of 12 kVA, 300 VDC amplifier test bed as shown in Figure 6.30. The whole system setup consists of a six-phase transformer, a twelve-pulse thyristor bridge circuit, and SDAF circuit. The transformer specifications and DC active filter parameters for the design cases are given in Table 6.6. The AMCC transformer in Figure 6.30 is built from an iron-based Metglas® amorphous alloy combining low loss characteristic with high saturation flux density, 1.56T. The JNHF based transformer in Figure 6.30 is made from high gradient silicon steel sheets, trading the lower AMCC core loss for higher saturation flux density, 1.88T. Besides using different core material, the two SDCT designs have a different target magnetizing intended to investigate the impact of transformer design on the amplifier performance requirements. Both transformers were designed by following (6.6) and ensuring (6.7) is maintained.

The test conditions for both transformers is with a steady state voltage reference of 300V<sub>DC</sub>. The twelve pulse rectifier is loaded with a 1kW load. The load is provided by a Chroma DC electronic load set for constant power operation. A 1kΩ resistor is also in parallel with the Chroma to provide a minimum load of 90 watts for the rectifier.

Transient performance of the two transformers was also tested. In order to examine the voltage excursion damping of the SDAF, a load step up was also tested. In this case, the load stepped from 700w to 1kW for step up response. Load steps for the AMCC and JNHF cores are displayed in Figure 6.32 and Figure 6.34 respectively.

In order to experimentally verify the proposed control structure, the SDAF is tested in a 4 kVA 380 V<sub>DC</sub> laboratory test bed, Figure 6.30. The DC bus is loaded with a programmable load

that is varied from 0.1 – 1 PU. The SDAF rides through all load changes and works to compensate AFE ripple at each loading point. Two transformers with air gaps and two without air gaps were designed using JFE high silicon steel and AMCC amorphous Metglas. In each case, the transformer is designed to have a magnetizing inductance between 10-12mH. It was found that the DCAF provided sufficient ripple compensation on the load and so the following results show just the DCAF action without the passive LPF.

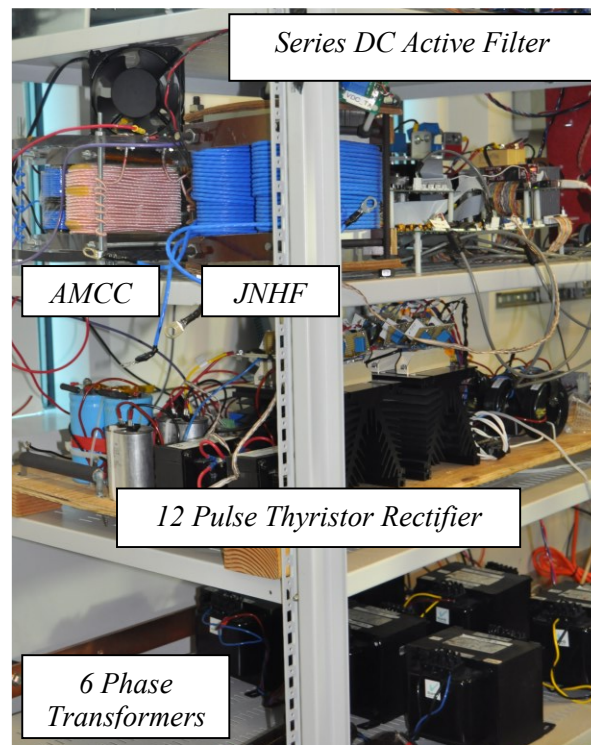


Figure 6.30: Medium Voltage DC Test bed Experimental Set-Up.

Table 6.6: Experimental Parameters.

Transform Parameter	Design A	Design B
Core material	Iron-based Metglas® Amorphous Alloy	JFE Super Core: Cold Rolled Silicon Steel
Core type	AMCC-400 C-cores	10JNHF600
Stacking Number	2	3
Stacking Factor	.82	.946
Saturation Flux Density	1.56T	1.88T
Primary Turns	93	72
Magnetizing Inductance	12.3mH	11.3mH
Primary Leakage Inductance	3.39mH	3mH
Primary Winding Resistance	0.151Ω	0.126Ω
<b>DCAF Parameters</b>		<b>Values</b>
Switching Frequency	21 kHz	
Primary DC Current	3.4A @ 1kW Load / 2.4A @ 700w Load	
Primary AC Voltage Max	250V @ 720Hz sinusoidal fundamental	

### 6.2.8.2 Air Gap Operating Results

Figure 6.31 shows the transformer DC side voltage and current. It also shows the resulting filtered DC voltage of the rectifier. As shown in these figures, the SDCT provides significant ripple reduction. Figure 6.31 and Figure 6.33 show the steady state performance of the active filter for a 1kW load for the AMCC and JNHF cores respectively. A large sample window was taken to enable analysis of the hysteresis loop of the transformers presented below in Figure 6.35 and Figure 6.36.

A load step up response was also tested for the transformer performance. In this case, the load was set to 700w and then stepped to 1kW. As can be seen in Figure 6.32 and Figure 6.34, the DC active filter responds to the step by damping the voltage drop and decreasing the settling time of the DC bus. In the following figures for air gap testing results, Figure 6.31 to Figure 6.34, CH1: Filtered DC Voltage, CH2: DCAF Injected Voltage, CH4: DC Load Current.

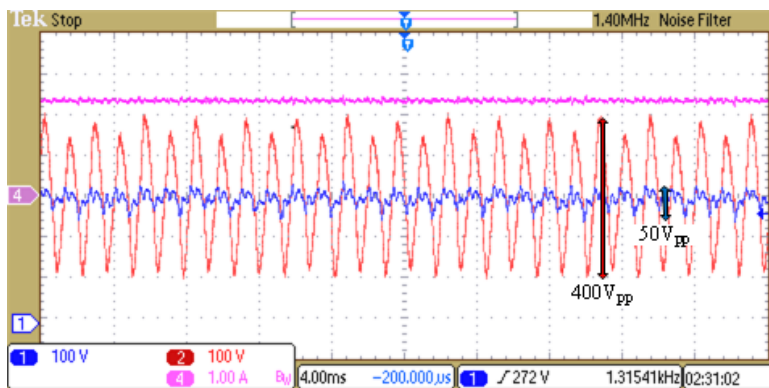


Figure 6.31: AMCC Core: Steady State Filtering, 1kW Load.

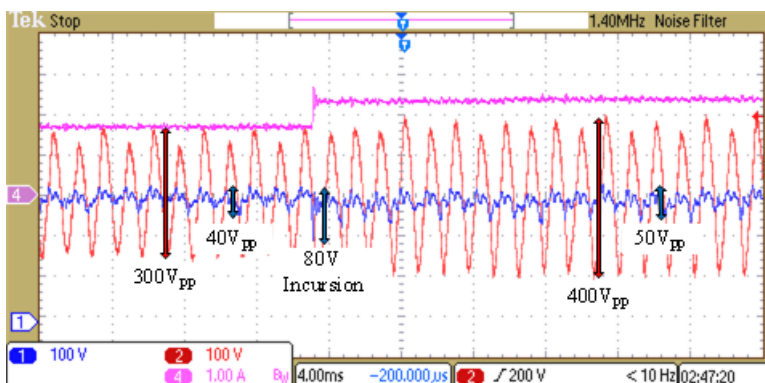


Figure 6.32: AMCC Core: 300w Load Step.

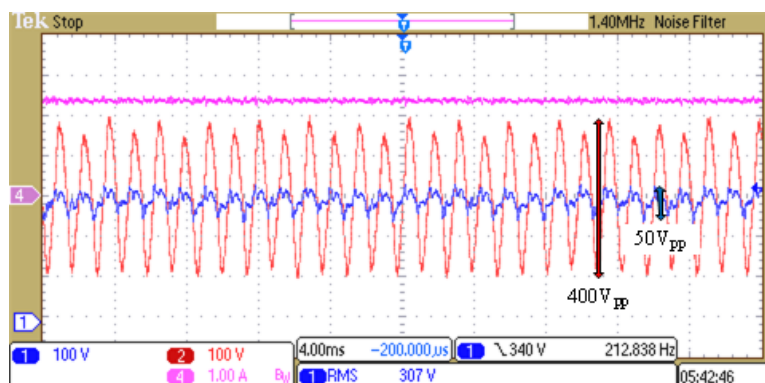


Figure 6.33: JNHF Core: Steady State Filtering, 1kW Load.

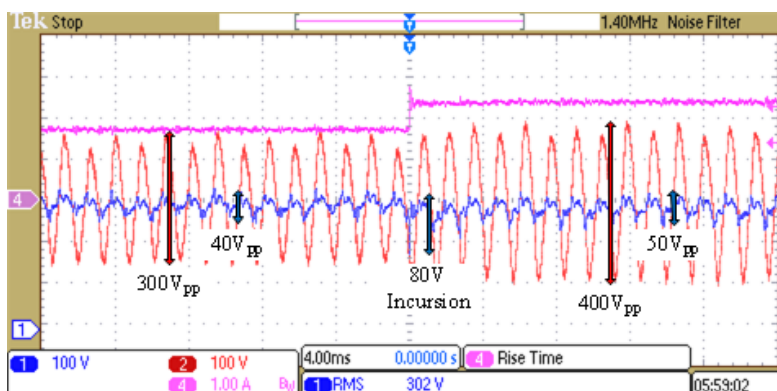


Figure 6.34: JNHF Core: 300w Load Step.

The results displayed in Figure 6.31 to Figure 6.34 were imported into Matlab for post processing and inspection of the hysteresis curve of the transformers. For clarity, both voltage and current were attenuated by low pass filters, removing the high frequency measurement noise and also the very small amplitude switching ripple.

Figure 6.35 shows the dominant flux density and magnetizing force ripples for one cycle of fundamental injection. Next Figure 6.36 shows the hysteresis curves for the entire window of the results of Figure 6.31 to Figure 6.34. As expected, neither core saturates. By taking the area within the hysteresis curve of the two transformers the wasted energy can be found. At this load level it is clear that the JNHF core dissipates less hysteresis energy per cycle than the AMCC core. The AMCC core suffers from additional turns and smaller cross sectional area relative to the JNHF core and therefore the magnetizing force is much higher, driving the difference in the loss level. By investigating Figure 6.35, it is also apparent that the greater efficiency of the JNHF core persists through load level changes.

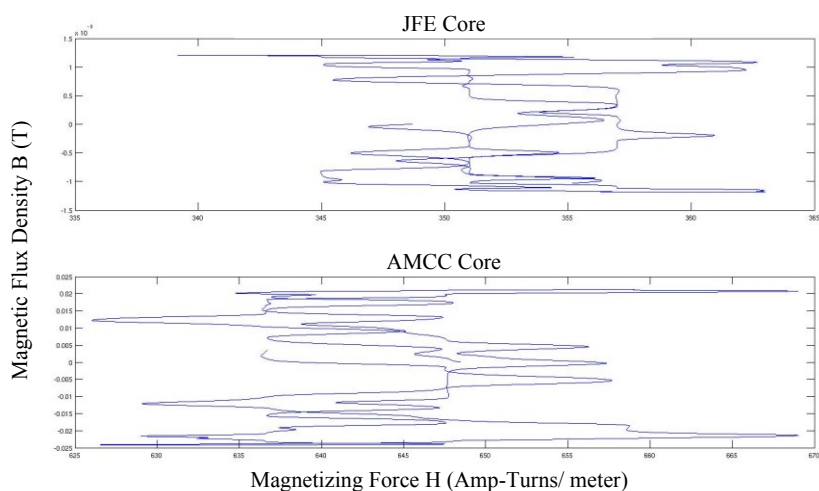


Figure 6.35: Hysteresis Loop for one 720Hz Cycle.

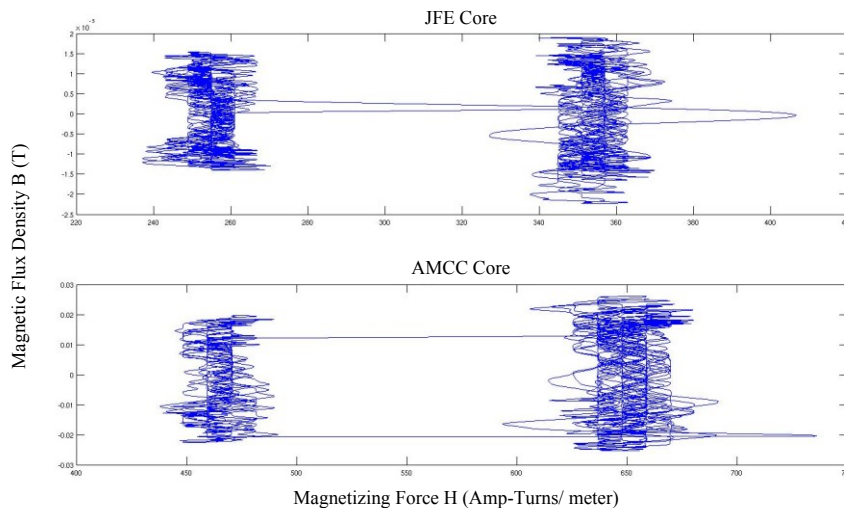


Figure 6.36: Hysteresis Loop for Oscilloscope Window During Step Load Change

The main reason for restricting the maximum load tested to 1kW was the significantly loud noise produced by the JNHF type core. Magnetostrictive properties for this core material were not available at the time of construction. Another core by JFE, the JNEX, purports to have zero magnetostriction. However, this is not the case for the JNHF type. More work is being taken to discuss the issue with JFE. Similarly, improvements in the experimental transformer construction are being investigated.

Audible noise was measured at a distance of 1 meter from the test bed. Table 6.7 presents the results of these measurements and it is obvious that the JNHF material transformer is prohibitively noisy.

Table 6.7: Measured Transformer Noise.

Material	Number of Gaps	Gap Location	700 W	1000 W
AMCC	2	Center	72dB	75dB
JNHF	4	Corners	83dB	92dB

One other contribution to the difference in noise is the construction differences of the two transformers. We were able to use C type cores from AMCC. This enabled two gaps in the center of the transformer. For the JNHF cores, we used I type. This means that there are four joints at the corners of the rectangle for the transformer to vibrate. In an attempt to minimize the possible

vibration, both transformers have thick bracket plates with threaded steel rod bolting the plates together. The transformers were also clamped to the experimental test bed to provide a large mass anchor. An improved design will isolate the different lamination zones and clamp joints individually e.g. three bracket plates for the JNHF core.

### 6.2.8.3 Active Mitigation Design Cases

As mentioned above, four transformer designs were constructed. Figure 6.37 shows a photograph of the various designs and provides a visual reference for the reduction in core and winding size for the gapless transformer. Table 6.8 further highlights this point showing the percent reduction from gapped to gapless designs.

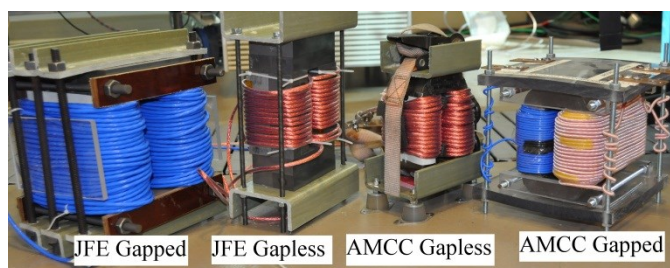


Figure 6.37: Comparison of Series DC Coupled Transformers.

Table 6.8: Comparison of Transform Designs.

Material	Gapped Volume	Gapless Volume	Reduction
AMCC 400	769.5 cm <sup>3</sup>	384.7 cm <sup>3</sup>	50%
10JNHF 600	2250 cm <sup>3</sup>	1344 cm <sup>3</sup>	40%
	Gapped Turns	Gapless Turns	Reduction
AMCC 400	93	29	69%
10JNHF 600	72	13	82%

### 6.2.8.4 Active Mitigation Operating Results

While all four cores were tested to sufficient operation, only the operating results for the gapless AMCC SDCT are presented for conciseness. An illustrative scope capture was taken at the 0.35 PU loading conditions in Figure 6.38 and Figure 6.39. These figures show a comparison between the operation without active DC injection. In the following four sets of measurements and BH loops, two types of ripple filters were employed. The first, voltage type, allowed the

switching ripple current back through the thyristor rectifier to ultimately be damped by the six phase YY/Y $\Delta$  transformer and appearing as high frequency voltage on the rectifier output. The next filter pushed the current towards the load where it can be seen in the load current.

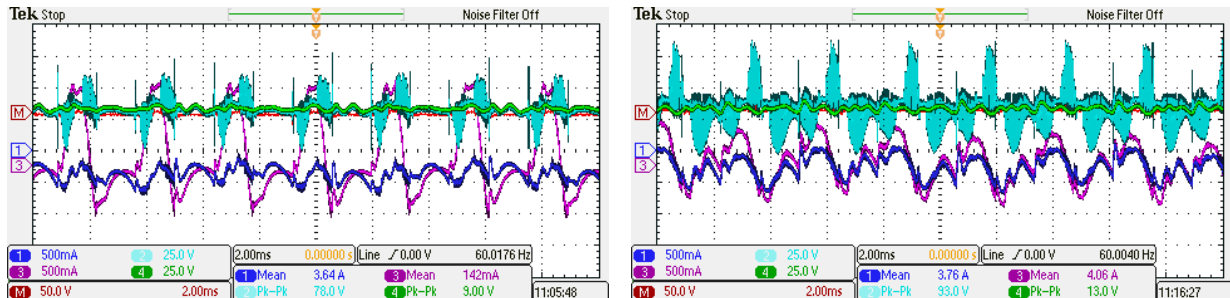


Figure 6.38: 2 kW DCAF Without (Left) and With (Right) Active DC Injection Operation with Voltage Type Filter.

Ch 1 = Load Current, Ch 2 = Thyristor Output, Ch 3 = SDAF Current, Ch 4 = Output Load Voltage, Voltages have -380 V and Currents have -4 A Offset (Left I DCAF has 0 A offset).

It is clear from analyzing the DCAF current in Figure 6.38 that the transformer is either on the verge of or in saturation. This is evident from the high current amplitude despite the relatively low voltage injection. At the same loading condition with active DC injection, the AC component of the current is stabilized and under control.

In order to investigate this phenomenon further and get an understanding of the core loss, the DCAF current and the SDCT compensation voltage on the DC bus side can be used to generate a hysteresis plot, Figure 6.39. Show the respective hysteresis plots of the SDCT core for no active DC injection and DC injection. This method is difficult and prone to error however as small DC bias leads to off center traces.

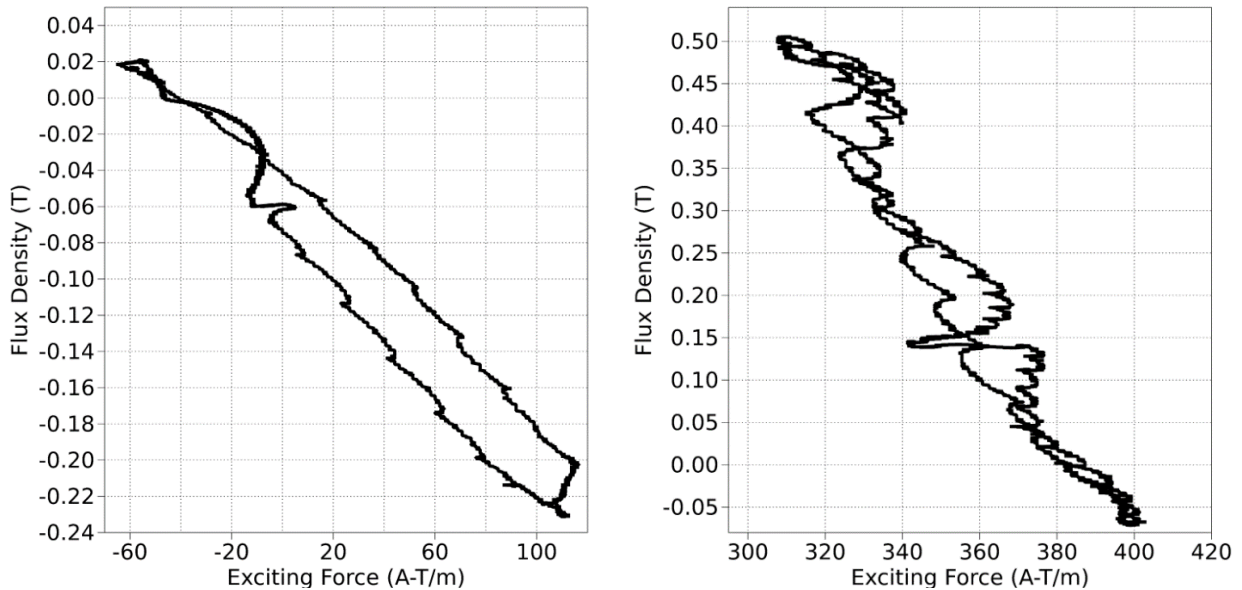


Figure 6.39: Measured BH Curve of SDCT Without (Left) and With (Right) DC Flux Cancellation.  $H$  is Proportional to DCAF Injected Current and  $B$  is Proportional to Time Integrated Voltage Injection

Based on Figure 6.38 is clear that when there is DC flux in the core that is not compensated by the DCAF as active DC injection, there are increased core losses. This is measured by the increase area enclosed in the BH curve. Similarly, the active DC injection provides a bias  $H$  that shifts the BH loop in the positive  $X$  direction. Further insight into the SDCT behavior can be gathered by calculating the ratio of  $B$  and  $H$  at the maximum  $H$  point. This is a typical way of determining the magnetic permeability from a hysteresis plot. In the case where DC flux is not compensated, the relative permeability is around 2000. When the DC flux is compensated, the core relative permeability is around 9300. This further confirms that the core is near saturation when DC flux is not compensated and it is well within the linear region when the DC flux is compensated. The manufacture reported permeability is around 10000 and given some frequency and temperature roll off, the experimental results are within expectations for BH knee and BH linear operation.

While at steady state, this near saturation effect is undesirable, however it can be useful for improved dynamic performance. Reducing the magnetizing inductance by a factor of 5 can weaken the stiffness of the DC bus allowing for a faster response. Similarly, the magnetizing inductance can be designed larger than necessary. A deliberate mismatch in DC flux cancellation would bring the inductance down to appropriate levels for steady state. By matching the DC flux cancellation, the inductance can be raised, increasing the magnetizing inductance to increase the bus stiffness for heavy load transient conditions as an example.

Below are two alternative screen captures and BH loops. The filter was changed such that the switching ripple injected from the DCAF transitioned from voltage dominant to current dominant.

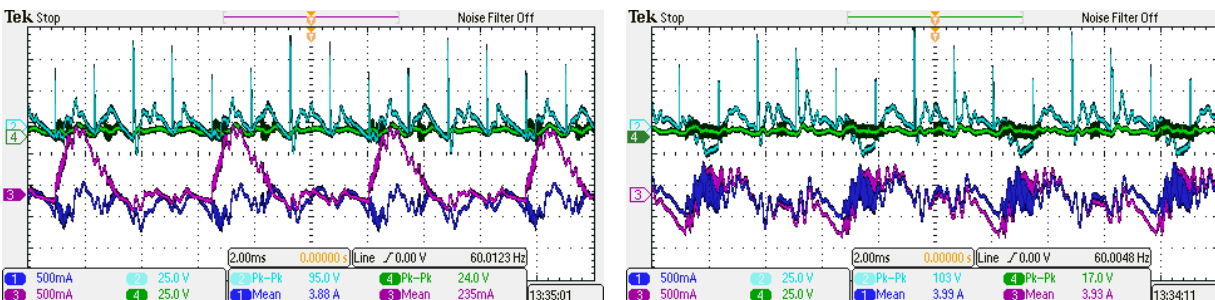


Figure 6.40: 2 kW DCAF Without (Left) and With (Right) Active DC Injection Operation with Current Type Filter.

Ch 1 = Load Current, Ch 2 = Thyristor Output, Ch 3 = SDAF Current, Ch 4 = Output Load Voltage, Voltages have -380 V and Currents have -4 A Offset (Left I DCAF has 0 A offset).

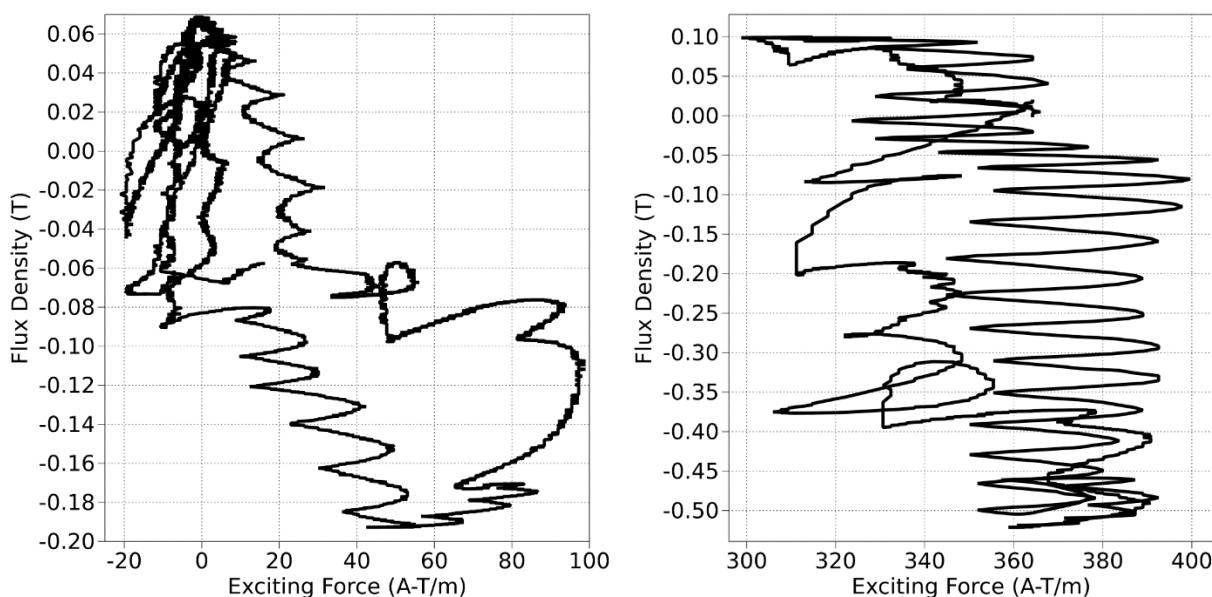


Figure 6.41: Measured BH Curve of SDCT Without (Left) and With (Right) DC Flux Cancellation with Current Type Filter.

$H$  is Proportional to DCAF Injected Current and  $B$  is Proportional to Time Integrated Voltage Injection

It is clear from Figure 6.40 that the core is highly saturated without active DC injection. Once this injection is applied, the SDAF is able to supply ripple compensation without core saturation. These perspectives are even more clear from Figure 6.41 where the effective relative permeability of the SDCT is 550 and 10000 for the zero compensation and full compensation modes respectively.

It should also be noted that the switching ripple now appears in the load current instead of the rectifier voltage. This means that designers can choose where the unfiltered switching noise goes in the system. If the load is sensitive and the source is robust, the first filter would be a good choice. However, if the load is robust and the source is sensitive, as in generator powered remote mining operations, this second filter should be preferred. In either case, the DC active filter has been shown to be capable of reducing the ripple of a line commutated rectifier using either an air gap or active DC mitigation. The sections below will provide a summary of the performance of the two solutions over various loading conditions.

### **6.2.9 MVDC Amplifier Performance with Air Gap Mitigation**

Figure 6.42, Figure 6.43 and Figure 6.44 show a summary of the performance of the DC active filter when using an air gapped series DC coupling transformer. These results are for the JFE gapped core. Unfortunately, the AMCC gapped core resulted in significant audible noise and could not be tested beyond minimal power ratings. As such, those results are omitted. An interesting artifact present in the results of the JFE gapped transformer is the magnetizing force dependent relative permeability. This is shown in the jerk in results around the 1800w load. This occurs because the JFE material has a sharp increase, four times nominal, in relative permeability between 20 and 100 amps per meter. With the air gap design, this shifts this spike to between 2 kA/m and 10 kA/m. This can clearly be seen by the jerk in Figure 6.42 aligned with this region on the Y axis. This is also clear by the sharp drop in apparent impedance of the SDCT at 1800W. The impedance continues to drop slightly as the relative permeability has a soft decay beyond 3 kA/m. It is clear from Figure 6.43 that the DCAF is able to supply an output voltage over the entire loading range, limited only by the DC link of the DCAF. Furthermore, the DCAF is able to hold the load ripple voltage to nearly  $20 V_{\text{rms}}$  over the entire loading range.

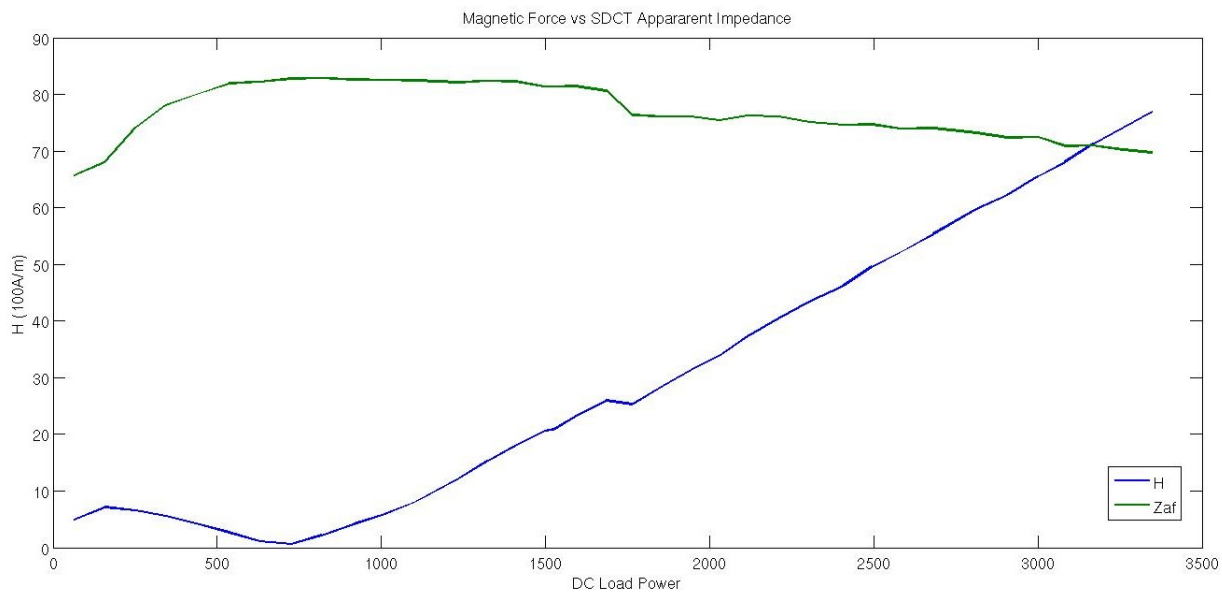


Figure 6.42: Air Gapped SDCT Impedance and Load DC Field, No Output Saturation.

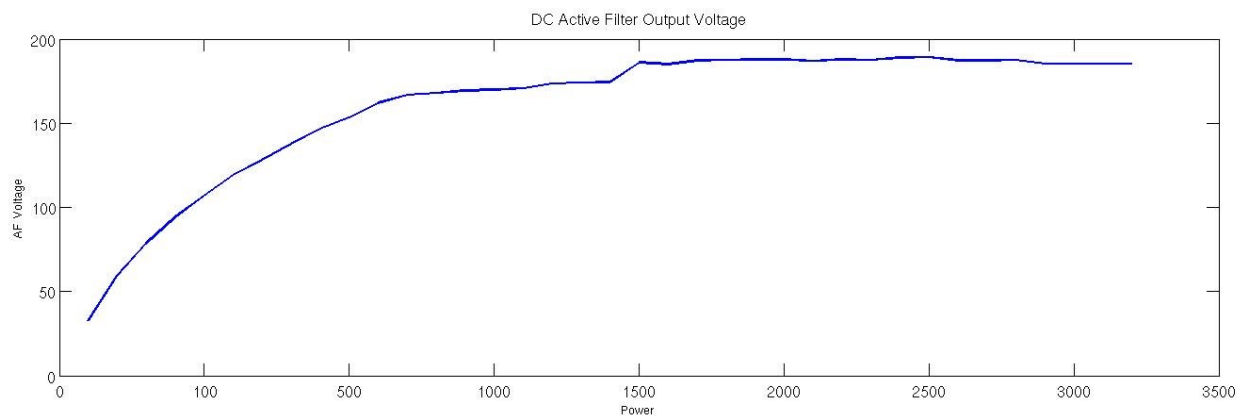


Figure 6.43: Output Voltage of DCAF vs Load Power Showing VDC Output Limit.

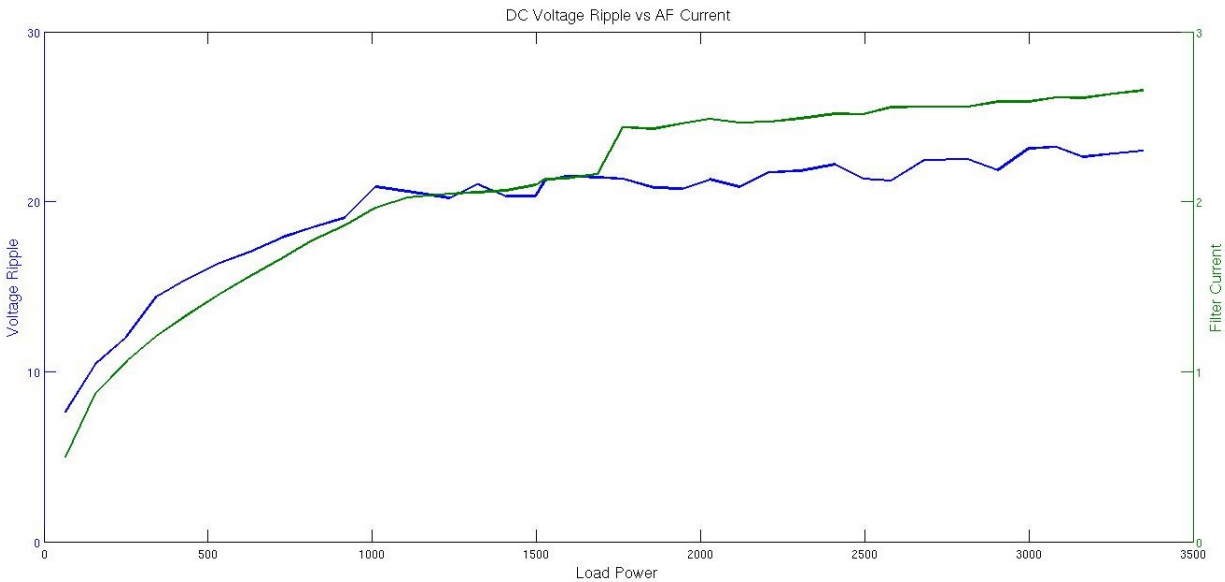


Figure 6.44: SDAF Current Output with Resulting Voltage Ripple vs Load.

These results show that the air gapped SDCT is a viable candidate for the DCAF. While not meeting the exact voltage ripple specs, a significant ripple reduction was achieved. Furthermore, these results are using significantly underrated passive components. This means that a slight increase in these components could very well bring the system performance into the desired specifications. One significant caveat is that peak loading conditions were unachievable even with the JFE core material due to large audible ringing. This leads to further desire to move towards a gapless design or even an uncut design. The active cancelation method is a viable control strategy to get this capability.

### 6.2.10 MVDC Amplifier Performance with Active Mitigation

As mentioned previously, the MVDC amplifier system is loaded over a wide operating range. The load voltage was recorded and imported into Simulink to analyze the ripple at particular frequencies of interest. The SDAF controller is designed with PR branches at the 6<sup>th</sup>, 12<sup>th</sup>, and 24<sup>th</sup>, harmonics. The feed forward branch compensates any other load ripple frequencies and it was found in post processing that the 18<sup>th</sup> was also a significant ripple. The

harmonic ripple magnitudes over the loading profile are shown in order in Figure 6.45 to Figure 6.48.

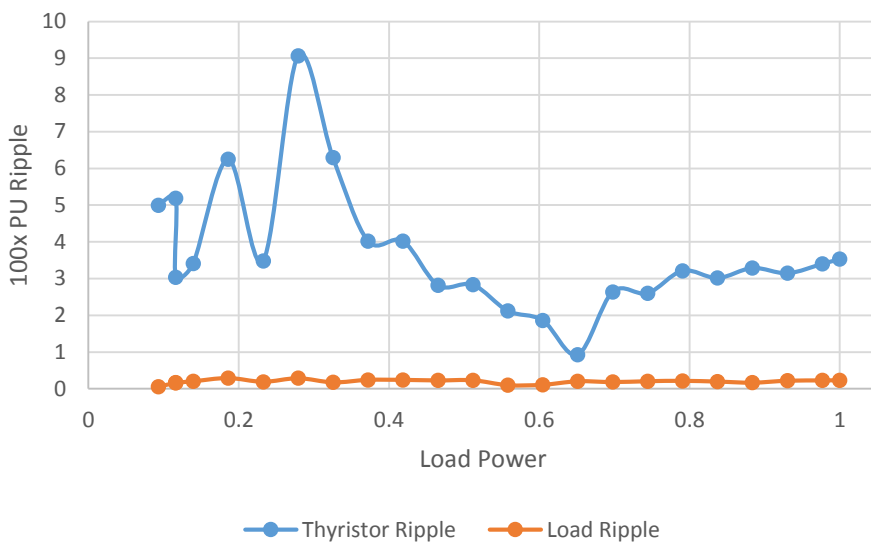


Figure 6.45: 6th Harmonic Component of DC Ripple Compared to Loading.

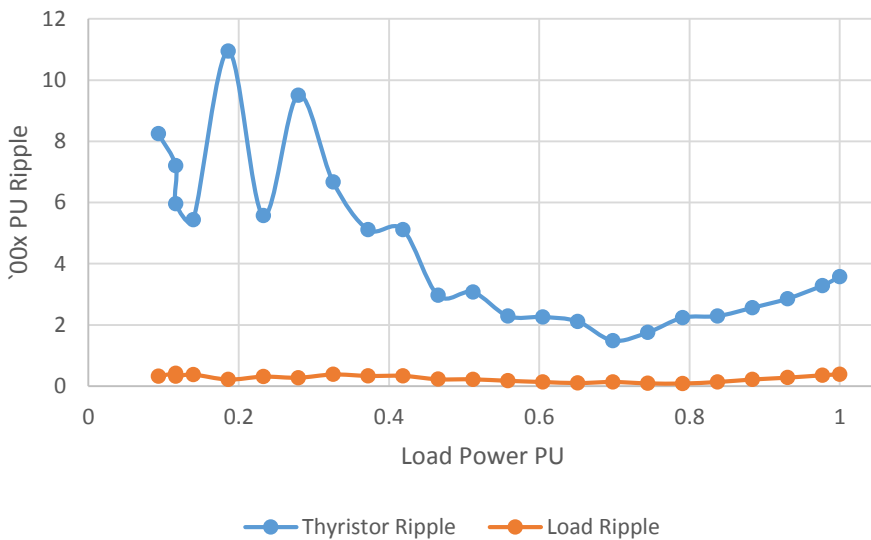


Figure 6.46: 12th Harmonic Component of DC Ripple Compared to Loading.

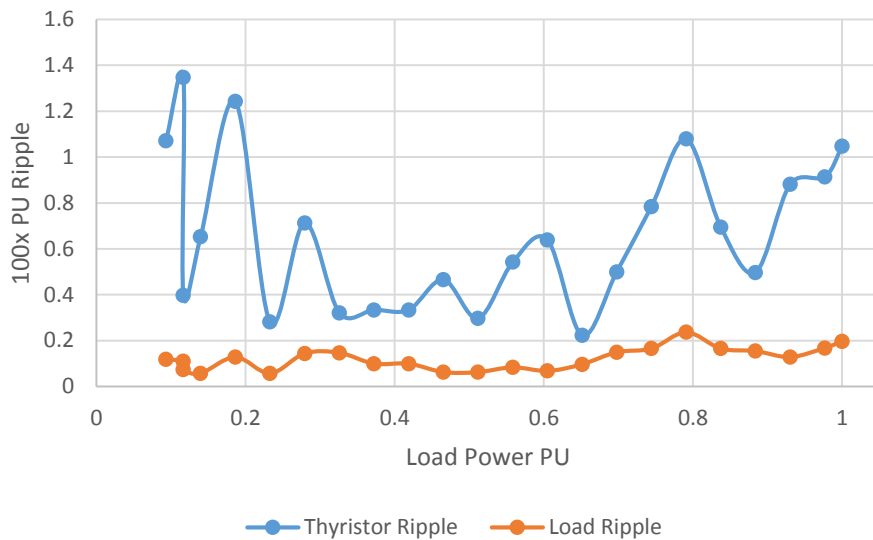


Figure 6.47: 18th Harmonic Component of DC Ripple Compared to Loading.

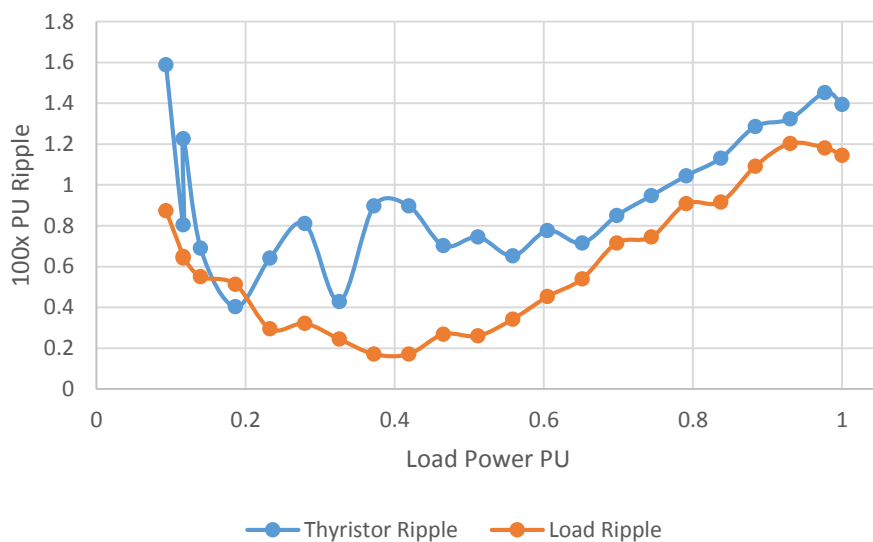
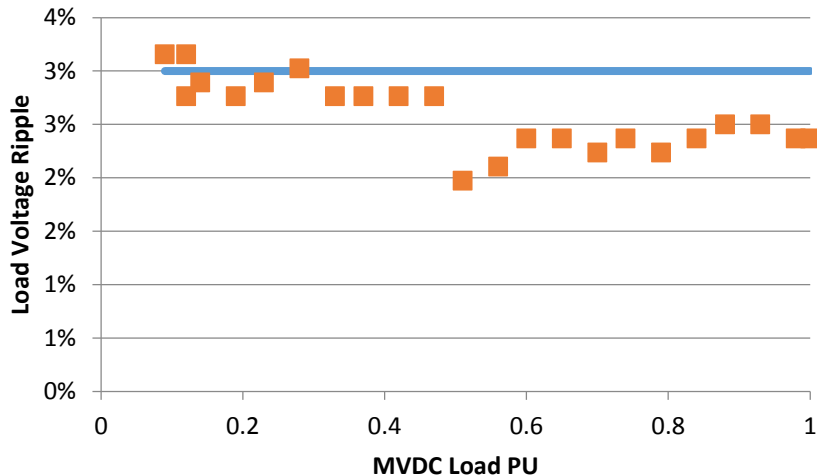


Figure 6.48: 24th Harmonic Component of DC Ripple Compared to Loading.

The overall compensated load voltage ripple over the loading profile is shown in Figure 6.49. It is important to note that the load is compensated to the rigorous specifications of [156] and Table 6.1. There are a few instances, at very low load and at 0.3 PU, where the load voltage ripple exceeds the threshold. However, further gain scheduling can improve the performance and bring the voltage ripple within specification at all loading conditions.



*Figure 6.49: Overall DC Output Ripple.  
Blue Line = 3% Ripple Limit, Square = Actual Load Voltage Ripple.*

The MVDC amplifier shows a significant ripple reduction that is well within the strict US Navy specs over a wide steady state operation. It also provides unique opportunities during transient operation. By supplying a DC current on the active filter side of the transformer. The DCAF stores significant energy in the magnetizing inductance of the DC coupled transformer. This energy can be used to respond to transients or even aid in arresting load faults. An example of this operation is shown below in Figure 6.50. These results demonstrate the DCAF capabilities but do not include a full protection scheme. As such, after the DCAF forced zero crossing, the system is allowed to oscillate and naturally dissipate energy. This uncontrolled state is because the DCAF switching protection and programmable load protection trip. Similarly, the thyristor controller tries to restore the DC bus voltage. Given full coordination, this secondary ringing would not be present as the source would be disconnected from the faulted load. Similarly, the fault condition is emulated by the programmable load. In this emulation, the load protection effectively resists a current zero crossing by reducing the load dynamically.

In Figure 6.50, Channel 3 is the load current with a -4 amp offset. This current begins rise due to a fault at a 0  $\mu$ S reference. DCAF detects a fault and injects a large amount of current,

Channel 1 with -4 amp offset. This introduces a large voltage across the transformer, the math channel, which is inverted to clearly show the DCAF impact. This voltage subtracts from the source voltage, Channel 4 with -250 volt offset, to provide a zero crossing for the load voltage, channel 2 with a -380 volt offset. During this zero crossing period of about 40  $\mu$ S, a traditional circuit breaker and other active protection such as load turnoff could open and prevent further sourcing of the of the load. The event timing is summarized in Table 6.9.

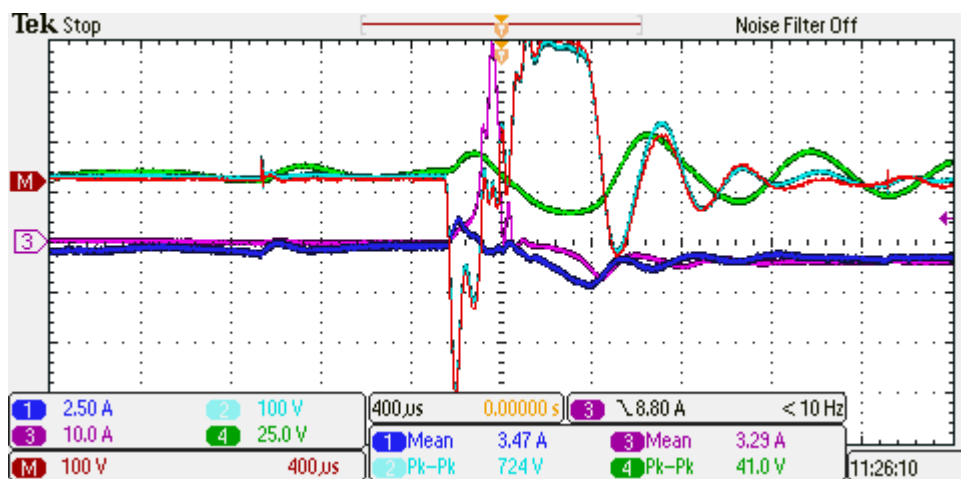


Figure 6.50: DC Circuit Breaker Operation of DCAF with Active DC Injection.

Table 6.9: DCAF Circuit Breaker Timing.

Event	Time ( $\mu$ S)
Fault Occurs	0
Fault Detected	4
First Zero Crossing	37.8
Source Takeover	57.33

This transient energy injection of the DCAF with active DC injection can be used for other purposes. This energy can, as demonstrated enforce a zero crossing of the DC voltage. It can also be used for load and source transient responses. As discussed in the air gap design, the load increase induced voltage dips must be limited. The DCAF with active DC injection and source some of the required suppression energy by rapidly injecting DC current. Similarly, the source voltage step request response time can be improved by temporarily propping up the load voltage with the DCAF while the thyristor rectifier catches up.

### 6.2.11 Conclusions and Discussion

This section described the motivation for the design of a series DC transformer. The SDCT will couple a DC active filter to the DC bus of a thyristor based rectifier. Filtering of a DC bus through active compensators has broad implications beyond those mentioned in [157] e.g. bus filter and stabilization in DC microgrids.

Paramount to the successful operation of the DC active filter is a properly designed SDCT. The limiting equations of the transformer design with an air gap were shown through the realization of a laboratory model. From this design the section describes the process to optimally design a transformer given certain priorities.

This section also presented a novel control and design method for series DC coupled transformers in series DC active filter. A proportional resonant controller is used to generate the ripple compensation. The resonant branches are tuned to dominant harmonics and the feed forward branch can compensate ripple in other spectrum. A key addition to the control is active DC injection that matches and mitigates the DC flux in the SDCT core.

The active DC injection enables the elimination of the need for an air gap in the core. This flux cancelation results in a significant reduction of the necessary turns for a target magnetizing inductance and the volume of the core. There are further loss savings by reducing the loss impact of DC premagnetization. By using the DCAF to inject the DC flux, this solution eliminates the need for a tertiary winding and DC current source converter. Further design flexibility can be achieved when deliberate DC flux mismatch is utilized. This method achieves a practical magnetizing inductance that is programmable by the user.

Two core material designs with both air gap and active flux mitigation were compared as the coupling transformer. Design requirements that can be calculated met expectations. However, the unknown magnetostriction properties greatly impacted the ability to design and test.

Ultimately, design of the series DC transformer requires several tradeoffs. In order to ensure sufficient design, parametric sweeps should be used to identify regions of various parameters that provide near optimal design. This section provides the design considerations and methodology for proper series DC transformer development.

The presented solutions offer new design flexibilities while also maintaining strict performance requirements. It enables new approaches to establishing clean DC busses as desired in many new power distribution schemes and systems. It similarly enables the use of relatively cheaper and more efficient line commutated converters for use in these high performance applications.

### **6.3 Magnetics for Active Bridges**

Active bridges are becoming one of the primary converters for high power applications that require galvanic isolation due to their high efficiency and relative robustness [62]. At higher powers and higher voltages, the converter will operate in the medium frequency range to limit switching device stress and  $dv/dt$ . Because of this medium frequency, and the high magnitudes of excitation voltage, metal amorphous nanocomposite magnetic ribbon cores offer a viable solution for high power density designs [176]. The fundamental operation allows bidirectional power flow through the transformer leakage inductance or an additional auxiliary inductor. In high power density designs, the leakage inductance is preferred because it is a part of the basic geometry of the transformer. However, as mentioned in CHAPTER 4:, this can introduce catastrophically high excess losses due to the leakage flux entering the broad surface of the

ribbon. As such, normal leakage flux should be minimized. This section will demonstrate two designs that incorporate this idea for MANC cores. The first design achieves this by minimizing the leakage inductance in the transformer and using auxiliary inductors. The second design will orient all of the core material such that the flux is tangential to the ribbon. In other works, the axis of the toroid cores is aligned with the axis of the flux thus it is called an axial design.

Many researchers developed control strategies for improving the DAB given a magnetics design. The converter soft switching region and the parasitic and magnetizing inductance effects on this region are described in [63]. Similarly, control strategies for minimizing the supplied reactive power, or expanding the soft switching region by varying the duty cycle were shown in [64] and [78]. Higher power and multiphase DABs are described in [106] and [177]. These works show the wide variety of improvements made to the DAB system as well as its viability in diverse applications. However, none of these works approach the issues of normal leakage flux or utilize advanced manufacturing strain annealing for designs.

This section will exam some of the advanced possibilities in a design comparison. The transformers will be designed for a three port active bridge setup that is a 10 kW prototype for the SunShot National Laboratory Multiyear Partnership (SuNLaMP) project. This project is geared towards developing an industrial scale converter that connects and manages power flow between the grid, a battery energy storage system and a photovoltaic generator. Both DAB transformer designs will focus on minimize losses due to normal leakage flux. An axial design will both minimize normal flux as well as utilize new, strain annealed, cores for a tuned core assisted leakage inductance.

Under the SuNLaMP program, many design variables were chosen due to constraints outside of an optimal magnetic design. Examples of these non-optimal choice constraints are to

meet particular program specifications, allow manufacturing limitations and accommodate industrial partner's commercial goals. The hardware prototypes then may not meet global optima's but the design process is still valid.

### 6.3.1 Emulating Active Bridge Power Flow

Using the dual voltage source test converter, a dual active bridge power flow can be emulated by exciting the primary winding and shorting the secondary, Figure 6.51. The dual voltage source converter is essential for this emulation as it can provide the necessary positive, yet low voltage needed to ensure a flat current profile during the off period. In order to properly scale this study to an active bridge excitation, a careful inspection of desired emulated waveforms is needed. It is clear that twice the desired emulated DC bus is needed for leakage excitation, Figure 6.52. The power waveforms for example emulations of the triaxial transformer are shown below in Figure 6.53, showing bidirectional power flow.

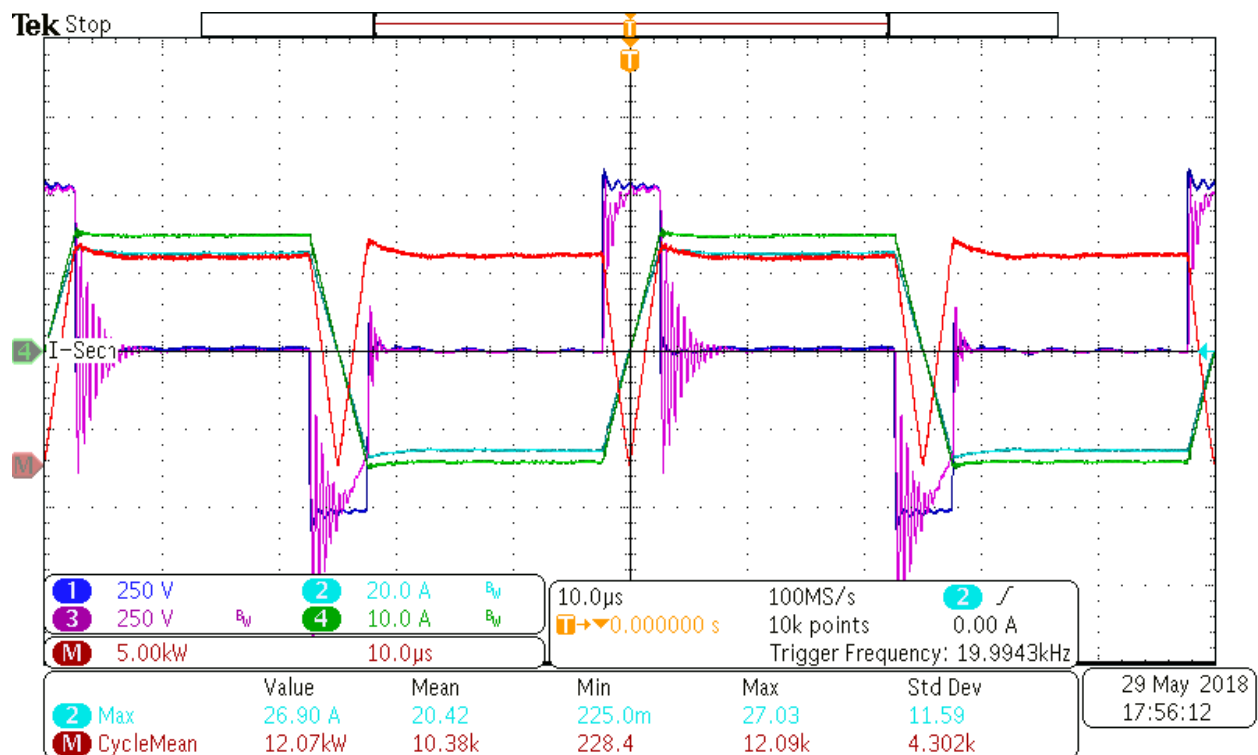


Figure 6.51: Active Bridge Emulation Waveforms Using Dual Voltage Source Converter.

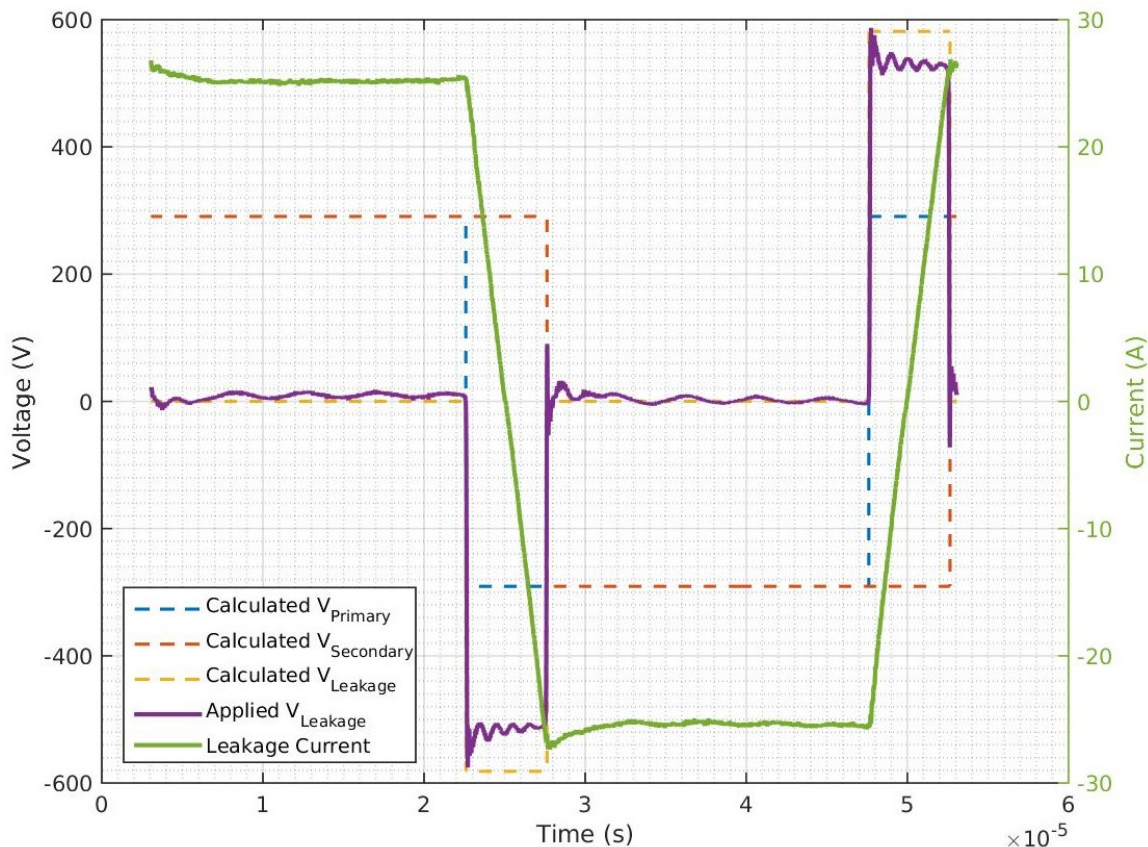


Figure 6.52: Calculated Active Bridge Waveforms From Dual Voltage Source Converter.

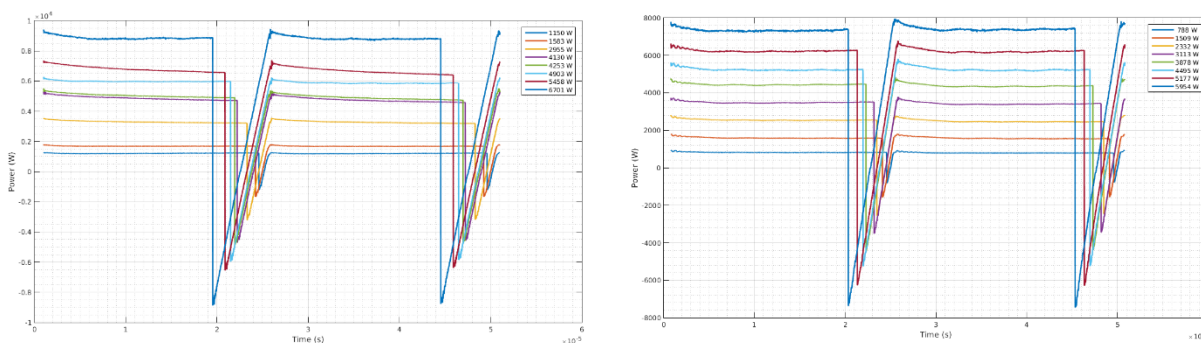


Figure 6.53: DAB Instantaneous Power Waveforms Emulated by Dual Voltage Source Core Tester Triaxial Transformer Power Flow: Primary to Secondary (1150 – 6700 W) (Left) and Secondary to Primary (788 0 5950 W)(Right).

This method of emulating the power flow waveforms of an active bridge will be used to characterize the performance of the two designs, concentric winding and triaxial transformers, for the three port active bridge for the SuNLAMP project.

### 6.3.2 Concentric Design

The underlying principal of the concentric design is minimizing the leakage inductance of the transformer. This means that less leakage flux could enter the broad surface of the ribbon and less leakage flux would need to be shielded. As such, the multiple excitation coils of the transformer are wound around each other. Furthermore, having magnetic core fully encompassing the winding enables broad surfaces of the cores to be connected to heat sinks or other thermal management systems. An example of this geometry is shown below in Figure 6.54, left, with a depth of  $d_m$  into the page. As previously discussed, the leakage inductance is minimal and what leakage flux there is, is predominately located between coils and not flowing into the magnetic ribbon material. This structure does lead to a higher winding to winding capacitance. The windings similarly need to ensure proper insulation as there is minimal distance between different coils.

In order to have the required leakage inductance needed for power flow and operating control in the DAB, auxiliary inductors are needed. The concentric design case study uses materials and manufacturing techniques that are broadly available currently. As such, the leakage inductors will utilize traditional MANC ribbons with an air gap to ensure saturation avoidance. An example of this structure is shown in Figure 6.54, right, with this inductor having a depth into the page of  $d_l$ . The windings should not be wound over the air gap to ensure fringing flux does not cross the conductor, exacerbating proximity effects. For the three port DAB, two inductors are required at a minimum however three is preferred because they will help to reduce the  $dv/dt$  that is applied to the transformer.

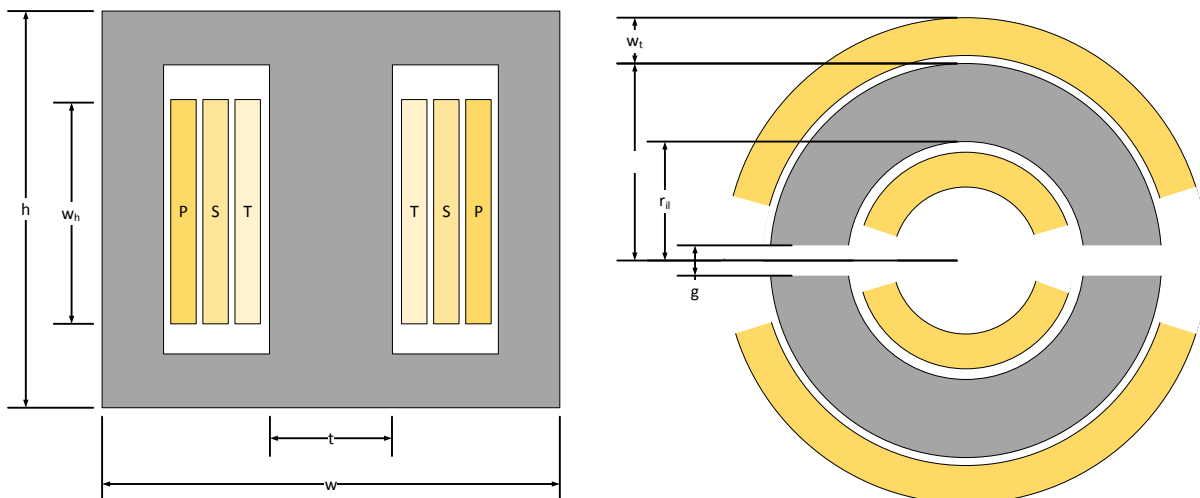


Figure 6.54: Three Port Concentric Winding Transformer with Auxiliary Inductor Dimensions. Magnetizing Transformer Core (Left), Auxiliary Leakage Inductor (Right).

The magnetizing core of this design follows many of the traditional transformer manufacturing guidelines available in textbooks e.g. [178]. That is, the core window should be sized to have a full fill of windings, accounting for copper fill factors. If Litz wire is used, a fill factor between 0.5 and 0.7 is common. Similarly, the flux density should be limited by losses using fitted Steinmetz parameters. Given active bridge operation, triangular parameters are appropriate, (6.29). The magnetizing flux density is shown in (6.30). An interesting concept that is highlighted here is equalizing the volts per turn for each exciting coil. This ensures that each coil contributes to the magnetizing branch evenly. The magnetizing inductance for the transformer is (6.31) while the air gapped inductors is (6.32). In order to meet power density requirements, it is important to count both the transformer and the inductors, (6.33). This volume is the displacement volume of the magnetic components and not the more conservative, rectangular enclosure. However, this allows for more direct comparison of the concentric and axial designs.

$$(6.29) \quad P = V_{core} k_{tri} f^{\alpha_{tri}} B_{pk}^{\beta_{tri}}$$

$$(6.30) \quad B_m = \frac{v}{kNfdt}$$

$$(6.31) \quad L_m = N^2 \frac{\mu_{rm}\mu_0 dt}{2h+w-8t}$$

$$(6.32) \quad L_l = \frac{N^2}{\frac{2\pi}{d\mu_{rl}\mu_0 \ln\left(\frac{r_{ol}}{r_{il}}\right)} + \frac{g}{\mu_0 d_l(r_{ol}-r_{il})}}$$

$$(6.33) \quad Volume = V_{mag} + 3V_{lk} = d_m hw + 3d_l \pi (r_{ol} + w_t)^2$$

Next it is important to account for the parasitic capacitances. In this design, each coil can be assembled as a single layer so partial layers and winding layout are not necessary considerations. Nomex paper is wrapped around each winding to further increase the insulation between windings. The winding to winding capacitance and the winding capacitance to the core can be modelled with parallel plate simplifications, shown below in (6.37)  $Volume = 2D\pi R_{oo}^2$ ). The space between two capacitive plate models is  $s$ .

$$(6.34) \quad C_{con} = 2 \frac{\epsilon_0 \epsilon_{rw} w h (d+t)}{s}$$

The design parameters and dimensions are shown below in Table 6.10. A photograph of the magnetizing transformer is show below in Figure 6.55.

Table 6.10: 10 kW Concentric Design Parameters.

Parameter	Dimension	Value
Switching Frequency	$f$	10 kHz
Magnetizing Depth	$d_m$	75 mm
Magnetizing Height	$h$	75 mm
Magnetizing Thickness	$t$	17 mm
Width	$w$	65 mm
Leakage Depth	$d_l$	25 mm
Leakage Outer Radius	$r_{ol}$	45 mm
Leakage Inner Radius	$r_{il}$	21.5 mm
Gap Length	$g$	1.5 mm (each side of core)
Turns {Primary, Secondary, Tertiary, Leakage}	$\{N_p, N_s, N_t, N_l\}$	{20, 13, 13, 22}

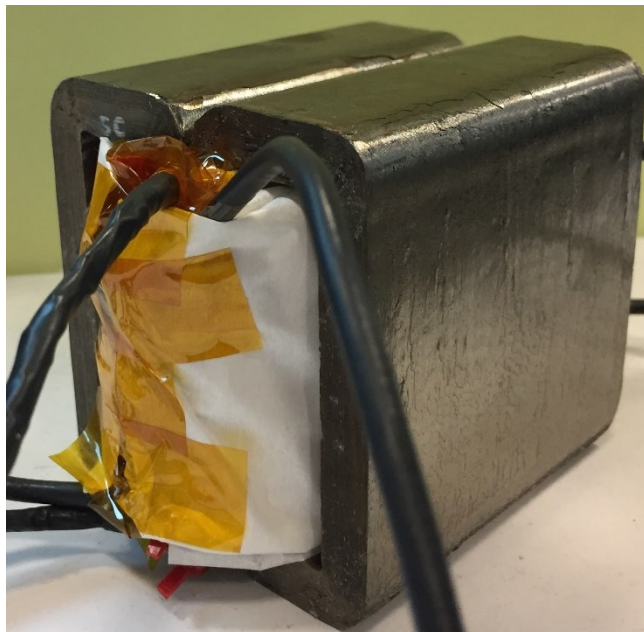


Figure 6.55: Prototype 10 kW Three Port Concentric Transformer.

In order to determine the series and parallel capacitances of this transformer a Keysight LCR meter was used to sweep impedances over frequencies. The leakage inductance is found by shorting a winding and applying the LCR meter to an excitation coil. This is similar to a traditional transformer short circuit test configuration. The series capacitance is easily measureable and is a stable impedance when the two LCR meter leads are connected to the two coils under inspection. The capacitance is determined with the leads of each coil shorted to themselves and connected to a meter lead. As an example, the two primary coil leads would connect to the positive LCR meter lead and the two secondary coil leads would connect to the negative LCR meter lead. This measures the series capacitance between the primary and

secondary windings. Determining the parallel capacitance requires more thought as the transformer magnetizing inductance is a dominant characteristic. Therefore, an admittance and phase plot is necessary. The magnetizing inductance can be determined from the low frequency measurements and then the parallel capacitance is easily determined by the resonant frequency, where the phase plot crosses the zero axis.

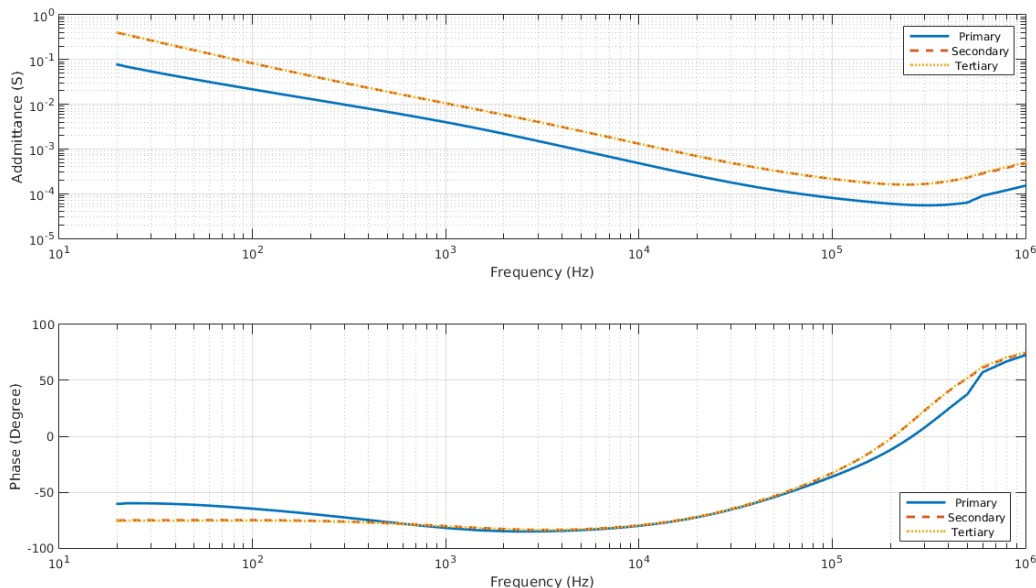


Figure 6.56: Concentric Winding Open Circuit Admittance Bode Plot.

The resonant frequency is where the phase plot crosses zero,  $f_0$ , and the parallel parasitic capacitance is determined by (6.35). It is important to note that the  $L_{mag}$  is the magnetizing inductance for the inspected coil and is sensitive to the number of turns. This magnetizing inductance can be found from the admittance at low frequencies because the dominant impedance will be the low frequency resistance and the magnetizing inductance. It is only at higher frequencies that the core losses appear in the measurements if at all because the excitation amplitude of the impedance analyzer is small. A summary of the important values is shown below in Table 6.11.

$$(6.35) \quad C_{par} = \frac{1}{(2\pi f_0)^2 L_{mag}}$$

*Table 6.11: Predicted and Measured Values of 10 kW Concentric Transformer.*

Value	Predicted (H, F, $\Omega$ )	Measurement (H, F, $\Omega$ )	Error
Primary Magnetizing	3.62E-2	3.57E-2	1.42 %
Secondary Magnetizing	1.53E-2	1.30E-2	17.67 %
Tertiary Magnetizing	1.53E-2	1.30E-2	17.67 %
Primary to Secondary Leakage	9.37E-06	1.06E-5	-11.42 %
Primary to Tertiary Leakage	1.87E-05	1.98E-5	-5.17 %
Secondary to Tertiary Leakage	3.96E-06	4.26E-6	-7.08 %
Primary Capacitance	3.30E-11	3.83E-11	-13.75 %
Secondary Capacitance	4.29E-11	4.35E-11	-1.34 %
Tertiary Capacitance	4.29E-11	4.36E-11	-1.56 %
Primary to Secondary Capacitance	1.06E-10	1.12E-10	-6.01 %
Primary to Tertiary Capacitance	7.31E-11	9.63E-11	-24.08 %
Secondary to Tertiary Capacitance	7.75E-11	1.10E-10	-29.54 %
Primary Series Resistance	1.27E-02	7.34E-2	-82.75 %
Secondary Series Resistance	8.76E-03	5.75E-3	52.33 %
Tertiary Series Resistance	9.29E-03	7.79E-3	19.24 %
Primary Auxiliary Leakage	1.52E-04	1.48E-04	2.35%
Secondary Auxiliary Leakage	1.52E-04	1.51E-04	0.33%
Tertiary Auxiliary Leakage	1.52E-04	1.40E-04	8.06%

It is clear that many of the measured values are very close to the predicted parameters. However, a few predictions are off somewhat and others are off by quite a bit. The errors are important to recognize for future design improvements. Optimization should be cautious or include tuning factors where there is uncertainty in the in the model, as with the series resistances. Part of the wide range of resistances is the inclusion of various effects. At low excitation levels, proximity effects will not be as significant and can lead to inflated estimates. Furthermore, and this applies to the capacitance models as well, manufacturing tolerances can have a significant impact on the predictive models. For example, if windings are a mix of orthocyclic and orthogonal, an orthogonal model assumption will underestimate capacitances. Therefore, it is important that a modelled design be assembled and the electrical model verified. Rigorous manufacturing controls can minimize the variation in predictive model and measured results but laboratory prototypes may still have a wide error.

The measured parasitic capacitances for this design are low and well within the 0.05 PU maximum required by specification. With this and the minimal leakage flux winding design this transformer is a viable candidate for the three active bridge converter. However, for power flow management and control limitations, a minimum leakage inductance is required for each

transformer leg. An auxiliary series inductor is used to boost the overall series inductance. A hardware example inductor for the preceding concentric transformer is shown below in Figure 6.57. While three inductors are recommended to aid in filtering common noise, only two are necessary as each node path will have a series inductance. This magnetic design results in the effective equivalent circuit shown in Figure 6.58.



Figure 6.57: Auxiliary Inductor for 10 kW Concentric Transformer.

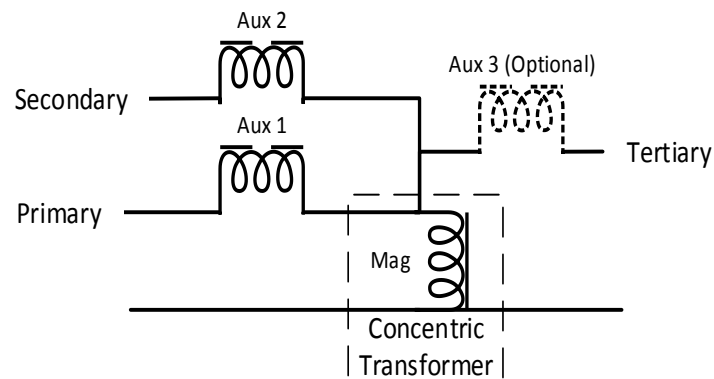


Figure 6.58: Effective Electric Circuit of Concentric Transformer with Auxiliary Inductors.

One interesting aspect of this design is the similarities with axial based designs. This is especially so when only two auxiliary inductors are used. Both designs have a series inductance asymmetry among the various paths. One advantage of the concentric design is that the two series inductors, *Aux 1* and *Aux 2* could be designed to be the same impedance. As will be discussed in the next section, the axial design is even more asymmetric and ultimately path dependent.

Using the testing method presented in the previous section, the concentric winding transformer with auxiliary inductors. Figure 6.59 and Figure 6.60 show the symmetry of the complete magnetic component through the similar effective relative permeabilities of the different paths. Furthermore, the winding that is an open circuit during testing is strongly coupled to the other two excited windings as shown in Figure 6.60. This means that the three port active bridge will have to control all three voltages and phase shifts to ensure that power flow is controlled.

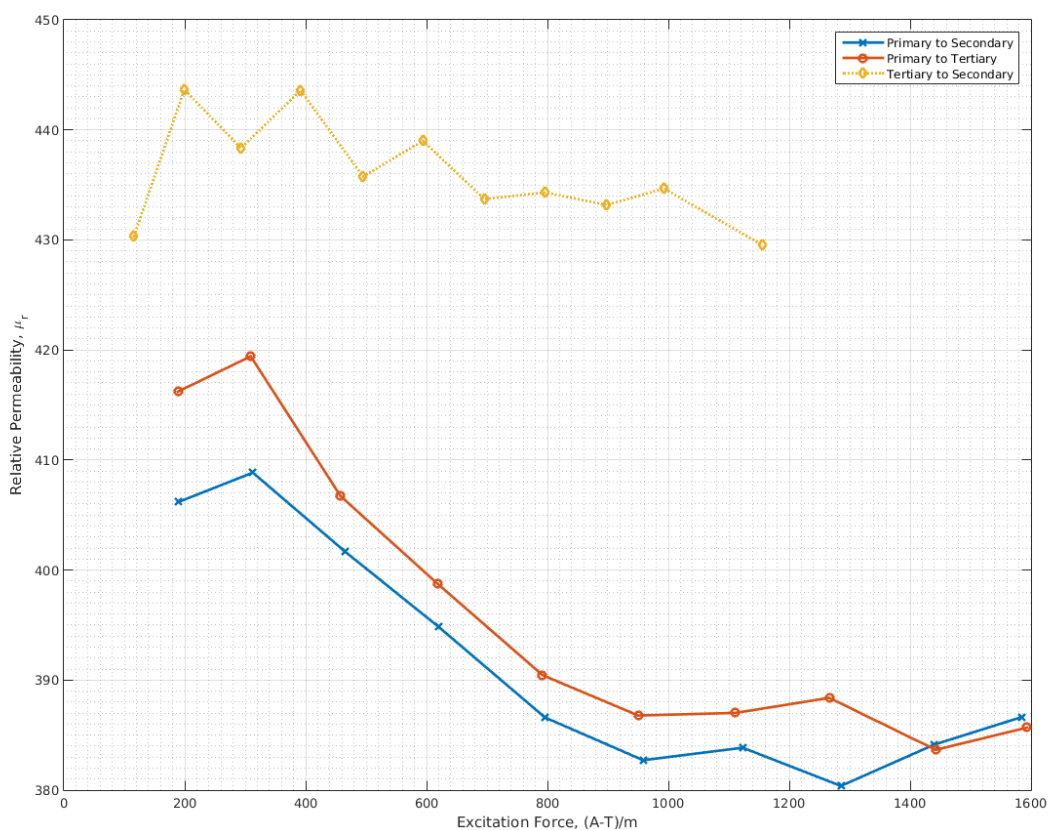


Figure 6.59: Effective Permeability of Concentric Transformer with Auxiliary Leakage Inductors.

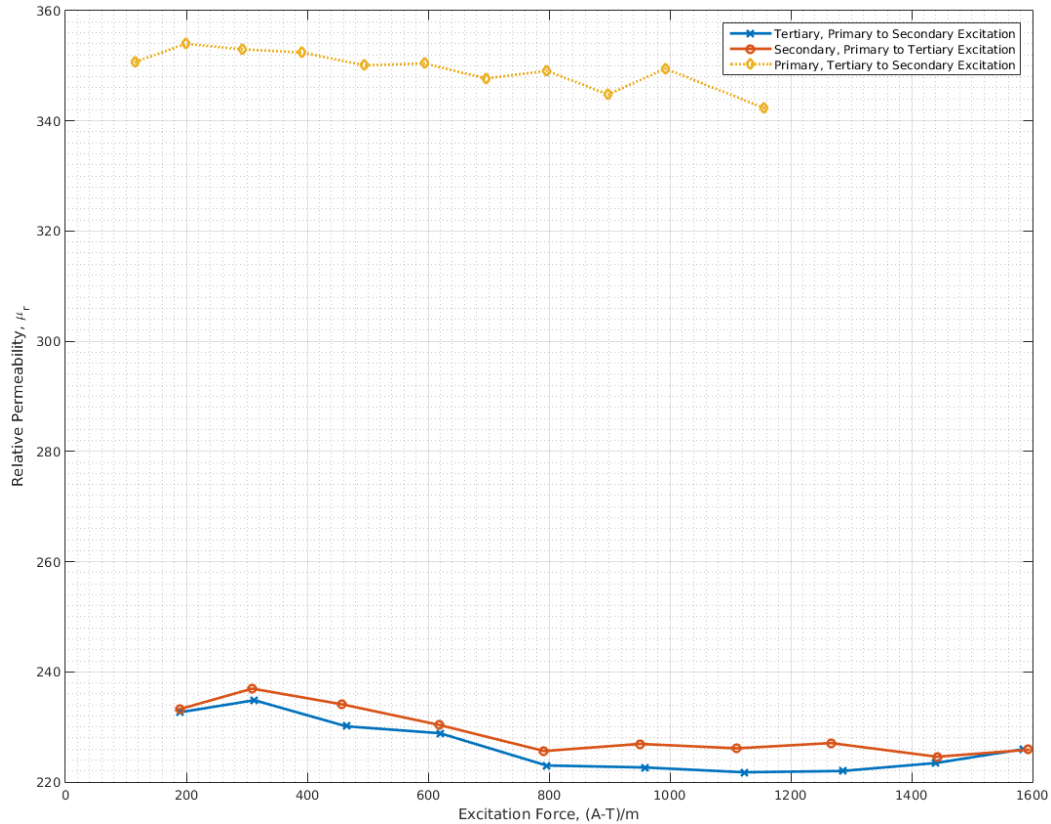


Figure 6.60: Effective Permeability of Open Circuit Winding in Triaxial Transformer with Strain Annealed Cores.

The concentric winding transformer with auxiliary inductors was subjected to as full of a load sweep as the current dual voltage test circuit and available DC power supplies could provide. In this case, the peak voltage was limited to 950V and therefore this specific efficiency map shows slightly lower efficiencies than desired. In the practical implementation, the voltage across the leakage path would be 1.8 kV. Therefore, the power rating on the X axis is a power that subjected the magnetic device to a lower voltage and a higher than desired current rather than rated voltage and current. Future testing will study the device efficiency in a three port active bridge system where desired voltage levels and rated current can be applied to the device. However, with these initial results, the component shows promising efficiencies. It also confirms the functionality of the component and its viability for use in the SuNLAMP system.

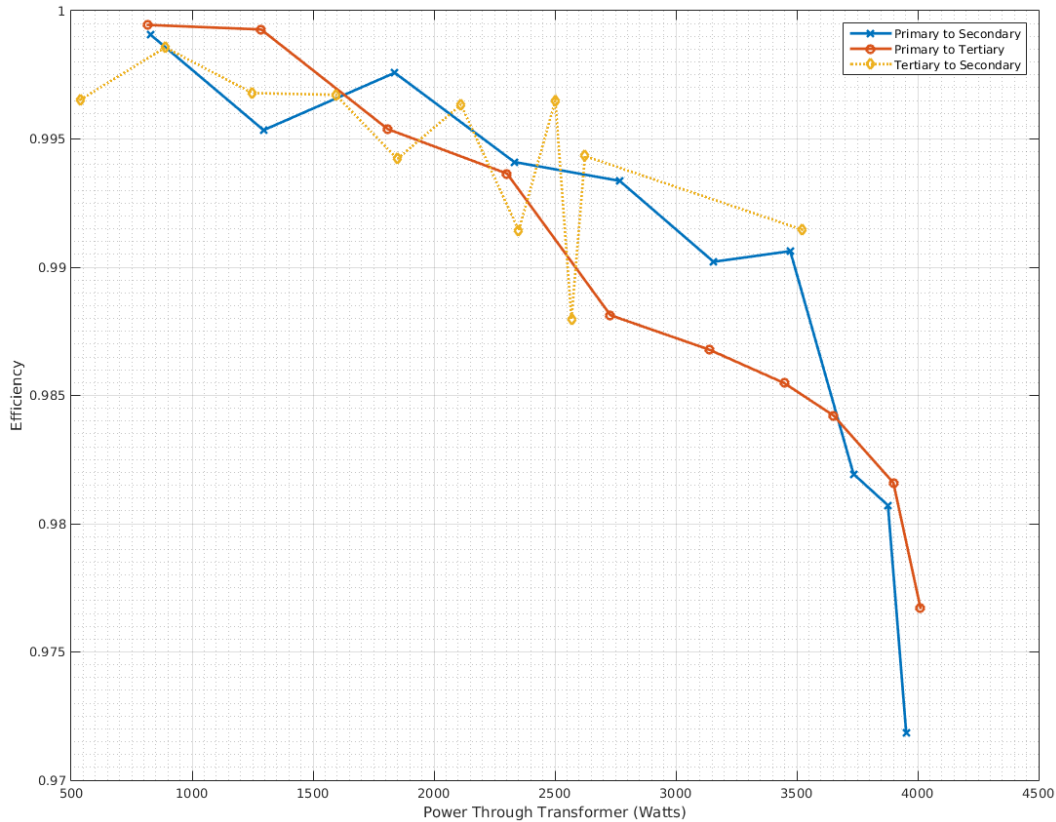


Figure 6.61: Efficiency Map of Concentric Transformer With Auxiliary Inductors Design.

### 6.3.3 Axial Design

Axial designs align a toroidal core axis with the centerline axis of flux. A two winding design is called a coaxial design, [179], [180], and a three winding design was proposed in [181] to supply two different output voltages. An advantage of the axial design is the explicit and easily predicable control of the leakage inductance [182], [183]. The design can include multiple windings and still operate effectively, demonstrating that a semi aligned flux axis and core axis is still effective, [184], [185]. Furthermore, the leakage inductance can be boosted by adding magnetic cores between layers of excitation coils, [186], [4]. However, this design used powdered core materials for the boost core. A novel design employing the latest in manufacturing techniques of advanced MANC materials is presented below. This design follows the traditional approaches of designing axial magnetics but employs strain annealed cores for the

leakage inductance boost. This provides another design tool to control the leakage core flux density as well as gain important inductance tenability independent of the volume. For a high power density design, this is a critical improvement in the design process.

The three port axial or triaxial design consists of three cores and three windings. Each winding and core axis of flux rotation is aligned. The center body is the primary conductor and then leakage cores and windings alternate until the outermost core, the magnetizing core, encompass the entire assembly, Figure 6.62. While only three ports were needed for this project any number of layers could be assembled together. This is a significant advantage for magnetic ribbon wound cores as there are minimal dimensional limitations. Rather than needing a larger press and extreme pressures as is the case for ferrites or powder cores, ribbons need only a larger winding mandrel.

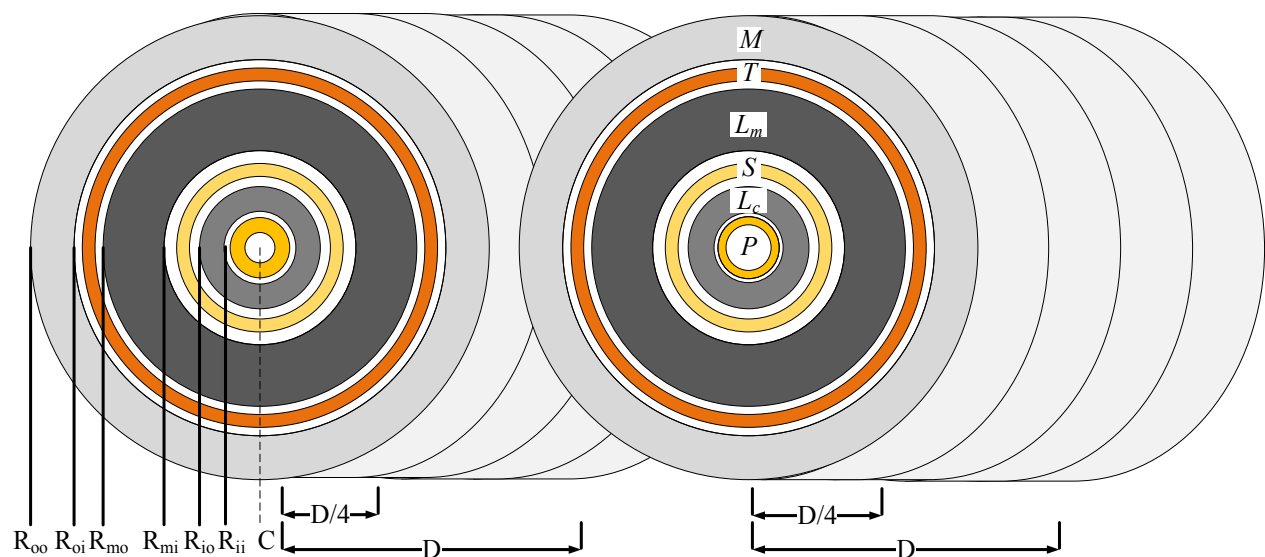


Figure 6.62: Three Port Axial (Triaxial) Transformer.

Many of the design guidelines that are appropriate for the concentric prototype are also appropriate for the axial design e.g. (6.36) and (6.37). However, now the leakage cores shall be uncut toroids. In order for these toroids to remain uncut special care must be applied to design of the core dimensions. One additional design variable is relative permeability of the leakage core,



The parasitic capacitance of the axial transformer requires careful consideration. The winding configuration leads to several concentric cylinders which have a simple capacitance model of (6.41). However, one must consider the layered effect if multiple layers of winding are present. Similarly, the corners of the wire, outside of the core, contribute to the effective length of the capacitive cylinder by mean length,  $l_o$ .

$$(6.41) \quad C = 2 \frac{2\pi\epsilon_r\epsilon_0(D+l_o)}{\ln\left(\frac{r_o}{r_i}\right)}$$

As presented, there are many different design tuning options in the triaxial design. However, not all tuning methods are as effective at altering performance metrics. One example of the tuning sensitivity of the axial based designs is shown below. The inductance, magnetizing or leakage, can be adjusted by adjusting both the inner radius or the thickness of the core. However, the sensitivity of either tuning is different. Specifically, the sensitivity to tuning the core thickness is shown in (6.42) and tuning the inner radius is shown in (6.43).

$$(6.42) \quad \frac{dL}{dt} \propto \frac{1}{r_i+t}$$

$$(6.43) \quad \frac{dL}{dr_i} \propto \frac{-t}{r_i^2+rt}$$

Given the local variance of these sensitivities, the contour plot below in Figure 6.64 shows how incremental changes in either thickness or inner radius will impact the inductance value. It is clear that when available, decreasing the inner radius increases inductance most effectively while decreasing the thickness reduces the inductance most effectively.

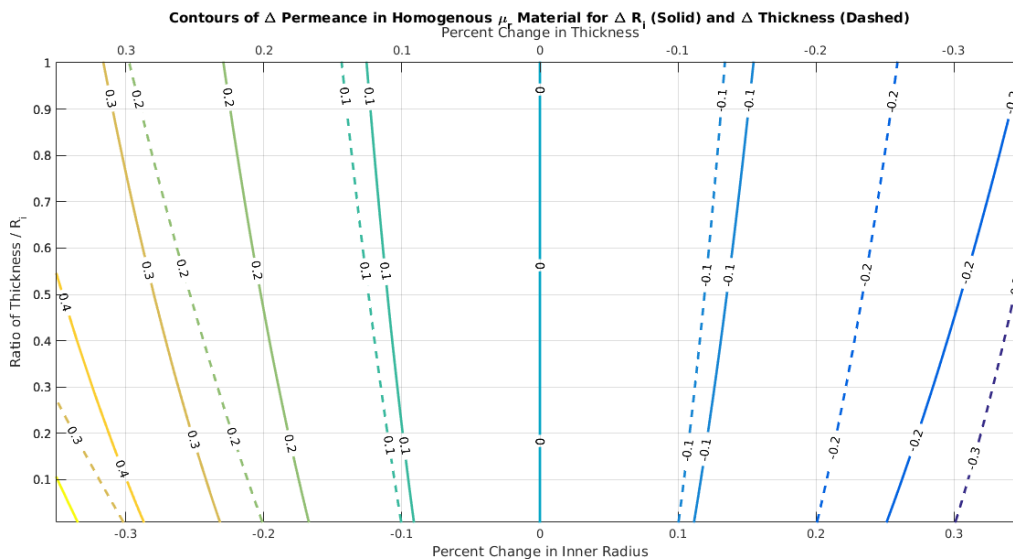


Figure 6.64: Inductance Sensitivity of Axial Designs.

The design parameters for the 10 kW SuNLaMP triaxial prototype are presented below in Table 6.12. Tolerances in the strain annealing process left some variability in leakage core relative permeability. However, the group of cores had an average permeability near the target, which is listed in the table below.

Table 6.12: 10 kW Triaxial Design Parameters

Parameter	Dimension	Value
Depth	D	100 mm
Magnetizing Radii	{ $R_{oi}$ , $R_{oo}$ }	{28.8, 33.9} mm
Magnetizing Permeability	$\mu_m$	>10,000
Middle Leakage Radii	{ $R_{mi}$ , $R_{mo}$ }	{16.6, 24.3} mm
Middle Permeability	$\mu_m$	~40
Center Leakage Radii	{ $R_{ci}$ , $R_{co}$ }	{9.8, 12.1} mm
Center Permeability	$\mu_c$	~30
Turns {Primary, Secondary, Tertiary}	{ $N_p$ , $N_s$ , $N_t$ }	{24, 14, 16}

A prototype construction is photographed below in Figure 6.65. A Keysight LCR meter was used to record the parasitic capacitances for the axial transformer as well. Again, the capacitances between windings were measured by shorting the two nodes of the coil together. The self-capacitances were determined by subjecting the winding to an admittance sweep with the other windings opened. This plot is shown below in Figure 6.66.



Figure 6.65: Prototype 10 kW Three Port Triaxial Transformer.

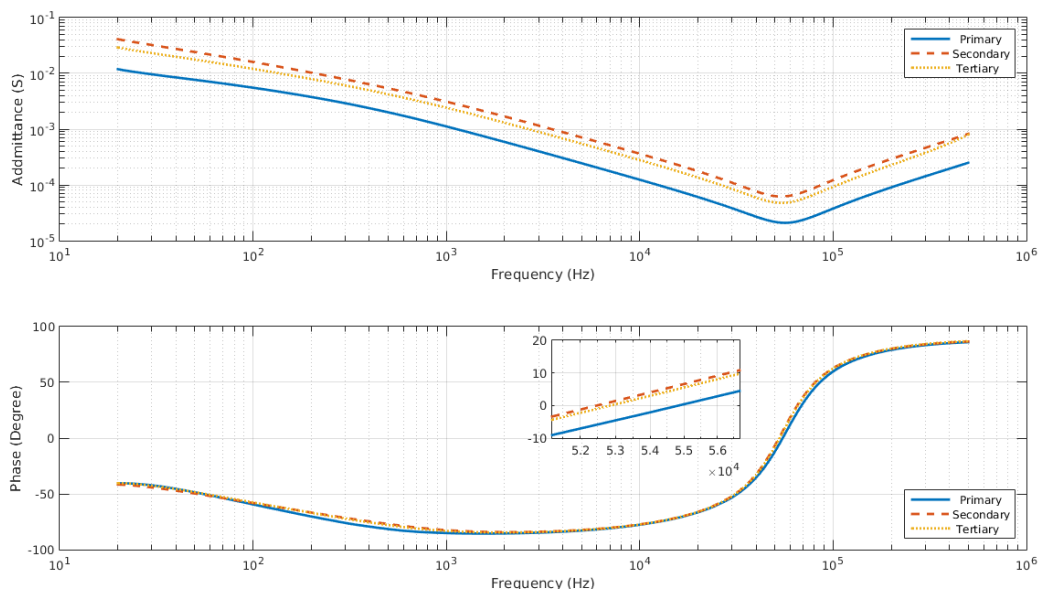


Figure 6.66: Concentric Winding Open Circuit Admittance Bode Plot.

The key model values and parasitic element values of the triaxial transformer are shown below in Table 6.13. The inductance values for both the magnetizing and leakage inductance are well predicted using the presented models. In all of the winding to winding capacitances, the concentric cylinder model is used with the radii of the of cores as a reference for the distance between the two plates. However, it is important to note that the length of the winding within the cores does not contribute to the overall capacitance. This is because the conductive core acts as

an isopotential that blocks the field from reaching other windings. The length within the cores contributes to the winding self-capacitance but not the winding to winding capacitance. This implies the ability to dramatically reduce the parasitic capacitance by increasing the length of winding outside the core to bundle and separating the coils away from each other. It is interesting to point out that capacitance between the primary coil, the center winding, and the tertiary coil, the outer most winding, is roughly half of the other series parasitic capacitances. This is due to the large physical space between these windings. This feature can be leveraged as a critical path for the highest required  $dv/dt$ . With the lower capacitance, this will result in less common mode noise than other configurations. Another key point is that this approach tends to overestimate the winding self-capacitance when a coil bundle is not fully packed in the perimeter. That is, when the outer perimeter of the coil is not filled by windings that are tangentially touching, the winding self-capacitance is lower. This is shown in the case of the primary and tertiary windings. The secondary winding, which is tightly packed, is well represented by the concentric cylinder model and the length of the core region. The prediction of loosely packed winding capacitances can be improved by estimating the proportion of surface that is not covered by windings. The primary winding has wire guide bobbins that orient the winding and leave nearly 50% of the surface uncovered. Similarly, the tertiary winding has significant bunching and only covers about 40% of the area. These reductions can bring the estimated capacitance within  $\pm 5\%$ . The series resistance is again error prone and this is partially due to the measurement method, lacking a micro-ohm meter, and imprecise values for the exact litz wire used as it was recycled from within the laboratory.

Table 6.13: Predicted and Measured Values of 10 kW Triaxial Transformer.

Value	Predicted (H, F, $\Omega$ )	Measurement (H, F, $\Omega$ )	% Error
Primary Magnetizing	1.34E-01	1.37E-01	-1.88%
Secondary Magnetizing	4.57E-02	4.70E-02	-2.68%
Tertiary Magnetizing	5.97E-02	6.12E-02	-2.38%
Primary to Secondary Leakage	1.50E-04	1.53E-04	-1.64%
Primary to Tertiary Leakage	4.88E-04	4.80E-04	1.63%
Secondary to Tertiary Leakage	1.15E-04	1.21E-04	-4.93%
Primary Capacitance	1.21E-10	6.36E-11	90.02%
Secondary Capacitance	2.10E-10	2.07E-10	1.24%
Tertiary Capacitance	3.68E-10	1.43E-10	157.99%
Primary to Secondary Capacitance	1.31E-10	1.28E-10	1.96%
Primary to Tertiary Capacitance	6.44E-11	7.08E-11	-9.04%
Secondary to Tertiary Capacitance	1.53E-10	1.40E-10	9.69%
Primary Series Resistance	1.42E-01	1.54E-01	-7.60%
Secondary Series Resistance	1.46E-02	1.01E-01	-85.53%
Tertiary Series Resistance	2.09E-02	2.90E-02	-28.10%

Figure 6.67 and Figure 6.68 below show loading examples of the three port axial transformer. Figure 6.67 demonstrates the basic power flow from the primary coil, center, to the secondary and tertiary, middle and outer, with resistive loads. The primary excitation voltage is recorded on Ch. 1 while the two load currents are on Ch. 2 and Ch. 4. This demonstrates the triaxial transformers ability supply power from one node to another two nodes unequally. This is similarly demonstrated in Figure 6.68. However, now the middle winding is excited and the primary, center, and tertiary, outer windings are short circuited. The secondary excitation voltage is measured on Ch. 1 and the primary current and tertiary current on Ch. 3 and Ch 4. Respectively. This demonstrates the possibility for bidirectional power flow between any of the three ports of the triaxial transformer.

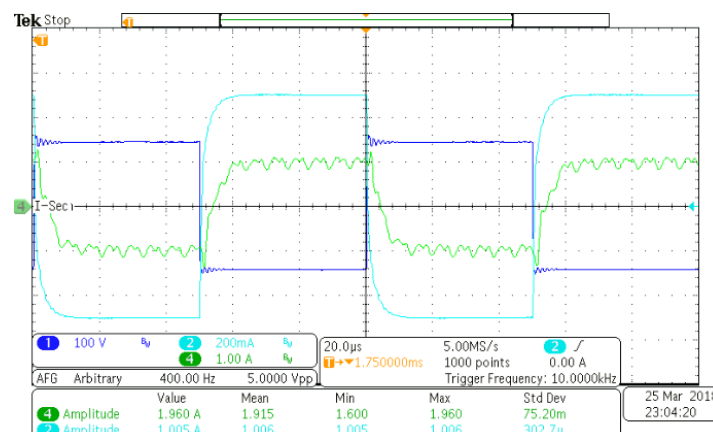


Figure 6.67: Triaxial Resistive Load Test: Primary to Secondary and Tertiary.

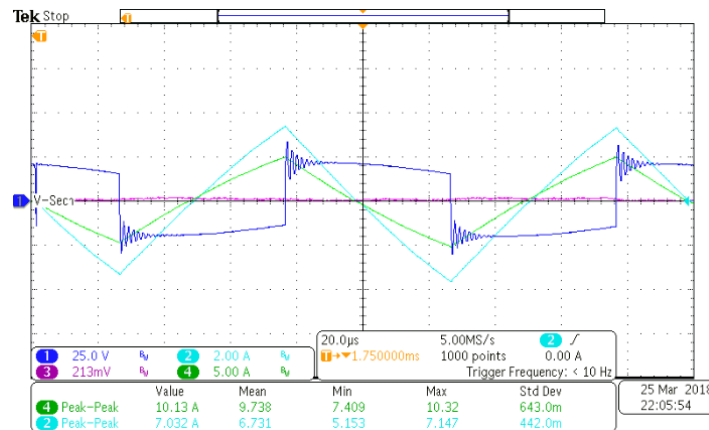


Figure 6.68: Triaxial Short Circuit Test: Secondary to Primary and Tertiary.

The triaxial transformer was also subjected to an active bridge emulation test. This characterization method leads to interesting insights into the behavior of the triaxial transformer. First, the performance of the strain annealed leakage flux cores is shown in Figure 6.69. This shows that cores excited from the primary winding outwards, generally exhibit expected behavior. However, excitation from the outer winding towards the center show a reduced effective permeability. This asymmetry can be leveraged in active bridge controls for intelligent power flow control that utilized the different effective series impedances of the various paths. Furthermore, when power is flowing between two windings, the third winding is generally unexcited, Figure 6.70. As the effective permeability of these paths is very low or even near one, neither the leakage core the magnetizing core is excited. Utilizing this concept could enable intelligent converter control that completely turns a converter off for specific power flow instances. This would could provide significant power savings as that converter would no longer contribute switching losses to the system total losses.

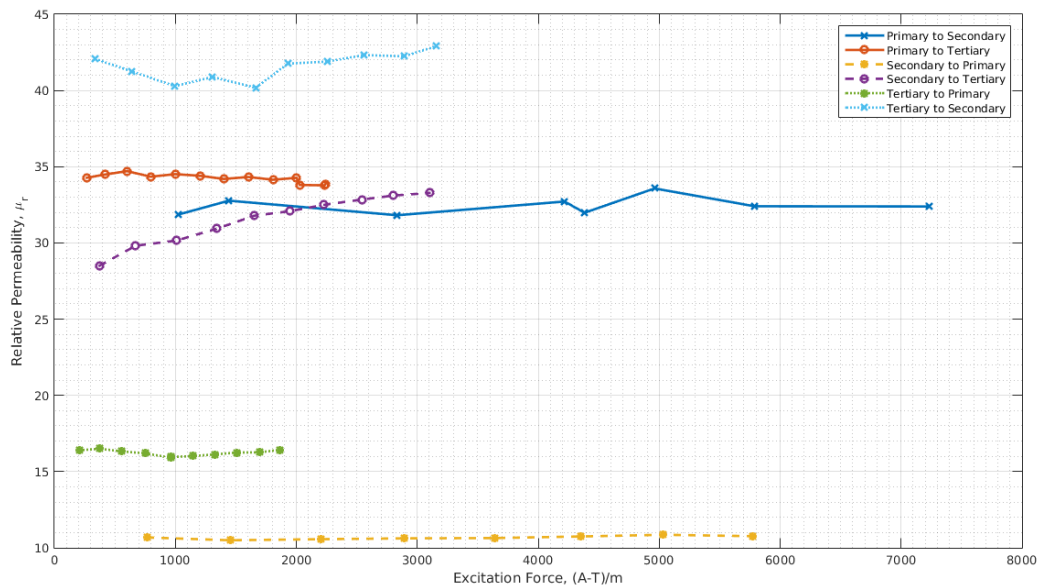


Figure 6.69: Effective Relative Permeability of Power Flow Paths in Triaxial Transformer with Strain Annealed Cores.

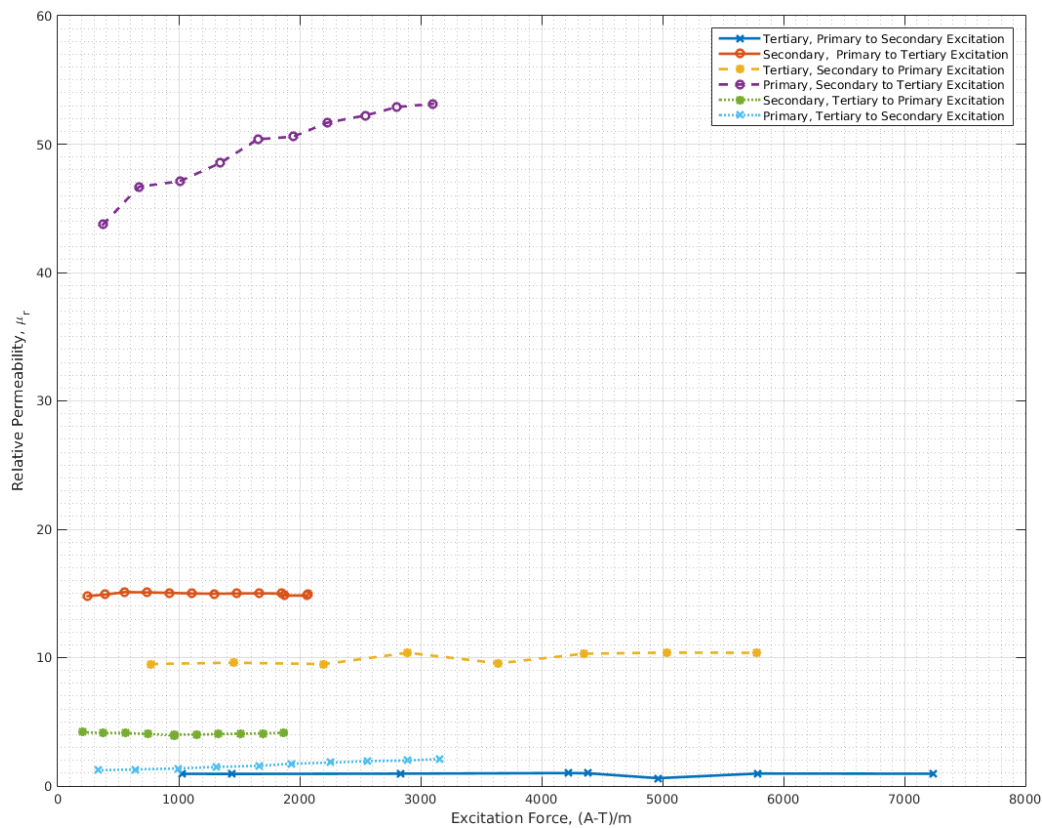


Figure 6.70: Effective Permeability of Open Circuit Winding in Triaxial Transformer with Strain Annealed Cores.

The efficiency map, developed by emulating an active bridge as discussed earlier, for the triaxial transformer is shown below in Figure 6.71. These initial results are for the specific excitation that the dual voltage source converter can provide. In this case, the excitation voltage was not as high as that which would be seen the three port SuNLAMP test bed due to device limitations. As a newer version of the dual voltage source converter is assembled utilizing more advanced switching devices, these tests can apply the desired higher voltages. In this excitation, the current was higher than the application requirements. This led to high ohmic losses and ultimately lower efficiencies. As such, the triaxial transformer is expected to have better performance in the test system. However, this is an effective demonstration of the application of the dual voltage source converter emulating an active bridge power flow. It is also a proof of concept that the triaxial transformer can effectively operate as a three port transformer.

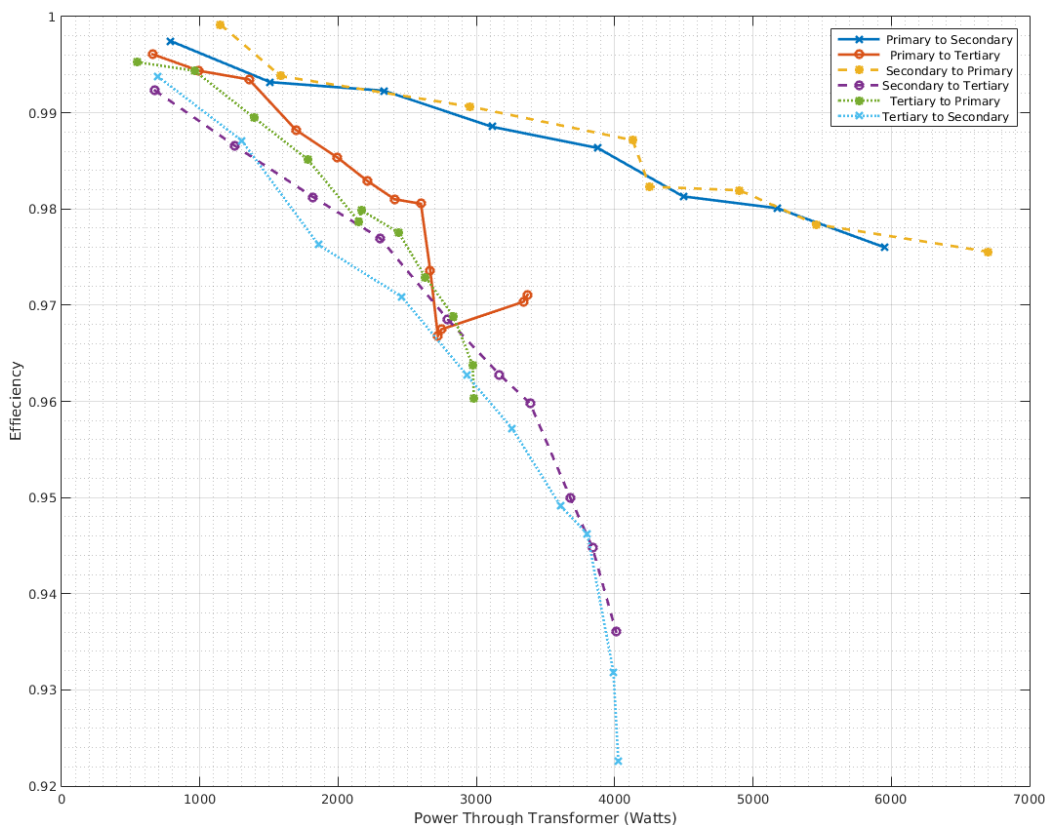


Figure 6.71: Efficiency Map of Triaxial Transformer with Strain Annealed Leakage Cores.

With the distinct difference in power flow path efficiencies of Figure 6.71, it is important to analyze the specific mass dependent losses of the leakage cores to ensure that there is not a fundamental problem in the leakage core material. Figure 6.72 shows that the leakage loss cores generally perform the same. The primary difference is when power flow is inwards and through the secondary winding. It is clear that this geometry introduces significant additional losses. It deserves further study but an initial explanation is that the flux through this secondary winding is causing locally induced eddy currents in the winding and thus resulting in higher losses.

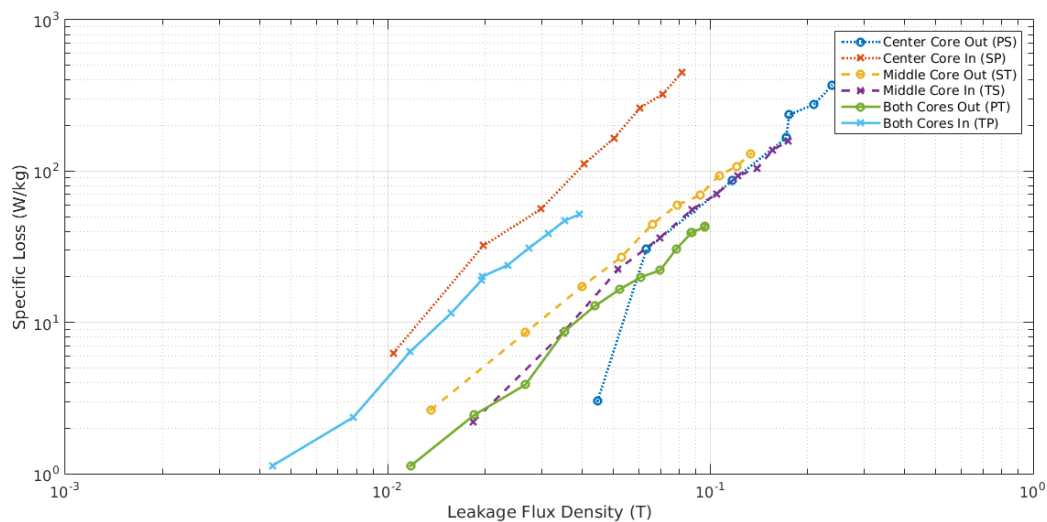


Figure 6.72: Normalized Specific Losses of Triaxial Transformer.

## 6.4 Conclusion and Future Work

Practical magnetics require understanding of system and control opportunities to reach better designs. Magnetics designs alone can provide local optima but may be far from a system optimal design. In the case of the series DC coupled transformer, this meant using the converter to supply a cancelation field to avoid saturating the core. Rather than the traditional, magnetics only solution of adding air gaps, active DC flux cancelation dramatically reduced core volume, winding count and improved compensation performance. This parallel thinking is also required in the active bridge magnetics design. Designs using only power converter principles can result

in magnetics with significant leakage flux induced losses. However, by applying advanced magnetic principles in the design process it is clear that the transformer leakage flux must be carefully minimized or carefully managed. Magnetics without or with minimal normal flux are possible. This requires no shielding. However, the designs either require more components such as auxiliary inductors or are complex geometries such as the axial transformer.

Strain annealing techniques again show significant advancement by providing low and tunable permeability without cut cores and gaps or other dimensional constraints. The wide range of permeability that is not limited to fixed values provides exceptional flexibility for further design control. This design control often requires multiple parameters to be tuned and it is useful to observe design sensitivities as tuning certain parameters is more effective for specific outcomes e.g. reducing the inner radius of the toroid for increased inductance rather than increasing the thickness.

Both transformer designs need to be fully characterized for efficiency and performance in the 10 kw experimental prototype of the SuNLaMP system. However, the initial design process properly accounts for the loss components and initial parasitic elements are shown to be minimal. The 99.5% efficiency targets are within reach.

There is significant future work to be done with the triaxial transformer. This thesis has produced a proof of concept of a novel triaxial transformer where power flow is bidirectional for all three ports. It has also leveraged novel, strain annealed cores for leakage inductance design. Further work can determine the tradeoffs and optimizations needed for volumetric, flux density, permeability, turns and many other design options for a more efficient or higher performance triaxial transformer.

## CHAPTER 7: CONCLUSION AND FUTURE WORK

This thesis has provided several advancements for high power medium frequency magnetics. It has introduced new material screening and characterization techniques. It has provided a novel testing circuit and testing superstructures for in depth studies of a variety of magnetic material behaviors and environmental responses. It has also identified and modelled a significant loss component of ribbon based materials. Similarly, it has highlighted the advantages of new processing techniques that make these same materials advantageous for loss reduction and thermal profile control. Finally, it provided application examples that highlight the combined design requirements and processes of general magnetics design with converter, control, and application oriented design. These advancements will have an impact in speeding the adoption of metal amorphous nanocomposite materials that will enable full utilization of the high power, high voltage wide bandgap devices.

Connections between the bulk behavior and the underlying physics are shown by starting with the fundamental material properties. This analysis gives engineers and practitioners the background necessary to make informed design decisions. It is also important to highlight where further work is needed and where our understanding and models fall short. This has given rise the need for detailed characterization of magnetic materials.

In order to understand the operational behavior of magnetic materials multiple parameters and testing conditions need to be qualified. This qualification and understanding is often more detailed than a typical manufacturer datasheet. However, this characterization will highlight edge cases and surprising behaviors that are not captured in the limited or single point analysis provided by suppliers. Unique circuits that can supply arbitrary excitation current and structural harnesses were presented to give engineers the tools necessary to map and characterize all of the

operational points their specific design needs. This enables engineers to better predict magnetics behaviors and ultimately determine better designs for converters. This further enhances the capabilities of wide bandgap devices by removing the bottleneck of poor magnetic design.

The leakage flux induced losses are another roadblock to better converter designs that this thesis provides solutions for. The fundamental physics behind why this phenomenon occurs as well as design tools to better understand the flux paths were presented. As the leakage flux returns to the exciting coil, it encounters magnetic ribbon material. If it enters the face of the core where the thin edge is exposed, minimal losses occur. However, as it enters the broad surface, e.g. the inside and outside of a wound core, the leakage flux induces large eddy currents which result in losses many orders of magnitude greater than magnetizing losses. A mixed material core was shown to have significant reductions in these losses by redirecting the leakage flux into a high resistivity path. This also opened the possibility of designing the magnetizing inductance and the leakage inductance independently of each other and the winding layout by using a wing shield. This independent design concept was taken further by showing the possibility of an all MANC design without any core cuts by utilizing low permeability strain annealed cores for the leakage path. This solves a significant barrier to the adoption and use of MANC and other ribbon core materials for high power medium frequency magnetics.

The processing technique of strain annealing is not limited to tuning for leakage inductances. This thesis also demonstrated that it can be used for loss and thermal management. The analytical expressions for local losses of various toroids show reductions in losses. These toroids had different strain induced relative permeability profiles. This approach also showed that, with the proposed anisotropic thermal model, the strain annealing profile can be used to

manage the radial temperature profile of a core. This concept was verified in laboratory prototypes where a significant reduction in peak core temperature was achieved.

Finally, practical application examples were demonstrated. These examples highlight the combined nature of magnetics design. As with the air gap based series DC transformer, designs that are developed in conjunction the power converter and control capabilities can have significant improvements in performance and capabilities such as the active DC injection SDCT. Alternatively, by understanding the leakage flux induced losses and the leakage inductance requirement of the dual active bridge, different transformer designs become appealing. The concentric wound transformer with auxiliary inductors is similar to very high power low frequency designs for transmission. More advanced designs that utilize strain annealing technologies can employ the axial based design. Both designs have similar magnetic design processes and both manage the leakage flux in the transformer to avoid inducing excess eddy currents. These application examples tie together the theoretical concepts into real world scenarios where practical constrains require informed designs were tradeoffs must be deliberate and understood.

This thesis paves the way for high power medium frequency magnetics. It has provided several fundamental concepts and testing processes to further our understanding. It provides many advancements that will enable faster adoption and better scalability of magnetic components for the high power wide bandgap devices that are growing in maturity. Many of the concepts discussed here are or are perceived to be roadblocks to full integration and utilization of magnetic materials for these devices and converters. With the solutions provided, these barriers have been lifted. Better materials and better material screen will require the advanced characterization techniques. These techniques will also enable targeted studies of magnetizing

physics and hopefully develop bulk material loss models that are less curve fitting and more physically accurate. Future work will continue to refine the models for leakage flux losses to provide a more nuanced understanding that better captures the underlying physics. The second and higher order effects can be incorporated in more advanced FEA models that allow more accurate prediction of this loss mechanism. This will enable better designs of magnetic shields that reduce the leakage flux induced losses even further. As the manufacturing process matures, strain anneal magnetic ribbon cores will become a critical tool for high power medium frequency magnetics design. Advanced designs will be able to find optimal tradeoffs between core geometry, inductance, and thermal and loss profiles. Finally, all of these concepts must mature and be proven in practical applications. High power medium frequency converters are coming and it will take the concepts presented in this thesis and more to enable the magnetic designs to excel.

High power medium frequency magnetics are a critical component to the coming power electronics based energy revolution. This thesis provides many of the tools that will be required to ensure that the magnetic materials are fully characterized and optimally designed. It represents a significant impact by providing solutions for immediate adoption while also setting the stage for further research.

## REFERENCES

- [1] M. Östling, R. Ghandi and C. M. Zetterling, "SiC Power Devices - Present Status, Applications and future Perspective," in *IEEE 23rd International Symposium on Power Semiconductor Devices and ICs*, San Diego, 2011.
- [2] E. Agheb, "Medium Frequency High Power Transformers for All-DC Wind Parks," PhD Dissertation, Norwegian University of Science and Technology, Trondheim, 2017.
- [3] A. Tripathi, "HV SiC Devices based Three-Phase Dual Active Bridge DC/DC Converter as a MV Isolator and Potential Component for MV dc grid," PhD Dissertation, North Carolina State University, Raleigh, 2016.
- [4] S. Baek, "High-Frequency AC-link Transformers for Medium-Voltage DC/DC Converters and Solid State Transformer Applications," PhD Dissertation, North Carolina State University, Raleigh, 2014.
- [5] C. Leung, "Design Considerations of High Voltage and High Frequency 3 Phase Transformer for Solid State Transformer Application," MS Dissertation, North Carolina State University, Raleigh, 2010.
- [6] S. Madhusoodhanan, "Design, Development and Control of Three-Phase Medium Voltage High Power Converters Based on Silicon Carbide Devices," PhD Dissertation, North Carolina State University, Raleigh, 2016.
- [7] A. De, "Soft Switched AC/AC Converters Enabled by Wide Band Gap SiC Power Devices," PhD Dissertation, North Carolina State University, Raleigh, 2015.
- [8] S. Dutta, "Controls and Applications of the Dual Active Bridge DC to DC Converter for Solid State Transformer Applications and Integration of Multiple Renewable Energy Sources," PhD Dissertation, North Carolina State University, Raleigh, 2014.
- [9] D. Boillot, "Design of an Isolation Gate Driver Transformer for a 12 kV/1.2 kV DC-DC Converter," MS Dissertation, North Carolina State University, Raleigh, 2010.
- [10] T. Miyazaki and H. Jin, *The Physics of Ferromagnetism*, 1 ed., Berlin, Germany: Springer-Verlag, 2012, pp. 330-331.
- [11] E. Barbisio, F. Fiorillo and C. Ragusa, "Predicting loss in magnetic steels under arbitrary induction waveform and with minor hysteresis loops," *IEEE Transactions on Magnetics*, vol. 40, no. 4, pp. 1810-1819, July 2004.
- [12] G. Bertotti, "Physical interpretation of eddy current losses in ferromagnetic materials. I. Theoretical considerations," *Journal of Applied Physics*, vol. 57, pp. 2110-2117, March 1985.
- [13] N. Soltau, D. Eggers, K. Hameyer and R. W. De Doncker, "Iron Losses in a Medium-Frequency Transformer Operated in a High-Power DC-DC Converter," *IEEE Transactions on Magnetics*, vol. 50, no. 2, pp. 953-956, February 2014.
- [14] J. Muhlethaler, J. Biela, J. W. Kolar and A. Ecklebe, "Improved Core-Loss Calculation for Magnetic Components Employed in Power Electronic Systems," *IEEE Transactions on Power Electronics*, vol. 27, no. 2, pp. 964-973, Feb. 2012.
- [15] A. Boglietti, A. Cavagnino, M. Lazzari and M. Pastorelli, "Predicting iron losses in soft magnetic materials with arbitrary voltage supply: an engineering approach," *IEEE Transactions on Magnetics*, vol. 39, no. 2, pp. 981-989, March 2003.

- [16] P. Allia, P. Mazzetti, G. P. Soardo and F. Vinai, "Structural instabilities and magnetic relaxation in amorphous ferromagnets," *Journal of Magnetism and Magnetic Materials*, vol. 15, pp. 1361-1363, 1980.
- [17] P. Allia, P. Mazzetti and F. Vinai, "Magnetic after-effects and structural instabilities in amorphous soft magnetic materials," *Journal of Magnetism and Magnetic Materials*, vol. 15, pp. 281-283, 1980.
- [18] J. Snoek, "Time effects in Magnetization," *Physica*, vol. 5, no. 8, pp. 663-668, 1938.
- [19] R. Street and J. C. Woolley, "A Study of Magnetic Viscosity," *Proceedings of the Physical Society. Section A*, vol. 62, no. 9, pp. 562-572, 1949.
- [20] P. Allia and F. Vinai, "Viscosity field and magnetic aftereffects in amorphous (Fe-Ni-P-B) alloys," *IEEE Transactions on Magnetics*, vol. 17, no. 4, pp. 1481-1486, July 1981.
- [21] S. E. Zirka, Y. I. Moroz, P. Marketos and A. J. Moses, "Viscosity-based magnetodynamic model of soft magnetic materials," *IEEE Transactions on Magnetics*, vol. 42, no. 9, pp. 2121-2132, September 2006.
- [22] S. E. Zirka, Y. I. Moroz, P. Marketos, A. J. Moses and D. C. Jiles, "Viscous Behavior of Ferromagnets in the Volgate and Current Driven Regimes," *IEEE Transactions on Magnetics*, vol. 44, no. 11, pp. 3189-3192, November 2008.
- [23] G. Bertotti, F. Fiorillo and P. Mazetti, "Basic principles of magnetization processes and origin of losses in soft magnetic materials," *J. Magn. Mang. Mater.*, vol. 112, pp. 146-149, 1992.
- [24] G. Bertotti, "General Properties of Power Losses in Soft Ferromagnetic Materials," *IEEE Transactions on Magnetics*, vol. 24, no. 1, pp. 621-630, 1988.
- [25] C. D. Graham Jr., "Physical origin of losses in conducting ferromagnetic materials," *J. Appl. Phys.*, vol. 53, pp. 8276-8280, November 1982.
- [26] B. Alessandro, C. Beatrice, G. Bertotti and A. Montorsi, "Domain-wall dynamics and Barkhausen effect in metallic ferromagnetic materials. I. Theory," *J. Appl. Phys.*, vol. 53, pp. 2901-2907, September 1990.
- [27] R. O'Handley, "Magnetization Process," in *Modern Magnetic Materials: Principles and Applications*, 1st ed., New York, Wiley, 2000, pp. 328-338.
- [28] D. Nitzan, "Computation of flux switching in magnetic circuits," *IEEE Transactions on Magnetics*, vol. 1, no. 3, pp. 222-234, September 1965.
- [29] S. Chikazumi and C. D. Graham, "Technical Magnetization," in *International Series of Monographs on Physics: Physics of Ferromagnetism*, Oxford, Great Britain OUP Oxford, 2009.
- [30] S. Chikazumi and C. D. Graham, "Technical Magnetization," in *International Series of Monographs on Physics: Physics of Ferromagnetism*, Oxford, Great Britain OUP Oxford, 2009.
- [31] R. O'Handley, "Magnetization Process," in *Modern Magnetic Materials: Principles and Applications*, New York, Wiley, 2000, pp. 338-347.
- [32] C. P. Steinmetz, "On The Law Of Hysteresis," *Transactions of the American Institute of Electrical Engineers*, vol. 9, no. 1, pp. 1-64, 1892.
- [33] E. C. Snelling, *Soft Ferrites: Properties and Applications*, vol. 1, 2, Ed., London: Iliffe, 1969.

- [34] E. G. Fish, "Soft magnetic materials," *Proceedings of the IEEE*, vol. 78, no. 6, pp. 947-972, June 1990.
- [35] G. Herzer, "Nanocrystalline Soft Magnetic Alloys," in *Handbook of Magnetic Materials*, vol. 10, K. H. J. Buschow, Ed., Amsterdam, Elsevier Science, 1997, p. 415.
- [36] M. E. McHenry and D. E. Laughlin, "Magnetic Properties of Metals and Alloys," in *Physical Metallurgy*, vol. 5, Oxford, Elsevier Academic Press, 2014, pp. 1881-2008.
- [37] S. J. Kernion, M. J. Lucas, J. Horwath, Z. Turgut, E. Michel, V. Keylin, J. Huth, A. M. Leary, S. Shen and M. E. McHenry, "Reduced Losses in Rolled Fe73.5 Si15.5 Nb3 B7 Cu1 Nanocrystalline Ribbon," *Journal of Applied Physics*, vol. 113, no. 17, p. 17A306, 2013.
- [38] J. Reinert, A. Brockmeyer, De Doncker and R.W.A.A., "Calculatoions of Losses in Ferro- and Ferrimagnetic Materials Based On The Modified Steinmetz Equation," *IEEE Transactions on Industry Applications*, vol. 37, no. 4, pp. 1055-1061, 2001.
- [39] D. C. Jiles and D. L. Atherton, "Theory Of Ferromagnetic Hysteresis," *Journal of Magnetism and Magnetic Materials*, vol. 61, pp. 48-60, 1986.
- [40] W. Li, I. H. Kim, S. M. Jang and C. S. Koh, "Hysteresis Modeling For Electrical Steel Sheets Using Improved Vector Jiles-Atherton Hysteresis Model," *IEEE Transactions on Magnetics*, vol. 47, no. 10, pp. 3821-3824, 2011.
- [41] A. Brockmeyer and L. Schulting, "Modeling Of Dynamic Losses In Magnetic Material," in *European Conference on Power Electronics and Applications*, Brighton, 1993.
- [42] S. E. Zirka, M. Y. I., P. Marketos and A. J. Moses, "Congruency-based hysteresis models for transient simulation," *IEEE Transactions on Magnetics*, vol. 40, no. 2, pp. 390-399, March 2004.
- [43] I. D. Mayergoyz, *Mathematical Models Of Hysteresis and Their Applications*, vol. 1, Oxford: Elsevier Academic Press, 2003.
- [44] S. Y. R. Hui and J. Zhu, "Numerical Modeling and Simulation Of Hysteresis Effects in Magnetic Cores Using Transmission-Line Modeling and the Preisach Theory," *IEE Proceedings in Electric Power Applications*, vol. 142, no. 1, pp. 57-62, 1995.
- [45] F. Fiorillo and A. Novikov, "An improved approach to power losses in magnetic laminations under nonsinusoidal induction waveform," *IEEE Transactions on Magnetics*, vol. 26, no. 5, pp. 2904-2910, Sep 1990.
- [46] P. Marketos, J. P. Hall and S. E. Zirka, "Power Loss Measurement and Prediction of Soft Magnetic Powder Composites Magnetized Under Sinusoidal and Nonsinusoidal Excitation," *IEEE Transactions on Magnetics*, vol. 44, no. 11, pp. 3847-3850, November 2008.
- [47] D. Aguglia and M. Neuhaus, "Laminated magnetic materials losses analysis under non-sinusoidal flux waveforms in power electronics systems," in *15th European Convergence on Power Electronics and Applications (EPE)*, Lille, 2013.
- [48] M. Mu and F. C. Lee, "A new core loss model for rectangular AC voltages," in *2014 IEEE Energy Conversion Congress and Exposition (ECCE)*, Pittsburgh, PA, 2014.
- [49] J. Li, T. Abdallah and C. R. Sullivan, "Improved Calculation of Core Loss With Nonsinusoidal Waveforms," in *Conference Record of the 2001 IEEE Industrial Applications Society Annual Meeting*, Cincinnati, 2001.

- [50] J. Muhlethaler, J. Biela, J. W. Kolar and A. Ecklebe, "Core Losses Under the DC Bias Condition Based on Steinmetz Parameters," *IEEE Transactions on Power Electronics*, vol. 27, no. 2, pp. 953-963, 2012.
- [51] R. Ridley and A. Nace, "Modeling Ferrite Core Losses," *Switching Power Magazine*, pp. 1-6, 2006.
- [52] R. Severns, "HF-Core Losses For Nonsinusoidal Waveforms," in *Proceedings of the High Frequency Power Conversion Conference*, Ontario, 1991.
- [53] M. Albach, T. Durbaum and A. Brockmeyer, "Calculating Core Losses in Transformers For Arbitrary Magnetization Currents - A Comparison of Different Approaches," in *Proceedings of the IEEE Power electronics Specialists Conference*, Baveno, 1996.
- [54] T. Durbaum and M. Albach, "Core Losses In Transformers With An Arbitrary Shape of The Magnetization Current," in *European Conference on Power Electronics and Applications*, Seville, 1995.
- [55] M. Mu, "High frequency magnetic core loss study," Ph.D. Dissertation, Virginia Polytechnic Institute and State University, Blacksburg, 2013.
- [56] C. R. Sullivan, J. H. Harris and E. Herbert, "Core loss predictions for general PWM waveforms from a simplified set of measured data," in *Twenty-Fifth Annual IEEE Applied Power Electronics Conference and Exposition (APEC)*, Palm Springs, CA, 2010.
- [57] C. Gu, Z. Zheng and Y. Li, "A Power Electronic Transformer (PET) With Multiport Bidirectional Resonant DC-DC Converters for Electric Traction Applications," in *Transportation Electrification Conference and Expo (ITEC)*, Dearborn, 2015.
- [58] K. Venkatachalam, C. R. Sullivan, T. Abdallah and H. Tacca, "Accurate Prediction of Ferrite Core Loss With Nonsinusoidal Waveforms Using Only Steinmetz Parameters," in *IEEE Workshop on Computers in Power Electronics*, Mayaguez, 2002.
- [59] W. Shen, "Design of high-density transformers for high-frequency high-power converters," PhD Dissertation, Virginia Polytechnic Institute and State University, Blacksburg, 2006.
- [60] D. Lin, P. Zhou, W. N. Fu, Z. Badics and Z. J. Cendes, "A dynamic core loss model for soft ferromagnetic and power ferrite materials in transient finite element analysis," *IEEE Transactions on Magnetics*, vol. 40, no. 2, pp. 1318-1321, 2004.
- [61] R. W. De Doncker, M. D. Divan and H. M. Kheraluwala, "A three-phase soft-switched high power density DC/DC converter for high power applications," in *Industry Applications Society Annual Meeting*, Pittsburgh, 1988.
- [62] B. Zhao, Q. Song, W. Liu and Y. Sun, "Overview of Dual-Active-Bridge Isolated Bidirectional DC-DC Converter for High-Frequency-Link Power-Conversion System," *IEEE Transactions on Power Electronics*, vol. 29, no. 8, pp. 4091-4106, 2014.
- [63] Z. Shen, R. Burgos and F. Wang, "Soft-switching capability analysis of a dual active bridge dc-dc converter," in *IEEE Electric Ship Technologies Symposium*, Baltimore, 2009.
- [64] H. Bai and C. Mi, "Eliminate Reactive Power and Increase System Efficiency of Isolated Bidirectional Dual-Active-Bridge DC-DC Converters Using Novel Dual-Phase-Shift Control," *IEEE Transactions on Power Electronics*, vol. 23, no. 6, pp. 2905-2914, 2008.

- [65] G. G. Oggier, G. O. García and A. R. Olivia, "Switching Control Strategy to Minimize Dual Active Bridge Converter Losses," *IEEE Transactions on Power Electronics*, vol. 24, no. 7, pp. 1826-1838, 2009.
- [66] G. Ortiz, H. Uemura, D. Bortis, J. W. Kolar and O. Apeldoorn, "Modeling of Soft-Switching Losses of IGBTs in High-Power High-Efficiency Dual-Active-Bridge DC/DC Converters," *IEEE Transactions on Electron Devices*, vol. 60, no. 2, pp. 587-597, 2013.
- [67] G. Guidi, M. Pavlovsky, A. Kawamura, T. Imakubo and Y. Sasaki, "Improvement of Light Load Efficiency of Dual Active Bridge DC-DC Converter by Using Dual Leakage Transformer and Variable Frequency," in *IEEE Energy Conversion Congress and Exposition (ECCE)*, Atlanta, 2010.
- [68] A. Tripathi, K. Mainali and S. Bhattacharya, "A series compensation enabled ZVS range enhancement of a dual active bridge converter for wide range load conditions," in *IEEE Energy Conversion Congress and Exposition (ECCE)*, Pittsburgh, 2014.
- [69] X. Zhan, H. Wu, Y. Xing, H. Ge and X. Xiao, "A high step-up bidirectional isolated dual-active-bridge converter with three-level voltage-doubler rectifier for energy storage applications," in *IEEE Applied Power Electronics Conference and Exposition (APEC)*, Long Beach, 2016.
- [70] W.-S. Chen, C.-S. Lin and C.-L. Chen, "Analytical Comparison Between Ferrite Core and Steel Laminations Losses of Multi-Polar Brushless DC Motor," in *IECON 2007 - 33rd Annual Conference of the IEEE Industrial Electronics Society*, Taipei, 2007.
- [71] L. Huang, Z. Zhang and M. A. Andersen, "Analytical Switching Cycle Modeling of Bidirectional High-Voltage Flyback Converter for Capacitive Load Considering Core Loss Effect," *IEEE Transactions on Power Electronics*, vol. 31, no. 1, pp. 470-487, 2016.
- [72] H. Akagi, T. Yamagishi, N. M. Tan, S.-i. Kinouchi, Y. Miyazaki and M. Koyama, "Power-loss breakdown of a 750-V, 100-kW, 20-kHz bidirectional isolated DC-DC converter using SiC-MOSFET/SBD dual modules," in *International Power Electronics Conference (IPEC-Hiroshima 2014 - ECCE-ASIA)*, Hiroshima, 2014.
- [73] G. Slemon, "Energy Conversion Processes," in *Magnetolectric Devices: Transducers, Transformers, and Machines*, 1st ed., New York, Wiley, 1966, pp. 38-49.
- [74] R. Beddingfield, D. Storelli and S. Bhattacharya, "Active elimination of DC bias flux in series DC active filter coupling transformer," in *IEEE Applied Power Electronics Conference and Exposition*, Tampa, 2017.
- [75] M. Ashby and Michael, *Materials Selection in Mechanical Design*, 3 ed., Burlington: Butterworth-Heinemann, 1999.
- [76] M. McHenry, M. Willard and D. Laughlin, "Amorphous and nanocrystalline materials for applications as soft magnets," *Progress in Materials Science*, vol. 44, no. 4, pp. 291-433, 1999.
- [77] S. Kulasekaran, R. Ayyanar and S. Atcitty, "Switching frequency optimization of a high-frequency link based energy storage system," in *IECON 2014 - 40th Annual Conference of the IEEE Industrial Electronics Society*, Dallas, 2014.
- [78] G. Xu, D. Sha, J. Zhang and L. Xiaozhung, "Unified Boundary Trapezoidal Modulation Control Utilizing Fixed Duty Cycle Compensation and Magnetizing Current Design for

- Dual Active Bridge DC–DC Converter," *IEEE Transactions on Power Electronics*, vol. 32, no. 3, pp. 2243-2252, 2017.
- [79] M. Nmikawa, H. Ninomiya and T. Yamaji, "High Silicon Steel Sheets Realizing Excellent High Frequency Reactor Performance," JFE Holdings, Tokyo, 2005.
- [80] V. J. Thottuvelil, T. G. Wilson and H. A. J. Owen, "High-Frequency Measurement Techniques for Magnetic Cores," *IEEE Transactions on Power Electronics*, vol. 5, no. 1, pp. 41-53, 1990.
- [81] D. Hou, M. Mu, F. C. Lee and Q. Li, "New core loss measurement method with partial cancellation concept," in *2014 IEEE Applied Power Electronics Conference and Exposition - APEC*, Fort Worth, TX, 2014.
- [82] S. Kernion, P. Ohodnicki Jr., J. Grossmann, A. Leary, S. Shen, V. Keylin, J. Huth, J. Horwath, M. Lucas and M. McHenry, "Giant Induced Magnetic Anisotropy in Strain Annealed Co-based Nanocomposite Alloys," *Applied Physics*, vol. 101, no. 10, p. 102408, 2012.
- [83] I. The Gund Company, "NEMA Grade. GPO3 Glass Polyester Laminate," The Gund Company Technical Library, St. Louis, 2007.
- [84] R. M. White, *Quantum Theory of Magnetism: Magnetic Properties of Materials*, 3rd ed., Berlin: Springer, 2007.
- [85] ABB Power T&D Company Inc., *Power Transformers and Reactors*, vol. 5, Raleigh: ABB Electric Systems Technology Institute, 1997, pp. 96-101.
- [86] A. Chub, D. Vinnikov, F. Blaabjerg and F. Z. Peng, "A Review of Galvanically Isolated Impedance-Source DC-DC Converters," *IEEE Transactions on Power Electronics*, vol. 31, no. 4, pp. 2808-2828, 2016.
- [87] M. N. Kheraluwala, R. W. Gascoigne, D. M. Divan and E. D. Baumann, "Performance Characterization of High-Power Dual Active Bridge DC-to-DC Converter," *IEEE Transactions on Industry Applications*, vol. 28, no. 6, pp. 1294-1301, 1992.
- [88] B. Cougo and J. W. Kolar, "Integration of Leakage Inductance in Tape Wound Core Transformers for Dual Active Bridge Converters," in *2012 7th International Conference on Integrated Power Electronics Systems*, Nuremberg, 2012.
- [89] C. J. Carpenter, "Theory of flux penetration into laminated iron and associated losses," *Proceedings of the Institution of Electrical Engineers*, vol. 124, no. 7, pp. 659-664, 1977.
- [90] R. F. Hemmings and G. D. Wale, "Heating in transformer cores due to radial leakage flux. Part 1: Experimental models and test results," *Proceedings of the Institution of Electrical Engineers*, vol. 124, no. 12, pp. 1064-1072, 1977.
- [91] C. J. Carpenter, K. O. Sharples and M. Djurovic, "Heating in transformer cores due to radial leakage flux. Part 2: Computed results," *Proceedings of the Institution of Electrical Engineers*, vol. 124, no. 12, pp. 1181-1186, 1977.
- [92] S. Yang, Z. Cheng, W. Yan, Q. Yang and Y. Du, "Stray loss analysis for magnetic shielding with lamination," in *International Conference on Electrical Machines and Systems*, Wuhan, 2008.
- [93] A. M. Milagre, M. V. Ferreira da Luz, G. M. Cangane, A. Komar and P. A. Avelino, "3D calculation and modeling of eddy current losses in a large power transformer," in *XXth International Conference on Electrical Machines*, Marseille, 2012.

- [94] Z. Cheng, N. Takahashi and B. Forghani, "TEAM Problem 21 Family (V.2009)," in *Compumag-2009*, Florianópolis, Brazil, 2009.
- [95] S. Sudhoff, *Power Magnetic Devices*, 1 ed., Hoboken, NJ: Wiley, 2014, pp. 45-87.
- [96] F. de Leon, S. Purushothaman and L. Qaseer, "Leakage Inductance Design of Toroidal Transformers by Sector Winding," *IEEE Transactions on Power Electronics*, vol. 29, no. 1, pp. 473-480, 2014.
- [97] A. Taher, S. Sudhoff and S. Pekarek, "Calculation of a Tape-Wound Transformer Leakage Inductance Using the MEC Model," *IEEE Transactions on Energy Conversion*, vol. 30, no. 2, pp. 541-549, 2015.
- [98] H. Roters, *Electromagnetic Devices*, 1 ed., New York: Wiley, 1941, pp. 116-147.
- [99] J. Ziske, H. Neubert and R. Disselnkötter, "Modeling of Anisotropic Laminated Magnetic Cores using Homogenization Approaches," in *COMSOL Conference*, Cambridge, 2014.
- [100] J. Silveyra, P. Xu, V. Keylin, V. DeGeorge, A. Leary and M. E. McHenry, "Amorphous and Nanocomposite Materials for Energy-Efficient Electric Motors," *Journal of Electronic Materials*, vol. 45, no. 1, pp. 219-225, 2016.
- [101] S. Simizu, P. R. Ohodnicki and M. E. McHenry, "Metal Amorphous Nanocomposite Soft Magnetic Material-Enabled High Power Density, Rare Earth Free Rotational Machines," *IEEE Transactions on Magnetics*, vol. 54, no. 5, pp. 1-5, May 2018.
- [102] T. Kim, K. Jee, Y. Kim, D. Byun and J. Han, "High-frequency magnetic properties of soft magnetic cores based on nanocrystalline alloy powder prepared by thermal oxidation," *Journal of Magnetism and Magnetic Materials*, vol. 322, no. 16, p. 242, 2010.
- [103] H. Kim, Y. J. Chung, S. N. Yang and T. K. Lee, "Development of Mold Inductor for Power Conversion System," in *The Minerals, Metals & Materials Society, TMS 2017 146th Annual Meeting & Exhibition Supplemental Proceedings*, San Diego, 2017.
- [104] B. Cogitore, J. P. Keradec and J. Barbaroux, "The two-winding transformer: an experimental method to obtain a wide frequency range equivalent circuit," *IEEE Transactions on Instruments and Measurement*, vol. 43, no. 2, pp. 364-371, 1994.
- [105] S. Madhusoodhanan, K. Mainali, A. Tripathi, D. Patel, A. Kadavelugu, S. Bhattacharya and K. Hatua, "Performance evaluation of 15 kV SiC IGBT based medium voltage grid connected three-phase three-level NPC converter," in *IEEE Energy Conversion Congress and Exposition*, Montreal, 2015.
- [106] A. K. Tripathi and e. al., "Design Considerations of a 15-kV SiC IGBT-Based Medium-Voltage High-Frequency Isolated DC-DC Converter," *IEEE Transactions on Industry Applications*, vol. 51, no. 4, pp. 3284-3294, 2015.
- [107] L. Dalessandro, F. da Silveira Cavalcante and J. W. Kolar, "Self-Capacitance of High-Voltage Transformers," *IEEE Transactions on Power Electronics*, vol. 22, no. 5, pp. 2081-2092, 2007.
- [108] J. Biela and J. W. Kolar, "Using Transformer Parasitics for Resonant Converters -- A Review of the Calculation of the Stray Capacitance of Transformers," *IEEE Transactions on Industry Applications*, vol. 44, no. 1, pp. 223-233, 2008.
- [109] M. Albach and J. Lauter, "The winding capacitance of solid and litz wires," in *7th European Power Electronics Conference EPE*, Trondheim, 1997.

- [110] C. Liu, L. Qi, X. Cui, Z. Shen and X. Wei, "Wideband Mechanism Model and Parameter Extracting for High-Power High-Voltage High-Frequency Transformers," *IEEE Transactions on Power Electronics*, vol. 31, no. 5, pp. 3444-3455, 2016.
- [111] T. Guillod, F. Krismer and J. W. Kolar, "Electrical shielding of MV/MF transformers subjected to high dv/dt PWM voltages," in *IEEE Applied Power Electronics Conference and Exposition*, Tampa, 2017.
- [112] R. W. Erickson, "Eddy Currents in Winding Conductors," in *Fundamentals of Power Electronics*, 2 ed., New York, Kluwer Academic Publishers, 2004, pp. 508-524.
- [113] C. R. Sullivan, "Optimal choice for number of strands in a litz-wire transformer winding," *IEEE Transactions on Power Electronics*, vol. 14, no. 2, pp. 283-291, 1999.
- [114] Jimenez, "AC Resistance Evaluation of Foil, Round and Litz Conductors in Magnetic Components," MS Dissertation, Chalmers University, Gothenburg, 2013.
- [115] F. Tourkhani and P. Viarouge, "Accurate analytical model of winding losses in round litz wire windings," *IEEE Transactions on Magnetics*, vol. 37, no. 1, pp. 538-543, 2001.
- [116] Barrios, Ursua, Marroyo and Sanchis, "Analytical Design Methodology for Litz-Wired High-Frequency Power Transformers," *IEEE Transactions on Industry Applications*, vol. 62, no. 4, pp. 2103-2113, 2015.
- [117] C. R. Sullivan, "Computationally efficient winding loss calculation with multiple windings, arbitrary waveforms, and two-dimensional or three-dimensional field geometry," *IEEE Transactions on Power Electronics*, vol. 16, no. 1, pp. 142-150, 2001.
- [118] J. Hu and C. R. Sullivan, "Analytical method for generalization of numerically optimized inductor winding shapes," in *30th Annual IEEE Power Electronics Specialists Conference*, Charleston, 1999.
- [119] J. Hu and C. R. Sullivan, "AC resistance of planar power inductors and the quasidistributed gap technique," *IEEE Transactions on Power Electronics*, vol. 26, no. 4, pp. 558-567, 2001.
- [120] J. Barranger, "Hysteresis and Eddy-Current Losses of a Transformer Lamination Viewed as an Application of the Poyting Theorem," National Aeronautics and Space Administration, Washington D.C., 1965.
- [121] L. Havez, "Contribution au Prototypage Virtuel 3D par Eléments Finis de Composants Magnétiques Utilisés en Electronique de Puissance," PhD Dissertation, National Institute of Technology, Toulouse, 2016.
- [122] C. C. Hwang, P. H. Tang and Y. H. Jiang, "Thermal analysis of high-frequency transformers using finite elements coupled with temperature rise method," *IEEE Proceedings - Electric Power Applications*, vol. 152, no. 4, pp. 832-836, 2005.
- [123] M. Djamali and S. Tenbohlen, "Hundred years of experience in the dynamic thermal modelling of power transformers," *IET Generation, Transmission & Distribution*, vol. 11, no. 11, pp. 2731-2739, 2017.
- [124] R. L. Steigerwald, R. W. De Doncker and M. H. Kheraluwala, "A comparison of high power DC-to-DC soft-switched converter topologies," in *Industry Applications Society Annual Meeting*, Denver, 1994.

- [125] V. M. Lyer, S. Gulur and S. Bhattacharya, "Hybrid control strategy to extend the ZVS range of a dual active bridge converter," in *2017 Applied Power Electronics Conference*, Tampa, 2017.
- [126] R. Beddingfield, D. Storelli and S. Bhattacharya, "A novel dual voltage source converter for magnetic material characterization with trapezoidal excitation," in *Applied Power Electronics Conference*, Tampa, 2017.
- [127] R. Beddingfield and S. Bhattacharya, "Multi-parameter Magnetic Material Characterization for High Power Medium Frequency Converters," in *146th Annual Minerals, Metals and Materials Society Supplemental Proceedings*, San Diego, 2017.
- [128] N. Aronhime, V. Degeorge, V. Keylin, P. Ohodnicki and M. McHenry, "The Effects of Strain-Annealing on Tuning Permeability and Lowering Losses in Fe-Ni-Based Metal Amorphous Nanocomposites," *Journal of Mineral Metals and Materials Society*, vol. 69, no. 11, p. 2164, 2017.
- [129] A. Leary, V. Keylin, A. Devaraj, V. DeGeorge, P. Ohodnicki and M. E. McHenry, "Stress induced anisotropy in Co-rich magnetic nanocomposites for inductive applications," *Journal of Material Research*, vol. 31, no. 20, p. 3089, 2016.
- [130] A. Leary, P. Ohodnicki, M. McHenry and V. Keylin, "Tunable Anisotropy of Co-Based Nanocomposites for Magnetic Field Sensing and Inductor Applications". United States of America Patent 15/205,217, 7 August 2016.
- [131] V. Keylin, P. Ohodnicki, A. Leary and M. McHenry, "Stress induced anisotropy in CoFeMn soft magnetic nanocomposites," *Journal of Applied Physics*, vol. 117, no. 17, p. 17A338, 2015.
- [132] A. Leary, P. O. P., M. McHenry, V. Keylin, J. Huth and S. Kernion, "Tunable anisotropy of Co-based nanocomposites for magnetic field sensing and inductor applications. US Patent (2016)". United States of America Patent US20140338793A1, 15 May 2013.
- [133] P. Ohodnicki, J. Long, D. Laughlin, M. McHenry, V. Keylin and J. Huth, "Composition dependence of field induced anisotropy in ferromagnetic (Co, Fe) 89 Zr 7 B 4 and (Co, Fe) 88 Zr 7 B 4 Cu 1 amorphous and nanocrystalline ribbons," *Journal of Applied Physics*, vol. 104, no. 11, p. 113909, 2008.
- [134] S. O. Kasap, "Essential Heat Transfer for Electrical Engineers," Web-Materials, Saskatchewan, CA, 2003.
- [135] W. G. Odenaal and J. A. Ferreira, "A thermal model for high-frequency magnetic components," *IEEE Transactions on Industry Applications*, vol. 35, no. 2, pp. 924-931, 1999.
- [136] T. Miyazaki and H. Jin, *The Physics of Ferromagnetism*, 1 ed., Berlin: Springer-Verlag, 2012.
- [137] A. Hilal, M. A. Raulet and C. Martin, "Magnetic Components Dynamic Modeling with Thermal Coupling for Circuit Simulators," *IEEE Transactions on Magnetics*, vol. 50, no. 4, p. 1, 2014.
- [138] A. K. Das, Z. Wei, S. Vaisambhayana, S. Cao, H. Tian, T. A. and P. Kjær, "Thermal modeling and transient behavior analysis of a medium-frequency high-power transformer," in *43rd Annual Conference of IEEE Industrial Electronics Society*, Beijing, 2017.

- [139] S. Kasap, *Principles of Electrical Engineering Materials and Devices*, 2 ed., Boston: McGraw-Hill, 2002.
- [140] T. Schutze, "Thermal Equivalent Circuit Models," Infineon, Warstein, Germany, 2008.
- [141] C. P. Kothandaraman, "An Overview of Heat Transfer," in *Fundamentals of Heat Transfer*, 3 ed., Daryaganj, New Age International, 2006.
- [142] C. P. Kothandaraman, "Transient Heat Conduction," in *Fundamentals of Heat Transfer*, 3 ed., Daryaganj, New Age International, 2006.
- [143] N. Seshasayee, "Understanding Thermal Dissipation and Design of a Heatsink," Texas Instruments, Dallas, 2011.
- [144] N. Laaidi, S. Belattar and A. Elbaloutti, "Thermal and Thermographical Modeling of the Rust Effect in Oil Conduits," in *European Conference on Non-Destructive Testing*, Moscow, 2010.
- [145] "3M Thermally Conductive Epoxy Adhesive TC-2810," 3M Electronics Materials Solutions Division Tech. Report, St. Paul, MN, 2014.
- [146] A. Leary, P. Ohodnicki and M. McHenry, "Soft Magnetic Materials in High-Frequency, High-Power Conversion Applications," *Journal of the Minerals, Metals and Materials Society (TMS)*, vol. 64, no. 7, p. 772, 2012.
- [147] "L Material," Magnetics, 2018. [Online]. Available: <https://www.mag-inc.com/Products/Ferrite-Cores/L-Material>. [Accessed 10 December 2017].
- [148] P. Xuewei, U. R. Prasanna and A. A. Rathore, "Magnetizing-Inductance-Assisted Extended Range Soft-Switching Three-Phase AC-Link Current-Fed DC/DC Converter for Low DC Voltage Applications," *IEEE Transactions on Power Electronics*, vol. 28, no. 7, p. 3317, 2013.
- [149] R. Beddingfield, P. P. Vora, D. Storelli and S. S. Bhattacharya, "Trapezoidal characterization of magnetic materials with a novel dual voltage test circuit," in *IEEE Energy Conversion Congress and Expo*, Cincinnati, 2017.
- [150] B. Cougo, "Optimal cross section shape of tape wound cores," in *2015 17th European Conference on Power Electronics and Applications*, Geneva, 2015.
- [151] F. W. J. Olver, A. B. Olde Daalhuis, D. W. Lozier, B. I. Schneider, R. F. Boisvert, C. W. Clark, B. R. Miller and B. V. e. Saunders, "Incomplete Beta Functions," NIST Digital Library of Mathematical Functions, 27 March 2018. [Online]. Available: <https://dlmf.nist.gov/8.17>. [Accessed 23 April 2018].
- [152] K. Byerly, P. Ohodnicki, S. Moon, A. Leary, V. Keylin, M. McHenry, S. Simizu, R. Beddingfield, Y. Yu, G. Feichter, R. Noebe and R. B. S. Bowman, "Metal amorphous nanocomposite (MANC) alloy cores with spatially tuned permeability for advanced power magnetics applications," *Journal of the Minerals, Metals and Materials Society (TMS)*, vol. 70, no. 6, p. 879–891, 2018.
- [153] M. Smith and D. Ton, "Key Connections: The U.S. Department of Energy's Microgrid Initiative," *IEEE Power and Energy Magazine*, vol. 11, no. 4, pp. 22-27, 2013.
- [154] Z. Jin, G. Sulligoi, R. Cuzner, L. Meng, J. C. Vasquez and J. M. Guerrero, "Next-Generation Shipboard DC Power System: Introduction Smart Grid and dc Microgrid Technologies into Maritime Electrical Networks," *IEEE Electrification Magazine*, vol. 4, no. 2, pp. 45-57, 2016.

- [155] C. Yuan, M. A. Haj-ahmed and M. S. Illindala, "An MVDC microgrid for a remote area mine site: Protection, operation and control," in *IEEE Industry Application Society Annual Meeting*, Vancouver, 2014.
- [156] "ONR's Broad Agency Announcement BAA#08," Office of Naval Research, Arlington, 2008.
- [157] N. Doerry, "ONR's Next Generation Integrated Power System (NGIPS) technology roadmap, Ser 05D/349," Naval Sea Systems Command, Washington, D.C., 2007.
- [158] H. Mirzaee, S. Bhattacharya and S. Bala, "Design Issues in a Medium-Voltage DC Amplifier with a Multi-Pulse Thyristor Bridge Front-End," in *IEEE Energy Conversion Congress and Exposition (ECCE)*, Raleigh, 2012.
- [159] H. Mirzaee, S. Bhattacharya and S. Bala, "A high power medium-voltage dc amplifier system," in *IEEE Energy Conversion Congress and Exposition (ECCE)*, Phoenix, 2011.
- [160] G. Xiao, J. Liu, K. Li and Z. Wang, "New control scheme for series DC active power filters coupled by transformers applied to high performance magnet power supplies," in *International Power Electronics and Motion Control Conference*, Xi'an, 2004.
- [161] H. Jimichi, H. Fujita and H. Akagi, "An Approach to Eliminating DC Magnetic Flux from the Series Transformer of a Dynamic Voltage Restorer," *IEEE Transactions on Industry Applications*, vol. 44, no. 3, pp. 809-816, 2008.
- [162] Z. Chen, M. Chen, Y. Luo and C. Wang, "Low frequency ripple current compensation with DC active filter for the single-phase aeronautic static inverter," in *IEEE Energy Conversion Congress and Exposition*, Phoenix, 2011.
- [163] X. Ma, B. Wang, F. Zhao, G. Qu, D. Gao and Z. Zhou, "A high power low ripple high dynamic performance DC power supply based on thyristor converter and active filter," in *IEEE Annual Conference of the Industrial Electronics Society (IECON)*, Sevilla, 2002.
- [164] R. Beddingfield, A. Davis, H. Mirzaee and S. Bhattacharya, "Investigation of series DC active filter and hybrid AC active filter performance in medium voltage DC amplifier," in *IEEE Electric Ship Technologies Symposium*, Alexandria, 2015.
- [165] H. Mirzaee, B. Parkhideh and S. Bhattacharya, "Design and Control of Series DC Active Filter (SDAF) for Shipboard Medium-Voltage DC Power System," in *IEEE Electric Ship Technologies Symposium (ESTS)*, Alexandria, 2011.
- [166] S. Bhattacharya, T. M. Frank, D. M. Divan and B. Banerjee, "Active filter system implementation," *IEEE Industry Applications Magazine*, vol. 4, no. 5, pp. 47-63, 1998.
- [167] J. P. Joule, "On the Effects of Magnetism upon the Dimensions of Iron and Steel Bars," *The London, Edinburgh and Dublin Philosophical Magazine and Journal of Science*, vol. 30, no. 199, pp. 76-87, 1847.
- [168] M. J. Heathcote, "Transformer Construction," in *The J & P Transformer Book*, 13th ed., London, Newnes, 2007.
- [169] M. J. Heathcote, "Basic Materials," in *The J & P Transformer Book*, 13th ed., London, Newnes, 2007.
- [170] H. Chen and D. Divan, "Soft-Switching Solid State Transformer (S4T)," in *IEEE Energy Conversion Congress and Exposition (ECCE)*, Milwaukee, 2016.
- [171] H. Chen and D. Divan, "Design of a 10-kV·A Soft-Switching Solid-State Transformer (S4T)," *IEEE Transactions on Power Electronics*, vol. 33, no. 7, pp. 5724-5738, 2018.

- [172] M. S. Hamad, M. I. Masoud and B. W. Williams, "Medium-Voltage 12-Pulse Converter: Output Voltage Harmonic Compensation Using a Series APF," *IEEE Transactions on Industrial Electronics*, vol. 61, no. 1, pp. 43-52, 2014.
- [173] R. Beddingfield, A. De, H. Mirzae and S. Bhattacharya, "Design methodology of series DC coupling Transformer in a medium-voltage DC amplifier system," in *Applied Power Electronics Conference and Exposition (APEC)*, Charlotte, 2015.
- [174] R. G. Lyons, *Understanding Digital Signal Processing*, 3 ed., Boston: Pearson Education Inc., 2011, pp. 762-765.
- [175] A. G. Yepes, "Digital Resonant Current Controllers for Voltage Source Converters," PhD Dissertation, Univeristy of Vigo, Vigo, 2011.
- [176] T. Hatakeyama and K. Onda, "Novel evaluation method for the volume of transformers with various magnetic cores," in *2011 IEEE Ninth International Conference on Power Electronics and Drive Systems*, Singapore, 2011.
- [177] K. Mainali, A. Tripathi, D. C. Patel, S. Bhattacharya and T. Challita, "Design, measurement and equivalent circuit synthesis of high power HF transformer for three-phase composite dual active bridge topology," in *2014 IEEE Applied Power Electronics Conference and Exposition*, Fort Worth, 2014.
- [178] R. Erickson, *Fundamentals of Power Electronics*, New York: Kluwer Academic Publishers, 2004.
- [179] M. H. Kheraluwala, D. W. Novotny and D. M. Divan, "Design considerations for high power high frequency transformers," in *21st Annual IEEE Conference on Power Electronics Specialists*, San Antonio, 1990.
- [180] M. S. Rauls, D. W. Novotny, D. M. Divan, R. R. Bacon and R. W. Gascoigne, "Multi-turn high frequency co-axial winding power transformers," in *Conference Record of the 1992 IEEE Industry Applications Society Annual Meeting*, Houston, 1992.
- [181] H. Weigman, "A DC/DC Converter for A Dual Voltage Automotive System," MS Dissertation, University Wisconsin, Madison, 1991.
- [182] K. Klontz, "Analysis and Design of a Coaxial Winding Transformer Interface for an Electric Vehical Charging System," PhD Dissertation, University of Wisconsin, Madison, 1995.
- [183] M. H. Kheraluwala, D. W. Novotny and D. M. Divan, "Coaxially wound transformers for high-power high-frequency applications," *IEEE Transactions on Power Electronics*, vol. 7, no. 1, pp. 54-62, 1992.
- [184] C. Sun, N. H. Kutkut, D. W. Novotny and D. M. Divan, "General equivalent circuit of a multi-winding coaxial winding transformer," in *Industry Applications Conference*, Orlando, 1995.
- [185] M. S. Raul, D. W. Novotny, D. M. Divan, R. R. Bacon and R. W. Gascoigne, "Multi-turn high frequency coaxial winding power transformers," in *Conference Record of the 1992 IEEE Industry Applications Society Annual Meeting*, Houston, 1992.
- [186] S. Baek and S. Bhattacharya, "Analytical Modeling and Implementation of a Coaxially Wound Transformer with Integrated Filter Inductance for Isolated Soft-Switching DC-DC Converters," *IEEE Transactions on Industrial Electronics*, vol. 65, no. 3, pp. 2245-2255, 2018.

- [187] NEMA, *Guide to OSHA and NFPA 70E Safety Requirements When Servicing and Maintaining Medium-Voltage Switchgear, Circuit Breakers, and Medium-Voltage Controllers Rated above 1000 V*, NEMA SG 10, 2013.
- [188] S. Baek, S. Roy, S. Bhattacharya and S. Kim, "Power Flow Analysis for 3-Port 3-Phase Dual Active Bridge DC/DC Converter and Design Validation Using High Frequency Planar Transformer," in *IEEE Energy Conversion Congress and Exposition*, Denver, 2013.
- [189] A. Rodriguez, A. Vazquez, D. G. Lamar and M. M. Hernando, "Three-Port Power Electronic System for Energy Storage and Recovery Using a Parallel Connection of Power Factor Corrector Boost and A Dual Active Bridge," in *Power Electronics and Motion Control Conference*, Novi Sad, 2012.

**APPENDICES**

## Appendix A: Derivation for Linear Graded with Offset Permeability Profile

Let us first define the profiles for permeability and flux density when a linear permeability with an offset is desired.

$$\mu(r) = \mu_1 + \mu_s r = \mu_1(1 + gr) \qquad B(r) = \frac{\mu(r)NI}{2\pi r} = \frac{\mu_1(1 + gr)NI}{2\pi r}$$

We then apply these profiles to the local loss form of magnetizing power loss function.

$$P_{loc-\mu_1} = kf^\alpha \int C(r)B(r)^\beta dr$$

$$P_{loc-\mu_1} = kf^\alpha \int h2\pi r \left( \frac{\mu_1(1 + gr)NI}{2\pi r} \right)^\beta dr = kf^\alpha h2\pi \left( \frac{NI}{2\pi} \right)^\beta \mu_1^\beta \int r \left( \frac{1}{r} + g \right)^\beta dr$$

After simplifying by extracting all viable constants, it is clear that the remaining integral is nontrivial nor are typical integration and simplification techniques applicable. However, this integral is similar to the form of the special function, the Chebyshev integral. The following steps demonstrate the algebraic manipulations necessary for the proper form. The first simplification is to ensure that,  $r$ , the variable of integration, is only in the numerator.

$$P_{loc-\mu_1} = kf^\alpha h2\pi \left( \frac{NI}{2\pi} \right)^\beta \mu_1^\beta \int r \left( \frac{1}{r} + g \right)^\beta dr = kf^\alpha h2\pi \left( \frac{NI}{2\pi} \right)^\beta \mu_1^\beta \int r^{1-\beta} (1 + gr)^\beta dr$$

Next, the two exponentials must have the same base with the second exponential base being in the form of  $1-x$ . That is with  $x$  representing the variable of integration.

$$P_{loc-\mu_1} = kf^\alpha h2\pi \left( \frac{NI}{2\pi} \right)^\beta \mu_1^\beta \int \left( \frac{-gr}{-g} \right)^{1-\beta} (1 - -gr)^\beta dr$$

Then by extracting a  $\left( \frac{1}{-g} \right)^{1-\beta}$  from within the integrand, a form that is similar to the desired Chebyshev integral is found.

$$P_{loc-\mu_1} = kf^\alpha h2\pi \left( \frac{NI}{2\pi} \right)^\beta \mu_1^\beta (-g)^{\beta-1} \int (-gr)^{1-\beta} (1 - -gr)^\beta dr$$

Simple substitution, allows the transformation to the desired form to complete. Let  $z = -gr$ ,  $p = 1 - \beta$ ,  $q = \beta$ , and  $dz = -gdr$  then  $dr = (-g)^{-1}dz$ . This leaves only design constants the desired form for the integral with a known solution, as shown below.

$$P_{loc-\mu_1} = kf^\alpha h2\pi \left(\frac{NI}{2\pi}\right)^\beta \mu_1^\beta (-g)^{\beta-2} \int (z)^p (1-z)^q dz$$

We can then use the solution to the Chebyshev integral, which has a solution using the incomplete beta function. This can be used to find a solution the equation for local magnetizing power loss.

$$P_{loc-\mu_1} = kf^\alpha h2\pi \left(\frac{NI}{2\pi}\right)^\beta \mu_1^\beta (-g)^{\beta-1} B_{-gr}[2-\beta, 1+\beta]$$

The definite integral, representing the magnetizing loss for a core of finite dimensions, utilizes the above solution and is shown above in equation (5.28).

## Appendix B: Soft Start Switch for Medium Voltage

### Appendix B.1: Motivation

In order to take full advantage of the high induction magnetics and WBG devices while minimizing conduction losses, higher exciting voltages are expected. There is a need to charge the DC buses in a controlled manner. The following presents a novel switch configuration for such soft starting. It is also a question of developing test equipment and laboratory capabilities. Developing a safe and controlled medium voltage DC bus is a challenge and even more so when operating at medium voltage in a laboratory. Oftentimes, the laboratory power source is not rated to very high voltages due to the significant increase in safety and procedural requirements, [187]. However, higher current systems are easier to protect and thus construct and assemble.

Therefore, a high power, high current, low voltage source can be used with a boost type converter to gain medium voltage capabilities within test equipment.

Given the high short circuit capability and the need for a medium voltage bus, careful protection and energization schemes are needed to achieve the desired testing levels. A typical way to charge the medium voltage DC bus is to increase the circuit time constant with series resistors that are bypassed with a relay for steady state operation. Alternatively, an auxiliary circuit can charge the DC bus from a lower source voltage. Both of these solutions can successfully charge the main power bus in a controller manner. However, they do not offer fault protection and they cannot connect directly to medium voltage.

### Appendix B.2: Proposed Switch

A proposed solution is to connect a thyristor in parallel with an active switch, an IGBT. This thyristor will replace the traditional freewheeling diode that is typically parallel to these devices. An example of this IGBT / Thyristor device is shown below in Figure B.0.1, the IGBT collector is connected to the thyristor cathode and the IGBT emitter is connected to the thyristor anode. The gate of both the IGBT and thyristor are pulled out of the package for connection to control signals.

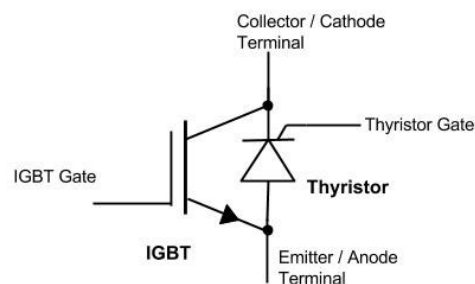


Figure B.0.1: IGBT Thyristor Topology.

### Appendix B.3: Converters with Proposed Switch

This device is intended to apply in AC to DC converters. The thyristor is only needed to replace a small portion of the freewheeling diodes in a converter. Examples of this partial replacement are shown in Figure B.0.2, Figure B.0.3, and Figure B.0.4 which are a non-exhaustive list of topology examples where the application of this device could be beneficial. The new process for soft starting these devices replaces a separate charge circuit. Commutating the Thyristor with the AC mains and a ramp increase to the firing angle allows a slow ramp of current magnitude to pass through the thyristor and additional diodes in the converter. Once the DC bus is charged to the desired level, the firing angle is held at this level. And the SiC device can begin PWM based operation. Since the Thyristor can be commutated for less than full conduction, this enables buck operation of the power converter. If, classic operation of the power converter is needed, the thyristor can be commutated at 180 degrees or always on and thus behave like the diode it replaces. In the case of a fault on the DC bus, turning off the Thyristor commutation prevents power flow through the remaining diodes. This will halt current within 1 half cycle of the AC wave and cause a collapse of the DC bus and subsequent decay of DC current feeding the fault.

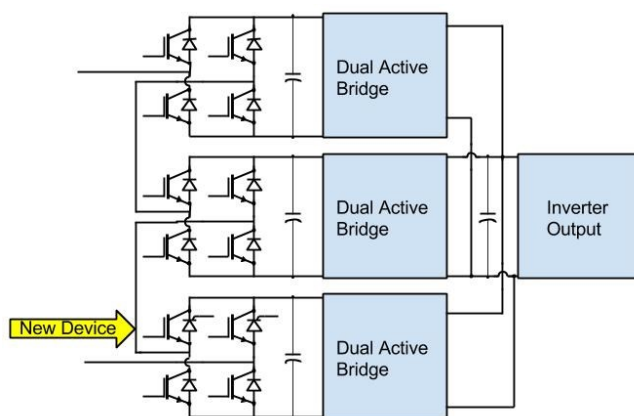


Figure B.0.2: SST With Soft Start Switch.

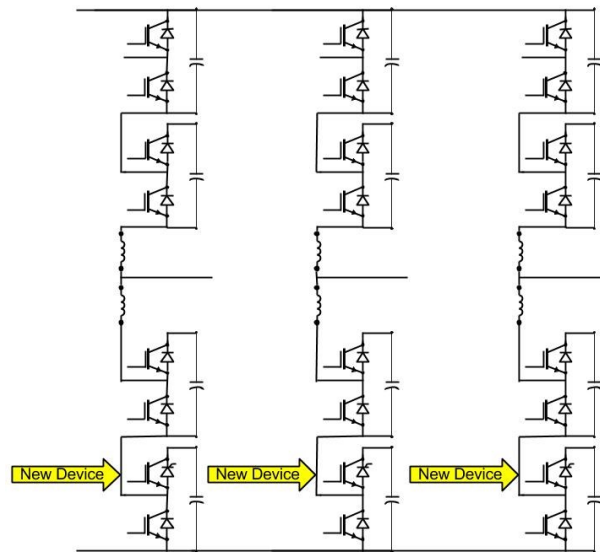


Figure B.0.3: MMC With Soft Start Switch.

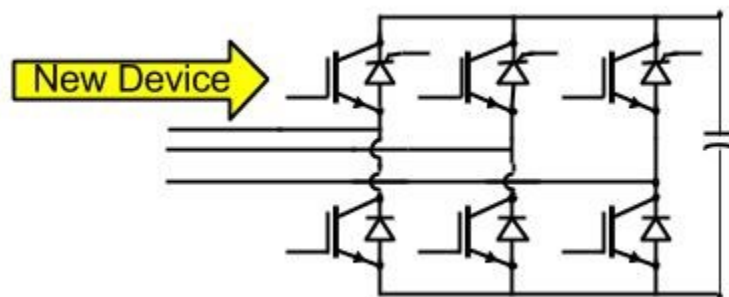


Figure B.0.4: Three Phase Active Front End with Soft Start Switch.

#### Appendix B.4: Charge Up

Circuit simulations are used to verify the efficacy of this approach. The simulations were performed using PLECS simulation. Figure B.0.5, below, shows the inrush current and DC Link charge up with a simple H-Bridge boost rectifier. In the surge charge, a low resistance is in series with the converter leading to a large current peak as the capacitor of the DC link is initially charged. All of this current flows through the traditional freewheeling diodes.

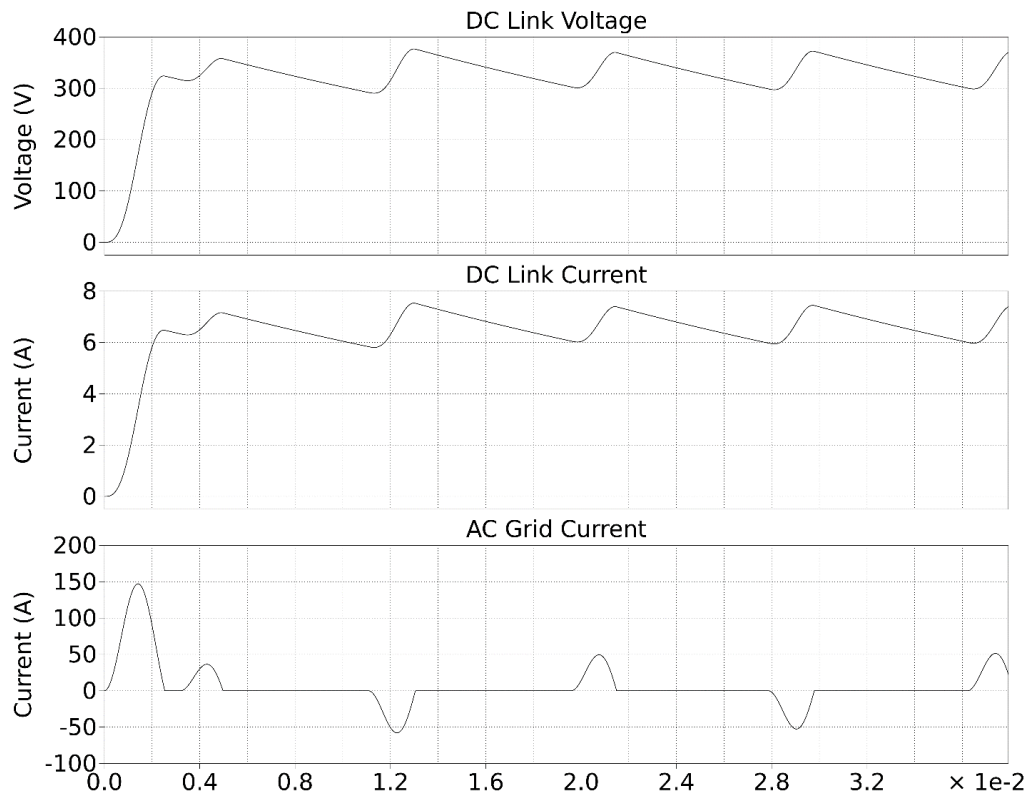


Figure B.0.5: Surge Start Through Low Resistance.

It is clear, that in the traditional circuit startup, a very high inrush current charges the DC link almost instantaneously. As the DC bus is charged, the current flows the diodes until the DC link voltage reaches steady state levels.

However, if a thyristor is used to replace the freewheeling diodes as proposed, the DC link can be charged in a controlled manner. Figure B.0.6 shows such a controlled charge operation. It is obvious from the time scale that this charging process is under deliberate control. Furthermore, the charge current is significantly limited and never surges beyond steady state levels. This means that a converter and all associated auxiliary components will experience less overloading stress during start up. This soft starting procedure was controlled by gradually reducing the firing delay angle of the thyristors, as seen in the bottom plot. This rate of change of firing angle ultimately controls the charge time of the DC link and could be modified as needed for specific applications.

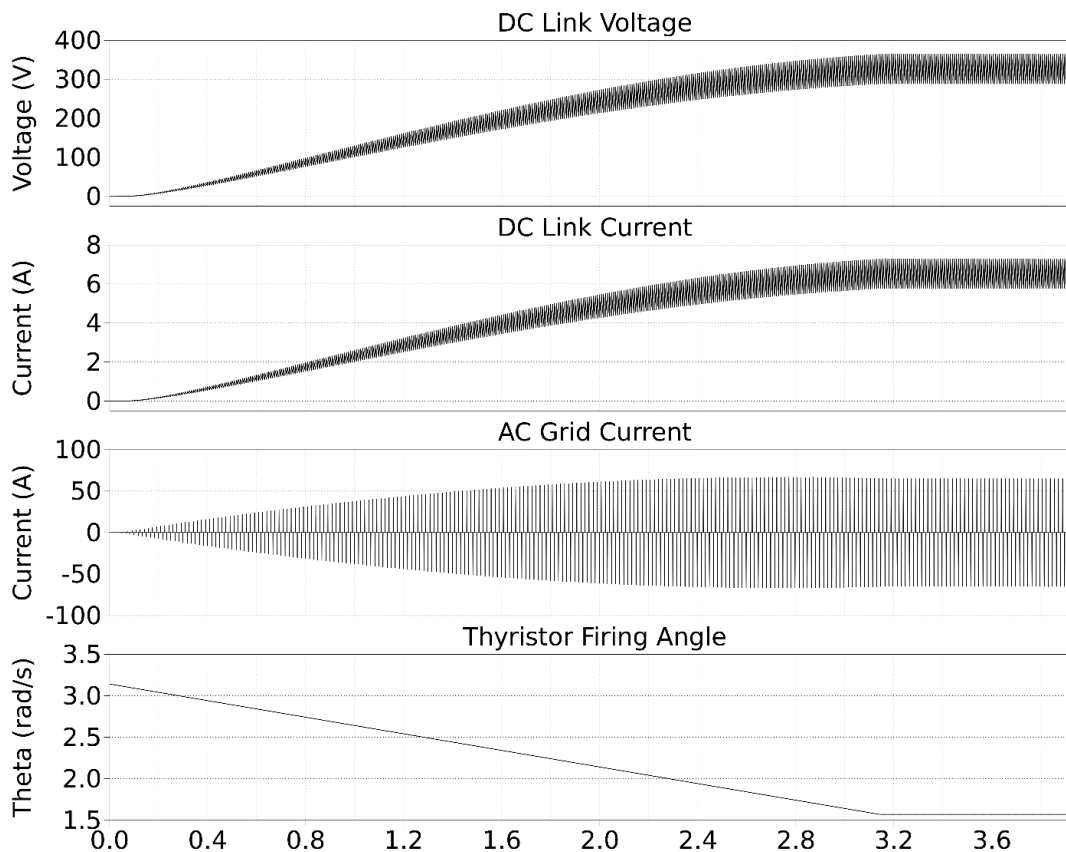
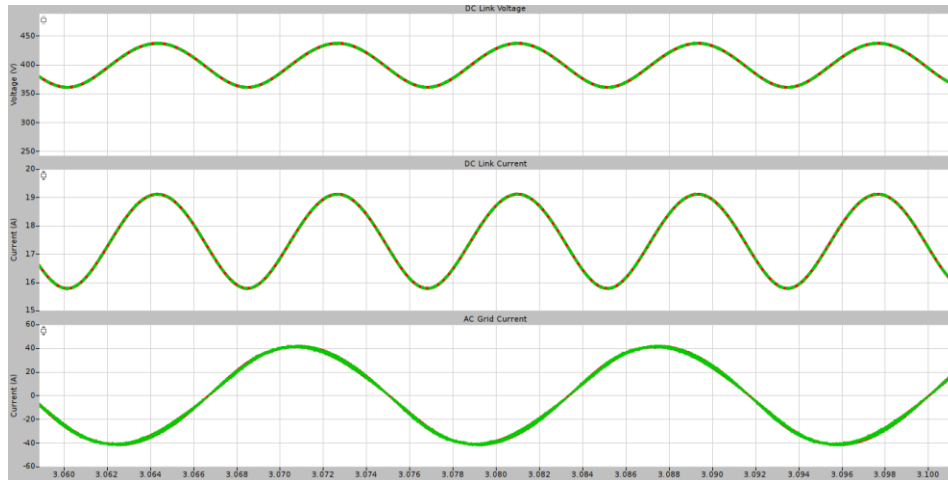


Figure B.0.6: Soft Start Through IGBT Thyristor Switch.

### Appendix B.5: Steady State

It is also important to compare the steady state operation of the traditional and proposed charging circuits. Once the DC link has reached steady state after either the surge charge or soft charge, the IGBTs can begin operating in boost mode as a synchronous boost rectifier. The thyristor behaves just as diodes do when their firing signal is held on. This enables the steady state operation of the diodes and thyristor based circuits to be indistinguishable even when the IGBTs are controlled as a boost rectifier.



*Figure B.0.7: Steady State Operation.  
Green = Traditional Parallel Diode; Red = Proposed Parallel Thyristor.*

## Appendix B.6: Fault Conditions

One of the drawbacks of the traditional voltage source converters is the inability quickly stop faults. Generally, an additional relay or circuit breaker is needed that can handle these faults. As can be seen in the below image, the IGBTs are cut off when the current reaches the 60 Amp trip threshold. However, because of the diodes, the fault continues to be supplied by the power converter. This will continue until a circuit breaker is activated and the AC source is disconnected from the converter. This could have a cascaded effect as circuit breakers generally feed multiple loads and systems. As the circuit breaker opens to protect one converters fault, everything downstream will also be disconnected.

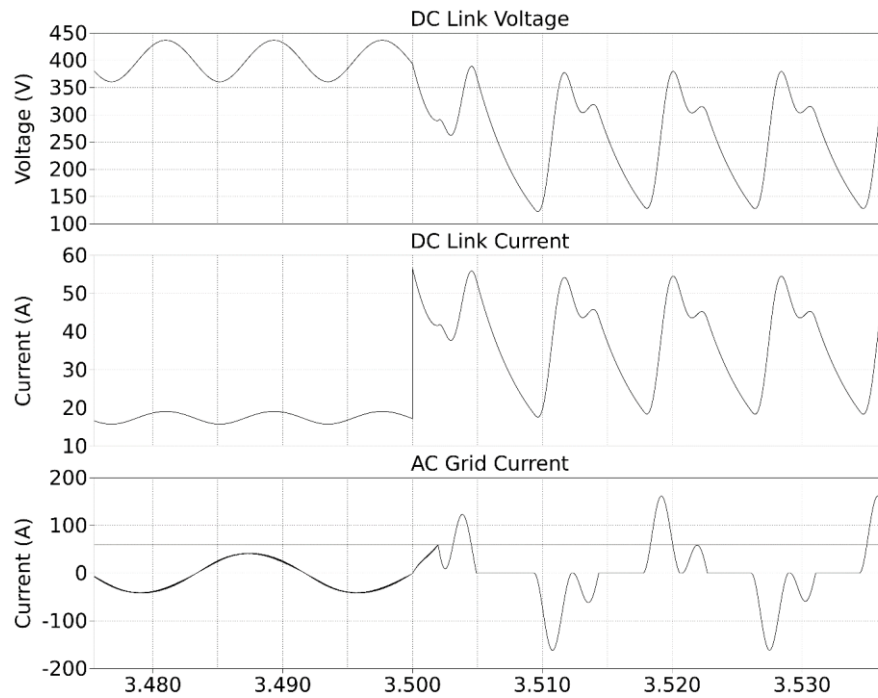


Figure B.0.8: Fault Condition in Traditional Active Front End.

One of the advantages of the parallel thyristor is the ability to discontinue gating once a fault condition is detected. This means that once detected, a fault will be cleared in at most one AC half cycle. The thyristor will continue to conduct after gating signals have been removed but will cease conduction when the switch voltage is reversed. Unlike the diode though, the thyristor will not begin conducting again with positive switch voltage. Another advantage of this protection scheme is that only the faulted converter is disconnected from the AC source leaving all other loads unaffected. The proposed topology not only clears faults quickly but has a reasonable chance of reducing the maximum fault current. This is because only the remainder of a half cycle will feed the fault. If the fault system is tripped after peak voltage, the resulting maximum fault current will be less than a traditional circuit which experiences a ‘second dose’ of fault current on the next half cycle. Furthermore, advanced protection schemes that are present in newer smart circuit breakers can also be employed with this protection scheme. This enables the parallel thyristor IGBT switch to be a robust protection solution.

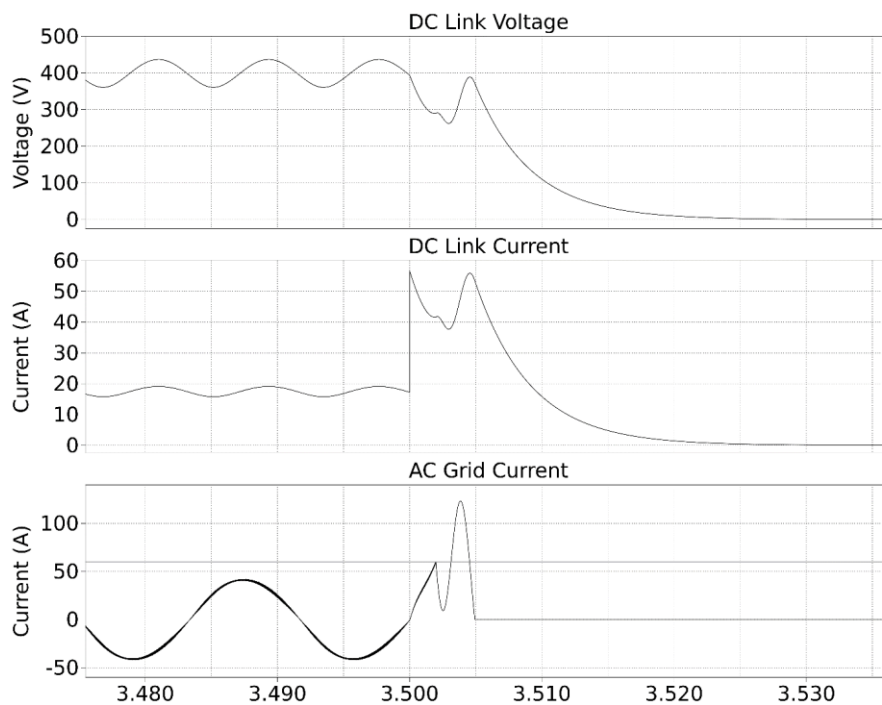


Figure B.0.9: Fault Suppression with Proposed Switch.

## Appendix B.7: Conclusion and Future Work

A proposed new IGBT switch topology that replaces a traditional freewheeling diode with a controllable thyristor has been simulated and shown to provide many benefits for medium voltage applications. While the motivation for this switch geometry is developing safe and effective testing equipment for medium voltage magnetics, this topology can be used in many application spaces. The thyristor enables equipment reductions as charge up or resistive soft charge circuits are no longer needed. It has the potential to further reduce equipment by eliminating the need for extra protective equipment as the thyristor can assist in arresting faults on the DC link. This new topology has significant potential for advanced rectifier designs in the medium voltage space.

Future work will develop laboratory prototypes to verify the efficacy of the simulations. Similarly, research in advanced packaging will enable better module integration of the IGBT and

Thyristor than discrete components on printed circuit boards. This will result in reduced parasitic elements and ultimately a more viable switch.